ABSTRACT

Title of Dissertation:	THE CONCENTRATION OF HYDROGEN IN INCOMPLETELY AND WHOLLY MELTED TERRESTRIAL BUILDING BLOCKS
	Liam D. Peterson, Doctor of Philosophy, 2024
Dissertation directed by:	Assistant Professor, Megan Newcombe, Department of Geology

Hydrogen (H) is the most abundant element in our solar system and exerts a primary control on the habitability, and geochemical and geodynamic evolution of rocky bodies. Therefore, constraining the source(s), timing of accretion, and abundance of H in the Earth and other bodies is of fundamental importance for understanding how planets evolve. Direct constraints on the source(s) of H and other highly volatile elements (HVEs; e.g., H, C, F, Cl, and S) to the bulk Earth can be provided by analyzing meteorites, which are the remnants of early-formed rocky bodies that were present during the accretion of the terrestrial planets. Such samples either directly sample or provide analogs for terrestrial precursor materials.

Rocky solar system materials can be subdivided based upon their nucleosynthetic isotopic compositions ("genetic" tracers; e.g., ^{50}Ti, ^{54}Cr) into two groups, which are thought to correspond to the inner- and outer- solar system. Materials may be further subdivided by their extent of thermal processing (i.e., unmelted, incompletely melted, and wholly melted). Earths H budget is commonly accounted for by addition of unmelted (i.e., chondritic) materials, namely

carbonaceous chondrite-like (CC-like) materials, thought to be derived from the outer solar system, which have high H concentrations (up to ~14 wt. % H_2O; total H as H_2O equivalents) and similar H isotopic compositions to the bulk Earth. Furthermore, chondrites derived from the inner solar system (e.g., ordinary and enstatite chondrites) are H-poor relative to carbonaceous chondrites. Similarly, all melted planetesimals are commonly assumed to be anhydrous. However, recent analyses of enstatite chondrites (ECs), which are formed in the inner solar system and are the closest match to the nucleosynthetic isotopic composition of the bulk Earth, suggest that ECs have a similar H isotopic composition to the bulk Earth and can account for its entire H budget. Furthermore, recent analyses suggest that melted (i.e., achondritic) bodies may retain considerable amounts of H, potentially enough to account for Earth's H budget in the case of the enstatite achondrites (i.e., aubrites). However, achondritic materials are predominantly highly H-poor relative to chondritic materials, and it is unclear if the aubrites are an anomaly, and at which stage of planetesimal evolution H and other HVEs are lost.

In chapter 2, I re-examine prior bulk analyses of H in aubrites, and by extension ECs, using *in situ* methods and suggest that nearly all H measured in aubrites by bulk methods reflects pervasive terrestrial contamination and alteration, a result which may extend to concurrent bulk H analyses of ECs. In chapters 3 and 4, I examine the H content of incompletely melted (i.e., primitive achondritic) planetesimals to constrain at what stage of planetesimal evolution H is lost. Chapter 3 characterizes the H contents of the ureilites, a group of C-rich primitive achondrites, and chapter 4 characterizes the H contents of the acapulcoite-lodranite clan which represents the "prototypical" primitive achondritic parent body. I find that primitive achondritic parent bodies are highly H-depleted relative to chondrites, requiring that H is efficiently lost prior to or at the onset of planetesimal melting, and that Earth's H budget is accounted for by

accretion of thermally primitive materials (e.g., chondrites). Within my primitive achondrite data sets, I observe apparent disequilibrium with respect to H between olivine, pyroxene, and feldspar. In chapter 5, I explore whether this apparent disequilibrium is the result of extrapolating high pressure experimental data to low pressures. I conduct olivine–melt H partitioning experiments at low pressures (10 – 200 MPa) and find that the olivine-melt H partition coefficient increases at low pressures, contrary to extrapolation from high pressure data. This observation is best explained by a control of H speciation in the melt on the partitioning of H between olivine and melt.

THE CONCENTRATION OF HYDROGEN IN INCOMPLETELY AND WHOLLY MELTED TERRESTRIAL BUILDING BLOCKS

by

Liam D. Peterson

Dissertation submitted to the Faculty of the Graduate School of the
University of Maryland, College Park, in partial fulfillment
of the requirements for the degree of
Doctor of Philosophy
2024

Advisory Committee:
Assistant Professor Megan Newcombe, Chair
Professor Richard Walker
Dr. Philip Piccoli
Dr. Richard Ash
Professor Jessica Sunshine

Preface

The majority of the research presented in this document has been submitted to and/or accepted in peer-reviewed journals. Chapters 2 and 3 are verbatim transcripts of works previously published in *Earth and Planetary Science Letters* and *Geochimica et Cosmochimica Acta*, respecitvely. Chapter 4 is a verbatim manuscript that has been accepted for publication in *Geochimica et Cosmochimica Acta*. Chapter 5 has not been submitted but has been prepared for submission to a peer reviewed journal at a later date. The author of this dissertation is the lead author of all of these works but benefitted greatly from editorial comments and revisions from co-authors Megan Newcombe, Sune Nielsen, Conel Alexander, Phil Piccoli, Austin Gion, Adam Sarafian, Jianhua Wang, Frieder Klein, Glenn Gaetani, Addi Bischoff, and David Bekaert.

Dedication

Dedicated to my parents, Dave and Susan, and my late mother, Brenda. You have supported me through the trials of life, years of a global pandemic, and the many ups-and-downs of completing a PhD. Your encouragement, and sometimes pressure, to have me outside fishing, hiking, exploring the woods and picking up shells and rocks because they were “cool” helped bring me to where I am today. Your persistent love, support, and care are pillars to strive for. I hope to continue to make you all proud.

Dedicated to my brother, Ben, the unwilling role model for much of my life. Much of my desire to learn or try new things as a child was so I could be like you. I am constantly grateful for your willingness to listen, help, or simply distract me when whatever I am grappling with starts to become overwhelming.

Dedicated to my late grandparents, Don and Nancy, and Wayne and Sharon, who were unendingly proud and loving and encouraged me to learn and love the outdoors.

Dedicated to my many friends. You are sources of joy in my life, which is no small thing.

Most importantly, dedicated to my life partner Sarah. We’ve been through growing pains, a global pandemic, financial, and family struggles since we “started dating” 10 years ago. Your unending love, care, and support helped to carry me when I needed it most. I am incredibly lucky to have spent nearly half my life with you and look forward to many more years.

Acknowledgements

Foremost, I would like to thank my advisor, Megan Newcombe, for her patience, positivity, empathy, kindness, and support. You gave me freedom to structure my PhD program and research and always gave me room to voice my scientific understandings, even when I was wrong, or we didn't agree. Perhaps the greatest lesson, which was given by example, is to always approach science and others with empathy. It is simply a recipe for personal and communal growth and success. It's been a joy to work with you during the formative years of your lab.

I would also like to thank Phil Piccoli for his guidance, many scientific talks, both for research purposes and purely for fun, and for lending an ear these past years. I'd also like to thank Austin Gion, who in addition to Phil, taught me how to function in the experimental petrology lab as well as bringing my mind back around to approaching science from a theoretical, not purely physical, perspective. Additionally, I'd like to thank my other collaborators, Sune Nielsen, Conel Alexander, Jianhua Wang, Adam Sarafian, Frieder Klein, Glenn Gaetani, Addi Bischoff, and David Bekaert.

Finally, I would like to thank the University of Maryland Department of Geology. In particular, thank you to the current and former members of the Planetary Volcanism Lab, Euan Mutch, Silvia Castilla, Kyle Kim, Cosmo Varah-Sikes, Sumedha Desikamani, and Kathy Stepien. I would also like to thank Laura Sammon, Joe Galella, Christiana Hoff, Ashley Hanna, and Rumya Ravi for welcoming me as a colleague and a friend all these years.

Table of Contents

List of Tables

List of Figures

List of Abbreviations

γ_g^{min} – the activity coefficient of a species (g = H_2O, OH, O) in a mineral

a_g^z – the activity of a species (g = H_2O, OH, O) in a phase (z = mineral, melt, fluid)

ALC – acapulcoite-lodranite clan

ALH – Allan Hills

ALM-A – Almahata Sitta ureilitic trachyandesite

ALPB – Acapulcoite-Lodranite parent body

AMN – Antarctic Meteorite Newsletter

APB – Angrite parent body

AS – aperture slit

AuPB – main group Aubrite parent body

BLOD – background-corrected limit of detection

C2 – type-2 ungrouped chondrite

CAI – calcium-aluminum rich inclusion

CC – carbonaceous

CI – Ivnua-type chondrite

CK – Karoonda-type chondrite

CM – Mighei-type chondrite

CO – Ornans-type chondrite

CPX – clinopyroxene

CR – Renazzo-type chondrite

CV – Vigrano-type chondrite

$D_{H_2O_T}^{Ol/melt}$ – Olivine-melt partition coefficient for total H

$D_{OH}^{Ol/melt}$ – Olivine-melt partition coefficient for hydroxyl

EC – Enstatite chondrite

EET – Elephant Moraine

EPL – Earth and Planets Lab

EPMA – electron microprobe analyses

ES – entrance slit

fH_2O – water fugacity

$f_{H_2O}^0$ – the fugacity of pure water at the reference state

fO_2 – oxygen fugacity

FTIR – fourier transform infrared spectroscopy

GRA – Graves Nunataks

GRO – Grosvenor Mountains

GRV – Grove Mountains

H_2O_z – molecular H_2O in a phase (z = fluid,

melt)

HED – Howardite-Eucrite-Diogenite

HVE – highly volatile element

IOM – insoluble organic materials

IW – iron- wüstite

LAP – LaPaz

LAR – Larkman Nunatak

LOD – limit of detection

M – metal cation

M_E – Earth masses

MAC – MacAlpine Hills

MHC – molybdenum-hafnium-carbide

MI – melt inclusion

MIL – Miller Range

MM/YY – date in the month/year format

MORB – Mid-ocean ridge basalt

MP – Mt. Pavlof, 2016 Ash experimental starting material

MRP – mass-resolving power

NAMs – nominally anhydrous minerals

NC – non-carbonaceous

NNO – Nickel - Nickel Oxide

NWA – northwest Africa

O_z = unprotonated oxygen in a phase (z – mineral, melt)

OC – Ordinary chondrite

OD – outer diameter

OH_z – hydroxyl in a phase (z = mineral, melt)

Ol – olivine

OPX – orthopyroxene

Pyx – pyroxene

RC – Rumuruti-type chondrite

RSD – relative standard deviation

RTI – real-time imaging

SIMS – secondary ion mass spectrometry

SynFo – synthetic forsterite

TGA – thermogravimetric analyses

TZM – titanium-zirconium-molybdenum

UMD - University of Maryland

UPB – ureilite parent body

WT – wall thickness

X_g^z – the mole fraction of a species (g = H_2O, OH, O) in a phase (z = mineral, melt, fluid)

Chapter 1: Introduction and Background

Hydrogen is the most abundant element in our Solar system, comprising ~75% of its mass (Lodders et al., 2009; Lodders, 2021). The timing of accretion of H to the Earth, its abundance, and its distribution exerts primary controls on the physicochemical evolution and habitability of our planet. To constrain the source(s) of H to the Earth and other planets, we need to understand the H budgets of the materials that comprised the "feedstock" of the terrestrial planets (i.e., Mercury, Venus, Earth, and Mars). We can probe the composition of the terrestrial feedstock by analyzing meteorites, which are fragments of rocky material derived from extraterrestrial bodies, many of which formed very early in our Solar System's evolution. In this introduction, I will give an overview of early Solar System history, an introduction to meteoritics, and a brief summary of Earth's accretionary assemblage. I will then discuss prevailing models to account for Earth's H budget, existing constraints on the H budgets of small, melted bodies, and challenges to estimating the H budgets of melted bodies.

1.1 Overview of early solar system history, meteoritics, and Earth's accretion

1.1.1 "Birth" of the solar system

The Solar System was initially a large, rotating cloud of gas and dust prior to an external perturbation which caused the presolar cloud to collapse, ultimately forming the nebular disk. The nascent nebular disk had a thermal gradient, hot toward the center and cool toward the edge, resulting in preferential concentration and condensation of volatile elements in the outer portion of the disk. As the disk continued to cool, elements condensed according to their volatilities (e.g., Wood et al., 2019; Lodders, 2021). The first nebular condensates are calcium-aluminum rich inclusions (CAIs), which formed at ~4.567 Ga before present (Connelly et al., 2012). In

planetary geology, this date is taken as “time zero”, and hereafter all dates will be referenced as time after CAI formation. For major constituents, such as H, condensation fronts formed allowing for the subsequent buildup of materials, potentially leading to the formation of larger particles, pebbles, and ultimately small, primitive bodies (i.e., planetesimals; e.g., Flock et al., 2019; Johansen et al., 2021; Morbidelli et al., 2022). These amalgamations of bodies continued to collide, eventually depleting the disk of gas and dust and forming planetary embryos. The earliest generations of planetesimals accreted with a sufficient complement of short-lived radionuclides (e.g., ^{26}Al, ^{60}Fe) to drive wholescale melting and metal-silicate differentiation. Planetesimals that formed after ~ 1 – 2 Ma may have accreted insufficient amounts of short-lived radionuclides to generate wholescale melting and differentiation and therefore were only thermally metamorphosed or incompletely melted (Bizzarro et al., 2005; Chaussidon and Gounelle, 2007).

1.1.2 An introduction to meteoritics

Meteorites are rocky fragments of extraterrestrial bodies whose orbits intersected Earth’s resulting in their fall to Earth’s surface. Meteorites can broadly be subdivided into two orders: chondrites and achondrites. Chondrites are chemically primitive materials (e.g., solar-like refractory element ratios) that experienced limited geologic processing, primarily thermal metamorphism and aqueous alteration. Achondrites are meteorites with igneous or recrystallized textures that preserve textural and chemical evidence of melting (e.g., non-solar refractory element ratios). Achondrites can be further subdivided into two classes, primitive achondrites and differentiated achondrites, based on: 1) the preservation of primitive chemical and textural signatures; and, 2) their degree of melting. Differentiated achondrites (hereafter “achondrites”) are igneous products derived from extensively or wholly melted planetesimals that preserve no

primitive textural or chemical features. Primitive achondrites are igneous products that preserve primitive chemical and/or textural signatures, thereby making them intermediate to chondrites and achondrites. For the purposes of this dissertation, it is useful to consider the three stages of planetesimal melting and thermal processing represented by the chondrites, primitive achondrites, and achondrites: unmelted, incompletely melted, and wholly melted and differentiated.

Recently, nucleosynthetic isotopic work on meteorites has identified an isotopic dichotomy which has been dubbed the NC-CC dichotomy, where NC stands for non-carbonaceous and CC stands for carbonaceous (Warren, 2011b; Kleine et al., 2020). These groupings correspond to materials that are generally thought to have formed in the inner (NC) and outer (CC) solar system, as approximated by Jupiter's orbit (e.g., Warren, 2011; Kruijer et al., 2017; Bermingham et al., 2020), and are composed of chondrites, primitive achondrites, and achondrites. It is hypothesized that a growing proto-Jupiter (Kruijer et al., 2017) or pressure bump(s) in the nebular disk (e.g., Izidoro et al., 2022) maintained sufficient isolation of the NC and CC reservoirs such that their signatures were preserved in planetesimals.

1.1.3 Accretionary history of the Earth

Within the lifetime of the nebular disk (≤ ~10 Ma), the proto-Earth accreted up to ~0.25 M_E (Earth masses) by stochastic accretion of planetesimals and potentially incorporated nebular gases through equilibration with a surficial magma ocean (Sharp, 2017; Halliday and Canup, 2023). Accretion continued into a period of giant impacts (i.e., collisions between planetesimals and planetary embryos) from ~10 Ma up to 200 Ma. By ~50 Ma, the Earth had accreted to ~ 0.5 – 0.9 M_E with core formation occurring between ~34 – 100 Ma (Kleine and Walker, 2017). The giant-impact stage is considered to have ended when Theia, a moon- to Mars-size body, collided

with the Earth, forming the Moon at ~60 – 200 Ma (Borg and Carlson, 2023; references therein). Following the Moon-forming giant impact, the final < ~0.01 M_E was added to the Earth during a late accretionary event (i.e., the late accretion). The occurrence of the late accretion is supported by anomalously high highly-siderophile element concentrations in Earth's mantle following core formation (Walker, 2009).

Within the context of the NC-CC dichotomy, the Earth plots within the NC field in isotope discrimination plots (Kleine et al., 2020; Bermingham et al., 2020), suggesting it is primarily derived from inner solar system materials. Mixing models examining nucleosynthetic isotopes (e.g., ^{50}Ti, ^{54}Cr, ^{62}Ni, ^{95}Mo) can be used to constrain the proportion of CC-like material accreted to the Earth. The maximum permissible amount of CC-like material accreted to the Earth is sensitive to the choice of isotopic tracers, with estimates from ^{48}Ca and ^{66}Zn allowing up to ~15% and 40% percent of CC-like material to be accreted to the Earth, respectively (Schiller et al., 2018; Steller et al., 2022; Kleine et al., 2023). This large range of outcomes is due to variations in the chemical affinities of the elements (e.g., volatile vs. refractory, siderophile vs. lithophile), which results in different isotopic systems tracking different stages of accretion and differentiation. For models which consider a large number of nucleosynthetic isotopes, the maximum permissible amount of CC-like material is constrained to a few % of Earth's mass (e.g., Burkhardt et al., 2021). Overall, it is likely that Earth's accretionary assemblage was dominated by NC-like materials with addition of minor amounts of CC-like materials.

Beyond the isotopic constraints on Earth's accretionary assemblage, it is likely that the bulk Earth accreted from variably thermally processed materials, spanning from unmelted (e.g., chondritic) to wholly melted (e.g., achondritic). The dating of iron meteorites, which broadly represent the metallic cores of differentiated bodies, and achondrites using short-lived

radionuclides (e.g., ^{26}Al, ^{182}Hf) reveals that differentiated, and potentially large, bodies were accreting by $< \sim 1 - 2$ Ma (Kleine et al., 2012; Connelly et al., 2019; Scott, 2020). Similarly, chondritic parent bodies formed from ~1 – 5 Ma (Bouvier et al., 2007; Connelly et al., 2012). Altogether, this indicates that throughout nearly all of Earth's accretion, variably thermally processed materials were available. Therefore, it is likely that Earth's accretionary assemblage included bodies that fell throughout the spectrum of unmelted to wholly melted and differentiated. Overall, constraining the proportions of chemically (i.e., NC vs. CC) and thermally (i.e., unmelted vs. differentiated) variable materials that accreted to the Earth is difficult, however Earth's accretionary assemblage was likely variably thermally processed and composed predominantly of NC-like materials.

1.2 Prevailing sources of Earth's H

There are large uncertainties in estimates of the bulk Earth H budget (3900^{+32900}_{-3300} μg/g H_2O; total H as H_2O equivalents, hereafter H_2O) which are largely attributed to the H content of Earth's core (Sharp, 2017; Peslier et al., 2017). Conversely, the H budget of the bulk silicate Earth (BSE; ~700 - 3000 μg/g H_2O) is well constrained (e.g., McCubbin and Barnes, 2019). Initial models to account for Earth's H budget assumed Earth and other differentiated inner solar system bodies accreted dry or became dehydrated during melting and differentiation, thereby requiring an exogenous source of H. To account for the H observed on Earth's surface and its interior today, addition of comets, which are ice and organic rich, has been frequently invoked (e.g., Chyba, 1987; Delsemme et al., 1988; Delsemme, 1998). However, this model has largely fallen out of favor as the H and N isotopic compositions of comets are distinct from the Earth and rocky bodies (e.g., Alexander et al., 2018).

Carbonaceous chondrites (CCs) are H-rich (with some containing >10 wt. % H_2O) and are commonly invoked as a source of terrestrial H (e.g., Marty, 2012; Alexander et al., 2012; Saal et al., 2013; Sarafian et al., 2014). Accretion of CC-like materials is still a common model to account for Earth's H budget (Alexander, 2017; Greenwood et al., 2023), however this model requires ~2-4% of Earth's present mass to be acquired from Ivuna-type (CI) or Mighei-type (CM) chondrites. Coupling this observation with constraints from nucleosynthetic isotopes (Section 1.1.3) requires that Earth preferentially sampled CI or CM chondrite-like materials relative to other CCs during its accretion. Overall, the addition of CC-like materials is a viable model to account for Earth's H budget but remains contested due to external constraints (e.g., nucleosynthetic isotopes).

Contrary to CCs, enstatite chondrites (ECs) are the group of meteorites that represent the closest known match to the nucleosynthetic isotopic composition of the Earth (Javoy et al., 2010; Warren, 2011b). Historically, it has been assumed that ECs are nominally anhydrous. However, recent bulk and *in situ* analyses have shown that ECs carry measurable H (Piani et al., 2020; Thomassin et al., 2023). These bulk measurements suggest that primitive ECs have up to ~0.54 wt. % H_2O, which can readily account for the bulk Earth's H budget (~700 - 3000 μg/g H_2O; McCubbin and Barnes, 2019; Piani et al., 2020). This conclusion is contested, as ~80% of the H measured via bulk analyses is unaccounted for and can readily be attributed to common alteration phases that are unavoidable in bulk analyses (see Chapter 2). Regardless, materials similar to ECs and other non-carbonaceous chondrites, such as the ordinary (Alexander et al., 2018; Vacher et al., 2020; Grant et al., 2023) and Rumuruti-type chondrites (McCanta et al., 2008), likely supplied some of Earth's H budget.

The final model that is commonly invoked to account for some or all of Earth's H budget is ingassing of nebular H (Sharp, 2017; Wu et al., 2018; Olson and Sharp, 2019). In this model, a body quickly grows to ≥ ~0.3 M_E in the presence of the solar nebula. The large mass of this body allows it to capture an atmosphere of nebular H and He, which, combined with radiogenic heat, results in the formation of a surficial magma ocean. The magma ocean then equilibrates with the nebular atmosphere, allowing H to be dissolved and sequestered in the interior of the body. Nebular ingassing models face several challenges to incorporating and retaining H in the magma ocean, nominally the requirement for rapid growth of large bodies, although this may be permissible via pebble accretion (e.g., Johansen et al., 2021, 2023), degassing of volatiles during giant impacts (Chen and Jacobson, 2022), and atmospheric erosion due to impacts and high EUV and x-ray flux from the young Sun (Lammer et al., 2018; Chen and Jacobson, 2022).

Overall, it is likely that some combination of all of these sources (i.e., comets, chondrites, nebular ingassing) contributed to Earth's H budget as reflected in several hybrid models for the volatile element budget of the Earth (e.g., Wu et al., 2018; Bekaert et al., 2020; Sharp and Olson, 2022; Marty, 2022). One subsection of materials that is not covered by these models is incompletely and wholly melted planetesimals (<< 0.3 M_E), which are represented by primitive achondrites and achondrites. As described in Section 1.1.3, it is likely that some proportion of the materials that accreted to form the Earth are represented by melted planetesimals. Traditionally, these melted planetesimals were considered to be anhydrous due to accretion from dry materials or degassing of H. However, recent analyses of achondrites have revealed that, at minimum, some achondritic bodies have measurable H (e.g., Sarafian et al., 2017, 2019; Stephant et al., 2021; McCubbin et al., 2021). Therefore, it is important to characterize the H contents of a suite of primitive achondrites and achondrites to more fully constrain potential

sources of terrestrial H and whether H is fully degassed during thermal metamorphism, melting, and differentiation of planetesimals.

1.3 What constraints do we have on the H contents of melted planetesimals?

There are up to 28 and 23 parent bodies of primitive achondrites and achondrites (excluding irons), respectively, represented in terrestrial collections (Greenwood et al., 2020). Many of these bodies are represented by 1 or 2 anomalous or ungrouped meteorites. Excluding ungrouped meteorites, there are 6 groupings of primitive achondrites (i.e., Acapulcoite-Lodranites, Ureilites, Brachinites, Winonaite-IICD's, Tafassites, Tissemouminites) and 5 groupings, excluding iron meteorites, of achondrites (i.e., Angrites, Aubrites, Howardites-Eucrites-Diogenites (HEDs), Mesosiderites, and Pallasites). There has been limited work characterizing the H budget of these groupings and their parent bodies. Prior work on the Angrites (Sarafian et al., 2017a, c; Deligny et al., 2021) and HEDs (Sarafian et al., 2014, 2017b, 2019; Barrett et al., 2016; Stephant et al., 2021; McCubbin et al., 2021) has demonstrated that the parent bodies of these meteorites are H-poor relative to the Earth, with ~ 60 – 240 μg/g H_2O and ~4 – 70 μg/g H_2O in the bulk Angrite and HED parent bodies, respectively. Similarly, Newcombe et al. (2023) characterized a small number of ungrouped NC and CC achondrites and determined that their bulk parent bodies were extremely H-poor (< 38 μg/g H_2O) relative to the bulk Earth. These estimates are all juxtaposed by a single bulk measurement of the Norton County Aubrite of ~0.3±0.2 wt. % H_2O, which implies the Aubrite parent body is exceptionally H-rich. For primitive achondrites, only the H content of the Acapulcoite-Lodranite parent body (ALPB) has been studied outside of this work (Stephant et al., 2023), which provided the second estimate for the H content of a primitive achondritic parent body (see Chapter 3). Stephant et al. (2023) found that the ALPB was extremely H-poor (~3 – 19 μg/g H_2O) relative to the bulk Earth.

Overall, this limited work suggests the H contents of primitive achondritic and achondritic parent bodies are highly variable (~3 orders of magnitude) and, except the aubrites, are H-poor relative to the bulk Earth.

1.4 What are current challenges to estimating the H budgets of early-formed, melted bodies?

The H contents of a magmatic source are typically characterized using glassy melt inclusions because H readily dissolves in silicate melt (up to several wt. % dissolved H_2O is routinely measured in quenched terrestrial melts) and the melt inclusions are shielded from decompression-driven degassing by their mineral containers. However, melt inclusions are rare in primitive achondrites and achondrites, which are predominantly composed of nominally anhydrous minerals (NAMs; e.g., olivine, pyroxene, feldspar) with trace amounts of phosphates and metal/sulfides. Therefore, as an alternative to the use of melt inclusions, the H contents of meteoritic NAMs may be measured and used to estimate the bulk H contents of their parent bodies.

The use of NAMs as hygrometers for bulk parent bodies requires some knowledge of the melting history of the body and a robust constraint on the partitioning of H between NAMs and melt. Melting models constraining the style (e.g., batch, fractional, incremental) and degree of melting are typically based upon the major and trace element concentration of bulk materials and minerals (e.g., McCoy et al., 1997; Goodrich, 1999; Goodrich et al., 2007; Barrat et al., 2016). However, depending upon the constraints and goals of the model, multiple degrees of melting and melting styles may describe a single parent body (e.g., Goodrich, 1999; Goodrich et al., 2007; Warren, 2012; Barrat et al., 2016). The estimated bulk H contents are highly sensitive to the choice of melting style (discussed in Chapter 3 and shown in Fig. 3.7). Furthermore, these melting models require application of partition coefficients for H between NAMs and melt

($D_{H_2O}^{min/melt}$) to relate the H content of the NAMs to the bulk parent body. Experiments constraining $D_{H_2O}^{min/melt}$ for NAMs are predominantly conducted at terrestrial conditions, which are generally higher pressure and more oxidized than planetesimal conditions, and on terrestrial mantle compositions. The applicability of experimentally determined $D_{H_2O}^{min/melt}$ values determined at terrestrial conditions to meteoritic parent bodies is discussed at length in Sections 2.5.1.3, 3.5.1, and 4.4.2.1. The choice of $D_{H_2O}^{min/melt}$ can result in orders of magnitude variation in estimated bulk parent body H contents (e.g., Tables 3.4, 4.5). Overall, the choices of melting model and $D_{H_2O}^{min/melt}$ value represent major sources of uncertainty when estimating bulk parent body H contents.

1.5 Dissertation outline

This dissertation focuses on constraining the H contents of incompletely and wholly melted planetesimals by proxy of the primitive achondrites and achondrites. Here, I employ micron-scale *in situ* measurements of H in meteoritic NAMs via secondary ion mass spectrometry (SIMS). The H concentrations of these NAMs are combined with $D_{H_2O}^{min/melt}$ values from the literature and applied to simple melting models to estimate the bulk H contents of meteoritic parent bodies. I also employ experimental techniques to quantify the partitioning of H between olivine and melt at low pressures (10 – 200 MPa) that are relevant to Earth's uppermost crust and planetesimals. The primary goal of this research is to quantify to what extent and at what stage of planetesimal melting (i.e., unmelted, incompletely melted, wholly melted) H is lost. The results of this research place additional constraints on the dehydration of planetesimals, the types of materials that could supply Earth's H, the physicochemical evolution of the Earth,

and the characteristics of bodies that may retain sufficient H to be habitable. Each of the four chapters are summarized below:

- **Chapter 2** is a re-evaluation of the H contents of Aubrites using *in situ* methods. Measurements of H were made across all common silicate phases in the sample suite and were combined with the modal mineralogy of the samples to estimate the minimum bulk H contents of the meteorites. *Published as:*

  Peterson L. D., Newcombe M. E., Alexander C. M. O'D., Wang J., Klein F., Bekaert D. V. and Nielsen S. G. (2023) The H content of aubrites: An evaluation of bulk versus in situ methods for quantifying water in meteorites. *Earth and Planetary Science Letters* **620**, 118341.

- **Chapter 3** presents the first *in situ* measurements of H in primitive achondrites. I analyzed NAMs in a suite of Ureilites, which are the second-most carbon-rich group of meteorites in the terrestrial collections and an isotopic end-member for the NC reservoir. These measurements are then combined with several melting models to estimate the bulk H content of the Ureilite parent body. *Published as:*

  Peterson L. D., Newcombe M. E., Alexander C. M. O'D., Wang J., Sarafian A. R., Bischoff A. and Nielsen S. G. (2023) The H_2O content of the ureilite parent body. Geochimica et Cosmochimica Acta 340, 141–157.

- **Chapter 4** presents H measurements for a suite of Acapulcoite-Lodranite clan meteorites. Similar to Chapter 3, measurements of Acapulcoite-Lodranite NAMs are combined with melting models to estimate the bulk H content of the Acapulcoite-Lodranite parent body. *Accepted for publication at:*

  Peterson L. D., Newcombe M., Alexander C. M. O'D., Wang J. and Nielsen S. G. (*accepted*) The H-poor nature of incompletely melted planetesimals: the view from acapulcoites and lodranites. *Geochimica et Cosmochimica Acta*.

- **Chapter 5** presents the first experimental constraints on the partitioning of H between olivine and melt ($D_{H_2O}^{ol/melt}$) at pressures relevant to planetesimals and Earth's upper crust (10 – 200 MPa). The results of these experiments are used to evaluate if the relationship between $D_{H_2O}^{ol/melt}$ and pressure determined at high pressures (≥ 0.5 GPa) can reliably be extrapolated to low pressures (10 – 200 MPa). *{in preparation}*

The ***Conclusions*** chapter briefly summarizes key results and conclusions from these studies and highlights potential areas for future research.

Chapter 2: The H content of aubrites: An evaluation of bulk versus *in situ* methods for quantifying water in meteorites

Note: This chapter has previously been published at the following citation:

Peterson L. D., Newcombe M. E., Alexander C. M. O'D., Wang J., Klein F., Bekaert D. V. and Nielsen S. G. (2023) The H content of aubrites: An evaluation of bulk versus in situ methods for quantifying water in meteorites. *Earth and Planetary Science Letters* **620**, 118341.

Abstract

Aubrites and enstatite chondrites (ECs) are isotopically similar to the Earth and therefore may resemble the primary materials that accreted to form our planet. Recent bulk H elemental and isotopic analyses of ECs and the Norton County aubrite suggest that enstatite-rich materials are H-rich and may represent a significant source of terrestrial water, with measured values of 3000±2000 μg/g H_2O and 5300±900 μg/g H_2O in the bulk and enstatite fractions of Norton County (Piani et al, Science, 2020). Here, we present a detailed investigation of *in situ* H_2O concentrations in enstatite, diopside, forsterite, and plagioclase from a suite of main group aubrites, including Norton County, and Shallowater. We find that enstatite (4±2 μg/g H_2O), diopside (4.8±0.5 μg/g H_2O), and forsterite (5±3 μg/g H_2O) have similar H_2O concentrations, and all are significantly lower than plagioclase (24±3 μg/g H_2O). We combine our *in situ* analyses of H_2O contents with equilibrium partition coefficients and bulk mineralogies to estimate the bulk H_2O content of our samples. We compare these first order estimates with bulk volatile analyses conducted using sample pyrolysis and find that the previous bulk H_2O analyses of aubrites predominantly reflect terrestrial contamination and alteration. If our conclusion that the reported bulk H_2O analyses of Norton County primarily reflect terrestrial contamination and alteration extends to bulk analyses of ECs, then EC-like material may not be a significant source

of terrestrial water. Our results support the hypothesis that thermal metamorphism, melting, and differentiation leads to efficient desiccation of planetesimals relative to chondrites, and that differentiated planetesimals contributed, at most, trace amounts to Earth's water budget.

2.1 Introduction

Aubrites are the group of achondrites that most closely matches the O (Greenwood et al., 2017) and nucleosynthetic (e.g., Ca, Ti, Cr, Ni; Burkhardt et al., 2019; references therein) isotopic composition of the Earth – Moon system. Aubrites are considered to have formed under highly reducing conditions (about 5 to 7 log units below the iron - wüstite (IW) oxygen fugacity buffer; Righter et al., 2006), potentially indicating their formation in the innermost portion of the solar protoplanetary disk (Kallemeyn and Wasson, 1986; Shukolyukov and Lugmair, 2004). Additionally, due to their low intrinsic oxygen fugacity and the inferred low FeO and high S contents of Mercury, aubrites or aubrite-like materials are considered to be Mercurian analogs (Nittler and Weider, 2019; Steenstra and van Westrenen, 2020). Aubrites may thus relate to precursor materials for the Earth and Mercury.

Aubrites are nearly pure enstatite pyroxenites that are highly depleted in FeO and are thought to be derived from enstatite chondrite-like (EC) materials (Keil, 2010; references therein). Aubrites are derived from at least three parent bodies: the main group aubrite parent body (AuPB), the Itqiy parent body, and the Shallowater parent body (Keil, 2010). The AuPB likely experienced a magma ocean phase resulting in the homogenization of O isotopes (Barrat et al., 2016; Greenwood et al., 2017). The main group aubrites commonly exhibit cumulus textures (Keil, 2010); however, there is petrologic and geochemical evidence that there was subsolidus redistribution of trace elements, potentially linked to thermal metamorphism (Barrat et al., 2016; Okada et al., 1988). A potential metamorphic event is supported by the limited age data available

for the aubrites, which is consistent with cumulate formation by ~3 – 5 Ma after calcium aluminum rich inclusion formation (hereafter CAI), and a potentially protracted cooling history or resetting event (i.e., metamorphism) occurring > ~13 Ma after CAI (Baker et al., 2012; Keil, 2010; references therein). The AuPB is considered to have undergone or begun metal-silicate segregation (Ray et al., 2021; Zhu, 2021) and silicate-silicate differentiation (Zhu, 2021), although both processes may have been complex due to impact excavation, mixing, and reaccretion (Ray et al., 2021).

Material representing the crust of the AuPB (e.g., basaltic aubrites) is extremely rare (Fogel, 2005), and the earliest estimates of aubrite volatile contents were based upon this observation. To explain the apparent lack of basaltic aubrites, a small (< 100 km), volatile-bearing AuPB has been invoked, with volatiles acting as a propellant for explosive volcanism and subsequent loss of erupted material to space (Wilson and Keil, 1991). Several studies have used this model to evaluate the potential AuPB melt volatile content (Keil et al., 2011; Muenow et al., 1992; Wilson and Keil, 1991). Wilson and Keil (1991) argued that only a few hundred μg/g of volatiles (C, F, Cl, N, S) were required to drive explosive volcanism on the AuPB. This proposal is supported by the spectrometric degassing experiments of Muenow et al. (1992), who found 2000 – 3000 μg/g of volatiles were typically released during heating of ECs, suggesting that sufficient volatiles were present in aubrite precursor materials to drive explosive volcanism. More recently, Keil et al. (2011) examined a rare basaltic vitrophyre clast from the aubrite Larkman Nunatak (LAR) 04316 and argued that this clast was produced during pyroclastic volcanism on the AuPB. Considering the physical properties of the clast, which contained metal and sulfides (bulk density: ~6000 kg m^{-3}; diameter: ~20 mm), and assuming an AuPB radius of 40 – 100 km, Keil et al. (2011) estimated a maximum melt volatile content of 450 – 5000 μg/g.

Recently, the bulk rock (3000±2000 μg/g) and enstatite (5300±900 μg/g) H_2O content (total H quantified as H_2O; hereafter H_2O) of the Norton County aubrite were measured by pyrolysis (Piani et al., 2020). Additionally, Lorenz et al. (2020) investigated the speciation and concentration of H and C in enstatite and enstatite-hosted gas inclusions from the Pesyanoe aubrite. Gas inclusions were found to contain H and C-H bonded species and the host pyroxene was suggested to contain OH^- in the lattice structure (Lorenz et al., 2020). Step-wise crushing and heating experiments of enstatite from the Pesyanoe aubrite yielded a bulk H_2O content of ≥ 0.42 μg/g (Lorenz et al., 2020). In light of these two conflicting studies, the H_2O content of aubrites remains poorly constrained, with currently published data suggesting a wide range of H_2O contents with the highest estimates overlapping that of the bulk Earth (700 – 3000 μg/g H_2O; McCubbin and Barnes, 2019; references therein).

To further constrain the water content of the aubrite group, we conducted thermogravimetric analyses (TGA) of bulk volatiles and secondary ion mass spectrometry analyses (SIMS) of enstatite, forsterite, and plagioclase from a suite of aubrites. Importantly, we analyzed enstatite in the Norton County aubrite allowing for a re-evaluation of the Norton County H_2O contents reported by Piani et al. (2020). Our analyses indicate that enstatite and forsterite in aubrites are extremely volatile poor and that the bulk volatile content of the aubrite group is likely dominated by C, F, Cl, and S released from sulfides and trace phases, some of which are likely of secondary origin.

2.2 Samples

Detailed sample descriptions and petrography for all samples can be found in Keil (2010) and Wilbur et al. (2022). The general petrography and modal mineralogy for our aliquots and bulk material of all samples studied here are described below and summarized in Tables 2.1 –

2.2. All silicates are nearly devoid of FeO, and orthopyroxene and olivine are near end-member enstatite and forsterite, respectively (Table 2.4; Keil, 2010; Wilbur et al., 2022).

2.2.1 Main group aubrites

Allan Hills 78113 (ALH 78113), Allan Hills 84007 (ALH 84007), LaPaz 02233 (LAP 02233), Larkman Nunatak 04316 (LAR 04316), Miller Range 13004 (MIL 13004), and Norton County are main group aubrites. For all main group aubrites studied herein, the aliquots are composed almost entirely of whitish-grey enstatite with minor to trace metal/sulfides and trace amounts of forsterite. Sample MIL 13004 contained trace amounts of albitic glass (Appendix A1; Table A8). In their bulk samples, the main group aubrites studied herein are chiefly composed of enstatite, with minor to trace amounts of forsterite, diopside, feldspar, silicate glass, sulfides, and metal (Keil, 2010; Wilbur et al., 2022). All samples, except Norton County, are Antarctic finds and exhibit minor weathering features (weathering grades A – Be; Table 2.1). Norton County is an observed fall. All samples exhibit signatures of shock, with shock stages varying from S2 – S5 (Rubin, 2015). All main group aubrites studied here are brecciated except for LAP 02233, which is classified as unbrecciated (Rubin, 2015).

Table 2.1) Physical and chemical properties of aubrite samples analyzed for highly volatile elements (HVEs)

Meteorite	Breccia Type	End-member Silicate Compositions	Major/Minor Silicate Phases	Pyx Shock Stage	Weathering Grade*	Notes	References
ALH 78113	Polymict Fragmental Breccia	Fa0; Fs0.15Wo0.7	En, Diop, Fo, Plag, Orth	S2 - S5	A/Be (3)	Si-rich glass; Non-native chondritic fragements in some aliquots	1, 2, 3, 4, 5
ALH 84007	Monomict Fragmental Breccia	Fa0; Fs0	En, Diop, Fo	S4	Ae (2)	ALH 83009 pairing group; Potentially a single, large igneous Fo in an aliquot	2
LAP 02233	Unbrecciated	Fs0.06Wo0.81	En. Diop	S5	B (4)		1, 2, 4, 5
LAR 04316	Regolith Breccia	Fs0-1	En, Diop	S4	A (1)	basalt-vitrophyre clast in one aliquot from parent clast	1, 2, 5
MIL 13004	Monomict Fragmental Breccia**	Fa0; Fs0	En, Fo, Plag, Diop	S3**	A/Be (3)		1
Norton County	Monomict Fragmental Breccia		En, Fo, Diop	S2-S3			4, 5
Shallowater	Unbrecciated		En, Fo, Diop	S2			4, 5

* number in parentheses indicates degree of weathering based upon weathering grade relative to other samples within the sample set
** inferred based upon sample description in references and comparison to other samples
[1]Zhao et al. (2020), [2]Keil (2010, [3]Lorenzetti et al. (2020), [4]Miura et al. (2007), [5]Rubin (2015)

Table 2.2) Modal mineralogy (vol. %) after Wilbur et al. (2022)

Meteorite	Enstatite	Forsterite	Diopside	Plagioclase	Ca-rich weathering	Metal	Schreibersite	Troilite	Alabandite	Daubreelite	Oldhamite
ALH 78113	95	trace	trace	trace	n.m.	3.2	trace	trace	trace	trace	trace
ALH 84007	96	trace	trace	trace	n.m.	0.6	trace	1.2	trace	0.5	trace
LAP 02233	99	n.m.	trace	trace	trace	trace	n.m.	trace	trace	trace	trace
LAR 04316	87	6	1	5	trace	0.6	trace	0.9	trace	trace	trace
MIL 13004	92	4	trace	3	n.m.	trace	n.m.	trace	n.m.	n.m.	n.m.
Norton County 967	96	trace	3	trace	trace	trace	n.m.	trace	trace	trace	n.m.
Norton County 960	67	29	2	trace	n.m.	n.m.	n.m.	0.5	0.5	trace	trace
Shallowater 922	92	3	trace	3	trace	0.9	n.m.	0.6	trace	0.6	trace
Shallowater 951	83	3	trace	2	trace	8.3	trace	3.5	trace	trace	trace
Shallowater 968	83	10	trace	2	trace	2	n.m.	3.5	trace	trace	trace

n.m. - not measured

trace - below 0.5 vol. %

Combination of trace values brings totals to 100%

Uncertainties are 2.3 to 7.2 vol. % (see Wilbur et al. (2022))

2.2.1.1 Norton County

Norton county is the largest aubrite in terrestrial collections (~1 ton of material) and is classified as a fragmental breccia composed of several lithologies (Keil, 2010). The fragment of Norton County analyzed here is whitish-grey in color and is composed almost entirely of angular, fragmented enstatite ranging from a few microns up to ~1 cm. Minor amounts of plagioclase are present as well as opaques (likely sulfides with minor metal). Our aliquot of Norton County is composed almost entirely of enstatite with minor amounts of plagioclase (~1 mm), highly fractured enstatite small (< ~250 μm), subhedral enstatite and plagioclase. Other silicate phases, such as forsterite, are likely present but were not identified. This most closely matches the "brecciated matrix" lithology described by Okada et al. (1988), which represents the most abundant lithology in Norton County.

2.2.2 Shallowater

Shallowater is an unbrecciated, coarse-grained orthopyroxenite, composed predominantly of enstatite and thought to be derived from a different parent body than the main group aubrites based upon a complex cooling history that is inconsistent with the main group aubrites (Keil, 2010). Shallowater enstatite exhibits evidence for mild shock (Rubin, 2015) and trace alteration phases have been identified from several chips (Wilbur et al., 2022). It has been proposed that Shallowater underwent a 3-stage cooling history involving the collision and incorporation of a partially molten or molten enstatite-rich body with an EC-like body (Keil, 2010, 1989). Our aliquot of Shallowater is composed predominantly of euhedral enstatite up to ~1.5 mm in their

longest axis with minor plagioclase and metal/sulfides. Metal/sulfides are anhedral and are frequently associated with grain interstices.

2.3 Methods

2.3.1 Sample Preparation

Sample preparation for Antarctic aubrites studied here follows the same procedure as Peterson et al. (2023). Antarctic aubrite samples were mounted in one 1-in. diameter In mount and one 10-mm diameter In mount. For Norton County and Shallowater, samples were received after polishing in epoxy, which has been demonstrated to produce high blanks for H_2O analyses (Mane et al., 2016). To mitigate the effects of the epoxy, we embrittled and dissolved the epoxy using triplicate baths of acetone, toluene, and isopropanol followed by gentle disaggregation of any remnant film. We then trimmed off all surfaces that contacted epoxy using a Princeton Scientific WS-25 wire saw before rewashing in triplicate baths of acetone, toluene, and isopropanol. Norton County and Shallowater were then mounted in a separate 1-in. diameter In mount than the Antarctic aubrites. Samples were placed in a vacuum oven at 60°C for > 48 hours prior to Au coating and then returned to the vacuum oven for > 24 hours. Samples were then placed in a single sample holder in the airlock sample exchange chamber of the Cameca nanoSIMS 50L at the Carnegie Earth and Planets Lab (EPL) for >72 hours prior to the start of analyses to allow for degassing of sample mounts. Following SIMS analyses at EPL, samples were returned to the University of Maryland – College Park (UMD) where the Au coat was removed with 0.25-µm alumina paste prior to C coating for electron microprobe analyses (EPMA).

2.3.2 Thermogravimetric analyses

We used a TA Instruments Q600 simultaneous thermal analyzer at Woods Hole Oceanographic Institution (Woods Hole, MA) for thermogravimetric analyses and differential scanning calorimetry to determine the weight loss during devolatilization of the studied meteorite samples. For each analysis, ~46 – 71 mg of finely powdered meteorite was heated from room temperature to 1100°C with a heating rate of 10°C per minute (Table 2.3). Analyses were performed in a N_2 atmosphere with a flow rate of 50 mL per minute. Repeated measurements of standard materials supplied by TA Instruments indicate that the temperature is accurate to 1°C and the weight change to 0.5 μg.

2.3.3 Secondary ion mass spectrometry

Analyses of enstatite, forsterite, and feldspar in aubrites followed existing procedures (Kumamoto et al., 2017; Peterson et al., 2023b; Newcombe et al., 2023). All calibration standards (OPX: SynFo, BCN-203, DGO-160, SLP-403, 109426-1, PR-7-5; CPX: SynFo, SLP-402; SMC31139, SLP-108, SC-J1, KH03-27, DGO-160; Glass: Suprasil 3001, ALV-519-4-1, D52-5, D30-1; Hauri, 2002; Kumamoto et al., 2017) were held in 10-mm diameter indium mounts distributed by phase (e.g., all orthopyroxene in one mount). Meteorite samples were distributed across an additional two 1-in. diameter indium mounts and one 10-mm diameter indium mount. All analyzed mounts contained secondary standards (Synthetic Forsterite (SynFo), Suprasil 3001 glass, Herasil glass, and ALV-519-4-1 glass), with the exception of the 10-mm indium sample mount (Fig. S10) due to space constraints. Additionally sample mounts and the glass standards mount did not contain SynFo. All indium mounts were held in the same sample holder to ensure identical analytical conditions within each analytical session. Analyses

Table 2.3) Summary of estimated mass loss (µg/g) from our aubrite samples as a function of temperature during our thermogravimetric analyses.

	Analyzed mass (mg)	Temp. of first release (°C)	Total mass loss	Mass loss < 125 °C	Mass loss > 125 °C	Mass loss > Temp. 1st Release (~400°C)	Mass loss > 780 °C
ALH 78113	53.337	375	7200	2200	5000	3300	2000
ALH 84007	61.351	405	8600	2100	6500	4900	2100
LAP 02233	60.708	370	4000	1500	2500	2300	800
LAR 04316	70.74	400	8500	1600	6900	5400	1600
MIL 13004	46.014	375	2700	400	2300	1500	900

were split across three analytical sessions (01/22, 02/22, and 08/22), and the Cs^+ ion source on the nanoSIMS 50L was replaced between the 01/22 and 02/22 sessions. The vacuum during the 01/22, 02/22, and 08/22 sessions was maintained between 5.2×10^{-10} and 6.1×10^{-10} torr, 4.9×10^{-10} and 5.5×10^{-10} torr, and 8.8×10^{-10} tand 8.9×10^{-10} torr respectively. The analyses were conducted using entrance slit 5 (ES; 10×100 µm) and aperture slit 5 (AS; 40×40 µm). A ~2-nA Cs^+ primary beam (D1 aperture; ~500 nm beam size) was used to pre-sputter a 15×15-µm area for ~5 minutes to remove the Au coat and surface contamination and implant Cs^+ for increased secondary ion yields. Counts of $^{12}C^-$, $^{16}O^1H^-$, $^{19}F^-$, $^{30}Si^-$, and $^{35}Cl^-$ ions were simultaneously detected and heat maps of counts were observed using the "real time imaging" (RTI) function of the nanoSIMS 50L to check for sources of contamination such as cracks or resin. If cracks or hot-spots, which likely correspond to contamination, were identified in the RTI image, then the beam was moved to another location on the grain until an area free of contamination sources was identified. For the analyses, the raster size was reduced to 10×10 µm and electronic gating was applied to focus the collection of ions from the central 5×5-µm region of the analytical area. Counting times for all analyses was 250 seconds. Negatively charged $^{12}C^-$, $^{16}O^1H^-$, $^{19}F^-$, $^{30}Si^-$, and $^{35}Cl^-$ ions were simultaneously detected on electron multipliers with a mass resolving power of >8000 (MRP; as defined by Cameca), allowing discrimination of $^{16}O^1H$ from ^{17}O. The electron gun was used to charge compensate the sample surface due to implantation of Cs^+ ion beams and removal of negatively charged ions and electrons during analyses. Electron gun tuning followed the same procedure as Peterson et al. (2023).

Data reduction follows the method of Peterson et al. (2023). Briefly, counts of volatile ions were ratioed against $^{30}Si^-$ to account for instrumental drift and normalized to 50 wt.% SiO_2 (multiplied by $SiO_2/50$; where SiO_2 is the SiO_2 concentration of the target as determined by

electron microprobe) to account for matrix effects. The analytical blank for $OH/Si \times SiO_2/50$ was monitored using frequent analyses of Suprasil 3002 glass (~1.7 µg/g H_2O; Newcombe, 2022) and synthetic forsterite (SynFo; ~0 µg/g H_2O). Our standard mounts contained both Suprasil 3002 glass and SynFo; however, sample mounts contained only Suprasil 3002 glass. For the 01/22 analytical session, we only consider analyses of unknowns from ~91 to 193 hr. after the start of the analytical session (Table A3) as prior to that interval Suprasil and SynFo H_2O contents overlap within uncertainty, which suggests poor reproducibility due to blank effects at low total H_2O contents. All analyses following hour ~193 are excluded as repeat analyses of Suprasil 3002 glass and SynFo are variable and analyses of ALV-519-4-1 glass show decreasing counts, consistent with failure of the Cs^+ ion source at the end of the analytical session. For all analytical sessions, the analytical blank was determined by repeat analyses of Suprasil 3002 glass and SynFo (Table A3, A5, A7; Newcombe, 2022). For mounts that included SynFo, SynFo is used to estimate the analytical blank. For all other mounts, the $^{16}O^1H$ /$^{30}Si \times SiO_2/50$ of the analytical blank was estimated by subtracting the difference between Suprasil 3002 glass and SynFo on the clinopyroxene standard mount from the measured $^{16}O^1H$ /$^{30}Si \times SiO_2/50$ for Suprasil 3002 on sample mounts. For analyses of ALH 84007, which lacked secondary standards in the same mount (Fig. A10), the lowest measured blank was applied to the data. No blank correction was applied for C, F, and Cl as the C, F, and Cl content of Suprasil 3002 and SynFo are poorly constrained at the sub-µg/g level.

For the 01/22 and 08/22 analytical sessions, analytical drift occurred on the scale of several hours to days due to variations in analytical conditions (e.g., aging of the ion detectors, degradation of the Cs^+ ion source). Drift corrections were applied using a time-correlated approach based upon intervals bound by retuning of the primary beam and the electron gun,

similar to Peterson et al. (2023). No correction for instrumental drift is applied to the 02/22 analytical session as the measured values of Suprasil 3002 glass, Herasil, and ALV-519-4-1 were stable over the course of the analytical session.

Calibration curves for volatile element abundances were determined using York regressions (York et al., 2004; Wiens, 2021) of blank-corrected standard data forced through the origin (Fig. A1 – A3). When possible, matrix-matched calibration curves were used to calculate H_2O and F concentrations. For olivine, the orthopyroxene calibration curve was used to calculate H_2O concentrations as the slopes of the olivine and orthopyroxene calibration curves have been demonstrated to overlap within uncertainty (Kumamoto et al., 2017; Towbin et al., 2023). For plagioclase, the orthopyroxene calibration curve was used to calculate H_2O concentrations as prior work has demonstrated that the calibration curves for plagioclase and olivine, which overlap with orthopyroxene, overlap within uncertainty (Mosenfelder et al., 2015). For F in olivine and plagioclase, the orthopyroxene calibration curves were used as no matrix-matched standards were available, however the calibration curves for F between these phases have not been demonstrated to overlap. Within the 01/22, 02/22, and 08/22 analytical sessions, the slopes of the clinopyroxene and glass calibration curves deviate by a maximum of 28% relative to the orthopyroxene calibration curve. For C and Cl in all phases, the glass calibration curves are used as no matrix-matched standard set was available. Data was then filtered using C and Cl as indices of contamination. A generalized extreme studentized deviate (ESD) test (performed using the 'isoutlier' function in MATLAB R2022a) was used to determine outlier C and Cl concentrations. We employed a significance level of 0.05. All data points identified as outliers based upon C and Cl are identified in Tables A3, A5, and A7 and are excluded from our calculations and discussion. Additionally, F concentrations from the 01/22 session are excluded

due to detector issues. The uncertainty reported for all spot analyses is the propagated uncertainty due to counting statistics during analyses, the SiO_2 content of each phase, the analytical blank, the drift correction, and calibration curves (Tables A3, A5, A7).

2.3.4 Electron microprobe analyses

The major and minor element concentrations in individual enstatite, forsterite, and plagioclase grains were measured using the JEOL JXA 8900R EPMA at UMD following the method of Peterson et al. (2023). Average phase compositions and uncertainties (reported as 2 standard deviations from the mean) are reported in Table 2.4. The standards used to calibrate mineral analyses are outlined in Table A1.

2.4 Results

2.4.1 Thermogravimetric analyses

Mass thermograms are reported in the supplementary data (Fig. A4 – A8). As no element analyzer was attached to the heating chamber during TGA, the speciation (e.g., H_2, H_2O, CH_4, CO_x, F, Cl, SO_x) of gases evolved during the heating of the samples is unknown. We consider total mass loss over four temperature ranges, < 120 °C; > 120 °C (Piani et al., 2020), > ~400°C (see Section 5.2.1), and >780 °C Muenow et al. (1992, 1995). The total mass loss over each temperature interval is summarized in Table 2.3.

2.4.2 Secondary ion mass spectrometry

We analyzed H_2O in main group aubrite and Shallowater enstatite, forsterite, diopside, and plagioclase (Table 2.5). Blank- and drift- corrected H_2O concentrations range from < 1 to 8 µg/g (avg. 4±2 µg/g; 1 Std. Dev.; n = 83) for enstatite, 3 to 9 µg/g (avg. 5±3 µg/g; 1 Std. Dev.; n

= 3) for forsterite, 4.8 to 5 µg/g (avg. 4.8±0.1 µg/g; 1 Std. Dev.; n = 3) for diopside, and 20 to 27 µg/g (avg. 24±3 µg/g; 1 Std. Dev.; n = 4) for plagioclase. Notably, the H_2O concentration measured in Norton County enstatite is 3.8±0.2 µg/g (Table 2.5), which is three orders of magnitude lower than the H_2O concentration determined by bulk methods for this material (Piani et al. 2020). The reproducibility for H_2O analyses is assessed by calculating the difference between consecutive analyses of H_2O in SynFo (~0 µg/g H_2O) and Suprasil 3002 (~1.7 µg/g H_2O), and then taking the standard deviation from the mean of all differences (Newcombe et al., 2023). The reproducibility, quantified as the percent variability, of H_2O analyses is 21 %, 16 %, and 16 % respectively for the 01/22, 02/22 and 08/22 analytical sessions. Nearly all analyses of enstatite and forsterite from the 01/22 session (Table A3) are below or within uncertainty of the blank-corrected limit of detection (LOD; 4 µg/g H_2O; Long and Winefordner, 1983), with the exceptions of MIL 13004 enstatite (analysis # 470), MIL 13004 forsterite (analysis # 473), and ALH 78113 enstatite (analysis # 522 – 535, 538; Fig. 2.1). All analyses from the 02/22 session (Table A5) are within uncertainty of or fall below the blank-corrected LOD (4.8 µg/g H_2O; Fig. 2.1). All analyses from the 08/22 session (Table A7) are greater than the blank-corrected LOD (0.74 µg/g H_2O; Fig. 2.1). For analyses of ALH 84007, all data is excluded from the 01/22 analytical session (Section 3.3). Additionally, measurements of ALH 84007 from the 02/22 session are blank-corrected using the lowest measured blank from all mounts (2.3 µg/g H_2O; clinopyroxene standard mount) due to the lack of space for secondary standards on the ALH 84007 mount. We note that, had we elected not to apply a blank correction to our ALH 84007 data, the mean H_2O content of ALH 84007 enstatite would be ~3 µg/g H_2O, which

Table 2.4) Average phase compositions and uncertainty (2 standard deviations) determined by EPMA

	Mineral	n	Na_2O	Unc.	FeO	Unc.	TiO_2	Unc.	CaO	Unc.	Al_2O_3	Unc.	MgO	Unc.
ALH 78113	Enstatite	32	bdl		bdl		bdl		0.5	0.1	0.1	0.2	39.3	0.6
ALH 84007	Enstatite	44	bdl		bdl		bdl		0.5	0.2	0.1	0.5	40.3	0.7
LAP 02233	Enstatite	17	bdl		bdl		bdl		0.48	0.07	0.3	0.9	40	1
LAR 04316	Enstatite	50	0.02	0.03	0.1	0.4	bdl		0.5	0.5	0.2	0.4	39	1
MIL 13004	Enstatite	55	bdl		0.2	1.0	bdl		0.7	0.7	1	2	38	4
	Forsterite	13	bdl		0.1	0.4	bdl		0.11	0.04	0.1	0.5	57	2
	Glass	8	3.9	0.5	0	0.05	0	0.04	0.04	0.04	21	2	0.14	0.05
Norton County	Enstatite	7	0.02	0.04	0.0	0.2	bdl		0.5	0.4	0.08	0.09	39.8	0.7
	Diopside	4	0.16	0.05	Bdl		bdl		23.7	0.6	0.6	0.9	20.0	0.5
Shallowater	Enstatite	30	bdl		0.1	0.4	bdl		0.09	0.07	0.14	0.09	40.3	0.5
	Feldspar	6	8.4	0.4	0	1	bdl		4	1	23	1	0.00	0.01
mdl Antarctic meteorites			0.012		0.02		0.025		0.012		0.01		0.011	
mdl Norton County and Shallowater			0.011		0.05		0.018		0.01		0.01		0.0125	

	Mineral	n	MnO	Unc.	Cr_2O_3	Unc.	K_2O	Unc.	SiO_2	Unc.	End-member Composition
ALH 78113	Enstatite	32	0.05	0.06	bdl		bdl		60	1	Wo0.82En99.18
ALH 84007	Enstatite	44	0.03	0.06	bdl		bdl		59.4	0.9	Wo0.86En99.14
LAP 02233	Enstatite	17	0.09	0.05	bdl		bdl		59.8	0.9	Wo0.86En99.14
LAR 04316	Enstatite	50	0.1	0.1	bdl		bdl		60	1	Wo0.87En99.03Fs0.27
MIL 13004	Enstatite	55	0.0	0.2	bdl		0.0	0.2	59.7	0.9	Wo1.27En98.5Fs0.27
	Forsterite	13	0.02	0.06	bdl		bdl	0.02	42	2	Fo99.89
	Glass	8	0.01	0.03	N/A		1.62	0.09	74	1	
Norton County	Enstatite	7	bdl		c		bdl		59.4	0.7	Wo0.9En99.08Fs0.02
	Diopside	4	bdl		bdl		bdl		55.1	0.8	Wo46.09En53.91
Shallowater	Enstatite	30	bdl		bdl		bdl		59.6	0.5	Wo0.16En99.93Fs0.2
	Feldspar	6	bdl		bdl		0.462	0.128	65	2	An77.19Ab20.0Or2.8
mdl Antarctic meteorites			0.0175		0.035		0.009		0.03		
mdl Norton County and Shallowater			0.05		0.019		0.009		0.026		

mdl - maximum detection limit; bdl - below detection limit; n - number of analyses; N/A – not analyzed

Table 2.5) Highly volatile element concentrations measured in our Aubrite samples by secondary ion mass spectrometry

Meteorite	n	CO_2 (ug/g)	Unc	H_2O (ug/g)	Unc	F (ug/g)	Unc	Cl (ug/g)	Unc
Enstatite									
ALH 78113	15	1.1	0.2	4.7	0.5	1.1	0.7	0.02	0.01
ALH 84007	4	1.6	0.4	0.6	0.4	4	1	0.013	0.003
LAP 02233	7	1.1	0.1	2.2	0.3	2.6	0.3	0.015	0.009
LAR 04316	21	1.1	0.2	2	1	7	6.2	0.02	0.01
MIL 13004	23	0.4	0.1	5	2	6	6	0.006	0.003
Norton County	3	0.54	0.06	3.8	0.2	3.7	0.9	0.0045	0.0002
Shallowater	10	0.57	0.06	5.8	0.3	22	13	0.02	0.03
Diopside									
Norton County	3	0.5	0.2	4.8	0.5	24	1	0.0045	0.0006
Forsterite									
MIL 13004	3	0.9	0.1	5	3	34	31	0.012	0.007
Plagioclase									
Shallowater	4	0.78	0.06	24	3	4.5	0.6	0.06	0.08

n spots

Unc. - uncertainty calculated as one standard deviation from the mean

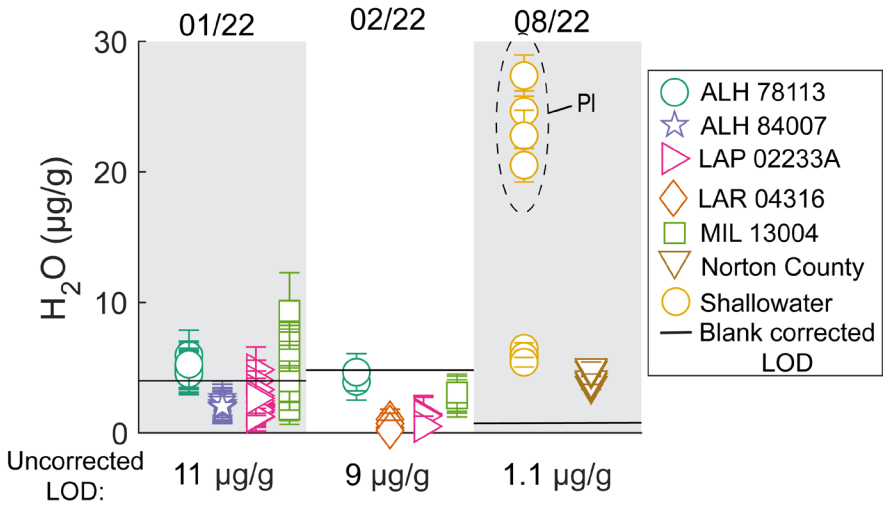

Fig. 2.1) Summary of aubrite NAMs analyses across the 01/22, 02/22, and 08/22 analytical sessions. Uncorrected LODs (no blank- or drift- corrections) are listed below the x-axis and blank- corrected LODs are plotted as horizontal lines. Concentrations for samples reanalyzed between the 01/22 and 02/22 sessions overlap, however, central values are slightly lower for the 02/22 session. Data points labeled "Pl" are analyses of plagioclase, while all other analyses are of enstatite, forsterite, or diopside.

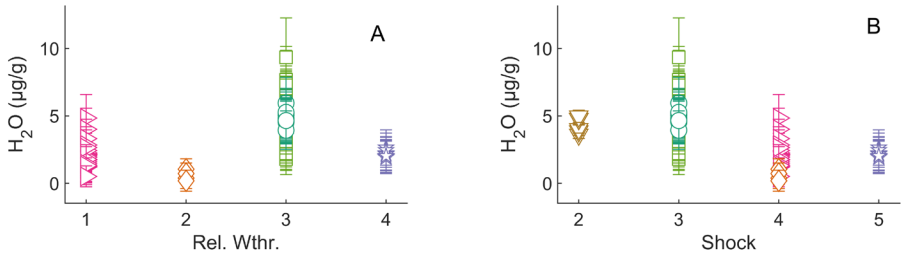

Fig. 2.2) Main group aubrite enstatite H_2O contents plotted against A) relative degree of weathering, and B) shock stage. Colors and symbols after Fig. 2.1. See Table 2.1 for weathering and shock classifications.

remains in agreement with all other aubrites. Across the dataset, enstatite H_2O concentrations are invariant with respect to the relative degree of weathering (Fig. 2.2A) and our least shocked samples have H_2O concentrations that extend to higher values than our most shocked samples (Fig. 2.2B). Additionally, the H_2O content of enstatite from LAP 02233, an unbrecciated aubrite,

is indistinguishable from the H_2O contents of the brecciated aubrites examined in this study (Table 2.5).

2.4.3 Electron microprobe analyses

We analyzed major, minor, and trace elements in aubrite enstatite, diopside, forsterite, and plagioclase (Table 2.4). The average composition of all phases studied here is given in Table 2.4 and are consistent with prior studies (Wilbur et al., 2022). We find that individual grains have homogeneous major and minor element contents (Table 2.4).

2.5 Discussion

2.5.1 Re-evaluation of Norton County H_2O contents

2.5.1.1 Challenges of analyzing nominally anhydrous samples using bulk methods

Prior studies investigating desorption of H_2O from geologically relevant materials (e.g., silicates and oxides) indicate that the majority of adsorbed H_2O is desorbed by heating samples up to ~120 – 200 °C (e.g., Hibbitts et al., 2011; Lupker et al., 2012; Potapov et al., 2018). However, for nominally anhydrous minerals (NAMs), "[bulk analytical methods overestimate] the water contents of the NAMs due to the inclusion of contaminating water… even after [samples are] 'dried' by heating to over 125 °C prior to analysis" (Rossman, 2006; references therein). An investigation of lunar analog materials by Hibbitts et al. (2011) suggests that H_2O desorption is structurally and compositionally dependent, and several studies have demonstrated that H_2O desorption temperatures for silicates extend up to ~500 °C (Hibbitts et al., 2011; Jones et al., 2020; Yokoyama et al., 2022; Zhou et al., 1992). Additionally, Beran et al. (1989) conducted simultaneous TGA and infrared analyses of sillimanite and found that indigenous H_2O loss did not occur until ~500 °C and did not dominate H_2O loss until >700 °C. The high

desorption temperature may also extend to alteration phases, such as goethite, for which prior studies have demonstrated H_2O loss occurs at temperatures up to ~650 °C (Epstein and Taylor, 1974; Muenow et al., 1995). For prior bulk analyses of Norton County, however, samples were only pre-heated to 120 °C (Piani et al., 2020), which was likely insufficient to remove all terrestrial contamination. Here, we evaluate the potential for significant terrestrial contamination of aubrite bulk H_2O analyses by comparing our *in situ* analyses of Norton County enstatite with previous bulk analyses of Norton County enstatite.

2.5.1.2 Re-evaluation of the H_2O content of Norton County enstatite

By *in situ* methods, we measured 3.8±0.2 μg/g H_2O in Norton County enstatite (Table 2.5), which is three orders of magnitude lower than the 5300±900 μg/g H_2O measured in Norton County enstatite by bulk methods (Piani et al., 2020). We argue that this discrepancy is likely due to pervasive terrestrial contamination. To a first order, our non-blank corrected LOD was 1.1 μg/g H_2O, which is more than two orders of magnitude lower than the 500 μg/g H_2O LOD reported for bulk analyses (Piani et al., 2020), suggesting that our analyses should be more accurate. We also argue that the LOD reported for prior bulk analyses, which was measured by repeat analyses of an empty Sn sample holder (Piani et al., 2020), is inappropriate for quantifying the blank or LOD for silicate materials, particularly powdered ones. Importantly, exposure of Sn to ambient atmosphere at room temperature can lead to the formation of a thin SnO film on a timescale of hours to days (Sutter et al., 2014). Tin oxide has a H_2O desorption temperature of ~120 – 300 °C (Gercher and Cox, 1995; Morishige et al., 1980), which is lower than the desorption temperature of silicate powders (~400 – 700°C; see Section 2.5.2.2). Furthermore, H_2O desorption from a powdered material relative to a planar material (e.g., a sample holder) can reasonably be expected to be less efficient, as has been observed for silicates (e.g., D'Souza and

Pantano, 2002). Therefore, the LOD as measured on an anhydrous, powdered silicate material would be expected to be higher than that measured on an empty Sn sample holder, particularly if samples were only preheated to 120 °C prior to analyses to remove terrestrial contamination. Considering that Norton County enstatite contains 3.8±0.2 μg/g H_2O (Table 2.5), it represents a nominally anhydrous silicate material appropriate to quantify the analytical blank for bulk measurements. However, prior bulk analyses of Norton County enstatite (5300±900 μg/g H_2O) were an order of magnitude greater than the reported LOD (500 μg/g H_2O; Piani et al., 2020). We suggest that the measured H_2O above the LOD by bulk pyrolysis likely represents significant terrestrial contamination of the Norton County enstatite. When combined with the inapplicability of quantifying the LOD for bulk analyses from an empty Sn sample holder, this result implies that the reported LOD for prior bulk analyses is a minimum. Therefore, prior bulk analyses of Norton County should be considered maxima and may reflect copious terrestrial contamination; we re-evaluate prior bulk H_2O analyses of bulk Norton County material below.

2.5.1.3 Re-evaluation of Norton County bulk H_2O contents

To re-evaluate the bulk Norton County H_2O content (3000±2000 μg/g H_2O; Piani et al., 2020), we combine our *in situ* measurements of enstatite, forsterite, diopside, and plagioclase in aubrites (Table 2.5) with published estimates of modal mineralogies (Table 2.2; Okada et al., 1988; Wilbur et al., 2022) and experimentally determined partition coefficients (Table 2.6) to estimate the H_2O content of unmeasured phases (e.g., silicate glass, metals, and sulfides; Appendix A2). Note, Piani et al. (2020; references therein) do not provide modal mineralogies or petrography for their measured **"**grey" and "dark" lithologies, so we assume a modal mineralogy based upon the work of Okada et al. (1988) and Wilbur et al. (2022). We use enstatite as our "reference" mineral when applying partition coefficients as our enstatite H_2O contents exhibit

minor variability and we collected more spot analyses of enstatite (n = 83), than forsterite (n = 3), diopside (n = 3), and feldspar (n = 4). For simplicity, we retain the measured forsterite and plagioclase H_2O contents from MIL 13004 and Shallowater for our calculations, as these phases were not measured in Norton County. We also consider the average enstatite H_2O content of all samples as there is limited variability across our sample set.

Table 2.6) Measured and estimated phase H_2O contents

	D	Est.	Val.	Ref.
Enstatite	-	-	4	-
Forsterite	-	-	5	-
Plagioclase	-	-	24	-
Diopside	-	-	4.8	-
Glass	0.004	1500	1500	1, 2
Metal/Sulfide	0.22	1	1	3

D - partition coefficient
Ref. - references
Est. - estimated H_2O contents by applying partition coefficient to enstatite value
Val. - value used for mass balance calculations
[1]Dobson et al. (1995), [2]Grant et al. (2007), [3]Gaillard et al. (2022)

Following a mineralogically–weighted approach, we estimate the bulk H_2O content of Norton County considering two cases, glass-free and 5 vol. % glass, which yield 7 μg/g H_2O and 80 μg/g H_2O, respectively (calculations are detailed in Supplementary file "Aubs_Calcs.xlsx"). In these calculations we make the assumptions that all phases are in equilibrium with respect to H_2O and that available experimentally determined partition coefficients are applicable to the aubrite parent body. Based upon existing experimental partition coefficients, we expect, in general, the H_2O contents of our nominally anhydrous minerals to be ordered as follows: plagioclase ≈ clinopyroxene ≥ orthopyroxene > olivine (e.g., Demouchy et al., 2017; Le Roux et al., 2021; Lin et al., 2019; references therein). Our sample set contains analyses of enstatite (5.1±1.7 μg/g H_2O) and forsterite (5 ± 3 μg/g H_2O) from MIL 13004, enstatite (3.8±0.2 μg/g

H_2O) and diopside (4.8±0.1 µg/g H_2O) from Norton County, and enstatite (5.8±0.3 µg/g H_2O) and plagioclase (24±3 µg/g H_2O) from Shallowater (Table 2.5). Within uncertainty, these analyses appear to be compatible with equilibrium as assessed by available experimentally determined partition coefficients. For example, the H_2O content of experimental orthopyroxene is commonly half of or equal to the H_2O content of co-existing clinopyroxene (Demouchy et al., 2017; references therein), consistent with H_2O measurements of orthopyroxene (3.8±0.2 µg/g H_2O) and clinopyroxene (4.8±0.1 µg/g H_2O) in Norton County. For terrestrial mantle conditions and compositions, the H_2O content of orthopyroxene is expected to be approximately five to 25 times that of co-existing olivine (Demouchy et al., 2017; Le Roux et al, 2021; references therein). However, prior investigations of plagioclase and pyroxene have shown that, under reducing conditions, water solubility is increased in Fe-bearing phases (Mosenfelder et al., 2020; references therein), which suggests that Fe-poor phases relative to mantle compositions, like the nearly Fe-free pyroxene and plagioclase in the aubrites studied here (Table 2.4), may exhibit different partitioning behavior. Prior experimentally determined enstatite-forsterite (i.e., Fe-free) H_2O partition coefficients of 2.28 – 3.31 are reported by Grant et al. (2006). We note that Grant et al. (2006) estimated the water content of their phases using the Fourier transform infrared (FTIR) calibration of Libowitzky and Rossman (1997), which is a general formulation that can be applied to any mineral. If we instead apply mineral-specific FTIR calibrations (e.g., Bell et al., 1995; Withers et al., 2012) to enstatite and forsterite data, we find that H_2O is similarly incompatible in enstatite and forsterite (corrected enstatite-forsterite H_2O partition coefficients of 0.6 – 2.5), consistent with our analyses of enstatite and forsterite from MIL 13004. We explore the potential for disequilibrium processes disturbing the H_2O content of our samples in Section

S3. Overall, we suggest that experimentally determined partition coefficients reasonably permit the assumption of equilibrium in our samples.

Crucially, both estimates (glass-free and 5 vol. % glass) yield bulk H_2O concentrations two to three orders of magnitude lower than prior bulk H_2O measurements of Norton County (3000±2000 μg/g H_2O). Notably, this discrepancy can be accounted for by including <3 vol. % of common terrestrial alteration products found in enstatite chondrites and aubrites (e.g., schollhornite, portlandite, smectites; Rubin, 1997). For bulk analyses, analyzing observed falls may be expected to minimize terrestrial contamination and alteration. While Norton County was an observed fall, the field expedition was not carried out for nearly two months after the fall date (Lapaz, 1948). Furthermore, studies of ordinary chondrites (OC) and Mighei-type chondrites (CM) suggest terrestrial alteration and contamination of meteoritic samples can occur on the timescale of days to years, even for observed falls stored under curatorial conditions (Lee et al., 2021; Velbel, 2014). Combining the delay in retrieval for Norton County and the readiness of terrestrial alteration of meteorites, even at curatorial conditions, suggests that there was sufficient time for terrestrial alteration phases to develop in bulk Norton County aliquots. This is supported by the identification of many hydrous terrestrial alteration phases in Norton County, such as portlandite (e.g., Okada et al., 1981; Okada and Keil, 1982). We conclude that the reported bulk H_2O content of Norton County (3000±2000 μg/g H_2O) is likely dominated by terrestrial contamination and alteration.

Altogether, we conclude that the previous bulk analyses of Norton County enstatite (5300±900 μg/g H_2O) and bulk Norton County (3000±2000 μg/g H_2O) predominantly reflect terrestrial contamination and alteration. We also argue that the reported LOD for prior bulk analyses of Norton County should be considered as a minimum, thereby implying that reported

bulk H_2O contents are maxima. If our results for Norton County extend to the bulk analyses of ECs that were conducted simultaneously and using the same method (Piani et al., 2020), then these bulk analyses of ECs may also be overestimates and should be subject to further scrutiny. However, testing this hypothesis will require further bulk analytical and *in situ* studies of the H_2O contents of ECs and their constituent phases.

2.5.2 Bulk volatile contents of Antarctic aubrite meteorites and Shallowater

We have conducted TGA analyses of our Antarctic aubrite meteorites without an element analyzer and, therefore, specific element concentrations are unconstrained. However, prior studies by Muenow et al. (1992, 1995) have characterized the concentrations of C-, H-, N-, S-, and Cl-bearing species for enstatite and ordinary chondrites by dynamic high-temperature mass spectrometry, which characterizes changes in volatile concentration and sample mass with temperature. Here, we use published thermograms from Muenow et al. (1992, 1995) as a means to estimate the H_2O contents from our thermograms. The first major weight loss extends up to ~400 °C and is assumed to terminate when the first derivative of the weight loss signal becomes quasi-invariant over an interval of ~50 °C. Based upon the analyses of Muenow et al. (1992), we attribute the first major weight loss event to be predominantly H-bearing species. We note that prior studies of ECs (Muenow et al., 1992), ordinary chondrites (Muenow et al., 1995), lunar regolith (Epstein and Taylor, 1974, 1973), Ryugu particles (Yokoyama et al., 2022), and nominally anhydrous minerals (Beran et al., 1989; Rossman, 2006) have consistently attributed volatile loss below ~400 – 700 °C to terrestrial contamination and alteration. Therefore, to provide an upper estimate of the indigenous volatile content of our samples, we assume that mass loss below ~ 400 °C in our mass thermograms is primarily caused by terrestrial contamination and alteration. Our inferred indigenous volatile contents (derived from integrated volatile loss

above ~400 °C) vary from 1500 – 5400 µg/g (Table 2.3) and likely represent some combination of H-, C-, N-, F-, Cl-, and S-bearing species, as also observed for enstatite chondrites (Muenow et al., 1992). The release of these elements at high temperatures is likely due to the breakdown of sulfides and trace phases with negligible contribution from nominally anhydrous phases. Thus, we consider our bulk volatile contents as upper bounds on the H_2O contents of our Antarctic meteorites.

For all Antarctic aubrite samples studied here, we calculate bulk H_2O content estimates following the same mineralogically-weighted approach as in Section 2.5.1.3. These calculations yield less than ~ 5 µg/g H_2O in all samples. For all aubrites, with the exception of a feldspathic clast in LAR 04316, silicate glass is, at most, an accessory or trace phase (Keil, 2010). If we were to add up to 5 vol. % of silicate glass to our estimates for the Antarctic aubrites, we would calculate bulk H_2O contents similar to that of Norton County with 5 vol. % glass (~80 µg/g H_2O). In any case, the average aubrite lithology contains zero to trace amounts of silicate glass and therefore we conclude that average aubritic material contains less than ~10 µg/g H_2O.

2.5.3 Implications for H_2O delivery to the terrestrial planets

While aubrites are thought to be derived from extensive partial melting of an EC-like source, aubrite petrogenesis is considered to be complex (e.g., Keil, 2010; McCoy and Bullock, 2017). Due to the complexity of aubrite petrogenesis, we do not attempt to calculate a bulk AuPB or Shallowater parent body H_2O content using petrogenetic models. Instead, we assume that the aubrites analyzed herein and our mineralogically-weighted estimate for the H_2O content of average aubritic material, less than ~10 µg/g H_2O, is representative of the bulk AuPB as the AuPB core was likely H poor (e.g., Gaillard et al., 2022). This inference is reinforced by a comparison of aubrite NAMs with NAMs from a range of early Solar System achondrites (Fig.

2.3), which shows that melted and differentiated planetesimals are highly H_2O-depleted relative to the Earth and CI chondrites (Newcombe et al., 2023; Peterson et al., 2023; Sarafian et al., 2019, 2017b). This supports the hypothesis of extensive desiccation of planetesimals, relative to existing estimates for the H_2O content of chondrites, due to heating and melting (Lichtenberg et al., 2019; Harries et al., 2023; Peterson et al., 2023b; Newcombe et al., 2023), and delivery of water to the terrestrial planets by parent bodies that experienced limited thermal processing (i.e., chondrites or icy bodies).

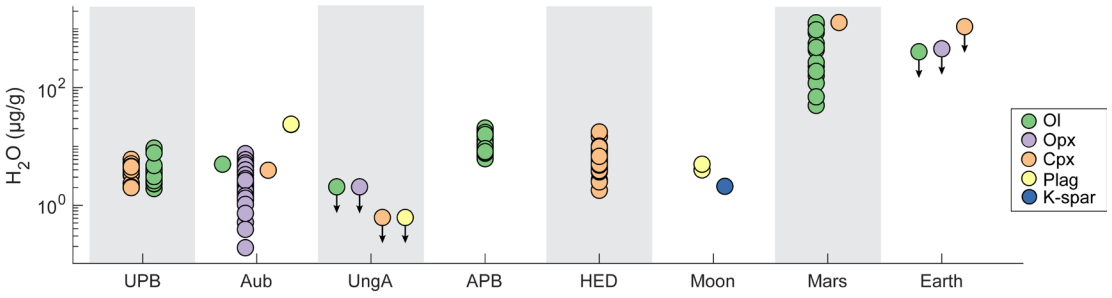

Fig. 2.3) Water concentrations measured in nominally anhydrous minerals from primitive achondritic and achondritic parent bodies. Data for the ureilite parent body (UPB; Peterson et al. 2023), aubrite parent bodies (Aub; this study), ungrouped achondrites (UngA; Newcombe et al. 2023), angrite parent body (APB; Sarafian et al., 2017b, 2017a), Howardite-Eucrite-Diogenite parent body (HED; Sarafian et al., 2019; Stephant et al., 2021), the Moon (Hui et al., 2017; Mills et al., 2017), Mars (Hallis et al., 2017; Mane et al., 2016), and the Earth (Peslier, 2010). Data for the ungrouped achondrites and the Earth represent maxima.

2.6 Conclusions

We have analyzed the H_2O contents of enstatite, forsterite, diopside, and plagioclase in a suite of main group aubrites and Shallowater, finding, on average, 4±2 µg/g H_2O in aubrite enstatite. We re-evaluate the previously reported enstatite and bulk Norton County aubrite H_2O contents measured by bulk methods and find a discrepancy of two to three orders of magnitude between *in situ* and bulk methods. The discrepancy between *in situ* and bulk methods is best

accounted for by pervasive terrestrial contamination and alteration in bulk analyses as aubrites, on average, are overwhelmingly composed of nominally anhydrous silicates (> 99 vol. %) and lack primary hydrous phases (Keil, 2010). We also suggest that the reported LOD for prior bulk analyses represents a minimum estimate, thereby implying that bulk analyses are maxima. If our results for Norton County extend to the bulk analyses of ECs measured by identical methods, we suggest that previous measurements of the water content in ECs may be overestimated. Comparison of our aubrite data with other meteoritic parent bodies reveal that enstatite achondrite parent bodies are significantly H-depleted relative to chondrites, in line with the efficient loss of water during parent body heating and melting as found for numerous other differentiated bodies. This conclusion further supports that delivery of water to Earth was facilitated by accretion of unmelted or ice-rich parent bodies.

Chapter 3: The H_2O content of the ureilite parent body

Note: This chapter has previously been published at the following citation:

Peterson L. D., Newcombe M. E., Alexander C. M. O'D., Wang J., Sarafian A. R., Bischoff A. and Nielsen S. G. (2023) The H_2O content of the ureilite parent body. *Geochimica et Cosmochimica Acta* **340**, 141–157.

Abstract

The fate of highly volatile elements (H, C, F, Cl and S) during planetary accretion and differentiation is debated. Recent analyses of water in non-carbonaceous chondrites (RC, OC, EC) and achondrites (angrites, eucrites) have been used to argue that inner solar system parent bodies accreted and retained their highly volatile element budgets from their primary feedstock without substantial loss during accretion, metamorphism and differentiation. An alternative model posits that differentiated inner solar system parent bodies (e.g., the angrite parent body, 4 Vesta, Earth) derived the majority of their water from a carbonaceous chondrite-like source, delivered during the final stages of accretion.

In order to add new constraints to this debate, we have measured water in nominally anhydrous minerals, melt inclusions, and interstitial glass in ureilites, the largest group of primitive achondrites in the terrestrial meteorite collection. Primitive achondrites did not experience global melting and homogenization. Therefore, these meteorites capture part of the transition from chondritic to achondritic parent bodies, allowing us to constrain the fate of water during the earliest stages of differentiation. Our nano-scale secondary ion mass spectrometry (nanoSIMS) analyses allow us to assess the viability of ureilite-like material as a potential source of terrestrial water. Analyses of pigeonite in main group ureilites yield a range of 2.0 – 6.0 μg/g H_2O, and analyses of high-Ca pyroxene and glass (glassy melt inclusions and interstitial glass) in the Almahata Sitta ureilitic trachyandesite yield ranges of 13 – 19 μg/g H_2O and 44 – 216 μg/g

H_2O, respectively. Mass balance, incremental melting, and batch melting calculations yield a preferred ureilite parent body H_2O content of 2 – 20 μg/g, similar to previous estimates of water in the eucrite parent body (4 Vesta), but lower than estimates of Earth's water budget. With these data, we demonstrate that 1) the ureilite parent body is H_2O-depleted relative to the Earth; 2) ureilite-like material is unlikely to be a primary source of H_2O to the Earth; 3) C and H are not necessarily coupled elements during planetary accretion and thermal processing; and 4) accretion, heating, partial melting, and degassing of rocky planetesimals likely results in significant depletion of H_2O.

3.1 Introduction

It is commonly assumed that Earth accreted all, or the majority, of its water through accretion of chondrite-like material. Note that "water", "H" and "H_2O" refer to any H-bearing species, including structurally bound hydroxyl and protons in minerals, that could react to form molecular H_2O incorporated in a melt, glass or gas. However, the timing and mechanisms of accretion of water and other volatiles to the Earth remain topics of much debate (e.g., Morbidelli et al., 2012; Marty, 2012; Alexander et al., 2012; Sarafian et al., 2014; Alexander, 2017; Bermingham et al., 2020). For instance, some have suggested that all of Earth's water was accreted from a few percent carbonaceous chondrite-like material (Marty, 2012, 2022; Alexander et al., 2012; Alexander, 2022). On the other hand, others suggest that the Earth may have accreted and retained a significant portion of its water from its primary feedstock (Halliday, 2013; Rubie et al., 2015; Piani et al., 2020).

Earth's primary feedstock likely included chondritic materials and planetesimals that formed in the inner solar system. Such materials can be identified in the terrestrial meteorite collection by their distinct isotopic compositions: a dichotomy observed in isotopic systems such

as Mo, Ni and Cr has been used to distinguish inner solar system (non-carbonaceous; NC) materials from outer solar system (carbonaceous; CC) materials (Warren 2011b). Potential candidates for chondritic materials that were likely present in the inner solar system during Earth's accretion include the enstatite (EC), ordinary (OC) and Rumuruti (RC) chondrites. There is petrologic, elemental, and isotopic evidence that OCs (e.g., Alexander et al., 1989, 2010; Jin and Bose, 2019; Vacher et al., 2020; Jin et al., 2021), RCs (e.g., McCanta et al., 2008), and ECs (Piani et al., 2020) accreted significant H, as water and organic matter (a source of water upon oxidation), and were able to retain some H after significant metamorphism (e.g., Dyl et al., 2012; Vacher et al., 2020; Piani et al., 2020; Lewis et al., 2022). Therefore, the water content of the terrestrial planets may be dependent on the retention efficiency of water from their primary feedstock. Analyses of achondrites (e.g., eucrites and angrites) suggest that fully differentiated parent bodies retain small amounts of H_2O; however, H_2O in the angrites and eucrites is thought to be derived from addition of CC-like material following metal-silicate differentiation (Barrett et al., 2016; Sarafian et al., 2017a, c, 2019; Stephant et al., 2021; Deligny et al., 2021; McCubbin et al., 2021). If correct, analyses of angrites and eucrites are unable to constrain how efficiently parent bodies can retain volatile elements from their primary feedstock throughout accretion and differentiation.

In order to assess the potential for H retention throughout the earliest stages of differentiation, we have analyzed the H_2O content of a suite of primitive achondrites. Primitive achondrites are "meteorites that exceeded their solidus temperature on the parent body – thus experiencing partial melting – but did not crystallize from a melt, or, if they were molten, are derived from parent bodies in which planetary differentiation did not achieve isotopic equilibrium" (Weisberg et al., 2006). Primitive achondrite parent bodies likely accreted near the

end of the timeframe in which there was sufficient ^{26}Al to drive partial or wholescale melting, formed within the first several half-lives of ^{26}Al but were catastrophically disrupted at the onset of melting and differentiation or did not grow sufficiently large drive to wholescale melting. Therefore, primitive achondrites provide a snapshot of the earliest stages of the planetesimal differentiation process, during the transition from chondritic to achondritic parent bodies. Primitive achondrites provide a proxy to evaluate if volatiles accreted by planetesimals prior to or during core formation can be retained during differentiation.

With over 600 associated meteorites, the ureilites are the largest group of primitive achondrites represented in terrestrial collections (https://www.lpi.usra.edu/meteor/), and are thought to be derived from a single parent body (Downes et al., 2008). Following the NC–CC classification of meteorites (Warren, 2011b), ureilites fall within the NC reservoir (Warren, 2011a), and are therefore thought to have formed in the inner solar system. The ureilite parent body (UPB) accreted ~1 Ma after CAI (Budde et al., 2015; Barrat et al., 2016; Schiller et al., 2018), began metal-silicate and silicate-silicate differentiation (Rankenburg et al., 2008; Bischoff et al., 2014; Barrat et al., 2016), and was disrupted ~6 – 7 Ma after CAI (Bischoff et al., 2014; Goodrich et al., 2015), effectively halting differentiation. Additionally, the ureilites have been proposed to be an end-member precursor composition for the Earth (Schiller et al., 2018) and have been invoked as a potentially important source of Earth's highly volatile elements (C, H, O, N, S; Hirschmann, 2016; Barrat et al., 2017).

Ureilites are C-rich meteorites predominantly composed of olivine and pyroxene (Goodrich, 1992; Goodrich et al., 2015). They can be subdivided into two primary groups, main group (monomict) and polymict ureilites, the former being generally interpreted as mantle restites following extraction of trachyandesitic (Bischoff et al., 2014; Barrat et al., 2016) and S-

rich metallic melts (Warren et al., 2006). A subgroup of the main group ureilites, the Hughes cluster (named after type-sample "Hughes 009"), are considered to be paracumulates (i.e., mixtures of mantle residues and cumulus material; Warren and Kallemeyn, 1989; Goodrich et al., 2001; Downes et al., 2008). In concomitance with the main group ureilites, rare feldspathic clasts in polymict ureilites (Cohen et al., 2004) and four trachyandesitic clasts (Bischoff et al., 2014, 2022) have been identified and are considered as conjugate melt(s) to the main group ureilites. Individual ureilites have homogeneous olivine and clinopyroxene core Mg# (Mg# = 100*[Mg]/[Mg+Fe]; [ ] denote molar concentrations; core is defined as the interior of grains that have not been modified by reduction upon disruption of the parent body), while the ureilite group as a whole exhibits a range of olivine core Mg# from 74 to 97 (Downes et al., 2008). The olivine core Mg# of ureilites are correlated with their bulk O-, C-, Cr-, and noble gas isotopic compositions, which is inconsistent with production by simple igneous fractionation and suggestive of the absence of a global magma ocean (Singletary and Grove, 2003; Warren, 2012; Goodrich et al., 2015; Barrat et al., 2017; Zhu et al., 2020; Broadley et al., 2020). Olivine core Mg# is typically used as a geochemical "signature" for each meteorite as, in general, it is homogeneous on the sample scale and correlates with several chemical and isotopic signatures.

The water content of primitive achondrites can be constrained by examining nominally anhydrous minerals (NAMs), such as olivine and pyroxene, which are commonly the first phases to crystallize from mafic magmas. The mineral-melt H_2O partition coefficients for olivine and pyroxene have been the subject of several studies (Aubaud et al., 2004, 2008; Hauri et al., 2006a; O'Leary et al., 2010; Tenner et al., 2012; Le Voyer et al., 2014; Adam et al., 2016; Sarafian et al., 2019), and can therefore be used to calculate the H_2O contents of a hypothetical silicate melt in equilibrium with these phases. These calculations can be combined with the results of

previous studies that constrain the style and extent of melting on the UPB (Goodrich, 1992; Barrat et al., 2016; Collinet and Grove, 2020b) to estimate the H_2O content of the UPB. This method assumes that 1) H_2O is present in trace quantities in olivine and pyroxene such that it follows Henry's Law, and 2) partition coefficients determined under terrestrial pressures, temperatures, oxygen fugacities, and compositions are applicable to the ureilite parent body (see Supplementary Section B1).

In this work, we report the first measurements of H, F, and Cl in olivine and pyroxene from a suite of main group ureilites and one "Hughes cluster" ureilite, spanning olivine core Mg# of 78.7 to 92.3. We also report analyses of H, F, Cl, C, and S in pyroxene-hosted melt inclusions and interstitial glass from the Almahata Sitta ureilitic trachyandesite (MS-MU-011; hereafter ALM-A). We use our data to calculate the range of bulk-silicate UPB H_2O contents. Our results imply that 1) ureilite-like material is an unlikely primary source of water to the Earth, 2) C and H are not necessarily coupled elements during planetary accretion and thermal processing, and 3) accretion and differentiation of planetesimals results in near total H loss relative to their accretionary budgets.

3.2 Samples

The main group ureilite meteorites studied here are described in detail in Singletary and Grove (2003), and ALM-A is described in detail in Bischoff et al. (2014, 2022). The petrography and mineralogy of the main group ureilites studied here and ALM-A are summarized below and in Table 3.1.

3.2.1 Allan Hills A78262

Allan Hills (ALH) A78262 is a main group ureilite composed dominantly of olivine (76 vol.%) and pigeonite (21 vol.%) with a carbon-rich matrix containing trace amounts of nickel-iron and troilite. Olivine and pigeonite are relatively homogeneous; the olivine core Mg# is 78.7 (Mason et al., 1980; Singletary and Grove, 2003). ALH A78262 is classified as "lightly shocked" as olivine and pyroxene exhibit minor fracturing and undulose extinction, and pyroxene exhibits rare polysynthetic twinning (Berkley and Jones, 1982). It was assigned a weathering grade of B/C, indicating a moderate degree of weathering because interior surfaces retain a brownish color throughout (Mason et al., 1980). ALH A78262 is paired with ALH 78019.

3.2.2 Elephant Moraine 83225

Elephant Moraine (EET) 83225 is a monomict ureilite composed dominantly of olivine (59 vol.%) and pyroxene (41 vol.%) with a C-rich matrix containing graphite and potentially diamond (Mason et al., 1985; Singletary and Grove, 2003). Olivine compositions vary slightly from olivine core Mg# of 87 to 92 with an average of 88.7 (Mason et al., 1985; Singletary and Grove, 2003). EET 83225 is classified as moderately shocked and assigned a weathering grade of B/C (Mason et al., 1985; Goodrich et al., 2013a).

3.2.3 Elephant Moraine 87517

EET 87517 is a monomict ureilite composed dominantly of olivine (45 vol.%) and pyroxene (55 vol.%) with thin rims composed of C-rich matrix (Mason et al., 1988; Singletary and Grove, 2003). Olivine and pigeonite compositions are relatively homogeneous; olivine core

Table 3.1) Ureilites analyzed as part of this study

Meteorite	*Classification*[a]	*Degree of Shock*[b]	*Degree of Alteration*[b]	*Ol Core Mg#*	*Cosmic Ray Exposure Age (Ma)**	*Modal (vol. %)*	*Mineralogy*	
						Ol	*Pyx*	*Ref.*
ALHA 78262	Ol-Pgt	Relatively unshocked (1)	B/C (3)	78.7	0.56 (0.31)	76	21	1,2,3
EET 83225	Ol-Pgt	Medium (3)	B/C (3)	88.7	<45 **	59	41	2,3,4
EET 87517	Ol-OPX	Low (2)	B/C (4)	92.3	8.8	45	55	2,5,6
EET 96314	Aug-bearing	Medium (3)	B (2)	87.2	<45 **	54	45	2,3,7
GRA 95205	Ol-Pgt	High (4)	B (2)	79.1	10.7 (0.9)	94	5	2,3,6,8
GRO 95575	Ol-Pgt	Relatively unshocked (2)	A/B (1)	78.7	5.8	90	9	2,9
ALM-A [b]	Trachyandesite[b]	Weakly shocked (1)	-	-	-	-	25	10

* Data from Leya and Stephenson (2019), ** No previous analyses, assumed to be less than the maximum age given for ureilites in Leya and Stephenson (2019)

[a] Classification after Goodrich et al. (2004)

[b] All information for this sample is from Bischoff et al. (2014); sample is an observed fall therefore terrestrial alteration is assumed to be negligible

Ol - olivine; Pyx - pyroxene

Parenthetical values for Degree of Shock and Degree of Alteration are relative values assigned based upon sample descriptions.
[1]Mason et al., (1980); [2]Singletary and Grove (2003); [3]Goodrich et al., (2013a); [4]Mason et al., (1985); [5]Mason et al., (1988); [6]Rankenburg et al., (2008); [7]Satterwhite and Lindstrom 1998a; [8]Satterwhite and Lindstrom, 1997); [9]Satterwhite and Lindstrom (1998b); [10]Bischoff et al. (2014)

Mg# is 92.3 (Singletary and Grove, 2003). EET 87517 is classified as low-shock with a severe degree of terrestrial alteration, and is assigned a weathering grade of B/C (Mason et al., 1988; Goodrich et al., 2013a).

3.2.4 Elephant Moraine 96314

EET 96314 is a monomict ureilite composed dominantly of olivine (54 vol.%) and pyroxene (45 vol.%) with a thin, carbon-rich matrix generally composing grain rims (Satterwhite and Lindstrom, 1998; Singletary and Grove, 2003). Olivine (average core Mg# = 87.2), pigeonite, and augite are relatively homogeneous (Singletary and Grove, 2003). This sample is classified as a "Hughes cluster" ureilite based upon the presence of interstitial augite, similar major element ratios to Hughes cluster samples, and petrographic textures suggestive of melt impregnation (Downes et al., 2008). EET 96314 retains undulatory extinction, polysynthetic twinning, and kink banding, similar to paired meteorites EET 96293 and EET 96331, and is classified as medium-shock (Satterwhite and Lindstrom, 1998; Goodrich et al., 2013a). EET 96293 was given a weathering grade of B by Satterwhite and Lindstrom (1998), whereas it is classified as severe by Goodrich et al. (2013a).

3.2.5 Graves Nunataks 95205

Graves Nunataks (GRA) 95205 is a monomict ureilite composed dominantly of olivine (94 vol.%) and pyroxene (5 vol.%) with a thin, C-rich matrix, containing trace amounts of Fe-Ni metal and troilite along grain rims (Satterwhite and Lindstrom, 1997; Singletary and Grove, 2003). Satterwhite and Lindstrom (1997) report a mean olivine core Mg# of 79 (no range or uncertainty reported), which is virtually identical to the value of 79.1±0.3 reported by Singletary and Grove (2003). We find a more magnesian olivine core Mg# that varies from 80.2 to 83.2,

with an average of 81.7 (Table B1); this suggests that olivine core Mg# in GRA 95205 is more variable than previously reported. We note that the proposed variation in olivine core Mg# for GRA 95205 is similar to ranges of olivine core Mg# found in other ureilites (e.g., EET 83225, GRO 95575). Small, unstrained olivine grains compose olivine aggregates, and are texturally similar to aggregrates found in OC impact melt breccias (Rubin, 2006). GRA 95205 contains small mosaicized olivine and polysynthetic pyroxene twins, common indicators of shock, and is classified as medium- to high-shock (Satterwhite and Lindstrom, 1997; Rankenburg et al., 2008; Goodrich et al., 2013a). It has been classified as weathering grade B and assigned a moderate degree of terrestrial alteration (Satterwhite and Lindstrom, 1997; Goodrich et al., 2013a).

3.2.6 Grosvenor Mountains 95575

Grosvenor Mountains (GRO 95575) is a monomict ureilite composed dominantly of olivine (90 vol.%) and pyroxene (9 vol.%) in a C-rich matrix containing trace amounts of Ni-Fe and troilite (Satterwhite and Lindstrom, 1998; Singletary and Grove, 2003). Olivine compositions are somewhat variable, exhibiting a range of olivine core Mg# from 79 to 84 (Satterwhite and Lindstrom, 1998), with an average of 78.7 reported by Singletary and Grove (2003). GRO 95575 is classified as low-shock (Satterwhite and Lindstrom, 1998; Rankenburg et al., 2008), and is assigned a weathering grade of A/B (Satterwhite and Lindstrom, 1998).

3.2.7 ALM-A

ALM-A is a weakly shocked trachyandesitic clast of asteroid 2008 TC_3 derived from the Almahata Sitta strewnfield and is composed predominantly of feldspar (~70 vol.%; anorthoclase and plagioclase), Cr-bearing Ca pyroxene with melt inclusions (~20 vol.%; $\sim Fs_{19–25}Wo_{34–41}$), low-Ca pyroxene (~5 vol.%; $\sim Fs_{32–42}Wo_{8–14}$), and accessory interstitial glass, phosphates,

ilmenite, spinel, sulfides, and Fe-metal (Horstmann and Bischoff, 2014; Bischoff et al., 2014). Melt inclusions and interstitial glass have an approximately rhyolitic composition (Bischoff et al., 2014). Terrestrial weathering is considered to be minimal in ALM-A as samples recovered from the Almahata Sitta strewnfield belong to the observed fall after the explosion of asteroid 2008 TC_3 in Earth's atmosphere.

Several melt inclusions were identified prior to analyses and images were collected using a reflected light microscope (Fig. B1). For melt inclusions that were identified during SIMS analyses, melt inclusion dimensions and petrography are not recoverable. Melt inclusions are roughly ellipsoidal in shape with average diameters of ~7 to 22 μm (Table 3.2). Four of six melt inclusions identified prior to SIMS analyses contained spherical vapor bubbles which varied in diameter from 2.7 to 5 μm.

In addition, fine-grained textured areas with skeletal pyroxene occur in the interstices between the major minerals, which we interpret as a late-stage crystallization product. We refer to this material as "interstitial glass" throughout this manuscript despite petrographic evidence for some crystallization. Interstitial glass was found in contact between pyroxene, feldspar, and phosphates (Fig. 3.1). The observed form and texture are similar to the interstitial melt identified in Bischoff et al. (2014) which is interpreted as a feature of rapid cooling.

3.3 Methods

3.3.1 Sample preparation

Meteorite chips from sample interiors were gently disaggregated using an agate mortar and pestle. Individual grains or grain aggregates were selected to avoid discoloration and staining commonly associated with terrestrial weathering. Additionally, main group ureilite grains and

grain aggregates were checked for interstitial glass and melt inclusions, however no glass was identified, consistent with previous work (Singletary and Grove, 2003). Meteorite grains, secondary standards (blank standard: Suprasil 3002 glass; check standards: Herasil 102 glass, ALV-519-4-1), and mineral standards (orthopyroxene: DGO-160, SLP-108, SLP-403, PR-705, BCN-203, 109426-1; clinopyroxene: SLP-142, SMC3-31139, SC-J1, KH03-27, DGO-160, SLP-108, SLP-402; Kumamoto et al., 2017) were mounted in Densply caulk orthodontic resin, polished to 9 μm using alumina papers, polished to 1 μm using diamond suspensions, and polished to 0.25 μm using alumina paste. Dental resin was selected for sample preparation as it has been demonstrated to be soluble in acetone and blanks prepared in dental resin have been found to have <1 μg/g H_2O (Mosenfelder et al., 2011). The dental resin was then removed by triplicate baths of toluene, acetone, and isopropanol. For ALM-A, the sample chip was polished in epoxy, from which it was subsequently removed by melting around the chip with a soldering iron. Sample preparation in epoxy has been demonstrated to result in high analytical backgrounds (Mane et al., 2016), however our analyses of ALM-A suggest degassing and contamination from the epoxy are minimal (see section 3.3.2). Samples and standards were subsequently pressed into an indium (In) mount. The pressed In mount was then repolished using 0.25 μm alumina paste to remove In from grain surfaces and improve contacts between the In and grain edges. The In mounts were then placed in a vacuum oven at ~60 °C for > 2 weeks prior to Au coating and then returned to the vacuum oven for ≥ 24 hr after coating. Samples were then transferred to the airlock chamber of the NanoSIMS 50L at Carnegie's Earth and Planets Laboratory (EPL) two weeks prior to analyses. Two days prior to analyses of the main group ureilites (11/20 analytical session; section 3.3.2.1), the airlock chamber was opened due to a malfunction of the sample holder carousel. Following NanoSIMS analyses, the In mounts

Table 3.2) HVE analyses of ureilite NAMs and ALM-A melt inclusions and interstitial glass

	H_2O (µg/g)	Unc.	F (µg/g)	Unc.	Cl (µg/g)	Unc.	CO_2 (µg/g)	Unc.	S (µg/g)	Unc.	Radius (µm)	
ALHA 78262												
ol_1	6.7	2.8	0.028	0.003	0.0051	0.0004	-	-	-	-	-	n=2
cpx_1	4.2	1.3	0.222	0.004	0.025	0.009	-	-	-	-	-	n=2
EET 83225												
ol_1	2.9	0.8	0.037	0.007	0.025	0.005	-	-	-	-	-	n=5
ol_2	excl	excl	excl	excl	excl	excl	-	-	-	-	-	excl
ol_3	3.6	0.6	0.04	0.01	0.028	0.006	-	-	-	-	-	n=8
cpx_1	3.3	0.9	0.05	0.01	0.025	0.007	-	-	-	-	-	n=5
cpx_2	excl	excl	excl	excl	excl	excl	-	-	-	-	-	excl
cpx_3	excl	excl	excl	excl	excl	excl	-	-	-	-	-	excl
EET 87517												
ol_1	4.7	0.5	0.049	0.001	0.109	0.003	-	-	-	-	-	n=1
ol_2	3.0	0.5	0.055	0.001	0.029	0.001	-	-	-	-	-	n=1
ol_3	2.3	0.5	0.044	0.005	0.03	0.01	-	-	-	-	-	n=1
ol_4	3.3	0.5	0.058	0.008	0.026	0.003	-	-	-	-	-	n=5
ol_5	3.9	1.2	0.07	0.02	0.07	0.06	-	-	-	-	-	n-2
EET96314												
ol_1	8.7	0.7	0.06	0.01	0.052	0.006	-	-	-	-	-	n=4
cpx_1	5.2	0.8	0.102	0.008	0.021	0.004	-	-	-	-	-	n=2
cpx_2	6.0	0.8	0.123	0.003	0.035	0.002	-	-	-	-	-	n=1
cpx_3	4.0	0.8	0.119	0.003	0.035	0.002	-	-	-	-	-	n=1
GRA 95205												
ol_1	excl	excl	excl	excl	excl	excl	-	-	-	-	-	excl
cpx_1	4.7	0.8	1.8	0.7	0.7	0.3	-	-	-	-	-	n=3
GRO 95575												
ol_1	6.7	2.3	0.036	0.005	0.023	0.008	-	-	-	-	-	n=2

Table 3.2 continued…

ALM-A												
pyx_1	15	3	8	1	0.015	0.04	-	-	-	-	-	n=7
pyx_3	16	2	6.2	0.1	0.015	0.001	-	-	-	-	-	n=1
pyx_5	13.4	0.5	8.8	0.3	0.02	0.01	-	-	-	-	-	n=2
pyx_?	19.1	0.5	8.8	0.4	0.009	0.001	-	-	-	-	-	n=3
MI1	160	16	290	30	3110	310	15.4	1.6	-	-	11.0	n=1
MI2	210	21	235	24	2700	270	3.1	0.3	100	10	6.8	n=1
MI4	92	9	300	30	3800	380	-	-	283	28	16.4	n=1
MI5	46	5	270	27	3100	310	1.1	0.1	228	23	-	n=1
Inc-53	97	10	246	25	2800	280	0.9	0.1	-	-	22.2	n=1
MI8	147	15	239	24	2600	260	4	0.4	182	18	11.8	n=1
MI9	60	6	221	22	2800	280	2.8	0.3	128	13	-	n=1
MI11	56	6	173	17	3000	300	1.1	0.1	152	15	-	n=1
MI13	169	17	300	30	3800	380	22.2	2.2	292	29	15.2	n=1
LSG	50.0	10	160	40	1600	130	7.0	6.0	400	300	-	n=4

excl - excluded as analyses collected after analysis 99 (see section 4.1)
n - number of spots averaged; where n > 1 spots were measured at different locations on the grain
Unc. - propagated uncertainty, calculated by propagating uncertainties from counting statistics on analyses, data corrections (see Sec 3.3.2), and calibration curves if n = 1 or one standard deviation from the mean if n > 1
LSG - interstitial glass
For ALM-A melt inclusions, where no value is reported, the detector was automatically switched "off" (i.e. tripped) during analyses to prevent rapid aging of the detector as the counts per cycle exceeded a user-defined threshold set an order of magnitude greater than expected counts (threshold: $> 10^6$ counts; expected: $\leq 10^5$ counts).

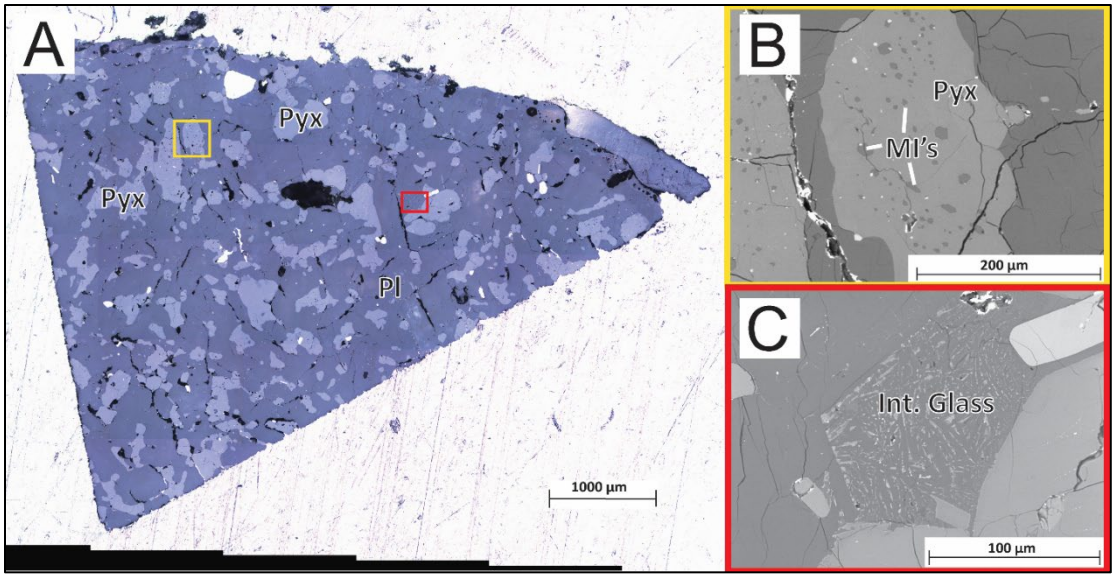

Fig. 3.1 A) Reflected light image of the studied ALM-A chip. The lighter grey-blue color is pyroxene (Pyx) while the darker grey-blue color is feldspar (Pl; anorthoclase and/or plagioclase). B) Zoomed back scatter electron (BSE) image of area from panel A showing pyroxene hosted melt inclusions (MI´s). C) Zoomed in BSE image of area from panel A exhibiting a fine-grained texture with skeletal crystals that we interpret as a late-stage crystallization product and refer to as interstitial glass.

were repolished with 0.25 µm alumina paste to remove the Au coat prior to C coating for analyses by electron probe microanalyzer (EPMA) at the University of Maryland – College Park (UMD).

3.3.2 Secondary ion mass spectrometry

3.3.2.1 Main group ureilite analyses (11/20 analytical session)

The concentrations of total H (calculated as H_2O; hereafter H_2O), F, and Cl in meteorite grains, secondary standards, and mineral standards (all in the same sample holder) were determined using a NanoSIMS 50L ion microprobe at Carnegie EPL following well established methods (Kumamoto et al., 2017; Shimizu et al., 2021). The vacuum in the sample chamber was maintained between 6.8×10^{-10} torr and 7.2×10^{-10} torr during the analyses. The analyses were

conducted using entrance slit (ES) 5 and aperture slit (AS) 4. Prior to each analysis, the analysis area was pre-sputtered for ~3 minutes using an ~2 nA Cs^+ primary beam to remove the Au coat and surface contamination and implant Cs^+ for increased secondary ion yields and counts of $^{12}C^-$, $^{16}O^1H^-$, $^{19}F^-$, $^{30}Si^-$, and $^{35}Cl^-$ were observed in imaging mode (using the 'real time imaging' function) to check for sources of contamination such as cracks or resin that could not be removed by additional pre-sputtering (images provided in Supplementary Data Files). If cracks or hot-spots corresponding to likely sources of contamination were identified during pre-sputtering, the beam was moved to another location on the grain. Following verification of the analytical area, an additional pre-sputtering was conducted for 100 seconds. For the analyses, an ~ 2 nA Cs^+ primary beam (beam size: ~800 nm) was used and the raster size was reduced to 10×10 μm and electronic gating was applied to focus the collection of ions from the central 5×5 μm region of the analytical area. The counting time for analyses was 250 seconds. Negatively charged $^{12}C^-$, $^{16}O^1H^-$, $^{19}F^-$, $^{30}Si^-$, and $^{35}Cl^-$ ions were simultaneously detected on electron multipliers. The mass resolving power (MRP; as defined by Cameca) was >8000, allowing discrimination of $^{16}O^1H$ from ^{17}O. The electron gun was used to charge compensate due to the implantation of Cs^+ ions on the sample surface and removal of negatively charged ions and electrons during analyses. The electron gun was initially tuned by maximizing the current at the FCo position and then by maximizing the secondary ^{30}Si signal on glass standard ALV-519-4-1. Using a 2 nA primary beam current, the aperture slit settings (ES5; AS4), the ^{30}Si count rates on ALV-519-4-1 are expected to be ~350k counts/s. Electron gun charge compensation was retuned at the beginning of each analysis.

Data reduction and calibration followed a protocol similar to Kumamoto et al. (2017). Data reduction and calibration proceeded as follows:

1) Counts of volatile (X = $^{12}C^-$, $^{16}O^1H^-$ (for H), $^{19}F^-$, and $^{35}Cl^-$) ions were divided by counts of $^{30}Si^-$ to account for instrumental drift.

2) Si-normalized volatile counts ($X/^{30}Si^-$) were normalized to 50 wt.% SiO_2 (multiplied by $SiO_2/50$; where SiO_2 is the SiO_2 concentration of the target as determined by electron microprobe) to account for matrix effects between phases. The normalization factor of 1/50 is used to be consistent with previous work (Hauri et al., 2002; Newcombe et al., 2020; Shimizu et al., 2021) and allows for ready comparison of normalized and un-normalized data, as basaltic glasses and minerals typically have ~50 wt.% SiO_2.

3) For $^{16}O^1H^-/^{30}Si^-\times SiO_2/50$, the analytical blank and limit of detection (LOD; Long and Winefordner, 1983) were monitored by replicate analyses of Suprasil 3002 glass, with a reference value of 2±0.43 μg/g H_2O (Newcombe, 2022). The analytical blank is estimated by:

$$OH_{Blank} = (^{16}O^1H^-/^{30}Si^-\times SiO_2/50)_{Sup} - (^{16}O^1H^-/^{30}Si^-\times SiO_2/50)_{corr}$$

where $(^{16}O^1H^-/^{30}Si^-\times SiO_2/50)_{Sup}$ is the measured value for Suprasil 3002 glass and $^{16}O^1H^-/^{30}Si^-\times SiO_2/50_{corr}$ is the $^{16}O^1H^-/^{30}Si^-\times SiO_2/50$ value corresponding to 2 μg/g H_2O as determined from a non-blank corrected glass calibration curve forced through the origin. Previous studies have demonstrated that H species have differing ionization efficiencies across different phases, which has been termed "matrix effects" (e.g., Hauri et al., 2002; Koga et al., 2003; Aubaud et al., 2007; Mosenfelder and Rossman, 2013). We have attempted to account for matrix effects in our analytical blank by applying a matrix correction based upon the SiO_2 content of the target as determined by EPMA (see above). Additionally, the slope of H_2O calibration curves for glass and NAMs generally differ by ~30 % (Fig. B5), which would result in minor changes to the reported analytical blanks. The LOD was estimated by:

$$LOD = OH_{Blank} + 3 \times \sigma,$$

where σ is the uncertainty for OH_{Blank}, determined by propagating the uncertainty (as one standard deviation) of all measured $^{16}O^{1}H^{-}/^{30}Si^{-}$ cycles for one analysis, the uncertainty on the calibration curve used to determine OH_{Blank}, and the accepted H_2O content of Suprasil 3002. Where multiple consecutive analyses of Suprasil 3002 glass were conducted, the average value was considered, however the propagated uncertainties always exceeded the standard deviation of analyses and were therefore used to calculate the LOD. The estimated LOD, determined at intervals throughout analyses of the unknowns, varied from 6.7 to 4.2 µg/g H_2O when converted to concentrations using the glass calibration curve, and varied with time due to the opening of the airlock sample exchange chamber two days prior to the start of the analytical session (see sec. 3.3.1; Fig. 3.2). Similarly, our blank corrected LOD, defined as three times the uncertainty of the analytical blank, is approximately 1.6 µg/g H_2O, as quantified using the glass calibration curve. Note, Suprasil 3002 has previously been assumed to contain <1 µg/g H_2O (Sarafian et al., 2017b, c; Newcombe et al., 2020) based upon infrared absorption analyses by glass

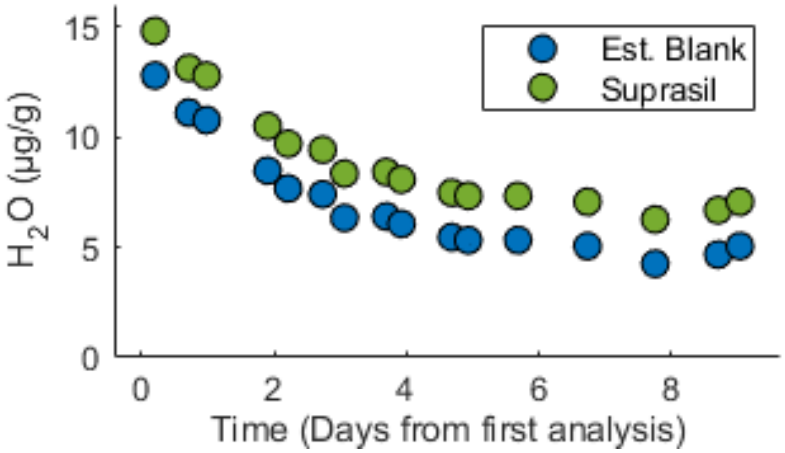

Fig. 3.2 Measured Suprasil analyses and estimated analytical blank from the 11/20 analytical session (referenced to Suprasil) plotted against time from first analysis (quantified as days = 24 hr. periods). The analytical blank (and therefore limit of detection) drew-down non-linearly with time due to opening of the airlock sample exchange chamber 2 days prior to the start of the analytical session.

manufacturer Heraeus. However, dissolved H_2 is weakly IR active and may be present in trace quantities in silicate glasses (Hirschmann et al., 2012), and HCl can be dissolved in silicates in trace quantities (Shinohara, 2009) and/or may have formed during the manufacturing of Suprasil 3002 glass by flame hydrolysis of $SiCl_4$ (Heraus Quarzglass, 2006; Behrens, 2010; Sarafian et al., 2017c). In addition, it cannot be ruled out that there is a matrix effect associated with Suprasil 3002 being pure SiO_2 while the reference SIMS glass standards span SiO_2 contents of ~49-57 wt.%. No blank-correction is applied to F and Cl, as F in main group ureilite NAMs is consistently lower than Suprasil 3002 (nominally F free; Fig. 3.3), and Cl is highly enriched in Suprasil 3002 (>~2000 µg/g Cl) and no suitable blank standard was available. Calculated uncertainties for F and Cl are considered to be minima due to low concentrations and lack of appropriate blank standards.

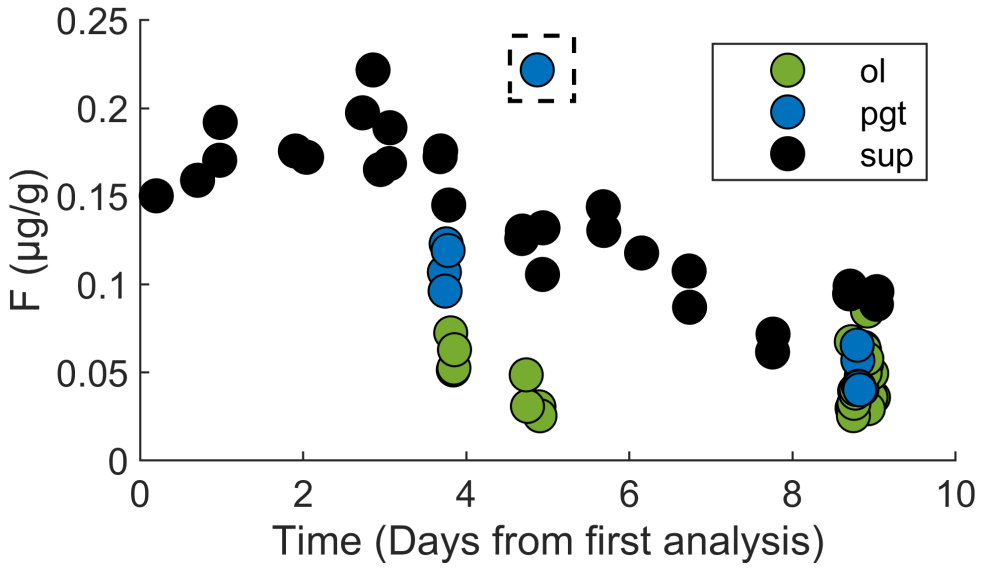

Fig. 3.3 Main group ureilite olivine (ol) and pigeonite (pgt) and Suprasil 3002 (sup) F concentrations. Error bars are smaller than plot symbols. All main group ureilite olivine and clinopyroxene have F contents lower than or unresolvable from Suprasil 3002 except ALH A78262-1 (dashed box), which is a clinopyroxene and is resolvable from neighboring Suprasil 3002 analyses. Time is defined as in Fig. 3.2.

4) Instrumental drift due to variations in detector efficiency, vacuum conditions, and electron gun tuning was further corrected for by applying a drift correction based upon replicate analyses of Herasil glass and ALV-519-4-1 collected, at minimum, at the beginning and end of each analytical day. Herasil glass was used to correct the drift for $^{16}O^{1}H^{-}/^{30}Si^{-}\times SiO_2/50$, as Herasil glass is considered to be homogeneous with respect to $^{16}O^{1}H^{-}$ and has a H_2O concentration (reported values of ~50 to 150 μg/g H_2O; Behrens, 2010; Heraus, 2011; Sarafian et al., 2017; Roskosz et al., 2018; Newcombe et al., 2020) that is expected to be within an order of magnitude of the unknowns. Drift corrections for $^{19}F^{-}/^{30}Si\times SiO_2/50$, and $^{35}Cl^{-}/^{30}Si\times SiO_2/50$ based upon ALV-519-4-1 are applied as the concentrations of the target species are considered to be well-characterized and homogeneous within this reference material (Hauri et al., 2002; Le Voyer et al., 2015; Kumamoto et al., 2017). Drift correction factors were determined by normalizing the measured value in the check standards (Herasil, ALV-519-4-1) to check standard analyses collected immediately following characterization of the calibration curves. Correction factors for $^{16}O^{1}H^{-}/^{30}Si^{-}\times SiO_2/50$, $^{19}F^{-}/^{30}Si\times SiO_2/50$, and $^{35}Cl^{-}/^{30}Si\times SiO_2/50$ of approximately 0.96 to 1.08, 0.62 to 1.87, and 0.88 to 1.12, respectively, were then applied to all analyses to account for instrumental drift.

5) Calibration curves are determined for blank-corrected $^{16}O^{1}H^{-}/^{30}Si^{-}\times SiO_2/50$ and non-blank corrected $F/^{30}Si^{-}\times SiO_2/50$ and $Cl/^{30}Si^{-}\times SiO_2/50$ data using a York regression (York et al., 2004; Wiens, 2021) forced through the origin (Fig. B5). The reported standards for the H_2O and F calibration curves for orthopyroxene and clinopyroxene are from Kumamoto et al. (see Sec. 3.3.1; 2017) . Note that the orthopyroxene calibration curve is appropriate for quantifying concentrations in olivine as the slopes of the calibration curves have been demonstrated to be within uncertainty (Kumamoto et al., 2017). Additionally, $X/^{30}Si^{-}\times SiO_2/50$ data for Suprasil

3002 is added to the H_2O and F calibration curves as a near-blank or blank value, respectively. The reported standards for the Cl and C calibration curves are based upon analyses of glass standards as described in Hauri et al. (2002) (glass: ALV-519-4-1, WOK28-3, 1833-11, 1846-12, 1833-1, 1654-3) as no matrix-matched standards were available. The use of non-matrix matched standards for C and Cl may result in inaccurate concentration data as has been reported previously (Hauri et al., 2002). We have attempted to correct for matrix effects by applying a Si-correction to data (see Sec. 3.3.2.1 #1-2). Furthermore, CO_2 concentrations (CO_2 quantified as total C) from NAMs are used only as an index of contamination and are not reported because C is highly incompatible in olivine and pyroxene (Rosenthal et al., 2015) and measured values are considered to reflect analytical backgrounds and terrestrial contamination. For Cl, we are unaware of any study that constrains matrix effects between nominally anhydrous minerals and glass.

6) Any analyses of ureilite grains in which $^{12}C/^{30}Si^{-}\times SiO_2/50$ is approximately an order of magnitude larger than in Suprasil 3002 are rejected because the analyzed areas likely included surface contamination or fractures in the minerals that potentially have affected all elemental abundances. Additionally, any data for $X/^{30}Si^{-}\times SiO_2/50$ that represent outliers relative to duplicate analyses are excluded. The excluded analyses are indicated in italics in the Supplementary Data Table B3. We note that three analyses of H_2O EET 83225 (Analyses #282, 283, 296; Table B3) are within propagated uncertainty of the LOD as determined above, and therefore are not resolvable from zero. Hence, estimates derived from these values may represent upper limits (section 3.5.3).

7) Concentrations for H_2O, F, and Cl are determined by multiplying blank- and drift-corrected $X/^{30}Si^{-}\times SiO_2/50$ values by the slope of an appropriate calibration curve (see #5 above).

For pigeonite, the clinopyroxene calibration curve is used as pigeonite is a low-Ca clinopyroxene. The pyroxene standards from Kumamoto et al. (2017) do not cover pigeonite compositions. If the pyroxene calibration is determined to be compositionally, not structurally, dependent, then the orthopyroxene calibration curve may be more appropriate resulting in a reduction of our reported pigeonite H_2O concentrations by a factor of ~0.8.

The uncertainty for all spot analyses is determined by propagating the uncertainties from counting statistics, the SiO_2 content of target phases, the accepted value of Suprasil 3002, drift correction factors, and calibration curves. The reported uncertainty for grain and sample averages is the higher value of either one standard deviation from the mean of all spot analyses or the lowest reported propagated uncertainty for corresponding spot analyses. For H_2O, F, and Cl, repeat analyses of ALV-519-4-1 (1700 µg/g H_2O; 95 µg/g F; 42 µg/g Cl) yielded reproducibilities (reported as 2 standard deviations from the mean) of 5.3%, 3.2%, and 2.7%, respectively. Additionally, the main group ureilite data presented here only include analyses conducted after the 70th hour of the analytical session (after analysis #99). This cutoff was applied to minimize contributions to the measurement uncertainties from the non-linear decrease in the background over the first ~70 hours (Fig. B2).

3.3.2.2 ALM-A pyroxene analyses (10/21 analytical session)

Volatile (CO_2, H_2O, F, and Cl) analyses of high-Ca pyroxenes from ALM-A using the nanoSIMS 50L followed a similar procedure to volatile analyses of main group ureilite NAMs. Volatile concentrations in check standards (Glass: ALV-519-4-1, Herasil, Suprasil 3002; Olivine: synthetic forsterite) were determined using orthopyroxene (DGO-160, SLP-108, SLP-403, PR-705, BCN-203, 109426-1), clinopyroxene (SLP-142, SMC3-31139, SC-J1, KH03-27, DGO-160, SLP-108, SLP-402), and glass (ALV-519-4-1, D52-3, D30-1, Suprasil 3002;

Supplementary Table B4) mounted in separate In mounts and placed in the same sample holder as the ALM-A sample mount. The analyses were conducted using entrance slit 5 and aperture slit 4. Throughout the analytical session, the vacuum in the sample chamber was maintained between 6.4×10^{-10} and 7.2×10^{-10} torr and did not vary between sample mounts as all standards and unknowns were located in the same sample holder. Prior to each analysis, ~2 nA Cs+ primary beam was rastered over a 15×15 μm area for ~3 minutes to remove the Au coat and any surface contamination and counts of $^{12}C-$, $^{16}O1H-$, $^{19}F-$, $^{30}Si-$, and $^{35}Cl-$ were observed using the "real time imaging" function of the nanoSIMS 50L to check for sources of contamination that could not be removed, such as cracks in the sample surface. If cracks or potential sources of contamination were identified using real-time imaging, the beam was moved to a new location on the grain until an appropriate area was identified. Following identification of a clean analytical area, an additional 300 seconds of pre-sputtering was conducted. The raster size was then reduced to 10×10 μm during analyses and electronic gating was applied to focus the collection of ions from the central 5×5 μm region of the analytical area. The counting time for analyses was 250 seconds. Analyses were conducted in multi-collector mode, and negatively charged $^{12}C^-$, $^{16}O^1H^-$, $^{19}F^-$, $^{30}Si^-$, and $^{35}Cl^-$ ions were simultaneously detected. The mass resolving power (Cameca definition) was ~7000 allowing discrimination of $^{16}O^1H^-$ and ^{17}O. The electron gun was used to charge compensate due to the implantation of Cs^+ ions on the sample surface and removal of negatively charged ions and electrons during analyses. Electron gun tuning followed the same procedures as the 11/20 analytical session.

As in Section 3.3.2.1, counts of volatile species were divided by $^{30}Si^-$ and multiplied by $SiO_2/50$ to account for instrumental drift and matrix effects. The blank and LOD of the ALM-A mount were monitored by repeat analyses of Suprasil 3002 glass in the sample mount and

quantified as in Section 3.3.2.1 #3. The concentration of H_2O in Suprasil 3002 glass, and by proxy the analytical blank and LOD, is not time variant over the analyses of unknowns (Fig. B3). The LOD and analytical blank were determined to be 6.7 µg/g H_2O and 10.7 µg/g H_2O, respectively. No drift correction, as in Section 3.3.2.1 #4, was applied as analyses of Herasil and ALV-519-4-1 glass are invariant over the analytical session (Fig. B4). Calibration curves and data filtering based upon $^{12}C/^{30}Si^{-}\times SiO_2/50$ proceeded as in Section 3.3.2.1. We assessed the reproducibility of low H_2O concentration analyses using repeat, paired analyses of Suprasil 3002 glass and synthetic forsterite in the clinopyroxene standard mount. Repeat analyses of Suprasil 3002 and synthetic forsterite consistently reproduced an offset of ~2±0.43 µg/g H_2O (Fig. B3; Newcombe, 2022) which we suggest is an indicator that low total H_2O contents can be reliably reproduced.

3.3.2.3 ALM-A glass analyses (01/22 analytical session)

Analyses of pyroxene-hosted melt inclusions and interstitial glass in ALM-A followed the same method as Shimizu et al. (2021). Highly volatile element (HVE; H_2O, CO_2, F, Cl and S) concentrations were characterized in standards and unknowns using the Cameca NanoSIMS 50L at Carnegie EPL. The vacuum in the analysis chamber was maintained between 8.3×10^{-10} torr and 8.6×10^{-10} torr throughout the analyses. The analyses were conducted using entrance slit 5 and aperture slit 4. Prior to analyses, a ~2 nA Cs^+ primary ion beam was rastered over a 20 µm × 20 µm area for ~3 minutes to remove the Au coat and surface contamination. Analyses were conducted by rastering a ~2 nA Cs^+ primary ion beam over a 15 µm × 15 µm area, with electronic gating applied to collect the inner most 10 µm × 10 µm area in imaging mode with 64 × 64 pixels/image. Analyses were collected over 250 seconds with count times of ~2000 µs/pixel such that 30 cycles were collected over the analysis time. Beam-blanking was not applied,

however corresponding contamination signatures (e.g., edge effects from SIMS pits) can be removed in post-processing. Electron gun tuning followed the same procedures as the 11/20 analytical session.

We used the L'image software (Larry Nittler, Carnegie EPL) to analyze collected images with corrections for counting system dead time and beam drift applied. See Shimizu et al. (2021) for a detailed description of post-processing procedures. A matrix correction was applied to all analyses by multiplying the $X/^{30}Si^-$ ratio by $SiO_2/50$ as for main group ureilite NAMs. A blank correction was applied by subtracting the average $X/^{30}Si^- \times SiO_2/50$ measured for Suprasil 3002 for all species except Cl, for which repeat analyses of synthetic forsterite (SynFo) was used. If Suprasil 3002 contains 2±0.43 µg/g H_2O as assumed for NAMs analyses, we may have systematically underestimated our H_2O concentrations by 2 µg/g H_2O, however this constitutes an error of <5% relative to our measured values (Table 3.2). Additionally, no correction for instrumental drift was applied as the reproducibilities (quantified as 2 standard deviations from the mean) were <5% for all elements in ALV-519-4-1 and H_2O in Herasil glass (Herasil is only suitable to assess H_2O). Calibration curves for CO_2, H_2O, F, Cl, and S were determined based upon analyses of ALV-519-4-1, D30-1, D52-5 (Fig. S7; Hauri et al., 2002), and Suprasil 3002 using a linear-regression forced through the origin. We assign a conservative estimate of 10 % uncertainty to calibration curves for all elements in accordance with Hauri et al. (2002); the uncertainty estimated by York regression is <4 % for all elements. The HVE detection limits (Long and Winefordner, 1983) were determined using replicate analyses of Suprasil 3002 glass mounted within the standards mount and the sample mount (Table B6). The limit of detection for Cl was determined using analyses of SynFo in the clinopyroxene standard mount which was in the same sample holder as the ALM-A sample mount (Table B7).

3.3.3 Electron microprobe analyses

The major and minor element concentrations in individual olivine and pyroxene grains, melt inclusions, and interstitial glass were measured using the JEOL JXA 8900R electron microprobe at the University of Maryland – College Park following methods similar to Dottin et al. (2018). Wavelength-dispersive spectroscopy analyses were conducted at an accelerating potential of 15 kV, with a 1-μm beam, 25-nA current, and a counting time of 20 seconds for Fe and 30 seconds for all other elements. Samples were C-coated and raw X-ray intensities were corrected by applying atomic number, absorption, and fluorescence corrections. The uncertainties on analyses (reported as 2 standard deviations from the mean) are reported in Table B1. The following standards were used to standardize olivine analyses: San Carlos Olivine – Fe, Mg, Si, Ni; Garnet 12442 – Ca. The following standards were used to standardize pyroxene analyses: Kakanui hornblende – K, Ti; Augite – Na, Fe, Al, Mg, Ca, Si; Hypersthene – Cr; Ilmenite - Mn. The following standards were used to standardize glass analyses: Yellowstone Rhyolite – Na, K; MPI St. Helens – Ca, Al, Mg, Si, Fe; Ilmenite – Ti; Rhodonite – Mn; $CePO_4$ – P.

3.4 Results

3.4.1 Mineral major and minor element concentrations

Olivine and pyroxene core Mg# and SiO_2 contents exhibit little variation (range < ~3 Mg# units, SiO_2 < 2% variation relative to the arithmetic means) within individual samples, consistent with prior investigations (Singletary and Grove, 2003). Therefore, phase specific average SiO_2 concentrations were applied to individual samples, instead of spot matched SiO_2 concentrations, when applying the SiO_2/50 matrix correction as described in Section 3.3.2.

Additionally, major and minor element concentrations measured adjacent to SIMS pits were found to be homogeneous, suggesting reduction rims are absent in analyzed grains or were not sampled as part of our analyses (Table B1).

Analyses of melt inclusions in ALM-A suggest little variation in SiO_2 concentrations (< 4% relative to the arithmetic mean), consistent with the SiO_2-rich glass analyses reported by Bischoff et al. (2014). Analyses of interstitial glass yield SiO_2 concentrations of ~67 wt.% SiO_2, slightly lower than the SiO_2-rich glass (~72.6 wt. % SiO_2) reported by Bischoff et al. (2014).

3.4.2 Volatile element (H_2O, F, Cl, and S) concentrations

We performed analyses of H_2O, F, and Cl concentrations in main group ureilite olivine and pigeonite and ALM-A high-Ca pyroxene, and CO_2, H_2O, F, Cl, and S in ALM-A melt inclusions and interstitial glass (Table 3.2; Supplementary Data Tables B3, B5, B7). Main group olivine and pigeonite water contents are a factor of ~1.2 to 2.5 greater than the analytical blank, resulting in large background corrections on the order of ~30-80% of the measured concentration. Due to the large background corrections applied to H_2O concentrations, and the absence of background corrections for F and Cl, all highly volatile element concentrations reported here are considered to be upper limits. For sample GRA 95205, F and Cl data are excluded due to hot-spots (i.e., surface contamination) identified in real-time images during pre-sputtering (see supplementary files).

Main group ureilite olivine and pigeonite water contents vary from 1.9±0.5 to 9.4±0.6 and 2.0±0.7 to 6.0±0.8 μg/g H_2O, respectively (Supplementary Data Table B3). However, one spot analysis of pigeonite in GRA 95205 yielded 18±1 μg/g H_2O (analysis #103; Supplementary Data Table B3), an outlier by a factor of ~3 relative to all other analyses; including this analysis results in a grain average of 8.2±6.9 μg/g H_2O (n = 4) for GRA 95205 cpx_1 compared to

4.7±0.8 μg/g H_2O (n = 3) when it is excluded. From here on, analysis #103 is excluded from the grain average for GRA95205 cpx_1. Grain-scale variations in H_2O range from ~0.1 μg/g to 4 μg/g with a median of 1.8 μg/g. The average mineral H_2O concentrations for individual meteorites (Table 3.3), range up to 8.7±0.7 μg/g H_2O (n = 4) in olivine and 5.1±0.8 μg/g H_2O (n = 4) in pigeonite. However, H_2O concentrations in olivine and pigeonite generally overlap across our sample set (Fig. 3.4). Measured F and Cl concentrations vary from 0.028 μg/g to 0.22 μg/g and 0.005 μg/g to 0.11 μg/g, respectively. For ALM-A pyroxenes, we measured ~13 to 19 μg/g H_2O, 6 to 9 μg/g F, and 0.009 to 0.02 μg/g Cl. Measured H_2O contents in ALM-A are resolvable from the LOD (6.7 μg/g H_2O) and F concentrations are above the limit of quantification (LOQ; 2.5 μg/g F based upon repeat analyses of Suprasil 3002 glass). ALM-A pyroxene Cl contents are low, ~0.009 to 0.02 μg/g Cl, and all fall within uncertainty of repeat analyses of nominally Cl free synthetic forsterite (0.015±0.009 μg/g Cl; 2 SD).

Excluding "Hughes cluster" ureilite EET 96314, main group ureilite olivine and pigeonite H_2O concentrations are uncorrelated with olivine core Mg# (Fig. 3.4A-B), relative degree of shock (Fig. 3.4C-D), and relative degree of weathering (Fig. 3.4E-F). Olivine F concentrations exhibit a weak positive correlation with olivine core Mg# and relative weathering but are not correlated with relative degree of shock (Fig. B8A, C, E). Pigeonite F concentrations exhibit a negative correlation with olivine core Mg# ($R^2 = 0.84$) and relative degree of shock ($R^2 = 0.67$) . However, this correlation is strongly controlled by a single data point. Pigeonite F concentration is independent of relative degree of weathering (Fig. B8B, D, F). Olivine and pigeonite Cl concentrations are not correlated with olivine core Mg#, relative degree of shock, and relative degree of weathering (Fig. B9).

Table 3.3) Average HVE concentrations per phase

Sample	H_2O (µg/g)	Unc.	F (µg/g)	Unc.	Cl (µg/g)	Unc.	CO_2 (µg/g)	Unc.	S (µg/g)	Unc.	
ALHA 78262											
ol	6.7	2.8	0.028	0.003	0.0051	0.0004	-		-		n = 2
cpx	4.2	1.3	0.222	0.004	0.025	0.009	-		-		n = 2
EET 83225											
ol	3.3	0.8	0.04	0.01	0.027	0.005	-		-		n = 13
cpx	3.3	0.9	0.05	0.01	0.025	0.007	-		-		n = 5
EET 87517											
ol	3.4	0.9	0.06	0.01	0.05	0.04	-		-		n = 10
EET96314											
ol	8.7	0.7	0.06	0.01	0.052	0.006	-		-		n = 4
cpx	5.1	0.8	0.11	0.01	0.027	0.009	-		-		n = 4
GRA 95205											
cpx	4.7	0.8	1.8	0.7	0.7	0.3	-		-		n = 4
GRO 95575											
ol	6.7	2.3	0.036	0.005	0.023	0.008	-		-		n = 2
ALM-A											
pyx	16	2	8	1	0.02	0.01	-		-		n = 13
glass	53	9	190	50	2400	800	5	5	300	200	n = 7

Reported uncertainty is 1 standard deviation from the mean
ALM-A glass is the average of our preferred values for melt inclusion HVE contents determined by averaging all interstitial glass data points with our three melt inclusions that overlap in H_2O content
n – number of spots

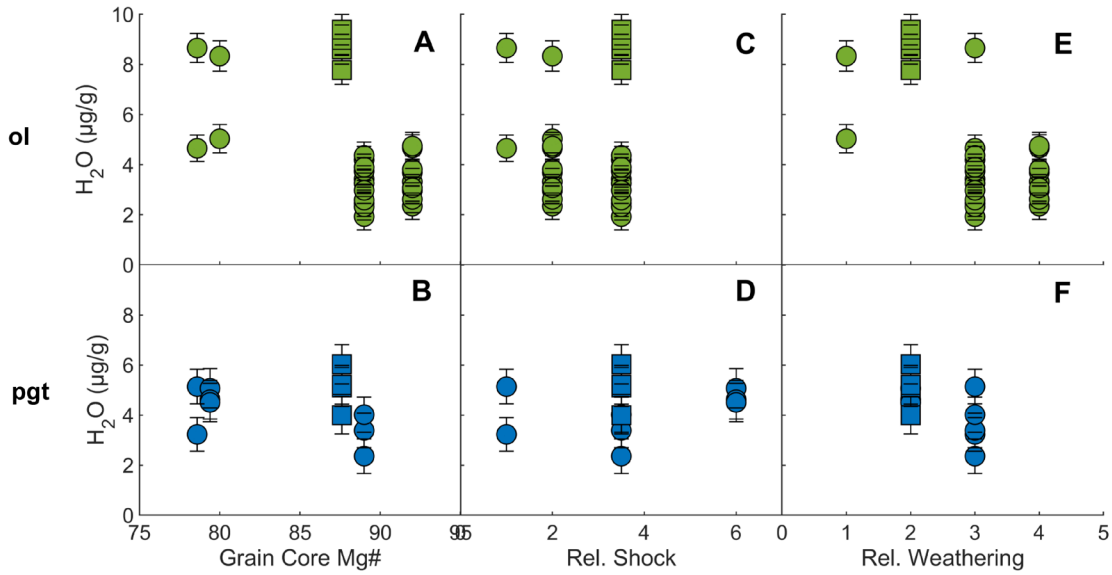

Fig. 3.4 Olivine (ol) and pigeonite (pgt) H_2O concentrations from spot analyses plotted against grain core Mg# (A,B), bulk relative degree of shock (C,D), and bulk relative degree of weathering (E,F). Circles represent main group ureilites and squares represent the Hughes Cluster ureilite (EET 96314) analyzed as part of this study. Relative degrees of shock and weathering placed on arbitrary scales based upon qualitative descriptions and classifications of weathering and shock features. Error bars are one standard deviation from the mean. All data shown are blank- and drift- corrected and are discernable from the limit of detection (not shown as it is variable with time and therefore analysis number).

The ALM-A melt inclusion and interstitial glass H_2O concentrations vary from 44 to 216 µg/g H_2O. The melt inclusion sizes were determined by averaging the largest and smallest diameters in the exposed sections of the melt inclusions (Table 3.2). For analyzed melt inclusions, H_2O concentration negatively correlates with melt inclusion size, consistent with modification of H_2O concentrations by post-entrapment crystallization of pyroxene (Fig. 3.5), but inconsistent with post-entrapment diffusive loss of water (for which a positive correlation with melt inclusion size might be expected). Additionally, melt inclusion water contents converge toward the H_2O content of the interstitial glass with increasing size (Fig. 3.5), which might suggest that the

interstitial glass has undergone relatively minor modification with respect to H_2O. We do not correct for the effects of post-entrapment crystallization as NanoSIMS analyses resulted in the destruction of analyzed melt inclusions, preventing characterization of the specific major element composition of each inclusion. Instead, we take our lowest melt inclusion H_2O concentrations, and the H_2O content of interstitial glass as estimates of the unmodified H_2O concentration of the melt (hereafter ALM-A glass; 40 – 60 µg/g H_2O).

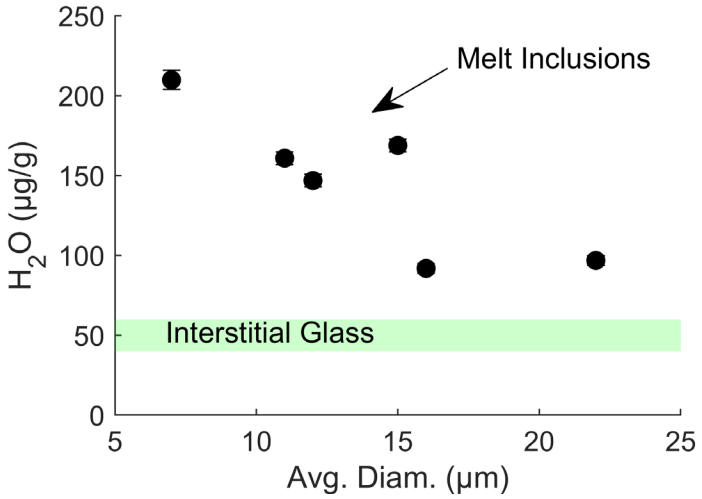

Fig. 3.5 Plot of ALM-A melt inclusion water contents (black points) and interstitial glass (green field) showing that melt inclusion H_2O content and diameter are inversely proportional, suggestive of modification of H_2O contents by post-entrapment crystallization.

3.5 Discussion

3.5.1 Overlap in olivine and clinopyroxene H_2O concentrations

Based upon previous studies, H_2O is expected to be approximately five to ten times more compatible in clinopyroxene than olivine (Aubaud et al., 2004; Hauri et al., 2006a; K. Grant et al., 2007; Tenner et al., 2009a; Kovacs et al., 2010). However, across our dataset olivine and pigeonite (i.e. low-Ca clinopyroxene) H_2O concentrations in individual samples, as well as the

data set as a whole, overlap within uncertainty (Table 3.2). The overlap in olivine (2.3 – 8.7 µg/g H_2O) and pigeonite (3.3 – 6.0 µg/g H_2O) H_2O concentrations could either reflect an analytical effect due to analyses approaching the limit of detection, or previously uncharacterized partitioning behavior.

Nearly all H_2O concentrations (87%) measured in main group ureilite olivine and pigeonite fall below the limit of quantification (Table B3). Per the definition of the limit of quantification (Long and Winefordner, 1983), analyses that fall below the limit of quantification may not have a measured concentration that is statistically resolvable from the analytical blank. We have attempted to correct for the contribution of the analytical blank to our measured H_2O concentrations using replicate analyses of Suprasil 3002 glass (Sec. 3.3.2). However, we observe that the offset between Suprasil 3002 and low H_2O clinopyroxene standard SMC3-31139 (5 +8/-5) decreased over the course of our analytical session (Fig B2). This suggests that the contribution of the analytical blank to our measured values may vary in a non-linear way that cannot be adequately accounted for by simply subtracting the excess counts measured in Suprasil 3002 as described in Section 3.3.2; therefore, all values reported here may be considered as upper limits. Further work is necessary to determine if there are any uncharacterized analytical blank effects on analyses of materials with low H_2O contents by SIMS.

If the olivine and pigeonite in our samples are considered to be in equilibrium, then we must address why our analyses yield a higher apparent olivine-clinopyroxene H_2O partition coefficient ($D_{H_2O}^{ol-cpx}$ = ~1) than expected based upon experimentally determined partition coefficients ($D_{H_2O}^{ol-cpx}$ = ~0.1-0.2).

If previously characterized olivine – clinopyroxene partitioning behavior holds at conditions relevant to the UPB, the similarity between H_2O in our olivine and pigeonite analyses

may be a result of our proximity to the detection limit; i.e., it is possible that the true olivine H_2O concentrations are 5 – 10 times lower than those of our pigeonites (true olivine H_2O concentrations < 2 μg/g). However, we have no direct evidence that under correction of the analytical blank exclusively occurs for olivine. Regardless, due to the combination of 1) the relative partitioning of olivine and clinopyroxene and 2) large background corrections (see Section 3.4.2) and associated uncertainties (e.g. calibration curves, analytical blank), we consider that our pigeonite H_2O analyses provide a more robust upper bound on the H_2O content of the ureilites than our olivine analyses.

Another possibility is that the high H_2O concentrations in our olivine crystals, relative to clinopyroxene, may be the result of previously uncharacterized partitioning behavior at low pressure and/or low total H_2O concentrations. An example of such a process could be scavenging of protons from the melt to charge balance olivine structural defects, potentially increasing the partition coefficient of H_2O in systems with low total H_2O concentrations. Non-zero H_2O concentrations measured at the edges of olivine crystals from systems undergoing dehydration into nominally dry environments lend credence to this hypothesis (Ferriss et al., 2018), but further experimental work is needed to confirm or rule out whether scavenging of protons occurs. Given that experimentally determined H_2O partitioning data for low pressures (0.1 – 200 MPa) is available for clinopyroxene (Sarafian et al., 2019), while all olivine partitioning data have been determined at pressures (0.5 – 13 GPa; Koga et al., 2003; Aubaud et al., 2004; Hauri et al., 2006; Grant et al., 2007; Tenner et al., 2009, 2012; O'Leary et al., 2010; Novella et al., 2014; Adam et al., 2016) that are likely inapplicable to ureilites (Warren, 2012; Goodrich et al., 2013c), we consider here that our pigeonite H_2O concentrations represent better mantle hygrometers than olivine in our dataset.

3.5.2 Secondary and tertiary processes that can affect absolute H_2O concentrations

Pyroxene and glass H_2O concentrations may have been modified by secondary or tertiary processes such as terrestrial weathering, shock, and post-disruption degassing. We have attempted to minimize potential contributions from terrestrial weathering by selecting olivine and pyroxene grains devoid of weathering signatures (e.g. rust-colored staining and discoloration of grains picked under a reflected light microscope) whenever possible. Additionally, ALM-A is an observed fall, therefore terrestrial weathering effects are considered to be minimal. We consider terrestrial weathering and alteration of main group NAMs to be insignificant in our dataset as the concentrations of H_2O, F, and Cl show no correlation with relative indices of terrestrial weathering (Fig. 3.4, B8-B9). Additionally, if terrestrial weathering and alteration contributed significantly to our volatile signatures, the reported concentrations would represent upper limits as weathering products in Antarctic meteorites are hydrous and may contain wt. % levels of Cl (Velbel, 1988; Velbel et al., 1991; Lee and Bland, 2004). As our reported concentrations in NAMs are near the limit of detection for all species, it seems unlikely that alteration phases dominate the measured concentrations.

All the meteorites examined as part of this study experienced some degree of shock, most likely during the catastrophic disruption of the UPB into approximately 10 to 100 m fragments (Herrin et al., 2010). The UPB is considered to have been hot upon disruption (~1100 – 1300 °C as recorded by pigeonite thermometry; Singletary and Grove, 2003; Herrin et al., 2010; Collinet and Grove, 2020) and fragmented into small pieces (~10 – 100 m; Herrin et al., 2010) which may have allowed for extensive devolatilization of ureilitic fragments. If extensive devolatilization of ureilitic fragments occurred, we would expect to observe normal zonation of H_2O concentrations in our NAMs. However, no clear gradients are observed (Fig. B10-B15), with the exception of

pigeonite EET 83225-2 (Fig. B11) which exhibits slight reverse zonation and is inconsistent with H_2O loss upon disruption of the UPB. It is also possible that impact devolatilization resulted in complete resetting of the H_2O content of ureilitic NAMs. Devolatilization of ureilitic fragments upon disruption of the UPB would have occurred under near-vacuum conditions and/or in the presence of CO gas (produced via oxidation of ureilitic graphite), which we expect would drive H_2O concentrations to 0 μg/g H_2O, contrary to our measured concentrations of ~2 - 6 μg/g H_2O in pigeonite. Additionally, the H_2O, F, and Cl contents of main group ureilite NAMs were not found to correlate with the relative degree of shock (Fig. 3.4, B8, B9). Therefore, we have no clear evidence that the catastrophic disruption of the UPB modified the H_2O content of ureilite NAMs.

Overall, we cannot rule out that our measured H_2O contents were modified by shock and post-disruption volatile loss. If the H_2O contents of our samples were modified by shock and post-disruption volatile loss, then estimates of the bulk UPB H_2O content may be considered lower limits. However, in the absence of predominant H_2O gradients and HVE correlations with indicators of shock in our samples, we suggest that our measured concentrations may reflect igneous processes. Even if the H_2O contents of ureilites were modified upon disruption of the UPB, we can still accurately evaluate if ureilite-like material (i.e., material resembling any individual ureilite) is a potential source of terrestrial H_2O.

3.5.3 H_2O content of the UPB

The main group ureilites are considered to be restites produced by extraction of ~15 – 25% partial melt (Goodrich, 1992; Barrat et al., 2016; Collinet and Grove, 2020b). Similarly, ALM-A is considered to be an early-formed melt derived from the UPB prior to the exhaustion of plagioclase (Bischoff et al., 2014; Collinet and Grove, 2020b, c). We can calculate a range of

bulk UPB H_2O concentrations by assuming that main group ureilite pigeonites represent the maximum H_2O content of the UPB mantle (i.e., the residue of melting) and the H_2O concentrations of ALM-A glass (corresponding to our preferred ALM-A glass value; see Table 3.3) represent melt extracted from the UPB mantle.

3.5.3.1 Mass balance

If we assume that the H_2O content of main group ureilite NAMs and ALM-A glass represent the H_2O content of the mantle residue and conjugate melt, respectively, due to partial melting of the UPB, we can consider the simple case of mass balance:

$$C_0 = F \times C_l + (1 - F) \times C_s$$

where C_s is the concentration of a species in the solid (i.e., the mantle residue), C_l is the concentration of a species in the liquid, C_0 is the concentration of a species in the original system, and F is the melt fraction. We consider a melt fraction of 0.15 – 0.25, corresponding to the minimum and maximum melt fraction estimates for the main group ureilites following exhaustion of plagioclase from the system (Goodrich, 1992; Collinet and Grove, 2020b), a residue (C_s) value of 2 – 6 µg/g H_2O corresponding to main group ureilite pigeonite, and a liquid (C_l) value of 44 – 62 µg/g H_2O corresponding to ALM-A glass. We consider our measured pigeonite H_2O concentrations to represent a maximum H_2O content for the residue as H_2O is more compatible in clinopyroxene than olivine and the analyzed main group ureilites do not contain significant quantities of other minerals that could host H_2O (Section 3.2; Aubaud et al., 2004; Hauri et al., 2006; Grant et al., 2007; Tenner et al., 2009; Kovacs et al., 2010). We note that ALM-A is thought to be the product of <15 % partial melting (Bischoff et al., 2014; Collinet and Grove, 2020b). Therefore, ALM-A glass H_2O contents can be used to approximate a maximum liquid value as early formed melts will be enriched in H_2O relative to later formed

melts because H is highly incompatible in the residue (Hauri et al., 2006a). Over the range of considered parameters, the calculated bulk UPB H_2O content is ~8 – 20 μg/g H_2O (Table 3.4; we perform similar estimates for F and Cl in Supplementary Section B4). This mass balance approach is advantageous because it does not rely on knowledge of mineral-melt partition coefficients which have large uncertainties (see Section 3.5.1). Conversely, the mass balance approach may not account for the possibility that ALM-A is not representative of all melts produced on the UPB. In order to account for this possibility, we consider more complex melting models based upon constraints from experiments and trace element systematics (Barrat et al., 2016; Collinet and Grove, 2020b, c).

3.5.3.2 Batch melting

We next consider a single-stage batch melting model of ureilite petrogenesis. The application of a batch melting model allows us to consider constraints from the main group ureilites and ALM-A separately, it avoids many of the assumptions inherent to more complex incremental melting models (see Section 3.5.3.3), and it is directly comparable to models used to estimate the H_2O content of the angrite and eucrite parent bodies (Sarafian et al., 2017c, 2019). We also note that previous work has argued that the aggregate melt produced by more complex incremental melting models is virtually identical to the melt produced by batch melting over the same total melt fraction (e.g. Shaw, 2000; Collinet and Grove, 2020). Using published estimates for the melt fraction required to produce main group ureilites (15 – 25%; Goodrich, 1992; Barrat et al., 2016; Collinet and Grove, 2020a) and our measured pigeonite H_2O concentrations, we can

Table 3.4) Parameters used to estimate bulk UPB maximum and minimum H_2O content

Method	*D Parameterization*		C_s (H_2O; µg/g)	C_l (H_2O; µg/g)	*D*	*F*	Bulk UPB (H_2O; µg/g)
Mass Balance		*Max. Bulk*	6	60	-	0.25	20
		Min. Bulk	2	40	-	0.15	8
Batch Melting	*200 MPa*	*Max. Bulk*	6	-	0.0071	0.25	220
		Min. Bulk	2	-	0.0089	0.15	35
Batch Melting	*0.1 MPa*	*Max. Bulk*	6	-	0.05	0.25	35
		Min. Bulk	2	-	0.15	0.15	4
Batch Melting	*O'Leary et al. (2010)*	*Max. Bulk*	6	-	0.013	0.25	120
		Min. Bulk	2	-	0.02	0.15	17
Batch Melting		*Max. Bulk*	6	-	0.013	0.25	30
		Min. Bulk	2	-	0.02	0.15	2
Batch Melting	*Hauri et al. (2006)*	*Max. Bulk*	-	62	0.007	0.15	10
		Min. Bulk	-	44	0.007	0.01	< 1
Incremental Melting (discrete increments)	*See text*	*Max. Bulk*	-	62	Table S6	< 0.15	2600
		Min. Bulk	-	62	Table S6	< 0.15	2
Incremental Melting (aggregate melt)	*See text*	*Max. Bulk*	-	62	Table S6	< 0.15	10
		Min. Bulk	-	62	Table S6	< 0.15	2

calculate the bulk UPB H_2O content via the following batch melting equation:

$$C_0 = \frac{C_s\big(D + F(1 - D)\big)}{D}$$

where C_s is the concentration of water in the solid (i.e., the mantle residue), C_0 is the concentration of water in the original system, D is the mineral-melt partition coefficient, and F is the melt fraction. We also perform the same exercise using the apparent pyroxene-melt partition coefficient derived from ALM-A (D = 0.06 – 0.4; Appendix B2). Similarly, using published estimates of the melt fraction required to produce ALM-A (<15%; (Bischoff et al., 2014; Collinet and Grove, 2020b) and our measured H_2O concentrations in ALM-A glass, we can calculate the bulk UPB H_2O content using the following batch melt equation:

$$C_0 = C_l\big(D + F(1 - D)\big)$$

where C_l is the concentration of H_2O in the liquid. Considering the variations in pigeonite and glass H_2O concentrations, solid-melt partition coefficients (Table 3.4; Hauri et al., 2006; O'Leary et al., 2010; Sarafian et al., 2019), and partial melt fractions (Goodrich, 1992; Barrat et al., 2016; Collinet and Grove, 2020b), we estimate the bulk UPB H_2O content to be < 1 – 200 μg/g (Table 3.4). This batch melting approach has the advantage of being relatively simple, with few assumptions compared to more complex melting models (e.g., incremental melting; see Section 3.5.3.3). However, it has been argued that batch melting is not applicable to the ureilite parent body as it is difficult to reproduce ureilite phase assemblages and rare earth element patterns via batch melting (Goodrich, 1999; Goodrich et al., 2007). Therefore, we consider a more complex incremental melting model in the following section.

3.5.3.3 Incremental Melting

Recent models of ureilite petrogenesis argue that incremental melting is required to reproduce the phase assemblage, phase composition, and rare earth element systematics of the main group ureilites (Barrat et al., 2016; Collinet and Grove, 2020b). We model incremental melting using the formulation of Shaw (2000), published total melt fraction estimates for ALM-A (< 15%; Bischoff et al., 2014; Collinet and Grove, 2020a), a melt increment of 0.02, a retained melt fraction of 0.02, the phase proportions of Barrat et al. (2016), and published partition coefficients (Table B8) assuming that the first melt increment is fully retained (Fig. 3.6). For a given initial H_2O concentration in the bulk UPB, the calculated incremental or aggregate melt must contain 44 – 62 µg/g H_2O prior to 15% melting, as ALM-A is considered to be the melt extracted from the UPB residue by < 15% melting.. Using these constraints, the maximum

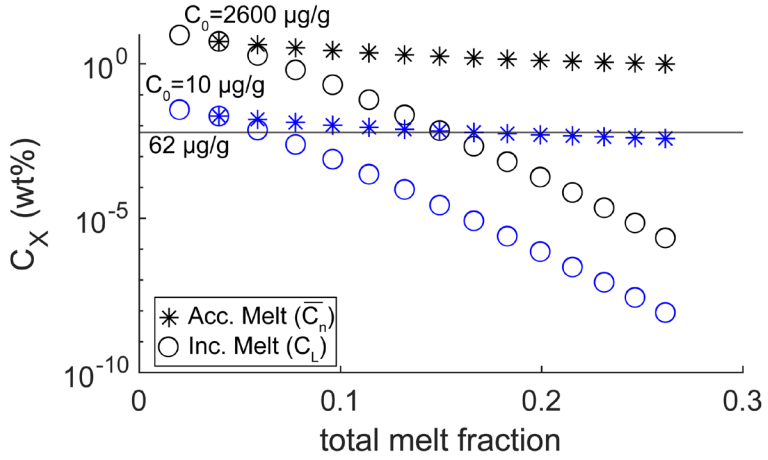

Fig. 3.6 Incremental melting model following the formulation of Shaw (2000) and parameters outlined in section 3.5.3.2. Symbols follow the nomenclature of Shaw (2000) where C_0 is the initial composition, C_L is the composition of the incremental melt, and $\bar{C}_n$ is the composition of the accumulated or aggregate melt. We have plotted the models that provide the maximum allowable bulk (C_0) H_2O that can reproduce the H_2O content of ALM-A glass (~ 44 – 62 µg/g) and the estimated melt fraction for ALM-A (< 0.15; Bischoff et al. 2014, Collinet and Grove 2020a)

permissible bulk UPB H_2O concentration is ~2600 µg/g H_2O considering ALM-A as a discrete melt increment (Fig. 3.6). However, we argue that ALM-A is unlikely to represent a discrete melt increment as the experiments of Collinet and Grove (2020a) only reproduce the ALM-A bulk composition and phase compositions as an aggregate melt (i.e., the sum of all melt increments over a total melt fraction). If we consider that ALM-A glass represents the aggregate melt, then the maximum permissible bulk UPB H_2O content is ~10 µg/g H_2O. For both the discrete melt increment and melt aggregate cases, the minimum bulk UPB H_2O content is 2 µg/g H_2O.

If hydrous phases such as amphibole or biotite were present in the UPB the melting models above may underestimate the H_2O content of the UPB; however no primary hydrous phases have been observed in ureilites (Goodrich, 1992; Singletary and Grove, 2003; Goodrich et al., 2015). We consider our UPB H_2O content estimates from our mass balance arguments (8 – 20 µg/g H_2O; Sec. 3.5.3.1) and from the aggregate melt case of our incremental melting model (2 – 10 µg/g H_2O; see above) to represent the most robust constrains on the UPB H_2O content. Therefore, we propose a preferred bulk UPB H_2O content of 2 – 20 µg/g H_2O (Fig. 3.7), which overlaps with the lowest estimates for the eucrite parent body (4 to 70 µg/g H_2O; Sarafian et al., 2019; Stephant et al., 2021; McCubbin et al., 2021).

3.5.4 UPB volatile depletion

The origin of the abundant C-bearing phases in ureilites is debated (Wlotzka, 1972; Boynton et al., 1976; Berkley et al., 1980; Goodrich and Berkley, 1986). However, there is not a clear correlation between C content and degree of shock, and there is petrologic evidence that

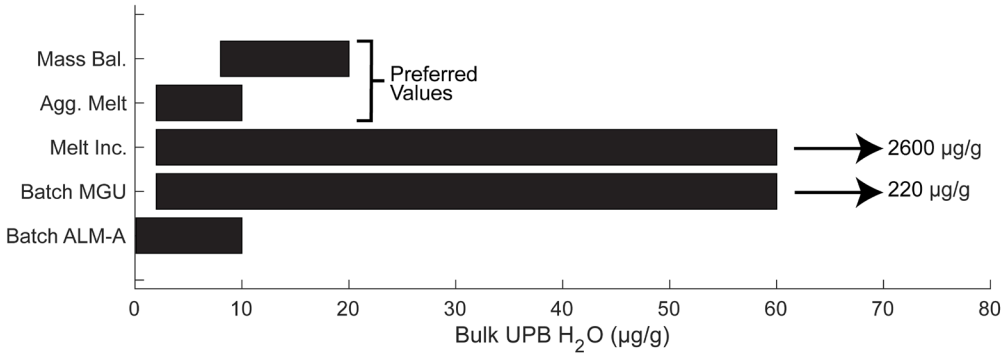

Fig. 3.7 Summary of estimated bulk UPB H_2O contents as calculated via mass balance (Mass Bal.), incremental melting (Agg. Melt = aggregate melt, Melt Inc. = discrete melt increment), batch melting starting from the residue (MGU = main group ureilites), and batch melting starting from the melt (ALM-A). Estimation methods are detailed in section 3.5.3.

ureilitic C has an igneous origin (Berkley et al., 1980; Berkley and Jones, 1982; Goodrich and Berkley, 1986; Treiman and Berkley, 1994). Assuming that ureilitic C has an igneous origin, the high C contents of ureilites (Grady et al., 1985) suggest that the ureilitic precursor materials are unlikely to have been as volatile-poor as we estimate the bulk UPB. Furthermore, C loss due to smelting on the UPB is thought to be minor (< ~0.5 wt. % C; Warren, 2011a), and C is predominantly in the form of graphite, making C loss due to heating and melting unlikely, at least in the interior of the UPB. Therefore, we can use ureilitic C as an index of the bulk UPB volatile content prior to heating and melting of precursor materials.

The H/C ratio has been used to compare and evaluate the H and C contents of terrestrial and cosmochemical reservoirs (Kuramoto, 1997; Hirschmann and Dasgupta, 2009; Marty, 2012; Halliday, 2013; Hirschmann, 2016). Here we assume that there was negligible C loss during partial melting and smelting of the UPB, and that the average ureilitic C content (2.91 wt%; Grady et al., 1985) is representative of the bulk UPB. In this case, the known H/C mass ratios of 1) CI chondrites (Kerridge, 1985; Alexander et al., 2012; Vacher et al., 2020), 2) LL chondrites

(Alexander et al., 2012) and 3) primitive insoluble organic material (Table 5; Alexander et al., 2007, 2017) provide a likely range for the bulk H contents in ureilitic precursors.

A CI chondrite-like ureilitic precursor material has been suggested based upon O isotopes and the high C content of ureilites (Goodrich et al., 2015). Additionally, experiments using a CI-like starting material (with respect to major elements) can reproduce the major silicate phases in ureilites (Collinet and Grove, 2020b). If we assume a hydrous CI-like H/C ratio (Alexander et al., 2012; Vacher et al., 2020), we estimate that ureilitic precursor materials contained approximately 11.6 or 7.2 wt. % H_2O depending on choice of CI composition. Considering the maximum of our preferred estimate of H_2O in the bulk UPB (20 μg/g), this corresponds to >99.9 % loss of H_2O prior to and during melting and differentiation. However, accreting such a large complement of H_2O would significantly influence the final oxidation state of the UPB. This is because when H_2O is mixed with an initially reduced silicate-metal-sulfide assemblage, as seems to have been the case for most or all chondrites, the H_2O would react with the Fe metal to produce H_2 gas and Fe oxides. To avoid catastrophic disruption of the parent body due to high pore pressures, the H_2 must escape to space resulting in oxidation of the parent body (e.g., Wilson et al., 1999; Rosenberg et al., 2001; Sutton et al., 2017). However, the occurrence of graphite is pervasive in main group ureilites, and graphite is only stable under reducing conditions (French and Eugster, 1965; Deines et al., 1974; Holloway et al., 1992). Also, estimates of the oxygen fugacity of main group ureilites (~IW -1 to -3; Goodrich et al., 2013b) are inconsistent with substantial H_2 degassing as the corresponding oxidation does not seem to have occurred. Therefore, we consider accretion of a CI-like complement of H_2O to be unlikely and consider this scenario as an upper bound.

The Cr, Ni, and Ti nucleosynthetic isotope anomalies in ureilites suggest that they were derived from the same reservoirs as ECs and OCs (Warren, 2011a). Additionally, experimental (Collinet and Grove, 2020b) and modeling studies (Goodrich, 1999; Warren, 2011a; Goodrich et al., 2015) suggest a LL OC-like precursor material can reproduce the phase composition of the ureilites. Assuming a Semarkona-(LL3.00)-like H/C ratio (Alexander et al., 2012), we estimate that ureilitic precursor materials contained approximately 5.3 wt. % H_2O prior to accretion. Considering the maximum of our preferred estimate of the UPB H_2O content (20 µg/g), this corresponds to > 99.9 % loss of H_2O.

The UPB is thought to have accreted in the inner solar system (Warren, 2011a). Models of the solar system's protoplanetary disk suggest that at least some of the planetesimals in the inner solar system must have accreted sunward of the water ice snowline, and therefore accreted nominally H_2O-free (Lecar et al., 2006; Min et al., 2011; O'Brien et al., 2014; Mulders et al., 2015; Morbidelli et al., 2016; Hartmann et al., 2019). Hence, it is necessary to consider a model in which the UPB accreted from H_2O-ice free precursor materials. Considering the H/C ratio of primitive organic material (Table 3.5; Alexander et al., 2007, 2017), we estimate that UPB precursor materials contained ~0.17 – 0.19 wt. % H, which is equivalent to ~1.48 – 1.74 wt. % H_2O if there is a sufficient source of O to oxidize the organics. In this scenario, the UPB degassed ~99.8 – 99.9 % of accreted H given an estimated maximum bulk UPB H_2O content of 20 µg/g.

The above cases assume that ureilitic C and H were derived from a single precursor material. This is likely an appropriate assumption as the ureilites represent an end-member

Table 3.5) Parameters used to estimate the H content of ureilitic precursors

	H (wt. %)	*C (wt. %)*	H/C	Calculated Precursor H (wt. %)	Precursor H_2O (wt. %)	Source
Ureilites	-	2.91	-	-	-	Grady et al. (1985)
CI	1.56	3.48	0.448	1.30	11.6	Alexander et al. (2012)
CI	0.96	3.48	0.276	0.80	7.2	Vacher et al. (2020)
LL3	0.12	0.59	0.203	0.59	5.29	Alexander et al. (2012)
Primitive Organic Material Max.	-	-	0.067	0.19	1.74	Alexander et al. (2007, 2017)
Primitive Organic Material Min.	-	-	0.057	0.17	1.48	Alexander et al. (2007, 2017)

The H/C ratios for primitive organic material are derived from analyses of CR chondrites

composition among NC meteorites (Warren, 2011a; Kruijer et al., 2020; Bermingham et al., 2020). However, recent models suggest that inner solar system parent bodies may have sampled a wide range of precursor materials, including limited admixture of CC material (Schiller et al., 2018, 2020; Johansen et al., 2021) and multiple NC materials (e.g., Yokoyama et al., 2019; Burkhardt et al., 2021; Shuai et al., 2022). Under these mixed-precursor models, the bulk ureilitic precursor may have resembled an intermediary composition between the models outlined above, however this would still suggest degassing of > 99.8 % of accreted H relative to thermally unprocessed precursor materials.

Formation of the UPB by accretion of two components, potentially as planetesimals, has been suggested based upon trends in $\Delta^{17}O$, olivine core Mg#, bulk FeO/MnO, C isotopes, and noble gas ratios (Murty et al., 2010; Sanders et al., 2017; Barrat et al., 2017; Broadley et al., 2020; Rai et al., 2020). There are few constraints on the volatile inventories of each component, although Broadley et al. (2020) and Barrat et al. (2017) argue that one or both components reflect a chondrite-like composition. If extensive H loss occurred on ureilite precursor bodies, then it is unclear to what extent H loss occurred on the UPB throughout accretion and differentiation. Regardless of the nature of ureilite precursor materials, our models for H loss outlined above still hold when compared to materials that are thermally unprocessed and therefore provide an estimate of H loss from thermally unprocessed precursor materials to the early stages of planetesimal differentiation. Additionally, compared to expected precursor H contents as outlined above, we suggest H and C are not required to remain coupled throughout planetesimal accretion, thermal processing, and differentiation due to the high C and low H content of ureilites.

3.5.5 Implications for Earth and early-formed parent bodies

Recent studies have suggested that differentiated (e.g., thermally processed) parent bodies may be an important source of volatiles to the Earth, potentially during a late accretionary event (Hirschmann, 2016; Li et al., 2016; Barrat et al., 2017; Grewal et al., 2019; Wang et al., 2021). In particular, ureilite-like material has been proposed as a viable source of H_2O and other volatiles to the Earth due to similar C/N ratios observed in ureilites and the bulk silicate Earth (Hirschmann, 2016). Our results show that ureilite-like material or material resembling the bulk UPB (Fig. 3.8) cannot be a major source of Earth's H_2O as both materials are H_2O depleted relative to the Earth by at least an order of magnitude. Additionally, the apparent decoupling of H and C in the UPB (Section 3.5.4) may suggest that reduced planetary bodies with refractory C phases (e.g., graphite), such as Mercury (Peplowski et al., 2016; Nittler and Weider, 2019), are likely to be highly H depleted.

Prior studies of small achondritic parent bodies (relative to the terrestrial planets), such as 4 Vesta and the angrite parent body, demonstrate that achondritic parent bodies can accrete and retain volatiles late in their accretion histories (Sarafian et al., 2017b, a, c, 2019). However, it is unclear to what extent their parent bodies were degassed prior to addition of CC-like material. Our analyses of the ureilites demonstrate that even parent bodies that did not undergo a magma ocean phase may still be highly volatile element depleted relative to potential precursor materials. We suggest that volatile elements retained through accretion, particularly H, are efficiently lost during the earliest stages of parent body heating, melting, and differentiation. Therefore, primitive achondritic and achondritic parent bodies are likely to degas a significant proportion of volatile elements acquired from their primary feedstock. This severe H loss implies

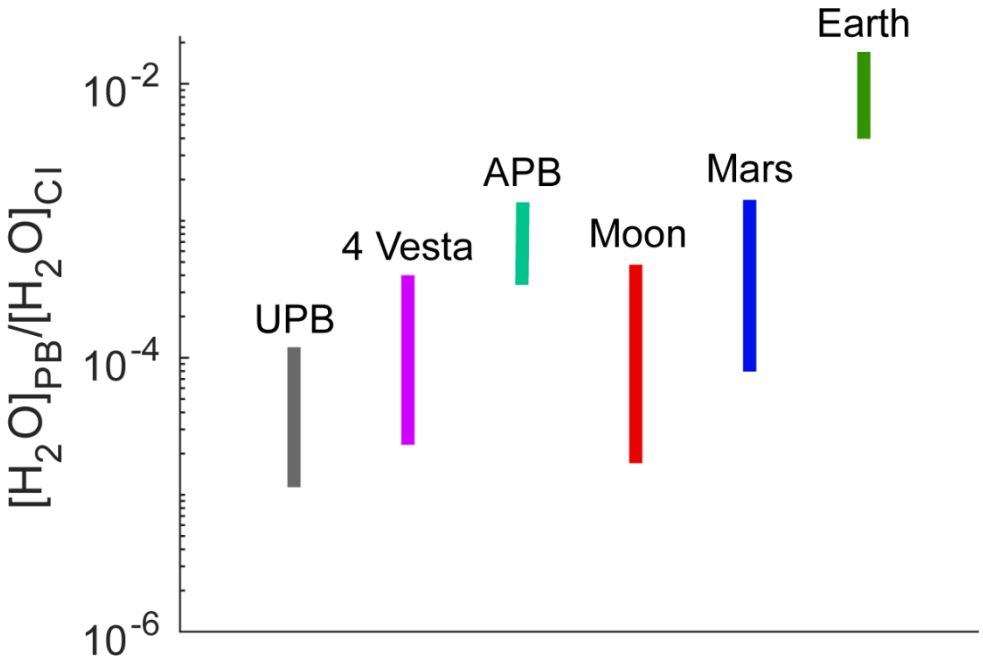

Fig. 3.8 Parent body (PB) volatile contents normalized to Ivuna-type carbonaceous Chondrite (CI) (Palme and O'Neill, 2014) for the ureilite parent body (UPB; this study), eucrite parent body (4 Vesta; Sarafian et al., 2019; Stephant et al., 2021; McCubbin et al., 2021), angrite parent body (APB; (Sarafian et al., 2017a, c), the Moon ((McCubbin and Barnes, 2019), Mars (Yoshizaki and McDonough, 2020), and the Earth (McCubbin and Barnes, 2019).

that primitive achondritic and achondritic parent bodies are unlikely to be major sources of H_2O to the Earth. Instead, our findings support models in which volatile-rich (relative to the bulk Earth) meteorites that experienced limited thermal processing (e.g. chondrites) deliver the bulk of Earth's H budget once Earth has grown to a sufficient size to limit atmospheric loss of H (e.g., Sarafian et al., 2017; Alexander et al., 2018; O'Brien et al., 2018; Piani et al., 2020).

3.6 Conclusions

We have performed the first thorough evaluation of the H_2O contents of the ureilites, the largest group of primitive achondrites in the terrestrial collections. We have measured 2 – 6 µg/g H_2O in main group ureilite pigeonite and 44 – 216 µg/g H_2O in ALM-A melt inclusions and

interstitial glass, corresponding to a preferred bulk UPB H_2O content of 2 – 20 μg/g. A combined examination of moderately volatile, volatile, and highly volatile elements suggests the UPB is highly volatile element depleted relative to chondrites, potentially as a result of evaporative loss of volatiles during heating, partial melting, melt extraction, and degassing. We argue that ureilite-like material is unlikely to be a major source of H_2O to the Earth and that H and C are not required to be coupled during planetary differentiation and degassing. Additionally, we suggest that heating, partial melting, and melt extraction during the earliest stages of planetesimal formation result in efficient loss of highly volatile elements. Further studies of primitive achondrites and suites of chondrites across petrologic types will be required to better constrain the extent of volatile loss during planetesimal heating, melting, and differentiation.

Chapter 4: The H-poor nature of incompletely melted planetesimals: the view from acapulcoites and lodranites

Note: This chapter has been accepted for publication and will be published under the following citation:

Peterson L. D., Newcombe M., Alexander C. M. O'D., Wang J. and Nielsen S. G. (accepted) The H-poor nature of incompletely melted planetesimals: the view from acapulcoites and lodranites. Geochimica et Cosmochimica Acta.

Abstract

The abundance of H in planetary building blocks is of fundamental importance for constraining the evolution of the terrestrial planets. It is commonly assumed that chondrites are the principal sources of Earth's H; however, recent studies have suggested that primitive achondrites and achondrites may retain a small complement of H. There are few constraints on the H budgets of primitive achondrites, which represent the transition from unmelted to melted planetesimals, but prior work suggests that bulk parent body H contents are several orders of magnitude lower than typical chondritic values. Therefore, to provide further constraints on H retention during the transition from unmelted to melted planetesimals, we have measured the H contents of olivine, orthopyroxene, clinopyroxene, and plagioclase from a suite of acapulcoite-lodranite clan meteorites. Acapulcoite-lodranite clan meteorites represent the "prototypical" primitive achondrite parent body and have bulk major element compositions more akin to the Earth than previously studied primitive achondrites (e.g., the ureilites). We find that the H_2O contents of olivine (~5 – 12 μg/g H_2O), orthopyroxene (~3 – 10 μg/g H_2O), and clinopyroxene (~5 – 8 μg/g H_2O) are broadly similar, while plagioclase (~2.5 – 5 μg/g H_2O) tends to be offset to lower values. Using a simple, single-stage batch-melting model, we calculate a preferred maximum acapulcoite-lodranite parent body H_2O content of 38 μg/g, which is similar to other

estimates for primitive achondritic and achondritic parent bodies. Furthermore, assuming chondrite-like precursor materials, our data are consistent with efficient loss of H prior to or during the onset of melting of early-formed planetesimals. This requires that Earth's H-budget was dominated by building blocks that underwent minimal thermal processing.

4.1 Introduction

The origins and abundances of volatile elements (e.g., H, C, O, N, S, F, Cl), particularly H, in planetary building blocks are of fundamental importance in constraining the accretion histories and evolution of the terrestrial planets. Although the major accretionary components of the Earth likely resided in the inner solar system (Dauphas, 2017), it is commonly assumed that the majority of Earth's volatile elements were sourced from a carbonaceous-chondrite-like (CC-like) source that formed in the outer solar system (e.g., Alexander, 2022; Marty, 2022). However, others suggest that Earth may have accreted a significant portion of its H from its primary, inner solar-system feedstock (Halliday, 2013; Rubie et al., 2015; Piani et al., 2020). This inner solar-system feedstock was likely a combination of undifferentiated (chondritic), partially differentiated (primitive achondritic), and fully differentiated (achondritic) parent bodies (e.g., Mezger et al., 2020; Liu et al., 2023).

Previous studies of the H contents of early-formed parent bodies have focused predominantly on chondrites (e.g., Stephant et al., 2017; Alexander, 2017; Vacher et al., 2020; Piani et al., 2020; Shimizu et al., 2021; Harries et al., 2023) and achondrites (Sarafian et al., 2017c, 2019; Stephant et al., 2021; Harries et al., 2023; Peterson et al., 2023b, a; Newcombe et al., 2023). Among chondrites, the CCs are typically, but not always, more H-rich than enstatite (EC), Rumuruti (RC), or ordinary (OC) chondrites (Alexander et al., 2018; Vacher et al., 2020; Piani et al., 2020; Alexander, 2022). Relative to chondrites and the bulk Earth, all achondrites

studied thus far, even those isotopically related to the CCs that presumably formed in the outer solar system, are highly depleted in H (Sarafian et al., 2017c, 2019; Stephant et al., 2021; McCubbin et al., 2021; Harries et al., 2023; Peterson et al., 2023b, a; Newcombe et al., 2023). This suggests that H is efficiently lost prior to or during melting of planetesimals. Furthermore, H isotopic compositions and volatile element ratios in angrites and eucrites are suggestive of post-differentiation addition of CC-like material to the angrite and eucrite parent bodies (Sarafian et al., 2017b, c, 2019). Overall, the existing data for meteoritic parent bodies suggests that chondrites are viable sources of H to the Earth, while achondrites are highly H-depleted and are unlikely to have been major sources of terrestrial H.

Primitive achondrites (e.g., acapulcoites, lodranites, tissemouminites, winonaites, silicate-bearing IAB irons, silicate-bearing IIICD irons, ureilites, brachinites, and tafassassites), as defined by Weisberg et al. (2006), are derived from isotopically heterogeneous parent bodies that likely avoided wholescale melting. Therefore, primitive achondrites can be taken as analogs to the chondrite – achondrite transition and the intermediate stages of planetesimal evolution. Recent studies have suggested that ureilite-like material may be a major source of terrestrial H (Hirschmann, 2016; Barrat et al., 2016). However, Peterson et al. (2023b) found that ureilite-like material is extremely H-poor relative to the bulk Earth, indicating that it cannot constitute a major contribution to the terrestrial H budget. On the basis of the ureilites, Peterson et al. (2023b) suggest that primitive achondrites are likely highly H-depleted relative to their precursors and the bulk Earth due to thermal processing and degassing. However, the ureilites are exceptionally C-rich and highly reduced, which may make them a poor analog for most other parent bodies. We are aware of three other studies that examined the H contents of primitive achondrites. Tartèse et al. (2019) measured the H contents of apatites and merrillites in the

brachinite-like meteorite GRA 06128 (Day et al., 2012; Greenwood et al., 2012) yielding ~20 – 60 μg/g H_2O (total H quantified as H_2O) in phosphates, but they made no estimate of the bulk parent body H content. Harries et al. (2023) measured the H contents of the acapulcoite Dhofar 125 and an olivine-rich brachinite, NWA 4969, and found that olivine and pyroxene contained <10 μg/g H_2O, with most analyses falling below the detection limit and made no estimate of parent body volatile contents. Stephant et al. (2023) measured the H contents and H isotopic composition of olivine, pyroxene, and phosphates from three acapulcoites and three lodranites. Based upon low and uniform H contents in olivine and pyroxene, a bulk parent body H_2O content of 3 to 19 μg/g was estimated (Stephant et al., 2023). The H isotopic composition determined for the acapulcoite and lodranite parent body was indistinguishable from prior studies of inner solar system bodies, which was interpreted as variable accretion of a H-rich, and isotopically deuterium (D) poor, material across the inner solar system (Stephant et al., 2023).

The ALC meteorites include acapulcoites, lodranites, and transitional samples, all of which are thought to be derived from a single, likely small (< 100 km radius) parent body that accreted by ~1.5 – 2 Ma after Ca-Al-rich inclusion formation (Touboul et al., 2009; Wilson et al., 2010; Wilson and Keil, 2012; Golabek et al., 2014; Keil and McCoy, 2018). The ALC parent body (ALPB) is widely considered to have had a layered structure, potentially with a nascent metallic core, a layered mantle of lodranites (lower), transitional samples (middle), and acapulcoites (upper), and a chondritic crust or regolith (Keil and McCoy, 2018; Li et al., 2018). The presence of relict chondrules in some acapulcoites and GRV 020043, classified as a type 4 chondrite, suggest a limited role for silicate partial melting in portions of the ALPB (McCoy et al., 2019). A thorough review of the ALCs is given by Keil and McCoy (2018).

In this work, we measure the H_2O (total H quantified as H_2O) contents of olivine, orthopyroxene, clinopyroxene, and plagioclase (nominally anhydrous minerals or NAMs) from a suite of acapulcoite-lodranite clan (ALC) meteorites (Table 4.1) that are previously unstudied for H_2O. We use our measured H_2O concentrations to assess whether ALC silicates are in equilibrium with respect to H_2O and assess the H_2O content of ALCs relative to other primitive achondrites and achondrites. We argue that 1) ALC NAMs are H_2O-poor, 2) ALC NAMs reflect poorly characterized partitioning behavior or reached a metastable condition with respect to H_2O, and 3) the acapulcoite-lodranite parent body (ALPB) was likely highly H-depleted, consistent with efficient loss of H prior to or during the onset of planetesimal melting (Harries et al., 2023; Peterson et al., 2023b; Newcombe et al., 2023).

4.2 Materials and Methods

4.2.1 Samples

A suite of seven Antarctic meteorites, Allan Hills (ALH) 81187, Meteorite Hills (MET) 01212, MET 01195, Elephant Moraine (EET) 84302, Graves Nunataks (GRA) 95209, Larkman Nunatak (LAR) 06605, and MacAlpine Hills (MAC) 88177 were analyzed as part of this study. The classification, modal mineralogy, shock stage, and weathering category are summarized in Table 4.1. The modal mineralogies are taken from Keil and McCoy (2018) as the small sizes of the sample chips analyzed as part of this study do not provide representative mineralogies of the bulk samples. The shock stages follow the classification scheme of Stöffler et al. (1991). The weathering categories follow the hand sample classification scheme used in the Antarctic Meteorite Newsletter (https://curator.jsc.nasa.gov/antmet/amn/weather.htm).

4.2.2 Sample preparation

Sample preparation for secondary ion mass spectrometry (SIMS) and electron probe microanalyses (EPMA) is detailed in Peterson et al. (2023a). In brief, sample chips were polished to 0.25 μm using alumina grit and suspensions. All sample chips were then pressed into a 1-in. diameter In mount and were repolished with 0.25-μm alumina and Au coated prior to SIMS analyses. Prior to SIMS analyses, the sample mount was degassed in a vacuum oven at 60°C for > 48 hr. and then transferred and degassed in the sample exchange chamber of the Cameca NanoSIMS 50L at the Carnegie Earth and Planets Laboratory (EPL) for >72 hr. prior to the start of analyses. Following SIMS analyses, the sample mount was repolished with 0.25-μm alumina to remove the Au coat and then a C coat was applied prior to EPMA at the University of Maryland – College Park (UMD).

4.2.3 Electron probe microanalysis

The major and minor element concentrations of olivine, orthopyroxene, clinopyroxene, and plagioclase were measured using the JEOL JXA 8900R EPMA at UMD following the methods of Peterson et al. (2023b). One to three EPMA analyses were conducted around each SIMS pit depending upon the availability of analyzable material. The standards used for the calibration of EPMA analyses are given in Table C1. The phase compositions are reported in Tables 4.2 and C2.

4.2.4 Secondary ion mass spectrometry

4.2.4.1 Analytical conditions and data processing

Analyses of H_2O, C, F, and Cl abundances were conducted using the NanoSIMS 50L at the Carnegie EPL and the methods are detailed in Peterson et al. (2023a). Briefly, the analyses

were conducted over two sessions (01/22 and 02/22), during which a set of aubrite meteorites were also measured (Peterson et al 2023a). Prior to analysis, a ~2-nA Cs^+ primary beam was rastered over a 15×15 µm area for ~5 minutes to remove the Au coat and surface contamination. The rastered area was then reduced to 10×10 µm and electronic gating was applied to focus the collection of ions from the central 5×5 µm region of the analytical area. Instrumental drift due to changing vacuum conditions, variations in the primary beam current and electron gun charge compensation was monitored using repeat analyses of Herasil glass and ALV-519-4-1 glass. The analytical background was monitored using a dry synthetic forsterite (SynFo; <<1 µg/g H_2O) and Suprasil 3002 glass (1.7±0.6 µg/g H_2O; 1 std. dev.; Newcombe et al., 2023). The following calibration standards were used to determine concentrations: OPX – SynFo, BCN-203, DGO-160, SLP-403, 109426-1, PR-7-5 (Kumamoto et al., 2017); CPX – SynFo, SLP-402; SMC31139, SLP-108, SC-J1, KH03-27, DGO-160 (Kumamoto et al., 2017); Glass – Suprasil 3002, ALV-519-4-1, D52-5, D30-1 (Hauri, 2002). For H_2O in olivine and plagioclase, orthopyroxene standards were used to calibrate analyses as the calibration curves for these phases have been shown to be similar (Mosenfelder et al., 2015; Kumamoto et al., 2017; Towbin et al., 2023). For F in olivine and plagioclase, we have elected to use the orthopyroxene calibration curve as no matrix-matched standards are available. We note that using the glass calibration curve results in a 10% and 30% increase in reported F concentrations relative to the orthopyroxene calibration curve for the 01/22 and 02/22 analytical sessions, respectively. For C, S, and Cl, the glass calibration curve was used for all phases as no matrix-matched standards were available. The sample mount and all standard mounts were held in the same sample holder

Table 4.1) Acapulcoite, transitional, and lodranite samples examined as part of this study

						Modal Mineralogy (%)				
Meteorite	*AMN Classification*[*]	*Patzer 2004 Classification*	*Keil and McCoy 2018*	*Shock*	*Weathering***	*Ol*	*Cpx*	*Opx*	*Pl*	*Ref.*
ALH 81187	*Acap*		*Acap*		*B/C*	21	2	51.5	5.9	1
MET 01212	*Acap*		*Acap*	*S1*	*B/C*					1,2
MET 01195	*Acap*		*Acap*	*S1*	*C*	25.6	42.8	0.9	6.6	1
EET 84302	*Trans*	*Trans Acap*	*Trans*	*S1*	*B/C*	4 to 21	0.5 to 1.3	31 to 50.7	6 to 16	1
GRA95209	*Lod*	*Trans Acap*	*Trans*	*S1*	*B*	13.9 to 35.4	3.8 to 6.6	8.5 to 25.3	3.6 to 13.4	1
LAR 06605	*Trans*		*Trans*	*S1*	*B*					1,2
MAC 88177	*Lod*	*Lod*	*Lod*	*S5*	*B/C*	48.7 to 52.5	1.6 to 7.6	38.4 to 44.1	0 to 0.2	1,2

[1]Keil and McCoy (2018) and references therein; [2]Lucas et al. (2019)

[*]AMN – Antarctic Meteorite Newsletter

** Hand sample weathering classification following AMN; B – Moderate rustiness, large rust haloes occur on metal particles and rust stains on internal fractures are extensive; C – Severe rustiness, metal particles have been mostly stained by rust throughout

Table 4.2) Summary of mineral compositions analyzed by EPMA

Meteorite		Orthopyroxene	Clinopyroxene	Olivine	Feldspar
ALH 81187	*Acap*	$Wo_{1.1\text{-}3.2}En_{89.9\text{-}98.5}Fs_{0.0\text{-}6.8}$	$Wo_{17.0}En_{8.9}Fs_{74.1}$	$Fo_{95.9\text{-}97.1}$	$An_{66.7\text{-}69.6}Ab_{29.3\text{-}31.8}Or_{1.1\text{-}1.5}$
MET 01212	*Acap*	$Wo_{1.1\text{-}2.1}En_{89.4\text{-}90.8}Fs_{7.7\text{-}8.7}$		$Fo_{90.8\text{-}92.0}$	$An_{68.5\text{-}72.1}Ab_{25.4\text{-}29.2}Or_{2.0\text{-}3.2}$
MET 01195	*Acap*	$Wo_{1.2\text{-}2.2}En_{89.1\text{-}91.6}Fs_{7.2\text{-}8.7}$		$Fo_{91.4\text{-}92.0}$	$An_{69.0\text{-}71.9}Ab_{26.1\text{-}28.6}Or_{2.2\text{-}2.7}$
EET 84302	*Trans*	$Wo_{1.4\text{-}2.6}En_{89.7\text{-}93.5}Fs_{4.9\text{-}8.4}$		$Fo_{90.9\text{-}93.0}$	$An_{59.9\text{-}63.7}Ab_{35.2\text{-}39.1}Or_{1.0\text{-}1.5}$
GRA95209	*Trans*	$Wo_{2.2\text{-}3.6}En_{89.4\text{-}94.9}Fs_{2.1\text{-}7.5}$	$Wo_{40.6\text{-}42.7}En_{54.1\text{-}55.7}Fs_{2.9\text{-}3.8}$	$Fo_{90.5\text{-}93.4}$	$An_{67.1\text{-}67.9}Ab_{30.9\text{-}31.7}Or_{1.2\text{-}1.3}$
LAR 06605	*Trans*	$Wo_{0.8\text{-}3.5}En_{84.8\text{-}88.9}Fs_{9.6\text{-}11.8}$		$Fo_{88.5\text{-}90.0}$	
MAC 88177	*Lod*	$Wo_{2.1\text{-}4.3}En_{83.0\text{-}87.8}Fs_{9.2\text{-}14.1}$		$Fo_{86.5\text{-}87.2}$	

to limit variations in analytical conditions, and all mounts contained Suprasil 3002 glass and ALV-519-4-1. Instrumental drift was accounted for by normalizing counts of volatile element ions (^{12}C, $^{16}O^{1}H$, ^{19}F, ^{32}S, and ^{35}Cl) to ^{30}Si. We multiply the ^{30}Si ratioed value for each element by the SiO_2 content of each phase, as determined by electron microprobe, divided by 50 (hereafter SiO_2 correction; Appendix C1; Aubaud et al., 2007; Mosenfelder and Rossman, 2013). Background corrections for H_2O analyses are described in detail in Section 4.2.4.2. The concentrations of C, F, Cl, and S contents in unknowns are frequently similar to or below those values measured for SynFo and Suprasil 3002 glass. Due to these low concentrations and the lack of robust constraints on the C, F, Cl, and S contents of SynFo and Suprasil 3002 glass at the <1 µg/g level, we elect not to apply a background correction for these elements. All reported C, F, Cl, and S data should be treated as maxima. Drift corrections were applied to the data following the methods of Peterson et al. (2023a). The uncertainties reported for all spot analyses are the propagated uncertainties due to counting statistics of the analyses, the SiO_2 content of each phase, the analytical background, the drift correction, and calibration curves. We also estimate the uncertainties of the H_2O analyses based upon the long-term reproducibility of Suprasil 3002 glass (Section 4.4.1). Data for each session were filtered based upon C and Cl abundances, which are considered indices of contamination, using a generalized extreme student deviate test for outliers (Taliaferro, 2022). For the 01/22 session, we only consider sample data from hours ~91 to 193 of the analytical session as repeat analyses outside this interval failed to reproduce an offset between Suprasil 3002 and SynFo, suggesting that low concentration H_2O analyses had poor reproducibility (Peterson et al., 2023a).

4.2.4.2 Background corrections for SIMS

The analytical background was monitored through repeat, paired analyses of Suprasil 3002 glass and SynFo when available. For the In mounts containing samples and the glass standards, only Suprasil 3002 glass was analyzed as SynFo was unavailable. The analytical background was characterized, at minimum, at the beginning and end of each analytical day. For mounts that contained SynFo, the SiO_2 corrected $^{16}O^1H/^{30}Si$ value ($^{16}O^1H/^{30}Si \times SiO_2/50$) was used as the background. For mounts that only contained Suprasil 3002 glass, we followed the workflow described in Fig. S1. In short, we take the average difference of $^{16}O^1H/^{30}Si \times SiO_2/50$ for Suprasil 3002 glass and SynFo (24% and 22% RSD for 01/22 and 02/22 sessions, respectively) held within other mounts from the same sample holder and subtract this value from Suprasil 3002 glass in mounts that lack SynFo.

We elect to apply our background-correction at this stage to be consistent with prior work (e.g., Kumamoto et al., 2017). We note that this approach may preserve interphase matrix effects that would otherwise be accounted for by blank-correcting using matrix-matched reference materials and/or concentrations determined from matrix-matched calibration curves. We expect interphase matrix-effects to be minor as the slopes of the orthopyroxene and glass calibration curves for H_2O have a percent difference of 8% and 13% for the 01/22 and 02/22 sessions, respectively, which is similar to the ~10% long-term reproducibility reported for the orthopyroxene and glass calibration curves (Hauri, 2002; Koga et al., 2003; Kumamoto et al., 2017). However, we note that Newcombe et al. (2023) observed consistent interphase differences in apparent H_2O concentrations (olivine H_2O > orthopyroxene H_2O in meteorites NWA 6704, NWA 2788 and NWA 10132; orthopyroxene H_2O > feldspar H_2O in meteorite NWA 8409) for analyses that were below or close to the reported detection limit, suggesting that the SiO_2

correction may be insufficient to fully account for matrix effects at very low H_2O concentrations. This may be due to variations in sputtering rate and ion yields or recombination effects due to compositional variations between phases. Varying ion yields and sputtering rates between silicate glasses (Hauri et al., 2006b) and lower $^{16}O^1H/^{30}Si$ values (reported by Mosenfelder et al., 2015) for plagioclase GRR145-HT (≤ ~1 μg/g H_2O) than anhydrous synthetic forsterite GRR1017 (~ 0 μg/g H_2O) may support this hypothesis. Further work comparing a large suite of anhydrous glasses, olivine, pyroxene, and feldspar will be required to test this.

4.3 Results

4.3.1 EPMA

We have measured the major and minor element concentrations of ALC orthopyroxene, clinopyroxene, olivine, and plagioclase grains analyzed by SIMS. Within our dataset, the major element compositions are homogeneous for all grains of a phase within a sample (Table C2). Furthermore, minor element compositions are nearly invariant with only a few outliers (Table C2). These findings are contrary to prior studies that have found major element zonation in orthopyroxene and clinopyroxene for some ALCs (Keil and McCoy, 2018; references therein). Notably, orthopyroxene from ALH 81187 has been reported to be zoned in Fe and Mg (Yugami et al., 1995). However, our SIMS analyses were not targeted at the outermost grain edges where zonation is expected to be most prominent, and therefore we may not have measured grain regions that were zoned in major or minor elements if they were present in our samples.

4.3.2 SIMS

4.3.2.1 Analytical background

For the 1-in. diameter In mount that contained our samples, we report analytical backgrounds of 7±1 μg/g H_2O (1 St. Dev.) and 4.2±0.7 μg/g H_2O (1 St. Dev.) for the 01/22 and 02/22 analytical sessions, respectively, based upon repeat analyses of Suprasil 3002 glass corrected as outlined in Section 4.2.4. Furthermore, we report the analytical background for the orthopyroxene, clinopyroxene, and glass standard mounts that were held in the same sample holder as the sample mount for both sessions (Table 4.3). Notably, the measured analytical background is mount dependent despite all In mounts being held in the same sample holder and, therefore, experiencing the same analytical conditions (Fig. C2). Mount dependent analytical backgrounds may be due to sample porosity and fracturing or small voids and topography in the indium that can preferentially retain adsorbed H_2O and are difficult to remove during preparation of chip samples. We determine background-corrected limits of detection (BLOD), defined as three times the uncertainty (1 St. Dev.) of the analytical background, reported as concentrations by referencing the $^{16}O^{1}H/^{30}Si \times SiO_2/50$ of the BLOD to the glass calibration curve, of 3 μg/g H_2O and 2.2 μg/g H_2O for the 01/22 and 02/22 sessions, respectively. We note that the BLOD is a modification of the limit of detection as defined by Long and Winefordner (1983) such that the value is directly comparable to data that has been background corrected, such as the data presented in this study.

Table 4.3) Values used for background-corrections converted to μg/g H_2O

	Background Value (H_2O μg/g)	
Mount	**01/22**	**02/22**
Sample 1 in.	7	4
OPX Std.	7	2
CPX Std.	4	2
Glass Std.	3	0.8

4.3.2.2 Samples

We have measured the H_2O, F, S, Cl and CO_2 (total C reported as CO_2 equivalents) contents of olivine, orthopyroxene, clinopyroxene, and feldspar from a suite of ALC meteorites (Table 4.4; Table C3). CO_2 and Cl are used as indices of contamination and were subject to statistical filtering for outliers (see Section 4.2.4), and are therefore not considered further (Data reported in Table C3). The majority of our S analyses are near zero (Table C3). We hypothesize that occasional high concentrations of S are attributable to small (≤ ~ 1 μm) sulfide inclusions. It is possible that analyses with high S concentrations (> 1 μg/g) reflect contamination, excluding these analyses does not affect our conclusions. The measured F concentrations are generally low (<~3 μg/g in all phases), except in sample GRA95209, which exhibits large inter-grain variations with concentrations reaching >200 μg/g in clinopyroxene grains 9 and 10 (Table 4.4). These high concentration in GRA 95209 grains 9 and 10 may reflect the presence of lamellae of alteration products (Mosenfelder and Rossman, 2013). However, the measured H_2O concentrations in the same grains are low (~5 and 7 μg/g H_2O, respectively) relative to hydrous alteration phases which suggests that alteration is either anhydrous or minimal. We treat H_2O data for GRA 95209 grains 9 and 10 as maxima. The background-corrected H_2O concentrations of olivine (~5 – 12 μg/g), orthopyroxene (~3 – 10 μg/g), clinopyroxene (~5 – 7 μg/g), and feldspar (~2.5 – 5 μg/g)

are frequently above the BLOD (01/22: 3 μg/g H_2O; 02/22: 2.2 μg/g H_2O). We evaluate the reproducibility of our analyses by using repeated paired analyses of Suprasil 3002

Table 4.4) Grain volatile contents

	Grain	Phase	n	H_2O (μg/g)	Unc[1]	Unc[2]	F (μg/g)	Unc[1]
ALH 81187	2	ol	3	6.4	1.9	2.1	2.9	0.7
ALH 81187	10	ol	3	5.9	1.8	2.0	1.8	0.2
ALH 81187	11	ol	3	9.4	2.7	3.2	1.8	0.6
ALH 81187	13	ol	2	7.3	2.2	2.4	2.61	0.08
ALH 81187	4	opx	5	4.2	0.8	1.4	0.9	0.3
ALH 81187	5	opx	4	3.4	1.3	1.1	0.53	0.09
ALH 81187	7	opx	3	5.6	1.8	1.8	1.7	0.5
ALH 81187	8	opx	3	6.4	2.0	2.1	0.9	0.5
ALH 81187	12	opx	3	5.8	1.9	1.9	1.9	0.5
ALH 81187	15	opx	3	6.5	2.1	2.2	1.1	0.7
ALH 81187	16	opx	1	5.1	1.8*	1.7	0.5	0.1
ALH 81187	17	opx	2	5.1	1.7	1.7	0.48	0.07
ALH 81187	18	opx	2	10.1	2.3	3.4	1	0.1
ALH 81187	6	pl	3	3.5	0.9	1.1	1.4	0.6
EET 84302	3	ol	3	7.0	0.7	2.6	1.5	0.5
EET 84302	1	opx	3	5.6	0.7	2.0	0.9	0.3
EET 84302	9	pl	2	4.3	0.7	1.5	0.36	0.04
GRA 95209	9	cpx	3	5.2	1.8	1.6	239.1	17.2
GRA 95209	10	cpx	2	7.5	2.3	2.5	254.5	28.8
GRA 95209	4	ol	3	7.8	2.3	2.6	21.1	1.1
GRA 95209	6	ol	3	7.9	2.3	2.6	10.6	1.9
GRA 95209	12	ol	1	9.5	2.8*	3.2	23	6.4
GRA 95209	1	opx	2	5.8	0.8	2.0	20.64	0.009
GRA 95209	2	opx	3	4.6	0.7	1.6	1.6	0.7
GRA 95209	3	opx	3	8.4	2.3	2.8	1.6	0.2
GRA 95209	5	opx	3	5.5	1.7	1.8	1.5	0.3
GRA 95209	7	opx	3	6.1	1.8	2.0	2	0.2
GRA 95209	8	opx	3	5.7	1.7	1.9	1.7	0.4
GRA 95209	11	pl	3	5.2	1.7*	1.8	1.2	0.4
LAR 06605	6	ol	1	11.9	3.4	4.1	0.8	0.2
LAR 06605	7	ol	3	8.2	2.3	2.7	0.4	0.3
LAR 06605	9	ol	3	8.0	2.3	2.7	0.33	0.05
LAR 06605	10	ol	3	8.7	2.5	2.9	0.16	0.04
LAR 06605	1	opx	12	7.6	2.1	2.6	0.44	0.06
LAR 06605	2	opx	6	5.9	1.7	2.0	0.36	0.05
LAR 06605	3	opx	3	5.3	1.6	1.7	0.34	0.06
LAR 06605	4	opx	3	7.2	2.1	2.4	0.39	0.04

LAR 06605	5	opx	1	6.9	2.1	2.0	0.3	0.1
LAR 06605	8	opx	3	6.2	1.9	2.1	0.31	0.05
LAR 06605	inc	opx	3	7.9	3.5*	2.6	0.2	0.1
MAC 88177	L6	ol	1	8.2	0.9	2.9	0.37	0.02
MAC 88177	L-Rand1-14	opx	1	4.0	0.7	1.4	0.26	0.01
MAC 88177	L-Rand1-16	opx	1	4.1	0.7	1.4	0.25	0.01
MET 01195	1	ol	2	6.2	0.7	2.1	2.29	0.03
MET 01195	6	ol	3	6.4	0.7	2.3	2.1	0.1
MET 01195	15	opx	2	10.0	0.7	3.5	2.9	0.3
MET 01195	16	opx	1	10.3	0.7	3.5	3.1	0.1
MET 01195	2	opx	3	5.2	0.7	1.8	2.1	0.2
MET 01195	8	pl	3	3.6	0.7	1.3	0.21	0.06
MET 01212	R4	ol	3	5.1	0.7	1.8	1.2	0.5
MET 01212	L2	ol	3	5.2	0.7	1.8	2.1	0.2
MET 01212	R2	opx	1	3.8	0.7	1.4	0.57	0.02
MET 01212	R3	pl	3	2.5	0.7	0.8	0.4	0.1

[1]Lowest propagated uncertainty due to uncertainties associated with counting statistics, SiO_2 corrections, background corrections, drift corrections, and the calibration curves among averaged points.
[2]Uncertainty based upon the long-term reproducibility of low H_2O reference materials (see Section 4.4.1)
*1 Std. Dev. from the mean

(~1.7 μg/g H_2O) and SynFo (~0 μg/g H_2O). The reproducibility is assessed by calculating the difference between the measured Suprasil 3002 and SynFo H_2O concentrations and then taking the mean and standard deviation of the differences. Over the filtered datasets (see Section 4.2.4), we report a reproducibility, quantified as the relative standard deviation (RSD), of 24% and 22% for low H_2O concentration analyses during the 01/22 and 02/22 analytical sessions, respectively. Repeat analyses of three meteorite grains from the 01/22 session were conducted in the 02/22 session to evaluate for biases in the data due to changed analytical conditions (e.g., the 02/22 session had a lower and a more stable analytical background). Analyses from the 01/22 analytical session are variably offset from values from the 02/22 session (Fig. 4.1), potentially reflecting the less stable background during the 01/22 analytical session or heterogeneity within the grains. However, relatively few grains could be reanalyzed, preventing

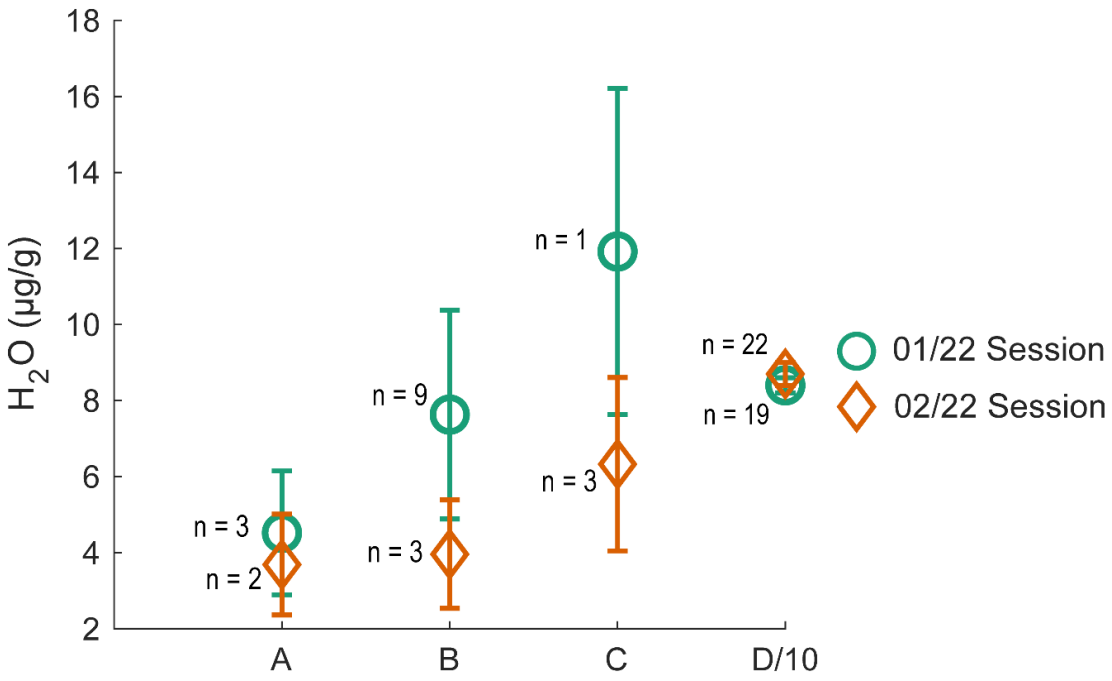

Fig. 4.1 Comparison of meteorite nominally anhydrous minerals (NAMs; A – C) and Herasil glass (D) analyzed during the 01/22 session and then reanalyzed during the 02/22 session following replacement of the Cs^+ ion source. Uncertainty for NAMs is a conservative estimate based upon the long-term reproducibility of Suprasil 3002 glass (section 4.1). The uncertainty plotted for Herasil glass is one standard deviation from the mean. Data for Herasil glass (D; ~80 µg/g H_2O) is divided by 10 such that meteoritic NAMs data is not condensed. A – ALH 81187 OPX-4, B – LAR 06605 OPX-1, C – LAR 06605 Ol-1, D – Herasil glass. n – number of analyses averaged.

a statistically robust evaluation. Nevertheless, analyses from the 01/22 and 02/22 analytical session overlap within our conservative estimates of the uncertainties (Fig. 4.1; section 4.4.1). If changing the Cs^+ source and retuning the instrument resulted in a consistent offset in concentrations reported between the 01/22 and 02/22 analytical sessions, we may expect an offset in H-bearing reference materials that are not near the analytical blank. We find that Herasil glass (~80 µg/g H_2O) has no resolvable variation between the 01/22 session (84±2 µg/g H_2O) and the 02/22 session (Fig. 4.1; 87±3 µg/g H_2O), indicating that changing the Cs^+ source and retuning the instrument did not result in variations for H analyses of materials that are not near the analytical blank. We elect to include data from the 01/22 analytical session such that data for

all samples is available, and we treat all data as quantitative despite plagioclase, as well as some pyroxene and olivine, H_2O concentrations falling below the BLOD. Ultimately, the decision to treat this data as a maximum value (i.e., the BLOD), would not affect the main conclusion of this study, namely our preferred estimate of the maximum ALPB H_2O content. This is because our estimate is based on the maximum measured H_2O concentration in clinopyroxene, which was resolvable from the BLOD (section 4.4.2 – 4.4.3; Table 4.4).

For all phases analyzed, the measured H_2O concentrations overlap within the uncertainties and are invariant with respect to relative depth and degree of melting (i.e., classification as an acapulcoite, lodranite, or transitional sample), weathering classification, and shock stage (Fig. 4.2). The low measured H_2O contents (< 12 µg/g H_2O) and the lack of apparent trends with degree of shock, weathering classification, and meteorite classification (e.g., acapulcoite, lodranite, or transitional) is consistent with prior studies (Harries et al., 2023; Stephant et al., 2023). Additionally, on the grain scale, transects and repeat analyses of grains within an analytical session yielded homogeneous H_2O concentrations (Fig. C7 – C24).

4.4 Discussion

4.4.1 Reproducibility of low H_2O analyses

We examine the intra-session reproducibility of our low H_2O NAMs analyses based upon repeat analyses of Suprasil 3002 glass and SynFo (Section 4.3.2.2). We emphasize that the reproducibility of very low H_2O analyses is dominated by the analytical blank and should therefore be assessed by reference materials with H2O contents similar to the unknowns. For example, during the 01/22 session Suprasil 3002 glass (1.7±0.6 µg/g H2O; 1 SD), Herasil glass (~80 µg/g H2O), and ALV-519-4-1 (1700±85 µg/g H2O; 2 SD) held in the sample mount were

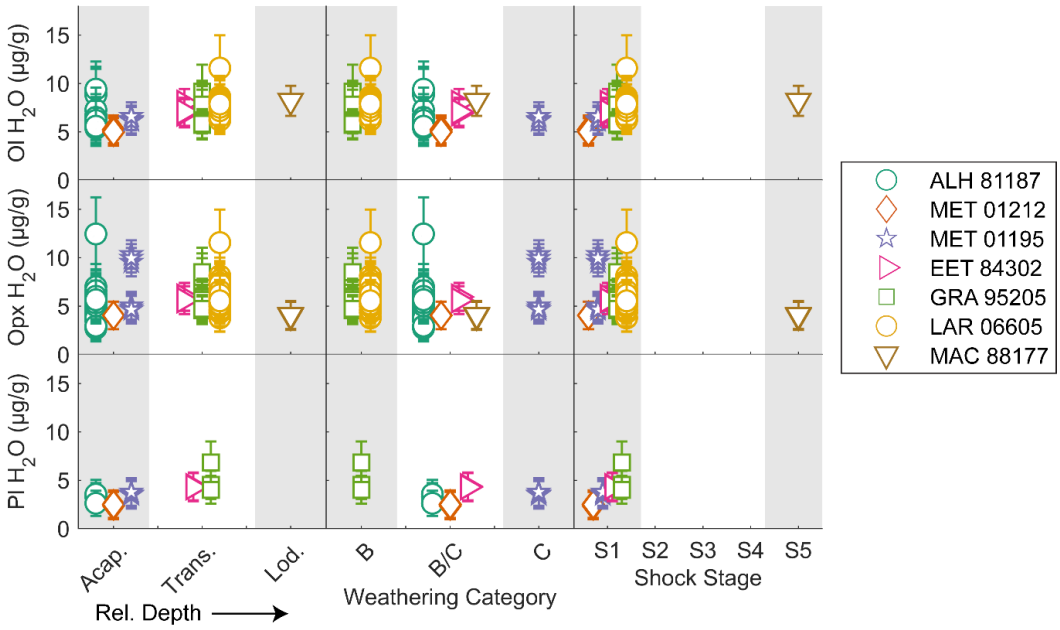

Fig. 4.2 Individual SIMS analyses of olivine (Ol), orthopyroxene (Opx), and plagioclase (Pl) H_2O concentrations plotted against relative depth or classification, assuming a layered parent body, weathering category, and shock stage. References for classifications, weathering categories, and shock stage are the same as in Table 4.1. Plotted uncertainty is the long-term reproducibility as assessed by Suprasil 3002 glass.

regularly reanalyzed; the RSD for H_2O concentrations for each reference material was 44% (n=16), 3% (n=19), and 1% (n=21), respectively. Similarly, for the 02/22 analytical session, the RSD of Suprasil 3002 glass, Herasil glass, and ALV-519-4-1 were 11% (n=22), 3% (n=22), and 1% (n=22), respectively. In both sessions, our reference materials containing 10's to 1000's µg/g H_2O have much lower RSD than Suprasil 3002 glass (1.7±0.6 µg/g H_2O), due to the smaller influence of the analytical background on the higher-water measurements. In an ideal scenario, all mounts would contain anhydrous reference materials that are concentration and matrix-matched for each target phase, allowing for a more accurate assessment of the reproducibility of low H_2O analyses. However, such reference materials are not widely available. Given the substantial increase in uncertainty once very low H_2O concentrations (~1 µg/g H_2O) are reached,

we recommend having at least one reference material with ≤ ~5 µg/g H_2O for low H_2O analyses. We note that Suprasil 3002 glass and San Carlos olivine are both suitable, widely available, low-water reference materials (provided the H_2O concentration of the San Carlos aliquot can be determined by an independent method).

The reproducibility of very low H_2O analyses is dominated by variability in the analytical background and heterogeneity of reference materials. The long-term reproducibility of low H_2O analyses is best constrained by determining an external reproducibility based upon repeat analyses of low H_2O reference materials. We determine the long-term reproducibility of our low H_2O analyses using the background-corrected (as referenced to SynFo) and drift-corrected values of Suprasil 3002 glass from the SIMSblank database (Section S1; Newcombe, 2022). The data from the SIMSblank database was collected across three mounts and 7 analytical sessions. The measured analytical background varied from ~1 to ~10 µg/g H_2O, and the average SiO_2 corrected, background-, and drift-corrected value of Suprasil 3002 glass is 1.7±0.6 µg/g H_2O (n = 204; 1 SD; Newcombe, 2022). We can also assess the long-term reproducibility of our low H_2O concentration analyses using a York regression over the SiO_2 corrected (no background- or drift-corrections) H_2O concentrations of Suprasil 3002 glass and SynFo from the SIMSblank database (Fig. 4.3). We calculate a Suprasil 3002 glass value of 1.9±0.2 µg/g H_2O (e.g., the y-intercept of the York regression; 1 standard error), where the uncertainty predominantly reflects the uncertainty attributed to the long-term reproducibility of calibration standards (Hauri et al., 2002; Kumamoto et al., 2017). While more uncertain, we prefer the long-term reproducibility as assessed by the SiO_2-, background-, and drift-corrected Suprasil 3002 glass values because it gives the more conservative estimate, and it provides a methodological match to how data is treated for unknowns. The existing SIMSblank database demonstrates that low concentration

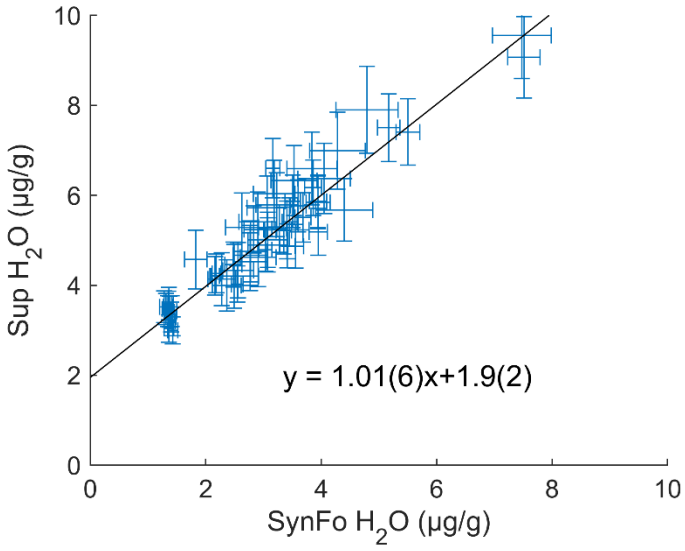

Fig. 4.3 Non-background corrected Suprasil 3002 glass (Sup) and Synthetic Forsterite (SynFo) H_2O concentrations from the SIMSblank database (Newcombe, 2022). Error bars are the larger value between the propagated uncertainty and the long-term reproducibility of the calibration curves (Hauri et al., 2002; Kumamoto et al., 2017). Data was collected across 3 indium mounts.

H_2O analyses can be reliably conducted with backgrounds up to ~10 µg/g H_2O (appropriate data for higher backgrounds is unavailable) as long as the background remains stable throughout an analytical session and low H_2O concentration standards can be discriminated.

In addition to the magnitude, the stability of the background is important. Background stabilization may take several hours to days depending on the preparation and storage history of the mount and the nature of the samples (e.g., mm-scale chips, individual mineral grains). Data collected with a variable analytical background may result in analytical artifacts (see Peterson et al. 2023b for further discussion). We suggest that paired analyses of low H_2O reference materials, like Suprasil 3002 glass or SynFo, be used to validate the accuracy of low H_2O analyses (i.e., by testing whether the H_2O concentration in Suprasil 3002 glass can be resolved from SynFo), particularly when the background is variable. If these reference materials are not available, replicate analyses of any homogeneous, low-H_2O ($\leq$~5 µg/g H_2O) material may be used to assess the accuracy of low-H_2O concentration analyses. This approach has been used for

the identification and removal of analyses for which the background is not sufficiently stable (Peterson et al., 2023b, a). We consider the long-term inter-session reproducibility of SiO_2 corrected, background-, and drift-corrected Suprasil 3002 glass (35% RSD) to be a reasonable, conservative estimate for the uncertainty of our analyses.

4.4.2 The H_2O content of ALC NAMs

4.4.2.1 Are ALC NAMs in equilibrium with respect to H_2O?

Prior work has suggested that existing experimentally determined mineral-melt and mineral-mineral H_2O partition coefficients, which are predominantly constrained under terrestrial conditions, may be applicable to meteoritic parent bodies (Peterson et al., 2023b, a). We present a detailed discussion of the applicability of experimentally determined H_2O partition coefficients to ALCs in Appendix C2. In short, based upon our existing knowledge of the primary controls on H_2O partitioning between olivine, pyroxene, and plagioclase, the existing relationships and datasets used to define the primary H_2O partitioning behavior in these phases may be applied to ALC meteorites, yielding mineral-melt ($D_{H_2O}^{X-melt}$; X = mineral) partition coefficients of $D_{H_2O}^{cpx-melt}$ = 0.015(2) (O'Leary et al., 2010), $D_{H_2O}^{opx-melt}$ = 0.003(1) or 0.0061(9) (Supplementary Section S3), $D_{H_2O}^{ol-melt}$ = 0.0009(3) (Towbin et al., 2023), and $D_{H_2O}^{pl-melt}$ = 0.006 to 0.046 (Lin et al., 2019). This in turn implies that H_2O compatibility in these phases is (in order from highest to lowest): plagioclase ≈ clinopyroxene > orthopyroxene > olivine. However, within our dataset, the H_2O contents of olivine and pyroxene overlap while the H_2O content of plagioclase is offset to slightly lower values (Fig. 4.2), conflicting with the expected differences in compatibility (Fig. 4.4). Furthermore, the H_2O contents of ALC NAMs are invariant with their classification as an acapulcoite, transitional sample, or lodranite, which is thought to be a proxy for relative depth

and relative degree of melting (Fig. 4.2; Keil and McCoy, 2018; references therein). This invariance is contrary to the expectation that, assuming a uniform, H-bearing protolith, NAMs from the samples that experienced the highest degree of melting (lodranites) should have the lowest H_2O contents as H_2O is highly incompatible in NAMs relative to melt. This lack of H_2O concentration variation with melt fraction could indicate that deeper regions of the ALPB were initially more H-rich, thereby compensating for the expected H_2O depletion produced by melting. However, the pattern of results used to justify such an explanation seems fortuitous. The disagreement with the expected H_2O compatibility and lack of variability with proxies for depth and degree of melting may indicate that the H_2O contents of NAMs were controlled by processes other than melting, such as shock or metamorphism.

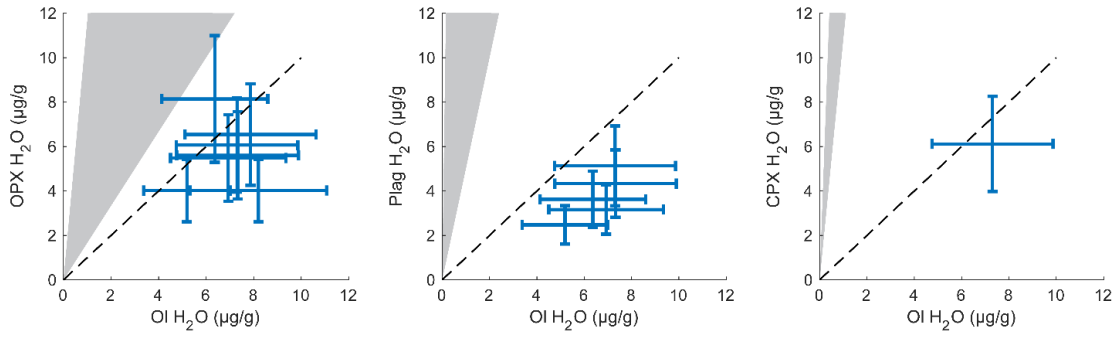

Fig. 4.4 A) Orthopyroxene (OPX), B) plagioclase (Plag), and C) clinopyroxene (CPX) H_2O concentrations plotted against olivine H_2O contents from the same sample. Uncertainties are the larger value between 1 standard deviation from the mean or the estimated uncertainty based upon the long-term reproducibility of Suprasil 3002 glass. The grey-fields represent the expected H_2O contents based upon experimentally determined partition coefficients (Section 4.2.1). The dashed line is the 1:1 line.

If the H_2O contents of ALC NAMs were modified during shock heating or thermal metamorphism, then we would expect to observe H_2O gradients or H_2O contents that are unresolvable from zero. However, intragrain H_2O contents are invariant (Fig. C7 – C24), H_2O contents of most grains are resolvable from zero, and the H_2O contents of ALC NAMs are

invariant with respect to shock stage. Widespread retrograde thermal metamorphism or hydrothermal alteration of the ALPB are ruled out by the trace element systematics of ALCs (Floss, 2000; Patzer et al., 2004), which are in agreement with numerous petrographic, experimental, and geochemical studies that suggest that the ALCs are solely the products of igneous processes (Keil and McCoy, 2018; references therein). To account for the uniform and non-zero H_2O contents observed in ALC NAMs, we infer that any global processing controlling the H_2O contents of ALC NAMs must have reached a metastable condition with respect to H.

We speculate that the relative proportion of H_2O in ALC NAMs could reflect poorly constrained partitioning behavior at low total H contents and pressures (Sarafian et al., 2019; Peterson et al., 2023b), either due to changes in the speciation of H in the melt (e.g., Adam et al., 2016) or due to defect-controlled retention of H_2O in the minerals (e.g., Behrens, 2021). At low total H contents (<< 0.1 wt.% H in the melt phase), the partitioning behavior of H_2O in NAMs may significantly deviate from those determined in hydrous (wt.%-level) partitioning experiments that are the basis of most current water partitioning literature. This inference is supported by the higher olivine-melt, orthopyroxene-melt, and plagioclase-melt H_2O partition coefficients in H_2O-poor experiments than in H_2O-rich experiments (Hauri et al., 2006a; Hamada et al., 2013; Lin et al., 2019; Potts et al., 2021), as well as clinopyroxene-melt partition coefficients at low total pressure and H contents (Sarafian et al., 2019) that are an order of magnitude greater than those predicted by a model based on experiments using high water contents and high pressures relevant to terrestrial melting processes (O'Leary et al. 2010). One potential explanation for increased mineral-melt H_2O partition coefficients at low total pressures and H_2O contents is a change in the speciation of H in the melt as detailed in Sarafian et al. (2019) and Adam et al. (2016). Another potential mechanism that may account for increased

partition coefficients at low total H contents or reaching a metastable condition with respect to H_2O, is defect-controlled loss of H from NAMs. Under this mechanism, H would be preferentially retained to charge balance extrinsic defects, resulting in non-zero H concentrations. even if a co-existing melt was very water poor. This mechanism is consistent with non-zero H_2O concentrations at the edge of olivine blocks and throughout plagioclase blocks during dehydration experiments (Ferriss et al., 2018; Behrens, 2021; Barth et al., 2023). Further detailed experimental work examining H-loss and partitioning at low total pressure and variably low H contents is required to evaluate these hypotheses. Overall, we suggest ALC NAMs reflect previously uncharacterized partitioning behavior, likely due to the low total pressures and H contents of the ALC system compared to existing experimental constraints, or a metastable condition with respect to H, potentially due to the preferential uptake or retention of H to charge balance intrinsic defects in the minerals.

4.4.2.2 The H_2O content of the ALPB

We can provide a first order assessment of the H_2O content of the ALPB by comparing the H_2O content of ALC NAMs to NAMs from other early formed primitive achondritic and achondritic parent bodies (Fig. 4.5). Notably, the H_2O contents of ALC NAMs are in line with values measured for the ureilites (Peterson et al., 2023b), ungrouped achondrites (Harries et al., 2023; Newcombe et al., 2023), aubrites (Peterson et al., 2023a), the HED parent body (Sarafian et al., 2019; Stephant et al., 2021; Harries et al., 2023), the angrites (Sarafian et al., 2017a, c), and the Moon (Hui et al., 2013, 2017; Mills et al., 2017; Simon et al., 2020). The ALCs and ureilites, both groups of primitive achondrites, are thought to have undergone similar degrees of partial melting (Goodrich, 1992; Keil and McCoy, 2018; Collinet and Grove, 2020b, a), which, when combined with the similar H_2O contents of their NAMs, is consistent with similar bulk

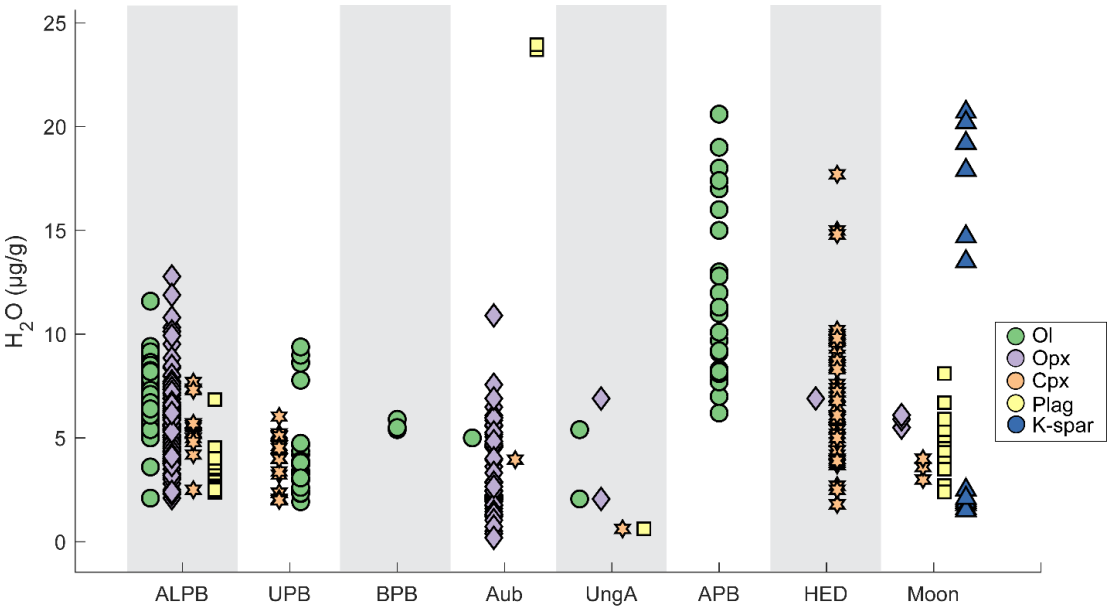

Fig. 4.5 Water concentrations measured in nominally anhydrous minerals from primitive achondritic and achondritic parent bodies. Data for the acapulcoites and lodranites (this study; Harries et al. 2023; Stephant et al., 2023) ureilites (Peterson et al. 2023), aubrites (Peterson et al., 2023a), ungrouped achondrites (Newcombe et al. 2023; Harries et al. 2023), angrites (Sarafian et al., 2017b, 2017a), Howardites-Eucrites-Diogenites (Sarafian et al., 2019; Stephant et al., 2021; Harries et al. 2023), and the Moon (Hui et al., 2017; Mills et al., 2017; Simon et al., 2020).

parent body H_2O contents (a few 10's of µg/g). Similarly, the overlap in H_2O contents of ALC NAMs with all other primitive achondrites and achondrites characterized to date is consistent with the ALPB being highly H-depleted relative to the Earth and type 3 chondrites.

If we assume that the H_2O content of one or more phases of ALC NAMs reflect equilibrium conditions, then we can apply simple melting models to estimate the bulk H_2O content of the ALPB. Prior work has argued that experimentally determined olivine-pyroxene H_2O partition coefficients are inconsistent with the H_2O contents of NAMs in primitive achondrites (Peterson et al., 2023b; Stephant et al., 2023), and therefore that the phases expected to be most H-rich are the best hygrometers (Newcombe et al., 2023). This would render clinopyroxene and plagioclase as the two best hygrometers for the ALCs. Considering that ALC NAMs likely do not reflect their expected relative partitioning based upon the primary controls

on partitioning for each phase (Section 4.4.2.1, Section C2), it would be inappropriate to apply experimentally determined partition coefficients reflecting these controls. In this case, the clinopyroxene-melt partition coefficient ($D_{H_2O}^{cpx-melt}$ = 0.10±0.05) of Sarafian et al. (2019), determined at 0.1 MPa and low total H (215 µg/g H_2O in the melt), may be most applicable to the formation conditions of ALCs. Additionally, we consider a batch melting model, which is consistent with prior experimental work to produce ALC compositions and phases (Collinet and Grove, 2020a) and prior estimates for primitive achondritic parent bodies (Peterson et al., 2023b; Stephant et al., 2023). Following the same single-stage batch melting formulation as Peterson et al. (2023b), we estimate a maximum ALPB H_2O content of 38 µg/g H_2O (Table 4.5) assuming a melt fraction, F = 0.2 (McCoy et al., 1997), a minimum $D_{H_2O}^{cpx-melt}$ = 0.05 (Sarafian et al., 2019), and our highest measured clinopyroxene H_2O content (8 µg/g H_2O). Alternatively, if we use partition coefficients obtained for more H-rich systems [$D_{H_2O}^{cpx-melt}$ = 0.013 (O'Leary et al., 2010) and $D_{H_2O}^{pl-melt}$ = 0.006 (Lin et al., 2019)] and F = 0.2, we estimate maximum bulk H_2O contents of 130 µg/g H_2O and 200 µg/g H_2O, respectively (Table 4.5), for the ALPB. We emphasize that these estimates are highly uncertain because ALC NAMs do not adhere to their predicted relative partition coefficients (Section 4.4.2.1). We prefer the maximum estimate based upon the clinopyroxene-melt partition coefficient of Sarafian et al. (38 µg/g H_2O; 2019) as

Table 4.5) Parameters used to estimate maximum bulk ALPB maximum H_2O content

Phase	$D_{H_2O}^{X-melt}$	*Reference*	C_s (H_2O; µg/g)	F	Bulk H_2O (µg/g)
Cpx	0.05	Sarafian et al. (2019)	8	0.2	38
Cpx	0.013	O'Leary et al. (2010)	8	0.2	130
Plag	0.006	Lin et al. (2019)	6	0.2	200

X – mineral or phase (e.g., cpx, plag)

the low pressure and total H contents of the experiments are likely more applicable to the ALPB. Our maximum estimates, ~130 – 200 μg/g H_2O, and preferred estimate, ≤38 μg/g H_2O, are in line with estimates from Stephant et al. (2023), who estimate up to 161 μg/g H_2O with a preferred value of 3 to 19 μg/g H_2O. In either case, these maximum estimates for the bulk ALPB H_2O content are similar to prior estimates for primitive achondrites, achondrites, and the Moon (Fig. 4.6; e.g., Mills et al., 2017; Sarafian et al., 2017c, 2019; Hui et al., 2017; Lin et al., 2019; Stephant et al., 2021; McCubbin et al., 2021; Peterson et al., 2023a, b; Newcombe et al., 2023), suggesting the ALPB is significantly H depleted relative to the Earth (~700 – 3000 μg/g H_2O; McCubbin and Barnes, 2019) and chondrites.

4.4.3 Origin and evolution of the H content of early-formed planetesimals

It is commonly assumed that melted parent bodies initially accreted from chondrite-like materials, and, by extension, that melted parent bodies' initial compositions likely resembled chondrites. If we extend these assumptions to H_2O, then the extremely H_2O-depleted nature of all primitive achondritic and achondritic parent bodies investigated to date suggests efficient H2O loss prior to or at the onset of planetesimal melting (this study; Sarafian et al., 2017a, c, 2019; Stephant et al., 2021, 2023; McCubbin et al., 2021; Harries et al., 2023; Peterson et al., 2023a, b; Newcombe et al., 2023). Using C as a proxy for the original total H content of source materials, Peterson et al. (2023b) estimated the ureilites degassed >99 % of their initial total H content, suggesting primitive achondrites may be highly degassed with respect to H.

Assuming the ALPB initially accreted from thermally primitive materials with compositions intermediate to enstatite and ordinary chondrites (McCoy et al., 1996; Floss, 2000),

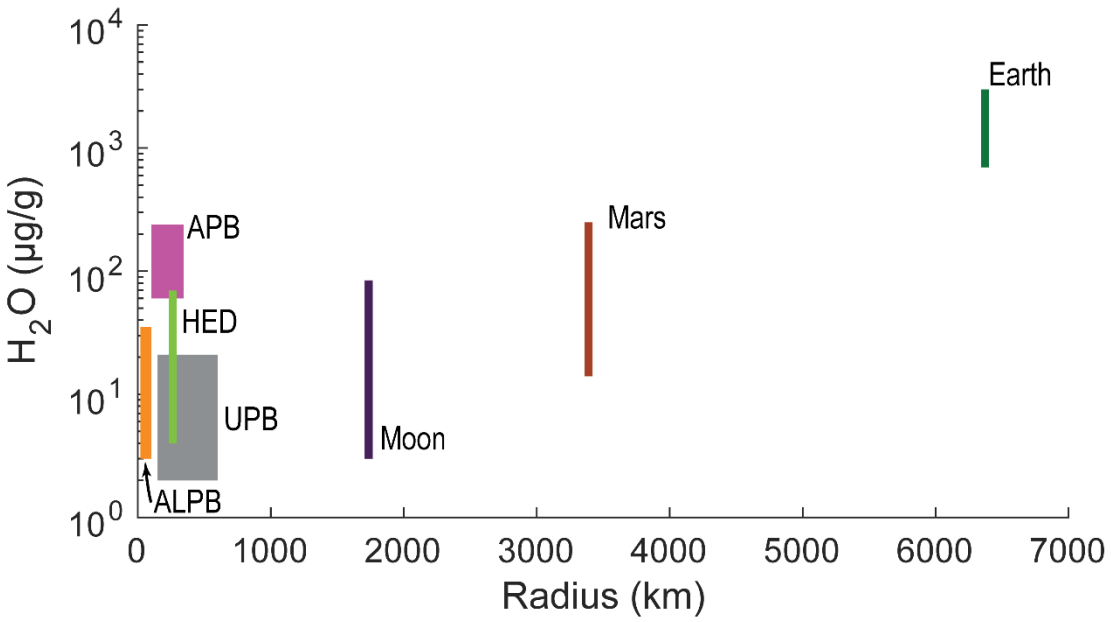

Fig. 4.6 Estimated bulk silicate H_2O contents (µg/g) vs. mean radius (km) for inner solar system parent bodies that have undergone melting. Bulk H_2O data for the acapulcoite-lodranite parent body (ALPB; this study; Stephant et al., 2023), ureilite parent body (UPB; Peterson et al., 2023b), ungrouped achondrites (UngA; Newcombe et al., 2023), howardite-eucrite-diogenite parent body (HED; Sarafian et al., 2019; McCubbin et al., 2021), angrite parent body (APB; Sarafian et al., 2017c), the Moon (Mills et al., 2017; Hui et al., 2017; Lin et al., 2019), Mars (Yoshizaki and McDonough, 2020; references therein), and the Earth (McCubbin and Barnes, 2019). The mean radii and corresponding references for all parent bodies are given in Table C12.

then the total H contents of their primitive precursor materials may have been ~0.5 to 3.6 wt. % H_2O (Alexander et al., 2012; Alexander, 2019; Vacher et al., 2020; Piani et al., 2020). Taking a bulk ALPB H_2O content of < 38µg/g H_2O following ALC genesis, this implies 99.3% to >99.9% of the initial total H budget of ALC precursor materials was lost prior to or at the onset of melting of the ALPB. Efficient loss of H_2O during thermal processing of planetesimals is also suggested by the bulk analyses of enstatite (Piani et al., 2020) and ordinary (Vacher et al., 2020; Grant et al., 2023) chondrites that show that petrographic type 5/6 (i.e., the most thermally metamorphosed) samples have lower bulk H_2O contents than primitive samples by up to ~1 order of magnitude. In particular, for the ordinary chondrites Vacher et al. (2020) measured ~3 – 4× lower H contents in LL5 and LL6 ordinary chondrites than LL3 ordinary chondrites, in stark

contrast to the estimate of <12% H loss during thermal metamorphism of ordinary chondrites by the numerical model of Jin et al. (2021). It is likely that much of the H loss from an enstatite or ordinary chondrite-like precursor relative to the ALPB is due to the breakdown of organics and mesostases, which are primary carriers of H, during thermal metamorphism (Alexander et al., 1989a, 2007, 2010; Piani et al., 2020; Thomassin et al., 2023). Based upon prior analytical work, we suggest that thermal processing of planetesimals results in efficient loss of total H relative to primitive, chondrite-like precursor materials, with integrated H loss potentially exceeding 99% of the initial H budget from metamorphism through the onset of melting.

Such large degrees of total H loss may be expected to produce large H isotopic fractionations, particularly if degassing of H occurred as H_2. However, it has been observed that early-formed primitive achondrite and achondrite parent bodies that are thought to be derived from the inner solar system have a roughly uniform δD value of approximately −250‰ that is not correlated with parent body H_2O contents (Stephant et al., 2023). This observation either requires a model with a subordinate role for degassing in setting the δD of planetesimals or requires the degassing of chondrite-like materials to be poorly described solely by degassing of H_2.

4.4.3.1 H addition to anhydrous materials

One proposed model to account for the observation of uniform δD in inner solar system parent bodies is variable addition of H_2O-bearing materials to initially anhydrous parent bodies, thereby allowing different bodies to accrete different amounts of the H_2O-rich source material(s) while retaining a uniform δD (Vacher et al., 2020; Piani et al., 2021; Stephant et al., 2023). The underlying assumption of this model is that the H budgets and isotopic compositions are set solely by accretion of the source material, not by parent body processes. However, primitive

achondrite and achondrite parent bodies have crystallization ages that preceded or were coeval with the formation ages of the chondritic parent bodies (Touboul et al., 2009; Sugiura and Fujiya, 2014; McCubbin and Barnes, 2019; references therein), and protracted accretion histories that overlap with and extend beyond the accretion ages of chondrites (McCubbin and Barnes, 2019; references therein). These melted parent bodies have uniformly lower H contents than primitive chondritic materials (Fig. 4.8) and likely sampled several feeding zones within the inner solar system, as indicated by their distinct O and nucleosynthetic isotopic compositions (e.g., Kleine et al., 2020). Considering the overlap in accretion and crystallization ages of some melted bodies and chondrites, and assuming that the feeding zones of melted and chondritic parent bodies were not mutually exclusive, this either requires that the melted planetesimals received a lower flux of H_2O-rich materials relative to chondrites or that melted planetesimals efficiently degassed H_2O throughout their accretion and, therefore, only record the δD of materials accreted during the final stages of accretion. It seems fortuitous that melted planetesimals received a lower flux of H_2O-rich materials relative to chondrites, especially considering that many partially and fully differentiated bodies have been shown to have accreted from chondrite-like materials (e.g., Righter and Drake, 1997; Keil, 2010; Collinet and Grove, 2020). Therefore, we suggest that degassing was a very efficient process throughout planetesimal evolution and, if the δD of inner solar system parent bodies predominantly reflects variable accretion of H_2O-rich materials, this is only recorded during the final stages of accretion, similar to what has been proposed for angrites and the HED parent body (Sarafian et al., 2017b, c, 2019).

4.4.3.2 Degassing of chondrite-like materials

The primitive precursor materials of the ALCs likely had a composition that was intermediate to enstatite and ordinary chondrites (McCoy et al., 1996; Floss, 2000). Within

enstatite chondrites, matrix, chondrule glass and organics are the primary carriers of H (Piani et al., 2020; Thomassin et al., 2023). Similarly, matrix, chondrule glass, organics, and phyllosilicates are the primary carriers of H in ordinary chondrites (e.g., Alexander et al., 1989, 2010; Grossman et al., 2002; Shimizu et al., 2021; Grant et al., 2023). Based upon the proportions of these phases, changes in fluid composition, if present, oxidation of Fe by H_2O and loss of H_2, and the variation from low-grade metamorphic to igneous temperatures, the extent and direction (positive or negative) of H isotopic fractionation may be highly variable.

Over metamorphic temperatures, the H isotopic evolution of chondritic organics is likely complex and dependent on the composition of organics present. In short, if thermal cracking occurs, H isotopic fractionations may be small (e.g., Schimmelmann et al., 2006; Sessions, 2016; Wang et al., 2017). Conversely, studies of the thermal maturation of bulk chondritic insoluble organic materials (IOM) demonstrates that large isotopic fractionations, positive and negative, can occur during heating depending on the compositions and abundances of labile and refractory organics (Alexander et al., 2007, 2010; Remusat et al., 2016, 2019). Altogether, this suggests that H isotopic fractionations due to breakdown of organics are compositionally dependent and therefore unpredictable without direct constraints.

To assess the extent of H isotopic fractionation due to loss of H from silicate materials during metamorphic heating, we can examine the multi-step (>2) heating experiments of hydrated silicates (e.g., Saccocia et al., 2009; Asaduzzaman and Ganguly, 2021) and chondrites (e.g., Kolodny et al., 1980; McCoy et al., 1993; Eiler and Kitchen, 2004; Lee et al., 2021). Over metamorphic temperatures (e.g., 200 - 800°C), dehydration of hydrated silicates yield total H isotopic fractionations of <100 ‰ (e.g., Saccocia et al., 2009; Asaduzzaman and Ganguly, 2021). Stepwise degassing experiments of ordinary (H, L, and LL) and enstatite (E) chondrites over

metamorphic temperatures yield highly variable results. A study of LL3 chondrites by McNaughton et al. (1982) found large total H isotopic fractionations (> 1000 ‰). However, these fractionations were largely attributed to break-down of abundant organic phases. Conversely, the studies of Robert et al. (1987) and McCoy et al. (1993) found relatively small total H isotopic fractionations (< ~200 ‰) in a suite of LL3, LL6, H3, H6, and E6 chondrites. Considering that 10 out of 12 samples studied in Robert et al. (1987) and McCoy et al. (1993) exhibit total H isotopic fractionations < 250 ‰ and that hydrous silicates exhibit small fractionations (< 100 ‰; e.g., Saccocia et al., 2009; Asaduzzaman and Ganguly, 2021), a reasonable estimate of the net H isotopic fractionation due to H loss from silicates at metamorphic temperatures was likely on the order of < a few 100's ‰. Additionally, positive and negative H isotope excursions were reported during step-wise heating of ordinary chondrites over metamorphic temperatures (Robert et al., 1987). This may imply sample-specific H isotopic evolution, further complicating a straightforward model for the H isotopic evolution of potential ALC precursor materials. Overall, degassing of chondrite-like materials through metamorphic temperatures is expected to be complex, but, to a first order, may reasonably be expected to produce net H isotopic fractionations of < a few 100's ‰, which is within the net difference observed for inner solar system bodies (~400 ‰; Stephant et al., 2023; references therein).

Relative to metamorphic temperatures, the H isotopic evolution of silicates at igneous temperatures (e.g., 800 - 1200°C) is better constrained. As H is highly incompatible in NAMs relative to silicate melt, it is likely that the bulk of degassing at igneous temperatures is associated with silicate melts. Therefore, we model degassing of a silicate melt starting with an initial $\delta D = -239 \pm 149$‰, which is the average δD of NAMs from ALC falls (Stephant et al., 2023), and modify the open- and closed-system equilibrium degassing model of Giachetti et al.

(2020) to accommodate H_2 and H_2O in the vapor (Appendix C3). Our simple model (Fig. 4.7) shows that even degassing of >99% of H is consistent with the H isotopic composition of the ALPB within uncertainty ($\delta D = -239 \pm 149‰$; Stephant et al., 2023). These models are highly sensitive to the choice of fractionation factors, which are controlled by the fraction of H degassing as H_2 or H_2O, and therefore the fO_2 of the system (Sarafian et al., 2017b, a). For oxidized melts that are rich in H_2O, degassing is expected to produce flat or negative H isotopic fractionations (Sarafian et al., 2017b, a), further demonstrating that the δD and water content of the ALPB is not inconsistent with water loss through severe degassing.

In summary, H isotopic fractionation during metamorphism and melting of silicates is complex and may produce positive or negative H isotopic fractionations. However, our results suggest that degassing of early-formed planetesimals was efficient, such that the δD of degassed inner solar system parent bodies was likely overprinted by accretion of H_2O-rich materials during the final stages of H_2O accretion.

4.4.4 Implications for H_2O retention and delivery to terrestrial planets

Assuming that all bodies accreted from chondrite-like precursor materials, comparisons between measured H_2O contents of NAMs in melted parent bodies (Fig. 4.5), and the bulk H_2O contents of chondrites, primitive achondrite and achondrite parent bodies, the Moon, Earth, and Mars (Fig. 4.8) allows us to evaluate the timing and degree of water loss during planetary evolution. Notably, all primitive achondritic and achondritic parent bodies are H-poor relative to the Earth and chondrites. The primary conclusion from this observation is that H was efficiently lost prior to or at the onset of planetesimal melting, not at the magma ocean stage (Harries et al., 2023; Peterson et al., 2023b, a; Newcombe et al., 2023), or that melted planetesimals are only

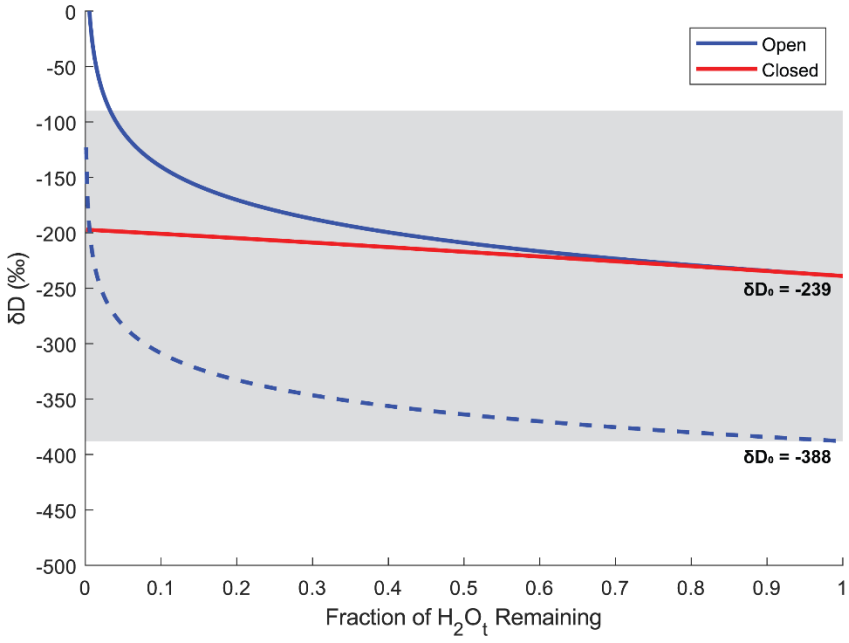

Fig. 4.7 Open- and closed-system degassing of a silicate melt at 980 °C and IW–1 following the methods described in Supplement S3. The x-axis is the fraction of total H quantified as H_2O (here defined as H_2O_t). The grey-field is the average δD of ALC falls (−239±149‰) from Stephant et al. (2023). Values for δD_0 are the average and minimum value within uncertainty of the δD of ALC falls from Stephant et al. (2023).

able to record the final stages of volatile accretion (Section 4.4.3.1). Secondly, melted or partially melted planetesimals constituted a negligible contribution to the Earth's H budget. Furthermore, for melted bodies, there is a rough correlation between parent body size and H_2O contents as the smaller primitive achondritic and achondritic parent bodies and the Moon have less H_2O than Mars and the Earth (Fig. 4.6). This may suggest that parent body size exerts a primary control on H retention (Sarafian et al., 2019; Newcombe et al., 2023), consistent with modeling studies (e.g., Lichtenberg et al., 2019, 2021). Overall, this implies that the H budget of the Earth must be accounted for by materials that have undergone minimal thermal processing such as chondrites, ice, and icy bodies (e.g., Piani et al., 2020; Alexander, 2022; Marty, 2022), or ingassing of nebular H (Sharp, 2017; Wu et al., 2018). However, the latter scenario requires that

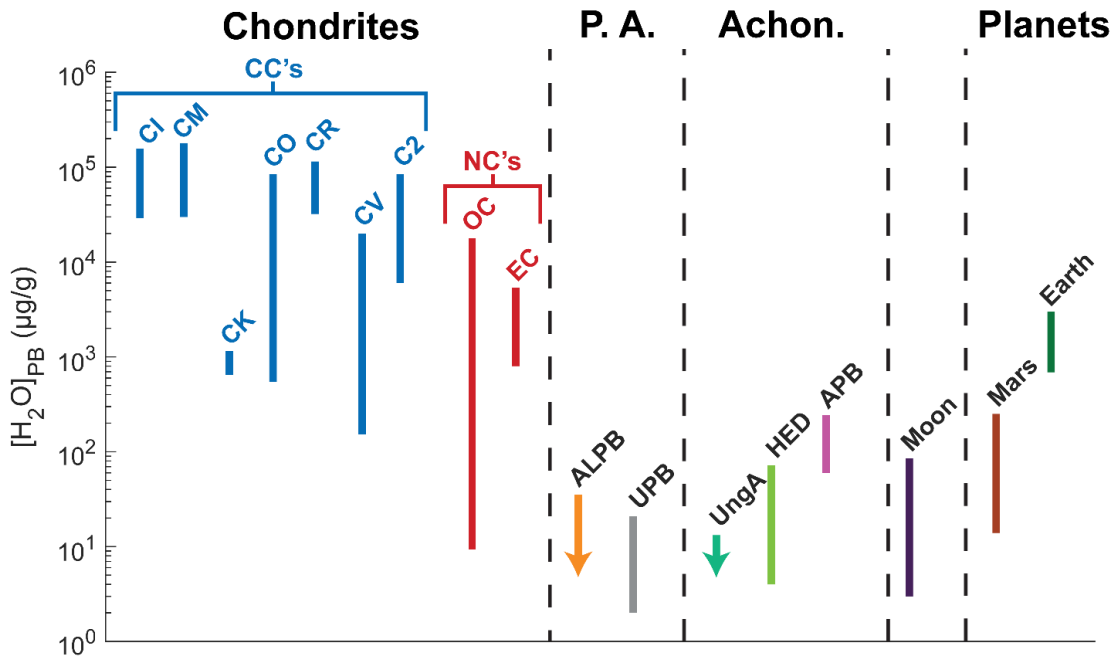

Fig. 4.8 Estimates for the H_2O content of chondritic, primitive achondritic (P. A.), and achondritic parent bodies (Achon.), the Moon, Mars, and the Earth. Chondrites are split into two categories following the carbonaceous (CC) and non-carbonaceous (NC) classification scheme of Warren (2011). Data for Ivuna-type (CI), Mighei-type (CM), Karoonda-type (CK), Ornans-type (CO), Renazzo-type (CR), Vigarano-type (CV), type-2 (C2), ordinary (OC), and enstatite (EC) chondrites are from Vacher et al. (2020) and Piani et al. (2020) and the compilation of McCubbin and Barnes (2019). Data for chondrites represents the variability in H_2O analyses by bulk methods, regardless of petrographic type. Abbreviations and data for primitive achondrites, achondrites, the Moon, Earth, and Mars the same as in Fig. 4.5 and 4.6.

the Earth accreted up to ~30% of its current mass within the lifetime of the nebular disk to gravitationally retain various species of H (Wu et al., 2018; Olson and Sharp, 2019; Newcombe et al., 2023).

4.5 Conclusions

We have measured the H_2O contents of orthopyroxene, clinopyroxene, olivine, and plagioclase in a suite of acapulcoite and lodranite clan meteorites. We find that H_2O concentrations for all phases are < ~10 µg/g H_2O and that the measured H_2O concentrations are inconsistent with the primary controls on the H_2O partitioning behavior of NAMs. We

hypothesize this reflects poorly characterized partitioning at low total pressure and H contents or a metastable condition in which minerals preferentially retain H to charge balance defects. Our analyses of NAMs and estimates for bulk ALPB H_2O contents are consistent with all prior studies of primitive achondrites and achondrites, demonstrating that melted planetesimals are H-poor relative to chondrites. Furthermore, assuming chondrite-like starting materials, this implies that H is efficiently lost prior to or at the onset of planetesimal melting. This further implies that the H budget of the Earth and other terrestrial planets is likely sourced from materials that underwent minimal thermal processing.

Chapter 5: The partitioning of hydrogen between olivine and melt at low pressures (10 - 200 MPa)

Abstract

The concentration and distribution of H_2O_T (defined here as the sum of H species and H-O species quantified as H_2O equivalents) between silicate minerals and melts exerts a primary control on the physicochemical properties of Earths crust and mantle. Furthermore, the partitioning of H_2O_T between minerals and melts is a key parameter that is used to constrain the bulk H_2O_T contents of planetesimals. In mafic systems, olivine is frequently the first crystallizing phase which makes it a useful tracer of primitive melt composition. Previously, the partitioning of H_2O_T between olivine and melt was only constrained at H_2O-undersaturated conditions and pressures ≥ 0.5 GPa, which are broadly applicable to Earths mid- to lower crust and uppermost mantle. We present the first experimental determination of the partitioning of H_2O_T between olivine and melt at low pressures (10 – 200 MPa) relevant to Earths upper crust and planetesimals. Contrary to predictions from experiments conducted at pressures ≥ 0.5 GPa, we find that the olivine-melt H_2O_T partition coefficient ($D_{H_2O_T}^{ol/melt}$) decreases with increasing melt H_2O_T and pressure. We calculate the concentration of dissolved OH in the melt, and assuming H is only dissolved as OH in olivine, calculate an olivine-melt OH partition coefficient ($D_{OH}^{ol/melt}$). For our data, we find that $D_{OH}^{ol/melt}$ is constant relative to melt OH contents ($D_{OH}^{ol/melt}$ = 0.0012±0.0002; 1 Std. Dev.). We also analyzed San Carlos olivine seed grains and olivine crystallized during the experiments held in the same capsules. We find that San Carlos olivine seed grains have lower H_2O_T concentrations than olivine crystallized during the experiments,

which is best explained by a difference in their extrinsic point defect populations. Overall, we find that at low pressures (≤ 200 MPa) the partitioning of H_2O_T between olivine and melt is primarily dependent upon fH_2O and the speciation of H in the melt, which are inter-related, and is likely influenced by the extrinsic defect population of the olivine. We apply our results to prior studies of H_2O_T in planetesimals that observed apparent disequilibrium for H_2O_T between nominally anhydrous minerals, and we also apply our results to estimates of magma decompression rates on Earth. For planetesimals, we find that our model for $D_{H_2O_T}^{ol/melt}$ based upon the speciation of H in the melt cannot account for the observed apparent disequilibrium in the context of the limited existing constraints. For magma ascent, we find that decompression rates characterized with a variable $D_{H_2O_T}^{ol/melt}$ following our parameterization of $D_{H_2O_T}^{ol/melt}$ are a factor of ~3 lower than for models with a constant $D_{H_2O_T}^{ol/melt}$, thereby implying that prior estimates of magma decompression based upon H diffusion in olivine may be overestimated.

5.1 Introduction

The concentrations of volatile elements (e.g., H, C, N, O, F, Cl, S) strongly influence the physicochemical properties and evolution of magmatic systems. In particular, H_2O_T (defined here as the sum of H species and H-O species quantified as H_2O equivalents) strongly influences the melting temperature (Kushiro, 1972; Holloway, 1973; Asimow and Langmuir, 2003; Aubaud et al., 2004; Hauri et al., 2006a), mineral proportions and melt composition (Eggler, 1972; Green, 1973; Sisson and Grove, 1993), rheology (Chopra and Paterson, 1984; Mackwell et al., 1985; Karato et al., 1986; Hirth and Kohlstedt, 1996; Jung and Karato, 2001; Kaminski, 2002; Dixon et al., 2004), electrical conductivity (Karato, 1990, 2011; Wang et al., 2008), and seismic velocity of the mantle (Inoue et al., 1998; Jacobsen et al., 2004; Karato, 2006) in addition to

magma decompression rates (Barth et al., 2019; Newcombe et al., 2020) and explosivity in volcanic systems (Stock et al., 2016; Barth et al., 2019; Popa et al., 2021; La Spina et al., 2022). The H_2O_T contents of nominally anhydrous minerals (NAMs; e.g., olivine, pyroxene, feldspar) are an increasingly common tool that is used to probe the H_2O_T contents of their magmatic source in terrestrial and planetary systems (e.g., Weis et al., 2015; Urann et al., 2022; Peterson et al., 2023b; Newcombe et al., 2023). Furthermore, diffusion-induced H_2O_T concentration profiles in NAMs have been used to constrain magma decompression rates in volcanic systems (e.g., Peslier and Luhr, 2006; Demouchy et al., 2006; Ferriss et al., 2018; Newcombe et al., 2020). Accurate assessment of the H_2O_T content of primitive melts, and magma decompression rates, requires accurate determination of the partitioning of H_2O_T between the mineral and the melt, which can be described in terms of a partition coefficient:

$$D_{H_2O_T}^{min/melt} = \frac{H_2O_{T_{min}}\ (wt.\%)}{H_2O_{T_{melt}}\ (wt.\%)} \quad (1)$$

where $D_{H_2O_T}^{min/melt}$ is the mineral-melt partition coefficient for H_2O_T between a mineral, *min*, and a melt, *melt*.

In mafic systems, olivine is frequently one of the first crystallizing phases and may therefore record the chemical signatures of primitive source magmas. Hydrogen is incorporated into the olivine structure to charge-balance metal or silicon vacancies, and in some cases participates in coupled substitutions with other trace elements (Table 5.1; Tollan et al., 2017). Keppler and Bolfan-Casanova (2006) subdivided the major hydrogen substitution mechanisms in olivine into three groups: 1) single protons coupled to a cation, 2) proton pairs that cannot be dissociated, and 3) clusters of 4 protons that cannot be dissociated. On a detailed level, H substitutes into the olivine structure to charge-balance defects and may also participate in complex defect structures, such as multi-site point defects (e.g., Berry et al., 2007; Tollan et al.,

2018; Demouchy, 2021). Common substitution mechanisms, their corresponding equilibrium relations and constants, as well as the implied relationship between fH_2O and the concentration of H_2O_T in olivine are summarized in Table 5.1. In short, depending on the substitution mechanism, the concentration of H_2O_T in olivine is expected to be proportional to fH_2O^n (n = 0.5, 1, 2).

Initial works by Tomlinson (1956), Russell (1957), and Burnham and Davis (1974) argued that H_2O dissolved exclusively as OH in silicate melt based upon a linear relationship between the square root of H_2O_T concentration and fH_2O for low pressure experiments. However, many subsequent works using infrared techniques have demonstrated the presence of dissolved H_2O and OH in silicate melts (Stolper, 1982b; Newman et al., 1988; Silver and Stolper, 1989). Stolper and colleagues developed a speciation-based ideal solution model to describe the dissolution of H_2O in the fluid as H_2O and OH in the melt (Stolper, 1982b, a; Silver and Stolper, 1985, 1989; Silver et al., 1990). The equilibrium relations, equilibrium constants, and implied relationships between melt H_2O_T concentration and fH_2O for the model of Stolper and colleagues is given in Table 5.1. In short, for dissolution of H_2O into a silicate melt as H_2O or OH, the concentration of H_2O and OH are proportional to fH_2O and $fH_2O^{0.5}$, respectively.

For a system that is H_2O-saturated, at a given pressure and temperature, and assuming that the fluid behaves as an ideal solution (Stolper, 1982a), the partition coefficient for H_2O_T between olivine and melt can be written as:

$$D_{H_2O_T}^{ol/melt} = \frac{C_{Ol}^{OH}}{C_{melt}^{OH} + C_{melt}^{H_2O}} \propto \frac{a f_{H_2O}^{n}}{b\sqrt{f_{H_2O}} + c f_{H_2O}} \quad (2)$$

Table 5.1) Summary of equilibrium relations, equilibrium constants, and the proportionality between the concentration of H_2O_T and fH_2O for various substitution mechanisms of H^+ in olivine or H_2O dissolution in glass modified from Keppler and Bolfan-Casanova (2006)

Substitution Mechanism	Phase	Equilibrium Relation	[1,4]Equilibrium Constant	[2]Proportionality between phase H_2O_T and fH_2O
		Single proton coupled to a cation		
* $H^+ + M^{3+} \leftrightarrow 2\,M^{2+}$ $H^+ + M^{3+} \leftrightarrow Si^{4+}$ $H^+ + M^{+} \leftrightarrow Mg^{2+}$	Olivine	$H_2O_{fluid} + O_{min} = 2\,OH_{min}$	$K_1 = \frac{\left(a_{OH}^{min}\right)^2}{a_{H_2O}^{fluid} a_O^{min}} = \frac{\left(\gamma_{OH}^{min} X_{OH}^{min}\right)^2}{\left(f_{H_2O}/f_{H_2O}^0\right)\left(\gamma_O^{min} X_O^{min}\right)}$	$C_{H_2O_T}^{min} \propto f_{H_2O}^{0.5}$
		Proton pairs		
* $2H^+ \leftrightarrow M^{2+}$ * $2H^+ + Ti^{4+} \leftrightarrow Mg^{2+} + Si^{4+}$ $2H^+ + M^{2+} \leftrightarrow Si^{4+}$	Olivine	$H_2O_{fluid} + O_{min} = (OH_{min})_2$	$K_2 = \frac{a_{(OH)_2}^{min}}{a_{H_2O}^{fluid} a_O^{min}} = \frac{\left(\gamma_{(OH)_2}^{min} X_{(OH)_2}^{min}\right)}{\left(f_{H_2O}/f_{H_2O}^0\right)\left(\gamma_O^{min} X_O^{min}\right)}$	$C_{H_2O_T}^{min} \propto f_{H_2O}$
		Cluster of four protons		
* $4H^+ \leftrightarrow Si^{4+}$	Olivine	$2H_2O_{fluid} + 2O_{min} = (OH_{min})_4$	$K_3 = \frac{a_{(OH)_4}^{min}}{\left(a_{H_2O}^{fluid}\right)^2 \left(a_O^{min}\right)^2} = \frac{\left(\gamma_{(OH)_2}^{min} X_{(OH)_2}^{min}\right)}{\left(f_{H_2O}/f_{H_2O}^0\right)^2 \left(\gamma_O^{min} X_O^{min}\right)^2}$	$C_{H_2O_T}^{min} \propto f_{H_2O}^2$
		H+ dissolution in melt		
	[3]Melt	$H_2O_{fluid} = H_2O_{melt}$	$K_4 = \frac{a_{H_2O}^{melt}}{a_{H_2O}^{fluid}} = \frac{X_{H_2O}^{melt}}{f_{H_2O}/f_{H_2O}^0}$	$C_{H_2O}^{melt} \propto f_{H_2O}$
		$H_2O_{melt} + O_{melt} = 2\,OH_{melt}$	$K_5 = \frac{(a_{OH}^{melt})^2}{a_{H_2O}^{melt} a_O^{melt}} = \frac{(X_{OH}^{melt})^2}{X_{H_2O}^{melt} X_O^{melt}}$	$C_{OH}^{melt} \propto f_{H_2O}^{0.5}$

M – a metal cation; H_2O_z – molecular H_2O in a phase (z = fluid, melt); O_z = unprotonated oxygen in a phase (z – mineral, melt); OH_z – hydroxyl in a phase (z = mineral, melt); a_g^z – the activity of a species (g = H_2O, OH, O) in a phase (z = mineral, melt, fluid); γ_g^{min} – the activity coefficient of a species (g = H_2O, OH, O) in a mineral; X_g^z – the mole fraction of a species (g = H_2O, OH, O) in a phase (z = mineral, melt, fluid); f_{H_2O} – the fugacity of water in the fluid; $f_{H_2O}^0$ – the fugacity of pure water at the reference state

[1]At the low total OH contents relevant to olivine, a_O^{min} is likely constant (Keppler and Bolfan-Casanova, 2006)

[2]For these simple relations H_2O_T is simply total OH quantified as H_2O equivalents for olivine or total OH and H_2O quantified as H_2O equivalents for melt

[3]Melt equilibrium relations assume homogeneous equilibrium of an ideal solution as in Stolper (1982a); mole fractions in the melt are on a single O basis

[4]Equilibrium constants as presented assume isothermal and isobaric conditions, however they are expected to vary with pressure and temperature as outlined by the relation between the equilibrium constant and Gibb's free energy: $-RT\ln K = \Delta G = \Delta H^{1\,bar} - T\Delta S^{1\,bar} + \Delta V^{solid}(P - P_0) \quad \{P_0 \equiv 1\text{ bar}\}$

*The four main H in olivine substitution mechanisms, or equivalent statements, as defined by Tollan et al. (2017)

where n = 0.5, 1, 2 based upon the H^+ incorporation mechanism in olivine (Table 5.1) and *a*, *b*, and *c* are constants. As the H_2O_T content of the melt increases, the proportion of dissolved OH to H_2O_m in the melt will decrease resulting in variable $D_{H_2O_T}^{ol/melt}$ values depending on the mechanism(s) of H incorporation in olivine. In Fig. 5.1, we present schematic $D_{H_2O_T}^{ol/melt}$ curves for the olivine H_2O_T incorporation mechanisms outlined in Table 5.1. The curves in Fig. 5.1 suggest that, depending on which H incorporation mechanism(s) are prevalent for any given melt H_2O_T concentration, $D_{H_2O_T}^{ol/melt}$ may increase or decrease.

The partitioning of H_2O_T between olivine and melt has been the subject of several experimental studies at lower crustal to upper mantle temperatures (T ≈ 1000 - 1450°C) and pressures (P ≈ 0.5 – 13 GPa) and H_2O-undersaturated conditions (Koga et al., 2003; Aubaud et al., 2004; Hauri et al., 2006a; K. J. Grant et al., 2007; Tenner et al., 2009b, 2012; O'Leary et al., 2010; Novella et al., 2014). As prior experimental studies were conducted at H_2O-undersaturated conditions, $D_{H_2O_T}^{ol/melt}$ cannot be directly related to fH_2O. However, prior work has shown that $D_{H_2O_T}^{ol/melt}$ has a positive, linear dependence on pressure (Novella et al., 2014; Adam et al., 2016), although this is anchored by few highly uncertain data points from 6 – 13 GPa (Tenner et al., 2012; Novella et al., 2014). Furthermore, data from 0.5 – 2 GPa exhibit significant scatter, which is greatly reduced when variations in analytical method are accounted for (Towbin et al., 2023); however, this also results in removal of any resolvable pressure dependence over 0.5 – 2 GPa (Towbin et al., 2023). The remaining scatter in $D_{H_2O_T}^{ol/melt}$ from 0.5 – 2 GPa may largely be attributed to variations in fO_2, fH_2O, temperature, and melt or olivine composition, thereby

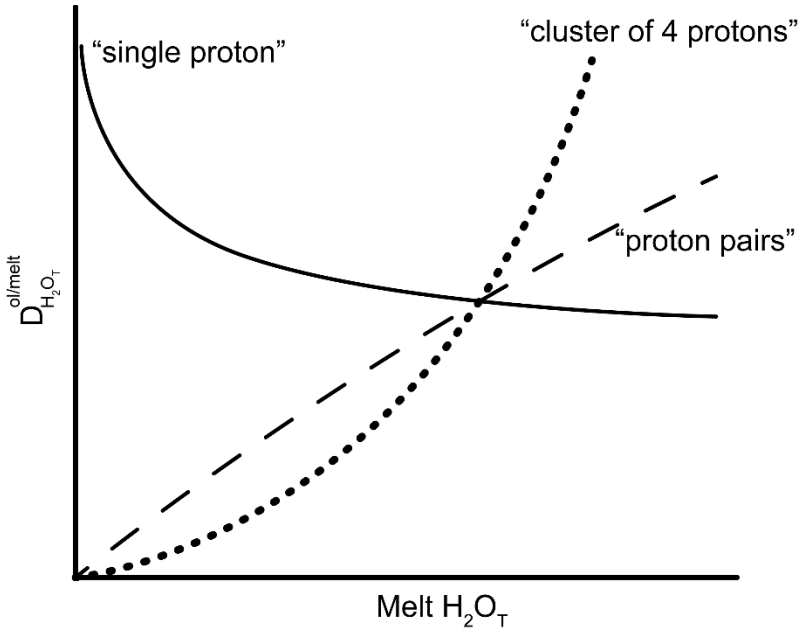

Fig. 5.1 Schematic diagram showing the general trend of $D_{H_2O_T}^{ol/melt}$ for the three groupings of H incorporation mechanisms in olivine as described in Table 5.1.

obscuring any pressure dependence. We are currently unaware of any published experimental constraints on $D_{H_2O_T}^{ol/melt}$ at low pressures, which are relevant to Earth's upper crust and planetesimals, or at H_2O saturated conditions.

In this study, we present: 1) experimental $D_{H_2O_T}^{ol/melt}$ partitioning data from new analyses of prior experiments (Gaetani et al., 1994; Médard and Grove, 2008); and, 2) newly conducted low pressure (20 – 100 MPa) experiments. New experiments were conducted on two natural starting materials, a basaltic-andesitic ash (MP; 2016 eruption of Mt. Pavlof, Alaska) and a primitive alumina-rich tholeiitic basalt (82-72f; primitive high-alumina basalt from Medicine Lake Volcano, CA, USA; See **Starting Materials**). Contrary to extrapolation from higher pressure experimental data, we find that $D_{H_2O_T}^{ol/melt}$ is negatively correlated with pressure in our experiments. We evaluate this result in the context of the extrinsic point defect population of olivine in our run products, pressure, fH_2O, and H speciation in the melt.

5.2 Experimental Design

5.2.1 Prior Experiments

Several charges from the experiments of Gaetani et al. (1994) and Médard and Grove (2008) were analyzed as part of this study and hereafter referred to as the "prior experiments". Experimental methods for the prior experiments are detailed elsewhere (Gaetani et al., 1994; Médard and Grove, 2008) and summarized here. In brief, the experiments from Gaetani et al. (1994) were conducted at H_2O-saturated conditions, at the Ni-NiO (NNO) fO_2 buffer, and at 200 MPa using a natural basaltic andesitic starting material (Sample 135-839B-15R-2, 63-67 cm recovered during the Ocean Drilling Program). Experiments were conducted in TZM (titanium-zirconium-molybdenum) and MHC (molybdenum-hafnium-carbide) cold-seal pressure vessels. We analyzed charges #5 and #7 from Gaetani et al. (1994; hereafter G5 and G7). The experiments analyzed herein from Médard and Grove (2008) were conducted at H_2O-saturated conditions, at the NNO fO_2 buffer, and at pressures of 10 – 100 MPa on a primitive high-alumina basalt from Medicine Lake Volcano, CA (sample 82-72f; hereafter 82-72f; Donnelly-Nolan et al., 1991; Médard and Grove, 2008) in MHC cold-seal pressure vessels. A subset of the experiments from Médard and Grove (2008) were conducted at 10 and 25 MPa did not visually contain H_2O at the end of experimental runs and were not considered to be H_2O-saturated by the authors. We analyzed charges #7, #8, #11, and #23 from Médard and Grove (2008; hereafter M7, M8, M11, M23). Run conditions and phase compositions are compiled in Tables 5.2 and 5.4

5.2 Starting Materials

For experiments performed as part of this work, the starting material was an olivine-rich basaltic-andesitic ash from the 2016 eruption of Mt. Pavlof, Alaska (hereafter MP; Table 5.3; Rasmussen and Plank, 2021). The MP starting material is enriched in SiO_2 relative to the typical

mafic arc magma (Kovalenko et al., 2010), and is similar in composition to subduction related high-Mg calc-alkaline andesites (Schmidt and Jagoutz, 2017). The starting material was ground in an agate mortar and pestle and sieved to remove the < 90 μm and 106 to 180 μm fractions. Olivine grains were the picked from the 106 – 180 μm and >180 μm size fractions to use as seed grains for charges containing the MP starting material.

A subset of experiments were performed on a natural, primitive high-alumina basalt starting material (82-72f). This starting material was selected as it was identical to the 82-72f starting material from Medicine Lake Volcano used by Médard and Grove (2008) and is similar in composition to a low pressure melt of a mantle lherzolite and a nominally primitive mid-ocean ridge basalt (Table 5.3; Bartels et al., 1991; Médard and Grove, 2008). Furthermore, sample 82-72f has been the subject of several other prior experimental studies (Bartels et al., 1991; Médard and Grove, 2008; O'Leary et al., 2010; Mitchell et al., 2017).

5.2.3 Experimental Methods

The experimental charges in this study used a capsule-in-capsule approach to hold starting materials, buffer fO_2, and monitor fO_2 following the method of Alex and Zajacz (2020; Fig. 5.2). For sample capsules, ~10 mg of starting material was packed into a 6 mm long, 3 mm outer diameter (OD), 0.127 mm wall thickness (WT) $Au_{80}Pd_{20}$ capsule with ~5 mg H_2O (Table D1). For capsules containing the basaltic andesitic starting material, ~8 – 10 olivine grains picked from the 106 to 180 μm and the >180 μm size fractions were added as seeds to the starting material (Table D1). For capsules containing the high-alumina basalt starting material, rectangular prisms of San Carlos olivine ≤ ~1 mm in their longest dimension were added to the starting powder (Table D1).

Table 5.2) Summary of Experimental Run Conditions

	Starting Materials	P (MPa)	T (°C)	Time (hr)	*f*O2 buffer	Measured *f*O2 (log)	Unc.	ΔNNO	Evidence of Saturation
New Experiments									
XP-02	MP	99	1000	23:05	NNO	-9.5	0.1	0.69	Same weight; vesicular
XP-03	MP	85	1000	20:35	NNO	-9.3	0.2	0.89	H_2O visually confirmed
XP-05	MP	99	1000	25:30	NNO	-8.9	0.2	1.2	Vesicular
XP-06	MP	99	1000	12:15	NNO	-9.74	0.04	0.45	Same weight; vesicular
XP-07	MP	30	1000	24:00	NNO				Vesicular
XP-09	MP & 82-72f	99	1000	23:45	NNO				H_2O visually confirmed
XP-10	MP & 82-72f	100	1000	24:00	NNO	-8.5	0.2	1.6	H_2O visually confirmed
XP-13	MP & 82-72f	96	1000	48:00	NNO	-8.2	0.2	2.0	Same weight; vesicular
XP-14	MP	57	1000	24:00	NNO	-9.51	0.09	0.67	Vesicular
XP-15	MP	50	1000	24:00	NNO	-9.69	0.08	0.49	Capsule "popped" when opening; vesicular
XP-17	MP	52	1000	24:00	NNO				Vesicular
XP-18	MP	52	1000	24:00	NNO				Vesicular
XP-19	MP	53	1000	24:00	NNO				Vesicular
Gaetani et al. (1994)									
G5	ODP B.A.	200	1020	24:00	NNO				H_2O visually confirmed
G7	ODP B.A.	200	1035	24:00	NNO				H_2O visually confirmed
Medard and Grove (2008)									
M7	82-72f	100	1173	2:00	NNO				H_2O visually confirmed
M8	82-72f	50	1190	3:06	NNO				H_2O visually confirmed
M11	82-72f	25	1204	2:00	NNO				
M23	82-72f	10	1220	1:30	NNO				

MP - Mt. Pavlof basaltic andesitic ash; ODP B. A. - Ocean Drilling Program Sample 135-839B-15R-2, 63-67 cm

Table 5.3) Composition of Proposed Starting Materials compared to melt in equilibrium with a lherzolite and N-MORB

Oxide (wt%)	Mt. Pavlof, 2016, Ash	82-72f	Lherzolite Melt[1]	N-MORB[2]	N-MORB[3]
SiO_2	54.2	47.7	50.0	49.51	50.42
TiO_2	1.12	0.59	0.73	0.9	1.53
Al_2O_3	17.9	18.5	17.6	16.75	15.13
FeO*	8.69	8.21	7.34	8.05	9.81
MnO	0.18	0.15	0.26	0.14	0.171
MgO	4.4	10.5	9.9	9.74	7.76
CaO	8.88	12	11.3	12.5	11.35
Na_2O	3.39	2.16	2.55	2.18	2.83
K_2O	0.66	0.07	0.16	0.07	0.14
P_2O_5	0.62	0.06	0.16	0.1	0.164

FeO* is all Fe reported as FeO

[1]Bartels et al. (1991)

[2]Workman and Hart (2005)

[3]Gale et al. (2013)

Table 5.4) Compositions of minerals and glasses from experimental run products

	SiO_2	TiO_2	Al_2O_3	FeO	MnO	MgO	Na_2O	CaO	K_2O	P_2O_5	Fo
Olivine											
MP-10	37.7(4)	0.02(2)	0.04(3)	25.7(5)	0.47(3)	36.4(4)	0.00(1)	0.17(2)	0.00(1)	N/A	71
MP-02	37.5(8)	0.03(2)	0.04(3)	28(3)	0.6(1)	33(2)	0.01(1)	0.20(2)	0.00(1)	N/A	67
MP-05	37.5(4)	0.02(4)	0.04(4)	26.0(9)	0.50(4)	35(2)	0.00(1)	0.22(3)	0.01(1)	N/A	70
MP-06	37.4(3)	0.03(2)	0.08(6)	27(2)	0.52(3)	35(2)	0.01(1)	0.21(2)	0.00(1)	N/A	69
MP-09	37.3(5)	0.04(5)	0.1(1)	27(2)	0.51(7)	34(2)	0.00(1)	0.25(3)	0.01(1)	N/A	68
MP-13	37.5(5)	0.03(2)	0.1(1)	25.9(3)	0.56(4)	35.9(4)	0.01(1)	0.21(3)	0.00(1)	N/A	70
MP-03	37.7(2)	0.01(3)	0.03(2)	27(2)	0.52(9)	35(2)	0.00(1)	0.23(5)	0.00(1)	N/A	69
MP-14	37.9(2)	0.03(3)	0.02(2)	25.8(7)	0.53(4)	36.0(7)	0.01(1)	0.18(2)	0.00(1)	N/A	71
MP-19	37.4(4)	0.03(3)	0.1(1)	27(2)	0.51(7)	35(2)	0.01(5)	0.21(7)	0.00(2)	N/A	70
MP-17	37.9(7)	0.03(3)	0.07(6)	27(2)	0.50(6)	35(3)	0.01(2)	0.3(3)	0.00(1)	N/A	69
MP-18	37.3(7)	0.03(3)	0.5(5)	27(2)	0.51(6)	34(3)	0.04(7)	0.26(8)	0.02(3)	N/A	68
MP-15	37.8(3)	0.01(2)	0.03(3)	26(1)	0.53(4)	36(1)	0.01(1)	0.22(3)	0.00(1)	N/A	70
MP-07	37.4(3)	0.02(4)	0.03(2)	25.6(2)	0.47(4)	36.3(4)	0.01(1)	0.19(2)	0.00(1)	N/A	71
PSM	37.6(2)	0.00(2)	0.04(4)	25.6(4)	0.47(3)	36.3(4)	0.01(1)	0.17(1)	0.00(1)	N/A	71
B-09	39.1(7)	0.00(1)	0.1(1)	18(4)	0.26(7)	43(3)	0.00(1)	0.39(7)	0.00(1)	N/A	81
B-10	39.5(6)	0.01(3)	0.05(2)	15(3)	0.23(7)	45(3)	0.01(1)	0.36(4)	0.01(1)	N/A	83
B-13	39.9(5)	0.01(3)	0.05(2)	15(3)	0.12(2)	45(2)	0.01(1)	0.36(5)	0.00(1)	N/A	84
B-07-SC	40.4(2)	0.01(3)	0.03(3)	8.9(2)	0.12(2)	49.7(3)	0.01(1)	0.07(1)	0.00(1)	N/A	91
B-10-SC	40.7(3)	0.00(2)	0.03(2)	8.9(2)	0.12(2)	49.8(3)	0.01(1)	0.07(2)	0.00(1)	N/A	91
B-11-SC	40.4(2)	0.00(2)	0.04(4)	8.9(1)	0.12(2)	49.8(3)	0.01(1)	0.08(2)	0.00(1)	N/A	91

Table 5.4 continued…

	SiO_2	TiO_2	Al_2O_3	FeO	MnO	MgO	Na_2O	CaO	K_2O	P_2O_5	Fo
B-14-SC	40.7(3)	0.00(2)	0.02(1)	8.9(2)	0.12(2)	49.9(4)	0.00(1)	0.07(1)	0.00(1)	N/A	91
*Raw SC	40.7(1)	0.00(2)	0.03(1)	8.9(2)	0.12(2)	49.4(2)	0.01(1)	0.07(1)	0.00(1)	N/A	91
g5	37.7(4)	0.002(3)	0.1(1)	18.7(4)	0.27(2)	41(1)	N/A	0.3(1)	ND	N/A	79
g7	38.1(7)	ND	0.1(1)	18.3(8)	0.26(1)	42(1)	N/A	027(7)	ND	N/A	80
m8	39(1)	ND	0.1(1)	12(2)	0.22(5)	47(3)	N/A	0.44(6)	ND	N/A	86
m23	39(2)	ND	0.1(1)	11(1)	0.17(4)	48(3)	N/A	0.4(1)	ND	N/A	88
m7	38(2)	ND	0.09(4)	10.6(4)	0.16(2)	50(2)	N/A	0.38(5)	ND	N/A	89
m11	39(1)	ND	0.05(1)	11.9(9)	0.17(2)	46(4)	N/A	0.37(3)	ND		87
Glass											
MP-10	58(2)	1.45(9)	16.3(4)	6.7(7)	0.16(6)	2.2(3)	3.0(1)	6.4(2)	0.97(7)	0.52(2)	
MP-02	60.9(6)	1.11(4)	15.8(8)	5.9(5)	0.17(5)	1.8(1)	2.9(3)	5.0(5)	1.19(6)	0.54(1)	
MP-05	55.5(7)	1.5(1)	16.1(3)	7.5(3)	0.2(2)	2.6(1)	4.2(1)	6.9(2)	0.95(2)	N/A	
MP-06	55.9(6)	1.5(1)	16.3(7)	7.6(4)	0.17(5)	2.5(2)	3.1(2)	6.7(3)	0.92(5)	0.43(1)	
MP-09	57.6(1)	1.31(3)	16.4(6)	7.5(1)	0.21(2)	2.1(3)	2.8(2)	6.1(3)	1.00(1)	0.48(1)	
MP-03	60.3(6)	1.04(5)	15.3(6)	6.2(4)	0.15(4)	1.88(9)	2.8(2)	4.8(4)	1.35(9)	0.50(5)	
MP-19	66(2)	1.0(2)	14.0(9)	5.0(8)	0.1(1)	2(1)	4.7(2)	3(1)	2.1(3)	N/A	
MP-17	66(3)	0.8(3)	15(3)	4.6(8)	0.1(1)	1.2(6)	5.2(3)	4(2)	2.2(7)	N/A	
MP-07	64(1)	1.3(2)	14(2)	5.5(6)	02(1)	2.0(4)	4.6(2)	4.5(7)	1.7(2)	N/A	
PSM	53(1)	1.4(1)	15(1)	10.3(4)	0.3(1)	3.7(1)	4.0(2)	6.9(3)	0.87(4)	N/A	
g5**	54.5(3)	0.74(3)	18.2(1)	8.1(2)	0.20(5)	5.49(6)	1.8(1)	10.5(1)	0.35(1)	N/A	
g7**	54.0(6)	0.67(2)	17.2(2)	8.2(2)	0.14(4)	6.4(1)	1.8(1)	11.1(2)	0.35(2)	0.16(1)	
m8***	48.4(4)	0.59(7)	18.8(1)	7.2(2)	0.16(3)	10.6(1)	2.3(1)	11.8(1)	0.09(3)	0.04(2)	
m23***	48.1(2)	0.54(6)	18.6(2)	8.2(2)	0.13(2)	10.2(1)	2.2(2)	11.8(1)	0.08(3)	0.08(2)	

Table 5.4 continued…

	SiO_2	TiO_2	Al_2O_3	FeO	MnO	MgO	Na_2O	CaO	K_2O	P_2O_5	Fo
m7**	48.0(2)	0.58(7)	18.7(1)	7.8(1)	0.16(3)	10.7(1)	2.3(1)	11.7(1)	0.09(3)	0.05(2)	

m11**	47.9(4)	0.54(8)	18.7(1)	8.2(3)	0.14(3)	10.4(2)	2.0(2)	11.7(2)	0.08(3)	0.04(2)

Values in parentheses are 1 standard deviation from the mean
N/A – not analyzed; ND – not detected
Fo – forsterite content of olivine
*Raw SC – is unprocessed San Carlos olivine starting material
**Data from Gaetani et al. (1994)
***Data from Medard and Grove
(2008)

For fO_2 sensors, a 0.37 Co: 0.63 Pd mix was placed into a 7 mm long, 2.5 mm OD, 0.127 WT Pt capsule with Y-Zr paper and ~3 mg H_2O and welded shut to prevent loss of material (Alex and Zajacz, 2020). Sample capsules and fO_2 sensors were then loaded with 50 – 100 mg of Ni-NiO powder and 15 – 30 mg of H_2O (2 mg NNO: 1 mg H_2O) into 17 mm long, 5 mm OD, and 0.127 WT Pt outer capsules. All capsules were welded shut to limit loss of H_2O, weighed, heated in an oven at 120°C for at least 12 hours, and then re-weighed to ensure capsules were fully sealed. Experimental charges were then loaded into a MHC cold-seal pressure vessel. The atmosphere inside the vessel was buffered to approximately the NNO fO_2 buffer by setting the partial pressure of H_2 in the system (Gion et al., 2018). The vessel was then pressurized using Ar gas. All experiments were conducted at 1000°C for 12 – 48 hr. Prior to quenching the vessel-furnace assembly was rotated causing the charge to drop through a water-cooled collar.

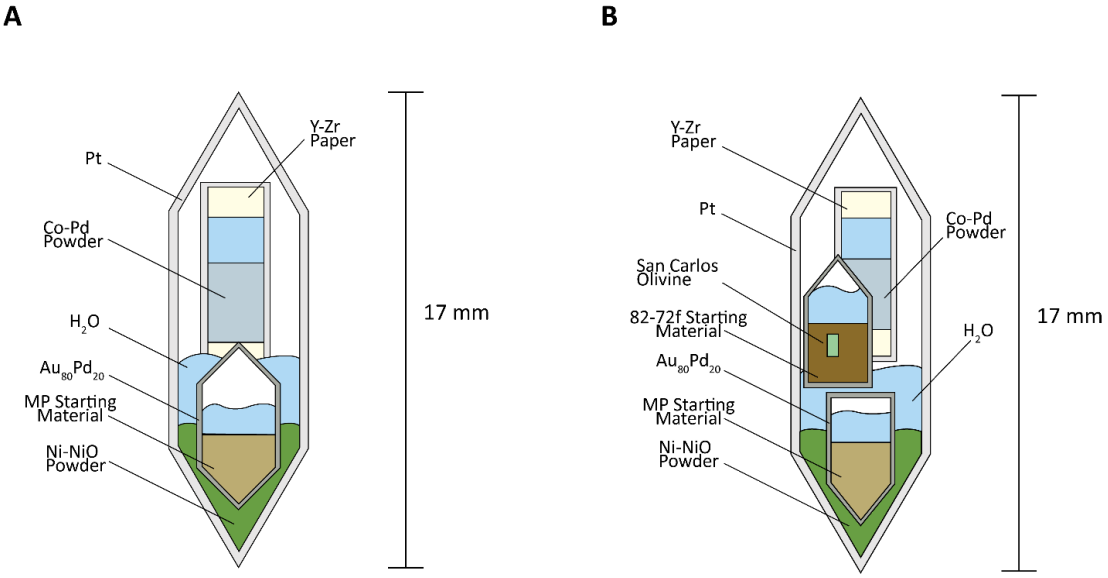

Fig. 5.2 Schematic diagrams showing the capsule set-up used in this study. A) Capsule set-up used for charges XP-02 to XP-05. B) Capsule set-up for all other charges. Capsule components are not to scale.

Following quenching, capsules were re-weighed and then checked for leaks by submerging sample capsules in acetone. Additionally, we attempted to visually confirm H_2O saturation

through direct observation of H_2O liquid or gas upon opening sample capsules. In the event that capsules lost mass and H_2O was not visually confirmed, we texturally evaluated H_2O-saturation by checking for vesicles within experimental run products. Run conditions and evidence of H_2O-saturation are given in Table 5.2.

5.3 Analytical Methods

5.3.1 NanoSIMS Analyses

5.3.1.1 Olivine analyses

Analyses of H_2O_T in olivine were conducted using the NanoSIMS 50L at the Carnegie Earth and Planets Laboratory (EPL) in Washington, DC. Analyses were conducted across three analytical sessions (MM/YY; 10/21, 08/22, 03/23). Analytical conditions and data processing procedures for the 10/21 and 08/22 analytical sessions are detailed in Peterson et al. (2023a, b). Olivine H_2O_T analyses were calibrated against a set of orthopyroxene standards from Kmamoto et al. (2017; BCN-203, DGO-160, SLP-403, SLP-108, PR-7-5, 109426), which generate a H_2O_T calibration curve within uncertainty of the olivine H_2O_T calibration curve (Kumamoto et al., 2017; Towbin et al., 2023). Calibration curves for orthopyroxene have been updated to match the revised standard values of Towbin et al. (2023), as has been done for the 03/23 analytical session. This results in a decrease of olivine H_2O_T concentrations by ~12 % and ~14 % for the 10/21 and 08/22 analytical sessions, respectively, relative to their original calibrations.

For the 03/23 analytical session, a ~2 nA Cs^+ primary beam was rastered over a 15×15 μm area for ~5 minutes to remove the Au coat and surface contamination. The raster size was then reduced to 10×10 μm and electronic gating and beam blanking were applied to focus ion collection from the central 5×5 μm portion of the raster and remove edge effects in the analytical

signal. Counts of $^{12}C^-$, $^{16}O^1H^-$, $^{19}F^-$, $^{30}Si^-$, and $^{35}Cl^-$ ions were simultaneously detected on electron multipliers with a mass resolving power >8000 (MRP; Cameca definition), allowing for discrimination of $^{16}O^1H^-$ from $^{17}O^-$. For each analytical area, "heat" maps of ion counts were observed using the real-time imaging (RTI) function of the NanoSIMS 50L to check for sources of contamination such as cracks or resin. If hot-spots, indicating likely sources of contamination, were identified using RTI, then the beam was moved to another location until a suitable analytical area was identified. Once a suitable analytical area was identified, it was pre-sputtered for an additional 240 seconds prior to 250 seconds of counting time. The electron gun was used to charge compensate the sample surface due to implantation of Cs^+ ion from the primary beam and removal of negatively charged ions and electrons during analyses. Electron gun tuning followed accepted protocols (Peterson et al., 2023a). The vacuum in the analysis chamber was maintained at ~6.6E-10 to ~9.2E-10 torr.

Data reduction for the 03/23 analytical session followed accepted protocols (Peterson et al., 2023a). The effects of instrumental drift due to variation in analytical conditions (e.g., instability of primary beam and electron gun, variations in detector efficiency and vacuum pressure) were accounted for by normalizing counts of volatile ions (e.g., $^{12}C^-$, $^{16}O^1H^-$, $^{35}Cl^-$) to $^{30}Si^-$, which effectively smooths these net effects. All data were then normalized to a factor of $SiO_2/50$, where SiO_2 is the wt. % SiO_2 of the target as measured by EPMA (Hauri et al., 2002; Shimizu et al., 2022; Towbin et al., 2023; Peterson et al., accepted). The analytical background for $OH/Si \times SiO_2/50$ was monitored using repeat analyses of Suprasil 3002 glass (~1.7±0.6 µg/g H_2O_T; 1 St. Dev.; Newcombe, 2022; Peterson et al., 2023a) held in the sample mount as well as dry synthetic forsterite (SynFo; <<1 µg/g H_2O_T) held in the standard mounts. A correction to the $OH/Si \times SiO_2/50$ of Suprasil 3002 glass to account for dissolved H was made following accepted

protocols (Peterson et al., 2023a, b) to determine the analytical background. Over the entire analytical session, repeat analyses of ALV-519-4-1 (~1700 µg/g H_2O_T) and Herasil glass (~80 – 100 µg/g H_2O_T) show no systematic variation in OH/Si×SiO_2/50 (Fig. D1). Therefore, we elect not to apply drift corrections to data from the 03/23 analytical session. Measurements of H_2O_T in olivine were calibrated using an orthopyroxene calibration curve, which has been demonstrated to be within the analytical precision of the olivine calibration curve (Kumamoto et al., 2017; Towbin et al., 2023). The fitting procedure for calibration curves follows accepted protocols (Peterson et al., 2023a), and calibration standards and calibration curves are reported in the supplement (Table D2; Fig. D6).

5.3.1.2 Glass analyses

Silicate glass from experimental run products as well as one glassy melt inclusion from an olivine grain in the MP starting material were analyzed for H_2O_T using the NanoSIMS 50L at Carnegie EPL. Analyses were conducted in imaging mode on the NanoSIMS 50L across two analytical sessions, 08/22 and 03/23, and followed the method outlined in Peterson et al. (2023b). For both analytical sessions, analyses were conducted using entrance slit 5 and aperture slit 4, a beam current of ~200 pA. A 15 ×15 µm area was pre-sputtered for 4 minutes using a 2 nA Cs^+ primary beam prior to analyses to remove the Au coat and surface contamination. The analytical area was then decreased to 10 ×10 µm and pre-sputtered for an additional 3 minutes using a 200 pA Cs^+ primary beam. Analyses were conducted using a 128 × 128 pixel working frame with 200 cycles over 670 seconds. A MRP (Cameca definition) of >8000 was used such that $^{16}O^1H^-$ could be discriminated from $^{17}O^-$. Beam-blanking was not applied, however corresponding analytical effects (e.g., edge effects from SIMS pits) were removed in post-processing. The

vacuum in the analysis chamber was maintained at ~9E-10 torr and 9.1E-10 to 8.6E-10 torr for the 08/22 and 03/23 analytical sessions, respectively.

Images were analyzed and post-processed following procedures outlined in Peterson et al. (2023b) and Shimizu et al. (2021). Analyses were calibrated against a set of basaltic glass standards (ALV-519-4-1, D52-5, D30-1; Hauri et al., 2002, 2006b) in additional to Suprasil 3002 glass, which was used as a blank material due to its exceptionally low H_2O_T concentration (~1.7±0.6 µg/g H_2O_T; 1 std. dev.; Newcombe, 2022) relative to unknowns (~0.17 – 4.5 wt. % H_2O_T). We assign a conservative estimate of ~10% uncertainty to the calibration curves for all elements based upon the long-term reproducibility of the glass standards (Hauri et al., 2002). The measured H_2O_T concentrations for Suprasil 3002 glass were ~5 µg/g H_2O_T for the 08/22 analytical session and varied from ~270 to ~30 µg/g H_2O_T during the 03/23 analytical session. No blank corrections were applied as the measured H_2O_T concentration of Suprasil 3002 glass is lower than the analytical uncertainty in non-blank corrected data.

5.3.1.3 Analyses of prior experiments

Analyses of H_2O_T were conducted using the Cameca NanoSIMS 50L at the Carnegie EPL. Analyses were conducted in 2017 and followed previously published methods (Hauri et al., 2002; Koga et al., 2003; Sarafian et al., 2017c). Briefly, olivine and glass analyses were conducted using a primary beam current of 5 nA and 1 nA, respectively. For all analyses, a 15×15 µm area was pre-sputtered, prior to decreasing the analytical areas to 5×5 µm and 10×10 µm for olivine and glass, respectively. Counts of ^{12}C, $^{16}O^1H$, ^{19}F, ^{30}Si, and ^{35}Cl, and ^{30}Si were simultaneously detected on electron multipliers. A MRP (Cameca definition) >8000 was used, which allows for discrimination of $^{16}O^1H^-$ from $^{17}O^-$. Suprasil 3002 glass (1.7±0.6 µg/g H_2O_T; 1 std. dev.; Newcombe, 2022; Peterson et al., 2023a), Herasil 102 (~80 µg/g H_2O_T), and ALV-519-

4-1 (1700 µg/g H_2O_T) were used as reference materials and were regularly analyzed throughout the analytical session to monitor instrumental drift and the analytical background. Reference materials were reanalyzed before and after changing beam currents to ensure calibrations were not affected by modification of the beam current. Blank corrections were applied to all data, except calibration curves for which blank materials were not analyzed, by subtracting the average OH/Si×SiO_2/50 of Suprasil 3002 glass analyses that bracketed unknowns. An additional correction to account for dissolved H in Suprasil 3002 glass was applied to blank estimates as in Peterson et al. (2023b). If this correction is not made, all reported concentrations are increased by ~1.7 µg/g H_2O_T, this results in a < 10% increase in H_2O_T concentrations in olivine and no change for the reported H_2O_T of silicate glass. Drift corrections were only applied to data from hours ~50 – 64 after the start of the analytical session, as the OH/Si×SiO_2/50 of ALV-519-4-1 was invariant outside this window. Drift corrections followed the same time variant approach used in Peterson et al. (2023a, accepted). Analyses of H_2O_T in olivine were calibrated against olivine standards: CMOL58, GRR1012, and ROM177. Analyses of H_2O_T in glass were calibrated against glass standards: 1654, 1833-11, 1833-1, 1846-12, ALV-519-4-1, and WOK 28-3. Standard values, calibration curves, and citations for standards are provided in the supplement (Table D2, Fig. D9).

5.3.2 EPMA Analyses

5.3.2.1 Olivine and glass analyses for new experiments

The major and minor element concentrations of olivine and glass were measured by using the JEOL JXA 8900R electron microprobe (EPMA) at the University of Maryland – College Park (UMD) following the methods of Peterson et al. (2023b, accepted) Dependent upon the

amount of suitable analytical area, one to three EPMA analyses were conducted around each SIMS pit. Phase compositions are reported in Table 5.4.

5.3.2.2 Olivine analyses for prior experiments

Major and minor element concentrations of the olivine were measured for the experiments of Gaetani et al. (1994) and Médard and Grove (2008) by using the JEOL JXA-8200 electron probe at the Massachusetts Institute of Technology. A 50 nA beam current and 15 kV accelerating voltage was used. We counted on peak for 400 s for TiO_2, Al_2O_3, and FeO and 40 s for SiO_2, Cr_2O_3, MnO, MgO, CaO, and P_2O_5. Analyses were calibrated against internal standards (synthetic fayalite, synthetic forsterite, and olivine P-140). Phase compositions are reported in Table 5.4.

5.4 Results

5.4.1 Run Products

All run products contained glass, olivine, and plagioclase. Run products from charges containing the MP starting material contained small (< a few μm), highly reflective, opaque grains that are likely Fe-Ti-oxides. Olivine grains are frequently subhedral, but some grains are euhedral with an angular and blocky appearance (Fig. 5.3). Olivine grains from charges containing the MP starting material are predominantly < 100 μm diameter in their long-axis. Angular, elongate olivine grains are likely remnant grains from the crushed starting material, whereas subhedral to euhedral olivine grains may represent new grain growth. Rare olivine grains >150 μm in diameter found in MP-07, MP-10, MP-14, and MP-17 are anhedral to euhedral, contain melt inclusions or melt embayments, and represent large seed crystals from the

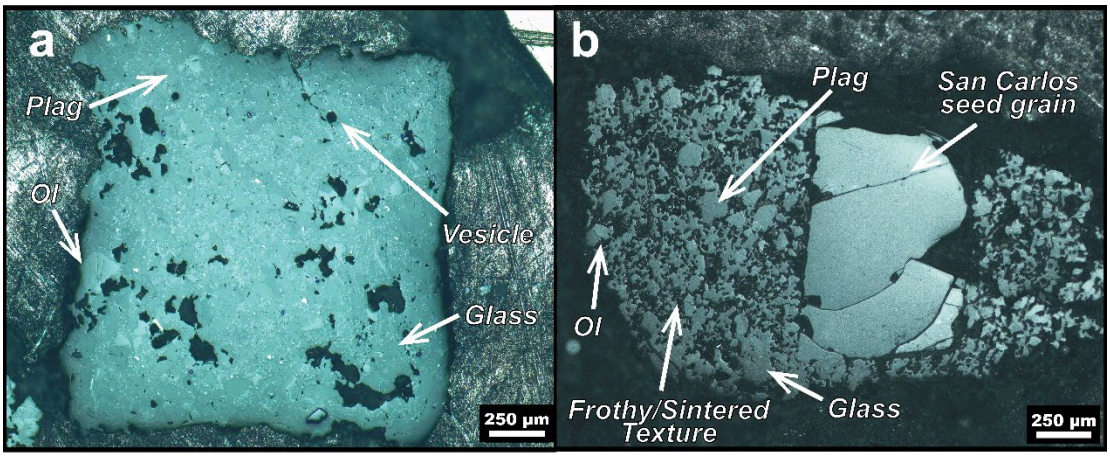

Fig. 5.3 Representative images of A) run products containing the Mt. Pavlof starting material (MP) as represented by MP-14 run products and B) run products containing natural basaltic starting material (BS) 82-72f from Medicine Lake Volcano as represented by charge B-10. Ol – olivine, Plag – plagioclase.

MP starting material (see Section 5.2.3). Olivine grains in the run products of the basaltic starting material are predominantly subhedral, with rare euhedral grains, and are < ~150 µm on their long axis. Olivine grains from charges containing the basaltic starting material are likely the product of grain growth as the starting material was a fine powder with a grain size <<100 µm. For all charges, glassy melt pools are <10 µm, except for MP-05 which has large melt pools (>75 µm).

5.4.2 H_2O Saturation

All run products contained roughly spherical to elongate voids interpreted as vesicles (please see Supplementary data file "Sample_Maps.zip"), suggesting that a fluid phase, likely H_2O vapor, was present when experiments were quenched. The outer capsule for MP-03, and inner capsules B-06, MP-09, B-09, MP-13, and B-13 visually contained water upon opening, confirming the presence of a hydrous fluid phase over the duration of the experiments. Furthermore, all charges contained H_2O_T-bearing glasses with H_2O_T concentrations consistent with or exceeding prior estimates for H_2O_T solubility in basaltic (Newman and Lowenstern,

2002) and basaltic-andesitic melts (Moore et al., 1998; Pineau et al., 1998). If extensive H_2O_T loss occurred prior to quenching, we would expect the H_2O_T contents of experimental glasses to be significantly lower than model predictions for H_2O_T solubility (Table 5.5). However, this is not the case, thereby suggesting that experimental charges were H_2O-saturated and in communication with a fluid phase for the duration of the experiment. Overall, we argue based upon visual confirmation of H_2O in several charges and the presence of vesicles that all charges were H_2O-saturated.

5.4.3 Approaches to equilibrium with respect to H

We use several lines of evidence to assess the approach to equilibrium with respect to H_2O_T in our experiments. First, at the temperatures of our experiments, H diffusion in olivine is rate-limited by diffusion of metal vacancies with the fastest diffusion occurring along the [0 0 1] axis. Using the diffusivity parameterization of Demouchy and Mackwell (2006), the approximation $x \approx \sqrt{Dt}$ (x = diffusion length; D = diffusivity; t = time), and a grain diameter of 500 μm, which exceeds the diameter of the largest olivine grain in run products, we estimate an equilibration time of ~17 hr. For our 1 mm San Carlos olivine seeds, we calculate an estimated equilibration time of ~67 hr. which exceeds the maximum length of our experiments, therefore we may expect to observe gradients with respect to H in these grains. Second, if olivine grains had not reached equilibrium with respect to H, we may expect to observe H gradients. For our experimental run products, transects within individual olivine grains, including San Carlos seeds, generally have uniform H_2O_T concentrations within analytical uncertainty (Fig. D10 – D24). Large grains in MP run products preferentially sample seed grains, which may contain glassy melt pockets (see Section 5.4.1) and are over-sampled for transects relative to small grains due to grain size limitations for analyses. Several seed grains from MP run products have scattered, but

broadly invariant olivine H_2O_T transects with outliers potentially representing concentrations that were partially buffered by concealed melt pockets (Fig. D18 – D24). The lack of observable gradients for H_2O_T in San Carlos olivine seed grains in run products and several olivine grains in the MP and 82-72f run products suggests equilibrium with respect to H was reached. Lastly, we conducted experiments at intervals of 12, 24, and 48 hr. which are consistent with a uniform olivine H_2O_T content and $D_{H_2O_T}^{ol/melt}$ value within analytical uncertainty after 24 hr. (Fig. 5.4). Experiment MP-05 represents an outlier as it has resolvably higher olivine H_2O_T contents in its run products than all other charges at 100 MPa. Similarly, MP-13, which represents the 48 hr. run for the MP starting material, is offset to higher olivine H_2O_T content and $D_{H_2O_T}^{ol/melt}$ values than 100 MPa experiments. One potential explanation for this is that MP-13 was unintentionally

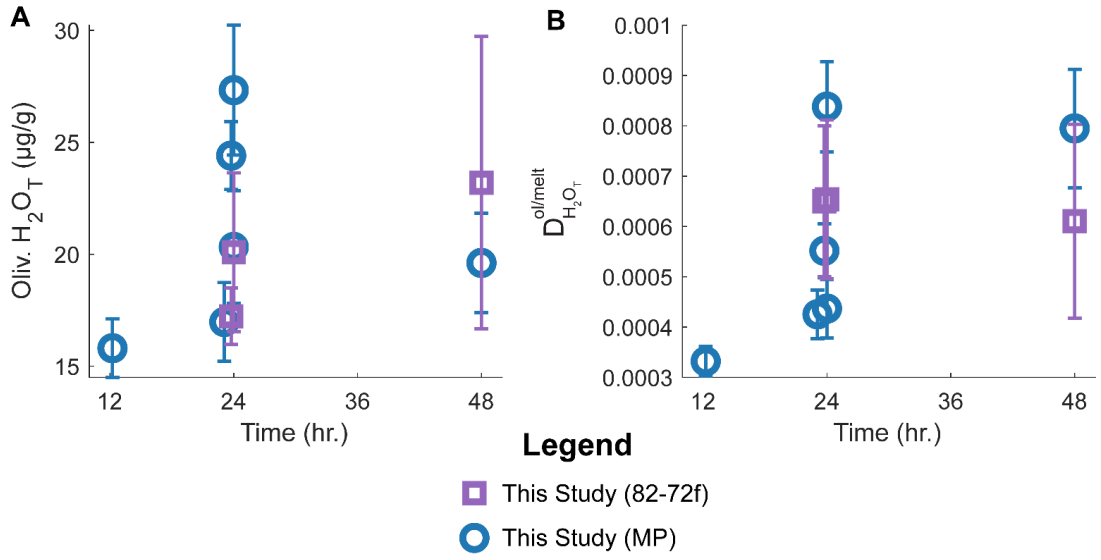

Fig. 5.4 A) Olivine H_2O concentration and B) $D_{H_2O}^{ol/melt}$ plotted against time for 100 MPa time series experiments.

Table 5.5) Summary of the H_2O_T contents of run products, predicted glass H_2O_T from the model of Moore et al. (1998) and H-speciation in the melt from Newman and Lowenstern (2002)

		SIMS				Moore et al. (1998)		Calculated OH and H_2Om (Newman and Lowenstern, 2002)			
		H_2O_T (µg/g)	Unc[1]	$D_{H_2O_T}^{ol/melt}$	Unc.	H_2O_T (µg/g)	Difference	OH	H_2O_m	$D_{OH}^{ol/melt}$	Unc.
MP-10	Glass	46500	2300	-	-	34800	11700	1.92	2.73	-	-
	Olivine	20	3	0.00044	0.00006	-		-	-	0.0011	0.0002
MP-02	Glass	39900	1800	-	-	34700	5200	1.85	2.14	-	-
	Olivine	17	2	0.00043	0.00005	-		-	-	0.0009	0.0001
MP-06	Glass	47600	1600	-	-	34400	13200	1.93	2.83	-	-
	Olivine	16	1	0.00033	0.00003	-		-	-	0.00082	0.0001
MP-09	Glass	44200	3300	-	-	34100	10100	1.90	2.52	-	-
	Olivine	24	2	0.00055	0.00005	-		-	-	0.00129	0.0002
MP-05	Glass	*32600*	*500*	-	-	35100	2500	1.73	1.53	-	-
	Olivine	*27*	*3*	0.0008	0.0001	-		-	-	0.0016	0.0002
MP-13	Glass*	24700	2300	-	-			1.53	0.94	-	-
	Olivine	20	2	0.0008	0.0001	-		-	-	0.0013	0.0002
MP-03	Glass	41400	1100	-	-	32000	9400	1.87	2.27	-	-
	Olivine	16	3	0.00040	0.00007	-		-	-	0.0009	0.0002
MP-14	Glass	20800	300	-	-			1.40	0.68	-	-
	Olivine	15	3	0.0007	0.0001	-		-	-	0.0010	0.0002
MP-19	Glass	16500	600	-	-	25200	8700	1.22	0.43	-	-
	Olivine	16	2	0.0009	0.0001	-		-	-	0.0013	0.0002
MP-17	Glass	13500	500	-	-	25000	11500	1.06	0.29	-	-
	Olivine	11	2	0.0008	0.0002	-		-	-	0.0011	0.0002
MP-18	Glass	12300	300	-	-			0.99	0.24	-	-

Table 5.5) *continued…*

		SIMS				Moore et al. (1998)		Calculated OH and H_2O_m (Newman and Lowenstern, 2002			
		H_2O_T (µg/g)	Unc[1]	$D_{H_2O_T}^{ol/melt}$	Unc.	H_2O_T (µg/g)	Difference	OH	H_2O_m	$D_{OH}^{ol/melt}$	Unc.
	Olivine	16	3	0.0013	0.0002	-		-	-	0.0016	0.0003
MP-15	Glass	13200	500	-	-			1.04	0.28	-	-
	Olivine	7	1	0.00052	0.00006	-		-	-	0.0007	0.0001
MP-07	Glass	14700	500	-	-	18100	3400	1.12	0.34	-	-
	Olivine	16	1	0.0011	0.0001	-		-	-	0.0014	0.0002
B-09	Glass	26500	5800	-	-			1.59	1.06	-	-
	Olivine	17	1	0.00065	0.00015	-		-	-	0.00109	0.0001
B-10	Glass	30700	5000	-	-			1.69	1.38	-	-
	Olivine	20	4	0.0007	0.0002	-		-	-	0.0012	0.0002
	San Carlos	5.4	0.5	0.00018	0.00003					0.00032	0.0000
B-13	Glass	38000	5400	-	-			1.82	1.97	-	-
	Olivine	23	7	0.0006	0.0002	-		-	-	0.0013	0.0004
	San Carlos	10.7	0.5	0.00028	0.00004	-		-	-	0.00059	0.00007
G5	Glass	48400	800	-	-	47800	600	1.94	2.91	-	-
	Olivine	23	11	0.0005	0.0002	-		-	-	0.0012	0.0006
G7	Glass	46300	800	-	-	48500	2200	1.92	2.71	-	-
	Olivine	23	1	0.00049	0.00003	-		-	-	0.0012	0.0001
M7	Glass	31500	4000	-	-	32700	1200	1.71	1.44	-	-
	Olivine	23	7	0.0007	0.0002	-		-	-	0.0013	0.0004
M8	Glass	20100	100	-	-	22000	1900	1.37	0.64	-	-
	Olivine	13	4	0.00066	0.00021	-		-	-	0.0010	0.0003

Table 5.5) *continued…*

		SIMS				Moore et al. (1998)		Calculated OH and H_2Om (Newman and Lowenstern, 2002			
		H_2O_T (µg/g)	Unc[1]	$D_{H_2O_T}^{ol/melt}$	Unc.	H_2O_T (µg/g)	Difference	OH	H_2O_m	$D_{OH}^{ol/melt}$	Unc.
M11	Glass	10200	100	-	-	14500	4300	0.86	0.16	-	-
	Olivine	9	2	0.0009	0.0002	-		-	-	0.0011	0.0003
M23	Glass	7500	100	-	-	8400	900	0.67	0.08	-	-
	Olivine	9	2	0.0011	0.0003	-		-	-	0.0013	0.0003
PSM	Melt Inclusion	25300	1100	-	-	-		-	-	-	-
	Olivine	13	3	0.00053	0.00013	-		-	-	-	-
**Raw SC	San Carlos	2.2	0.2	-	-	-		-	-	-	-
B-07 SC	San Carlos	3.8	0.3	-	-	-		-	-	-	-
B-14SC	San Carlos	2.6	0.1	-	-	-		-	-	-	-

*Sample charge was contaminated by C, likely during sample preparation; glass has ~60 µg/g CO_2 (total C quantified as CO2)
**Raw SC – San Carlos starting material that has not been subject to processing during experiments
[1]Uncertainty reported as the larger value between the propogated uncertainty and 10%, which represents a conservative estimate of the long-term reproducibility of the calibration curves

contaminated by C during sample prep. As measured by SIMS, melts in MP-13 run products contained ~60 µg/g CO_2 (total C as CO_2 equivalents) compared to < ~10 µg/g CO_2 for all other run products and Suprasil 3002 glass. Olivine H_2O_T and $D_{H_2O_T}^{ol/melt}$ are uniform between B-13 (48 hr.) and B-09 and B-10 (24 hr.), suggesting equilibrium may have been reached after 24 hr. (Fig. 5.4). Overall, attainment of equilibrium with respect to H in our experiments is supported by a lack of H_2O_T gradients in run product olivine grains, and agreement, within uncertainty, of $D_{H_2O_T}^{ol/melt}$ for experiments conducted for 12, 24, and 48 hr.

5.4.4 H Solubility in Olivine

We collected H_2O_T concentration data on olivine from 6 prior experiments and 17 new experiments, including 5 San Carlos seed olivine grains from charges containing the basaltic (i.e., 82-72f) starting material. The H_2O_T concentrations of olivine from MP run products are broadly within uncertainty of each other over the pressures of our experiments. The central H_2O_T concentration value for run product olivine grains from experiments conducted at 100 MPa is resolvably higher than for experiments conducted at 50 MPa and the MP starting material (MP starting material: 13±3 µg/g H_2O_T; 1 std. dev.; Fig. 5.5). The higher offset of run product olivine H_2O_T concentrations from 100 MPa experiments relative to 50 MPa experiments and the MP starting material is consistent with equilibration of newly crystallized olivine and re-equilibration of seed olivine grains with respect to H_2O_T. Based upon the "single proton coupled to a cation" substitution mechanism outlined in Table 5.1, we fit square root functions to the relationships between olivine H_2O_T concentration, pressure, $f$$H_2O$, and glass H_2O_T (Fig. 5.6). We also fit a linear function to the relationship between olivine H_2O_T and $f$$H_2O$ that can be compared to the

square root function to evaluate whether the "single proton coupled to a cation" or "proton pairs" mechanism for H substitution in olivine dominates for our experiments (Fig. 5.6, Table 5.1). Inter-comparison of the linear and square root fits of olivine H_2O_T to fH_2O suggest the "single proton coupled to a cation" mechanism is dominant for our experiments. We calculate fH_2O at H_2O saturation using the equation of state of Pitzer and Sterner (1994) as implemented in the calculator by Tony Withers (https://publish.uwo.ca/~awither5/fugacity/index.htm). We find that olivine H_2O_T concentrations are uncorrelated with olivine major and trace elements as measured by EPMA in this study.

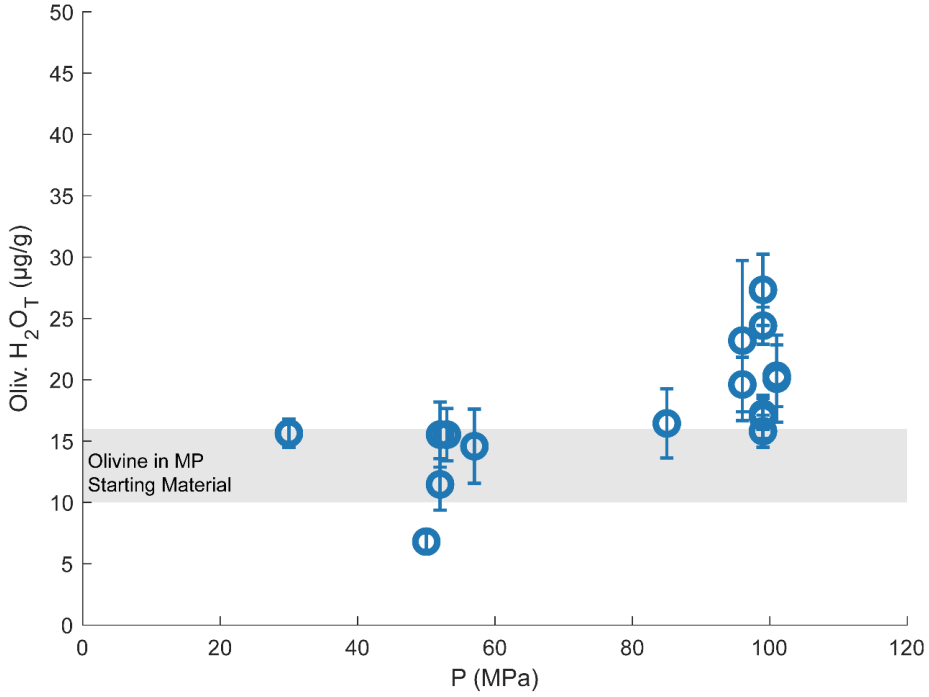

Fig. 5.5 Olivine H_2O concentrations from MP run products (blue) and the H_2O concentration of seed olivine from the MP starting material (grey box).

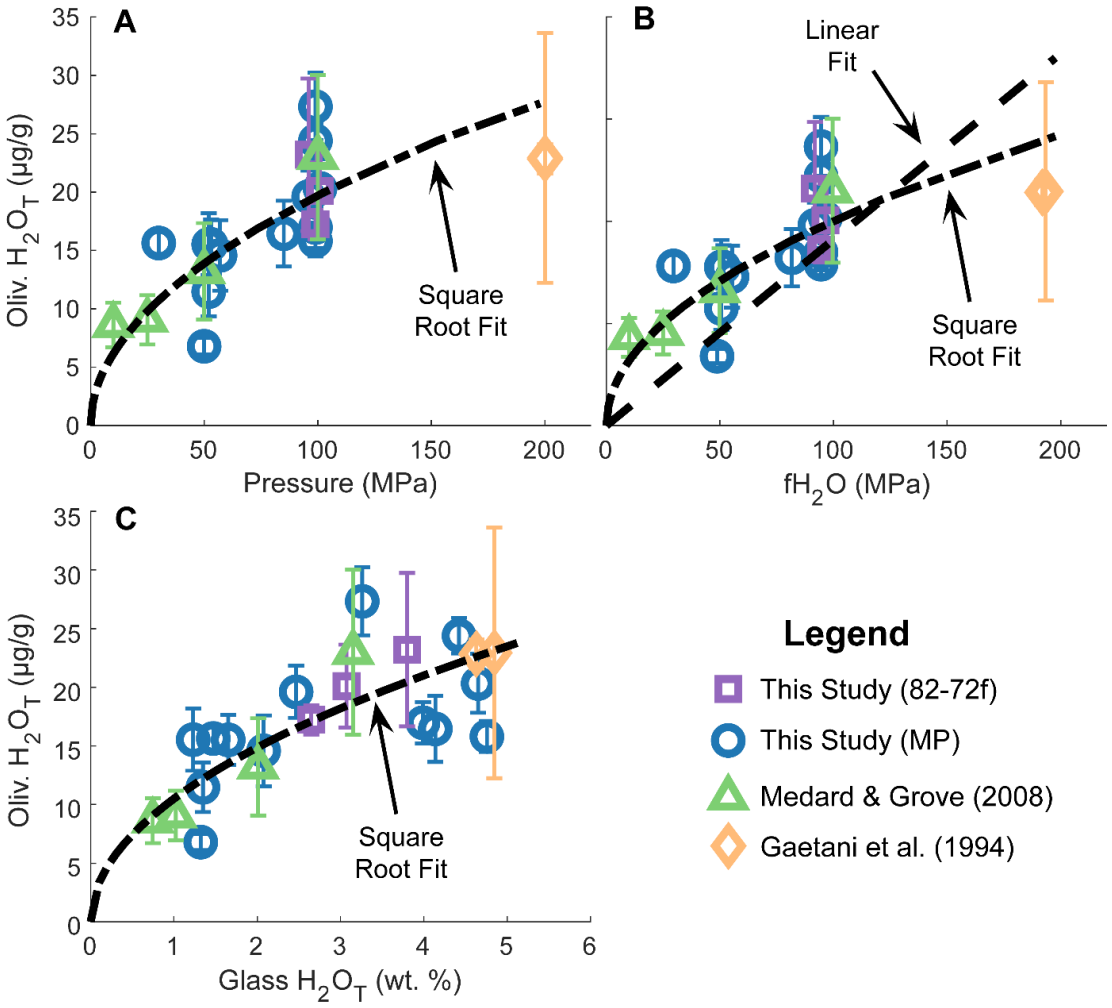

Fig. 5.6 Olivine H_2O concentrations plotted against: A) pressure, B) fH_2O, and C) glass H_2O_T for newly conducted and newly analyzed prior experiments considered in this study. Dashed lines are least squares fits to the data. 82-72f is the basaltic starting material from Medicine Lake Volcano, CA used in this study.

5.4.5 H Solubility in Basaltic and Basaltic-Andesitic Glass

We measured the H_2O_T concentration of glasses in run products of the MP and basaltic starting materials as well as prior experiments (Table 5.5). Within our dataset, we find that the relationships between glass H_2O_T, pressure, and fH_2O are reasonably fit by a square root relation (Fig. 5.7). For our 100 MPa experiments on the MP starting material, glass H_2O_T concentrations are negatively correlated with alkalis ($Na_2O + K_2O$; Fig. 5.7), although this trend is anchored

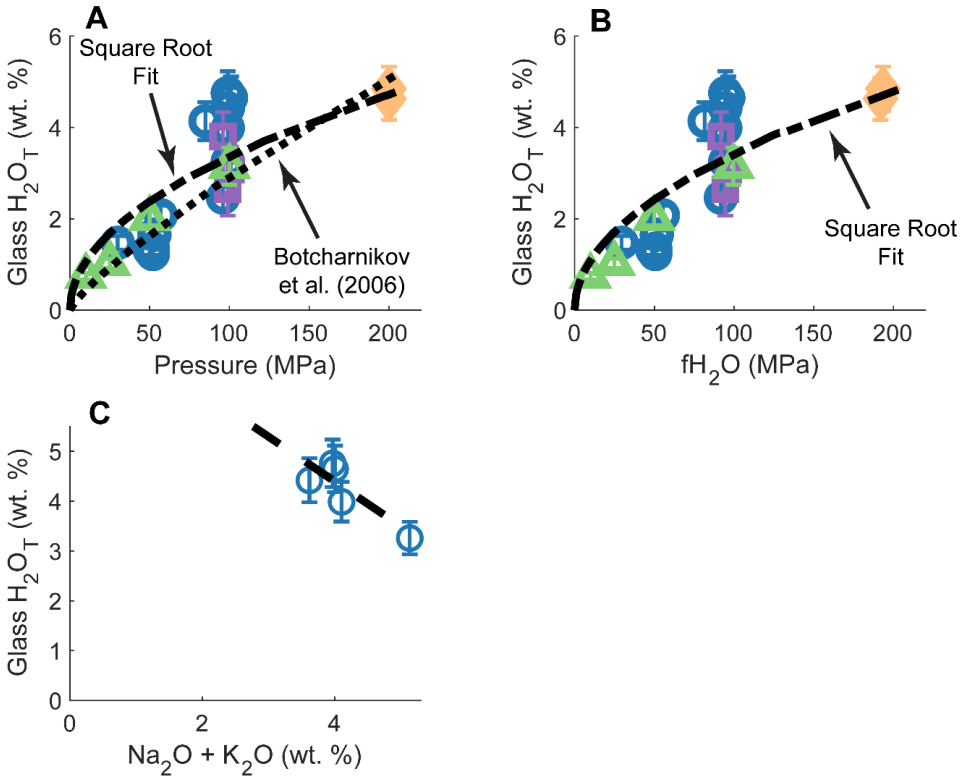

Fig. 5.7 Glass H_2O_T concentrations plotted against A) pressure and B) fH_2O for all newly conducted and newly analyzed prior experiments and C) for $Na_2O + K_2O$ for MP run products from experiments at 100 MPa. Dashed lines are least squares fits to the data with the exception of the empirical fit for glass H_2O_T to pressure from Botcharnikov et al. (2006). See text for description of how fH_2O is calculated. Legend as in Fig. 5.6.

by a single data point. We find that glass H_2O_T concentrations correlate with no other compositional parameters for our data set.

5.4.5.1 Comparison to existing H_2O_T solubility models

Several prior studies have examined the solubility of H_2O_T in basaltic to rhyolitic melts and developed corresponding H_2O_T solubility models (Moore et al., 1998; Pineau et al., 1998; Newman and Lowenstern, 2002; Iacovino et al., 2021). The H_2O_T contents of glasses generated from the basaltic starting material at 100 MPa, 1000 °C, and the NNO fugacity buffer are in good agreement with H_2O_T solubility models for basaltic melts (Table 5.5; Moore et al., 1998;

Newman and Lowenstern, 2002). Conversely, the H_2O_T contents of glasses generated from the MP starting material are in poor agreement with prior studies of H_2O_T solubility in basaltic andesitic melts (Table 5.5; Moore et al., 1998; Pineau et al., 1998). It is unlikely that the disagreement between the measured and predicted H_2O_T solubility of glasses in MP run products represents an analytical effect as glass H_2O_T contents are consistent within a charge, between charges, and across analytical sessions. Diffusive loss of H through capsule walls may result in lower total fH_2O in the charges, thereby lowering glass H_2O_T contents; however, this cannot account for the cluster of data at 100 MPa which are under-predicted by H_2O_T solubility models. Similarly, it is possible that the internal capsule pressure exceeded that of the pressure medium in the vessel. An excess internal capsule pressure seems unlikely as this would have caused capsules to bulge, which was not observed in our experiments. Overall, it is unclear why glass H_2O_T contents in MP run products are poorly reproduced by existing solubility models. We present our measured glass H_2O_T contents and predicted glass H_2O_T contents using the model of Moore et al. (1998) in Table 5.5, but only consider our measured glass H_2O_T contents for the remaining discussion.

5.4.6 Olivine-Melt Partitioning

We use our measured olivine and glass H_2O_T contents to calculate $D_{H_2O_T}^{ol/melt}$ (Table 5.5). At 100 MPa, we find no resolvable difference in $D_{H_2O_T}^{ol/melt}$ between run products from our MP and basaltic starting materials. Furthermore, our $D_{H_2O_T}^{ol/melt}$ data from 10 – 200 MPa decrease with increasing pressure, fH_2O, and glass H_2O_T concentrations and the relationships between these parameters are reasonably described by power laws (Fig. 5.8). The decrease of $D_{H_2O_T}^{ol/melt}$ with

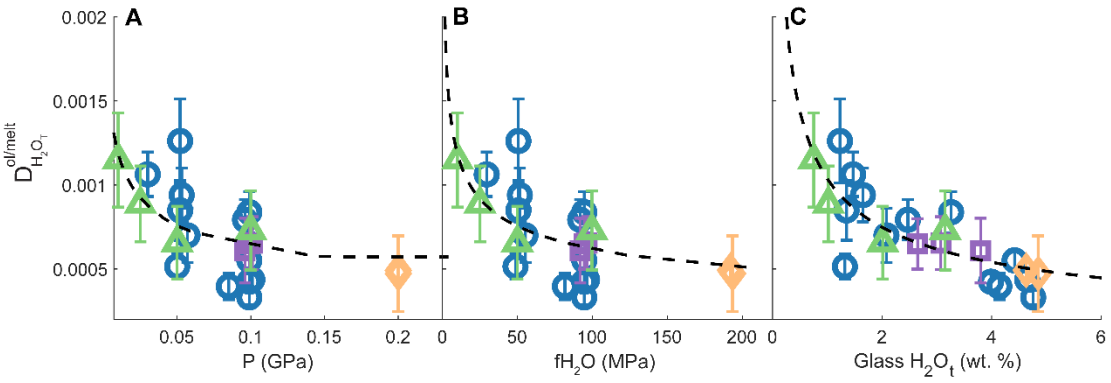

Fig. 5.8 $D^{ol/melt}_{H_2O}$ plotted against A) pressure, B) fH2O, and C) the concentration of H_2O_T in the glass for all newly conducted and newly analyzed prior experiments in this study. Dashed lines are least-squares power regressions to the data. Legend as in Fig. 5.6.

increased pressure for our experiments is contrary to the positive, linear relation previously identified for experiments from 0.5 – 13 GPa (Tenner et al., 2009a; Adam et al., 2016). Our data from 10 – 85 MPa are broadly unresolvable from the preferred $D^{ol/melt}_{H_2O}$ value at 0.5 – 3 GPa ($D^{ol/melt}_{H_2O_T}$ = 0.0009±0.0003; 1 std. dev.) determined by Towbin et al. (2023), although nearly all data from 100 – 200 MPa have central values that fall outside this range (Table 5.5).

5.4.7 San Carlos Seed Grains

Center to edge transects were measured in grains and grain fragments of San Carlos olivine seeds included in experiments containing the basaltic starting material. For all charges, except B-10, the San Carlos olivine seed grains recovered did not remain in contact with the melt following extraction. Due to the friability of the basaltic run products, removal, polishing, and mounting of materials proved difficult and resulted in limited availability of materials from the basaltic charges. We recovered and analyzed San Carlos seeds from charges B-07, B-10, B-13, and B-14. The H_2O_T of San Carlos seed grains are variable (2.6±0.1 – 10.7±0.5 µg/g H_2O_T; 1 std. dev.), and only the San Carlos seed from B-14 (2.6±0.1 µg/g H_2O_T; 1 std. dev.) is indistinguishable from starting material San Carlos olivine (2.3±0.3 µg/g H_2O_T; 1 std. dev.). The

H_2O_T of San Carlos olivine seeds is weakly pressure dependent (Fig. D2) and does not correlate with any measured trace element concentrations measured here (e.g., Ca, Ti, Na) as in prior experimental studies (Tollan et al., 2018). San Carlos seed grains and olivine grains crystallized during the experiments (hereafter "grown olivine") were measured in the run products of charges B-10 and B-13. Comparison of San Carlos seeds (Fo91) and grown olivine grains (~Fo83) allows for an assessment of H solubility for olivine grains with different major, minor, and trace element compositions under identical conditions. We find that the H_2O_T contents of grown olivine grains from B-10 (20±4 µg/g H_2O_T; 1 std. dev.) and B-13 (23±7 µg/g H_2O_T; 1 std. dev.) are resolvably higher than their corresponding San Carlos seeds (5.4±0.5 µg/g H_2O_T and 10.7±0.5 µg/g H_2O_T, respectively; 1 std. dev.). Overall, our data support a weak correlation between pressure and H_2O_T solubility in San Carlos olivine and a difference in H_2O_T solubility for olivine grains with different compositions and therefore defect populations.

5.5 Discussion

Our findings challenge the assumption that $D_{H_2O_T}^{ol/melt}$ is primarily dependent upon pressure as suggested by the linear dependence of $D_{H_2O_T}^{ol/melt}$ with pressure for experiments conducted at pressures ≥ 0.5 GPa. The distinct decrease of $D_{H_2O_T}^{ol/melt}$ over our experimental pressure range (10 – 200 MPa) may primarily be a function of pressure; however, it is possible that this deviation from the expected trend is related to crystallographic defects or pressure inter-related parameters. We explore the roles of crystallographic defects, $f$$H_2O$, and H speciation in the melt on $D_{H_2O_T}^{ol/melt}$.

5.5.1 Extrinsic crystallographic defects

We analyzed San Carlos olivine seed and grown olivine grains in the run products of B-10 and B-13, which were the only run products for which San Carlos seeds and grown olivine grains could both be analyzed. Grown olivine grains yielded higher H_2O_T concentrations than San Carlos seeds by ~70% and ~60%, respectively, for B-10 and B-13 run products (Fig. 5.9). One potential explanation for the discrepancy in the H_2O_T contents of grown and San Carlos seed olivine grains is a difference in their extrinsic point defect populations. We can use the trace element content (e.g., Na, Ca, Mn, Al, Ti) of experimental olivines, as measured by EPMA, as a first-order approximation of their extrinsic point defect populations (e.g., Berry et al., 2007; Tollan et al., 2018). On an anhydrous basis, grown olivine grains have ~50 – 100 % higher concentrations of trace elements (e.g., Na, Ca, Mn, Al, Ti) than San Carlos olivine seed grains from the same charge. The higher concentration of trace elements in grown olivine grains implies that they have a greater extrinsic point defect population than San Carlos olivine seed grains. A higher concentration of extrinsic point defects would provide more sites for H^+ to decorate, resulting in a higher solubility of H in grown olivine grains. This mechanism is supported by other experiments that doped magnesian olivine with trace element cations (e.g., Sc, Ti, Al, rare earth elements) and found H_2O_T solubility increased with trace element concentrations (e.g., Berry et al., 2007; Tollan et al., 2017). It is also possible that disequilibrium effects, such as trapping of nanoscale fluid inclusions, could account for the discrepancy between San Carlos olivine seed and grown olivine H_2O_T contents (Mosenfelder et al., 2006a). Disequilibrium effects may be evidenced in our experiments by homogeneous H_2O_T contents on the grain-scale, but heterogeneous H_2O_T on the charge-scale for grown olivine from B-10 and

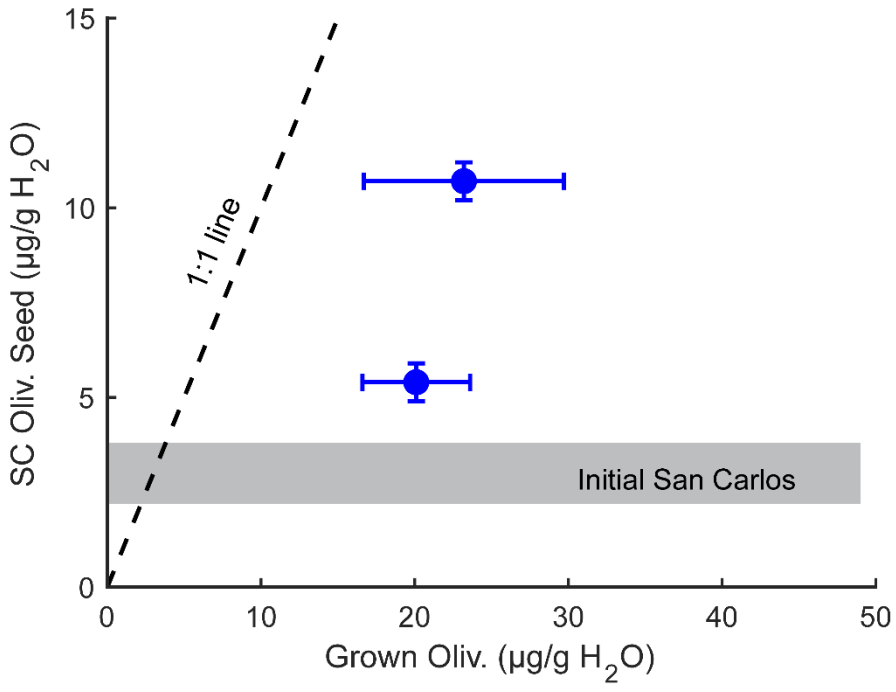

Fig. 5.9 Comparison of the measured H_2O concentrations of San Carlos seed olivine and grown olivine from charges containing the BS starting material.

B-13. The homogeneity of H_2O_T on the grain-scale for grown olivine in charges B-10 and B-13 would require a homogeneous distribution of nanoscale fluid inclusions, which seems fortuitous. Overall, we suggest that variations in the extrinsic defect populations of grown olivine relative to San Carlos olivine seed grains accounts for the difference in their H_2O_T contents, consistent with a defect control on H_2O_T solubility in olivine (Berry et al., 2007; Tollan et al., 2018).

Our experiments containing the MP starting material were seeded with olivine grains picked from a separate aliquot of the MP starting material (see Section 5.2.2). For olivine grains from MP run products, we found that olivine H_2O_T contents were not correlated with major or trace elements measured in this study. A lack of correlation between MP run product olivine major and trace element and H_2O_T concentrations is consistent with re-equilibration of olivine point-defects during experimental runs or a subordinate control of individual trace elements on olivine H_2O_T for these experiments. We observe that the relationship between olivine H_2O_T

contents and fH_2O is best described as a square root function (Fig. 5.6), which is consistent with incorporation of individual H^+ coupled to cations in olivine (Table 5.1). Despite some scatter in Fig. 5.6, a square root functional form between olivine H_2O_T and fH_2O implies that trace elements or metal vacancies exert some control on olivine H_2O_T solubility. Extrinsic defects and metal vacancies diffuse orders of magnitude slower than H in olivine (Kohlstedt and Mackwell, 1998; Demouchy and Mackwell, 2006; Jollands et al., 2023), which suggests that extrinsic defects and metal vacancies are unlikely to fully re-equilibrate during our experimental runs. Overall, we suggest that MP run product olivine H_2O_T contents are best accounted for by re-equilibration of H in the olivine structure as single H^+ coupled to cations in metal vacancies.

5.5.2 The Effect of Pressure on Olivine-Melt H Partitioning

Prior experimental work has shown that $D_{H_2O_T}^{ol/melt}$ has a positive, linear correlation with pressure at pressures ≥ 0.5 GPa (Tenner et al., 2012; Novella et al., 2014; Adam et al., 2016). A recent study by Towbin et al. (2023) demonstrated that once variability in analytical methods is accounted for, $D_{H_2O_T}^{ol/melt}$ values from experiments at 0.5 – 2 GPa have no resolvable variation with pressure ($D_{H_2O_T}^{ol/melt}$ = 0.0009±0.0003; 1 std. dev.). Taken separately and extending these results to our experimental pressure range would imply either a positive correlation or invariance of $D_{H_2O_T}^{ol/melt}$ with pressure. However, we observe a resolvable decrease in $D_{H_2O}^{ol/melt}$ from 10 to 200 MPa, contrary to predicted results by extending conclusions from higher pressure data (Fig. 5.8). We elect to fit a power law to the distribution between $D_{H_2O_T}^{ol/melt}$ and pressure for our experiments, similar to fits for H_2O_T in olivine (e.g., Fei and Katsura, 2020) and silicate glasses (e.g., Hamilton et al., 1964; Mitchell et al., 2017) to pressure. We find that a power law adequately describes the relationship between our $D_{H_2O_T}^{ol/melt}$ and pressure (Fig. 5.8). Furthermore,

at the conditions of our experiments, the general power-law relation shown in Fig. 5.8b is consistent with dissolution of H in olivine as single protons coupled to cations (Table 5.1). The change in functional form and slope of correlation (e.g., positive or negative) for $D_{H_2O_T}^{ol/melt}$ and pressure is consistent with a change of control from pressure to a pressure inter-related parameter (e.g., fH$_2$O, H speciation in the melt) or a change in H dissolution mechanism or equilibrium, at minimum, at low pressures for olivine or melt. We explore the roles of fH$_2$O and the speciation of H in the melt, which are strongly pressure-dependent at H$_2$O-saturated conditions, in the following section.

5.5.3 H_2O Fugacity and H Speciation in the Melt

The work of Stolper and colleagues has shown that the square of the mole fraction of H$_2$O$_T$ in silicate melt is proportional to fH$_2$O and is readily explained by the dissolution of OH and H$_2$O in the melt (Table 5.1; Stolper, 1982b, a; Silver and Stolper, 1985, 1989; Silver et al., 1990). Therefore, it is expected that the speciation of H (i.e., OH, H$_2$O) in the melt is closely tied to the fH$_2$O of the system. For the low pressures and H$_2$O-saturated conditions of our experiments, fH$_2$O is closely approximated by pressure, so $D_{H_2O_T}^{ol/melt}$ is expected to correlate with pressure, fH$_2$O, and melt H$_2$O$_T$ concentrations (Fig. 5.8). Following the model of Stolper and colleagues, the speciation of H in the melt should tightly correlate with $D_{H_2O_T}^{ol/melt}$, which can be evaluated by comparing $D_{OH}^{ol/melt}$ to the concentration of OH in the melt. We calculate $D_{OH}^{ol/melt}$ by using the H-speciation model built-in to VolatileCalc (Newman and Lowenstern, 2002) to calculate the amount of OH dissolved in glasses from our experimental run products and assuming H$_2$O$_T$ is dissolved in olivine only as OH (Table 5.5). We find that over our dataset, $D_{OH}^{ol/melt}$ is invariant ($D_{OH}^{ol/melt}$ = 0.0012±0.0002; 1 std. dev.) with respect to glass OH concentration (Fig. 5.10),

implying a tight correlation between H-speciation in the melt and $D_{H_2O_T}^{ol/melt}$. We can project our $D_{OH}^{ol/melt}$ to $D_{H_2O_T}^{ol/melt}$ by comparing the calculated glass OH concentrations with the measured glass H_2O_T concentrations. We define $D_{OH}^{ol/melt}$ projected to $D_{H_2O_T}^{ol/melt}$ to be $\left(D_{H_2O_T}^{ol/melt}\right)_{proj}$. Similarly, taking the H speciation model from VolatileCalc and our constant $D_{OH}^{ol/melt}$ (0.0012±0.0002; 1 std. dev.) we can generate a curve for the relationship between $\left(D_{H_2O_T}^{ol/melt}\right)_{proj}$ and melt H_2O_T (Fig. 5.10b). We find that the curve for $\left(D_{H_2O_T}^{ol/melt}\right)_{proj}$ reproduces the relationship between $D_{H_2O_T}^{ol/melt}$ and melt H_2O_T concentration for our experiments (Fig. 5.10b). Overall, for the experimental data presented in this study, fH_2O and/or H speciation in the melt can reasonably account for the observed relationship between $D_{H_2O_T}^{ol/melt}$ and pressure.

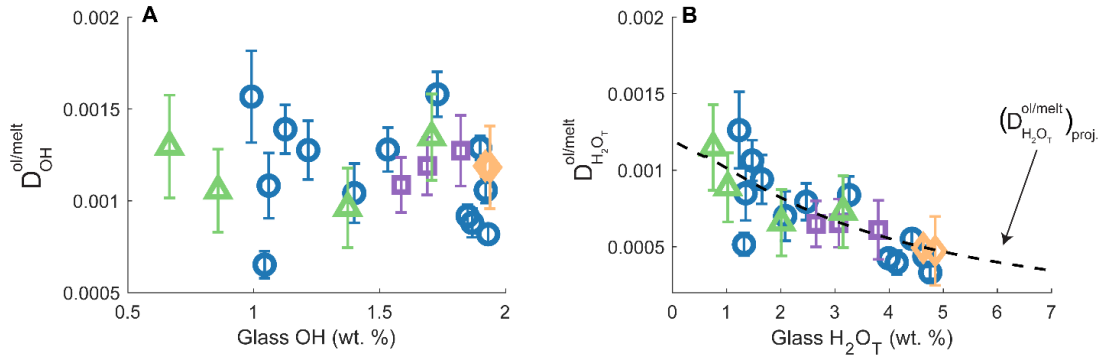

Fig. 5.10 a) $D_{OH}^{ol/melt}$ plotted against glass OH concentration, and b) $D_{H_2O_T}^{ol/melt}$ plotted against glass H_2O_T concentration. The dashed line in b) is a projection of a constant $D_{OH}^{ol/melt}$ (0.0018±0.006) to $D_{H_2O_T}^{ol/melt}$. See text for description of how $\left(D_{H_2O_T}^{ol/melt}\right)_{proj.}$ is calculated. Legend as in Fig. 5.6.

All literature experiments constraining $D_{H_2O_T}^{ol/melt}$ have been conducted at high pressures (≥ 0.5 GPa) and H_2O-undersaturated conditions preventing a direct constraint on fH_2O. However, following the work of Stolper and colleagues, we can provide an indirect constraint on the

control of fH_2O for high pressure experiments based upon the speciation of H in the melt. Following the same procedure as above, we calculate $D_{OH}^{ol/melt}$ for olivine-melt H partitioning experiments at pressures up to 3 GPa (Table D3). We note that VolatileCalc is not calibrated at pressures > 0.5 GPa (Newman and Lowenstern, 2002) and therefore calculated melt OH concentrations and $D_{OH}^{ol/melt}$ values are highly uncertain. For high pressure experiments, we find that $D_{OH}^{ol/melt}$ is highly variant at a nearly constant melt OH concentration (Fig. 5.11b), contrary to our low-pressure experiments. This either implies that the speciation model implemented in VolatileCalc is degenerate at the conditions of the high-pressure experiments or that the dissolution mechanisms and equilibria for H incorporation in olivine change with pressure.

5.5.3.1 Pressure dependence of OH and H_2O equilibration in silicate melts

The study of Hui et al. (2008) found that the equilibrium constant describing the equilibration of OH and H_2O in rhyolite melt is pressure-dependent from 1 – 3 GPa. An increase in the equilibrium constant for OH and H_2O in the melt implies that more H_2O is reacting with O in the melt to form OH, which is consistent with breaking of silicate tetrahedra in the melt due to compression of the melt at high pressures (Behrens, 2020). However, the model of Hui et al. (2008) is calibrated at low temperatures (~350 – 750 °C) relative to olivine-melt H_2O_T partitioning experiments (1000 – 1500 °C) and seems to show a diminishing pressure effect with increasing temperature (see Fig. 6 from Hui et al., 2008). Overall, the extent to which the equilibrium constant for OH and H_2O equilibration in basalt is dependent upon pressure at the conditions of olivine-melt H_2O_T partitioning experiments is unclear.

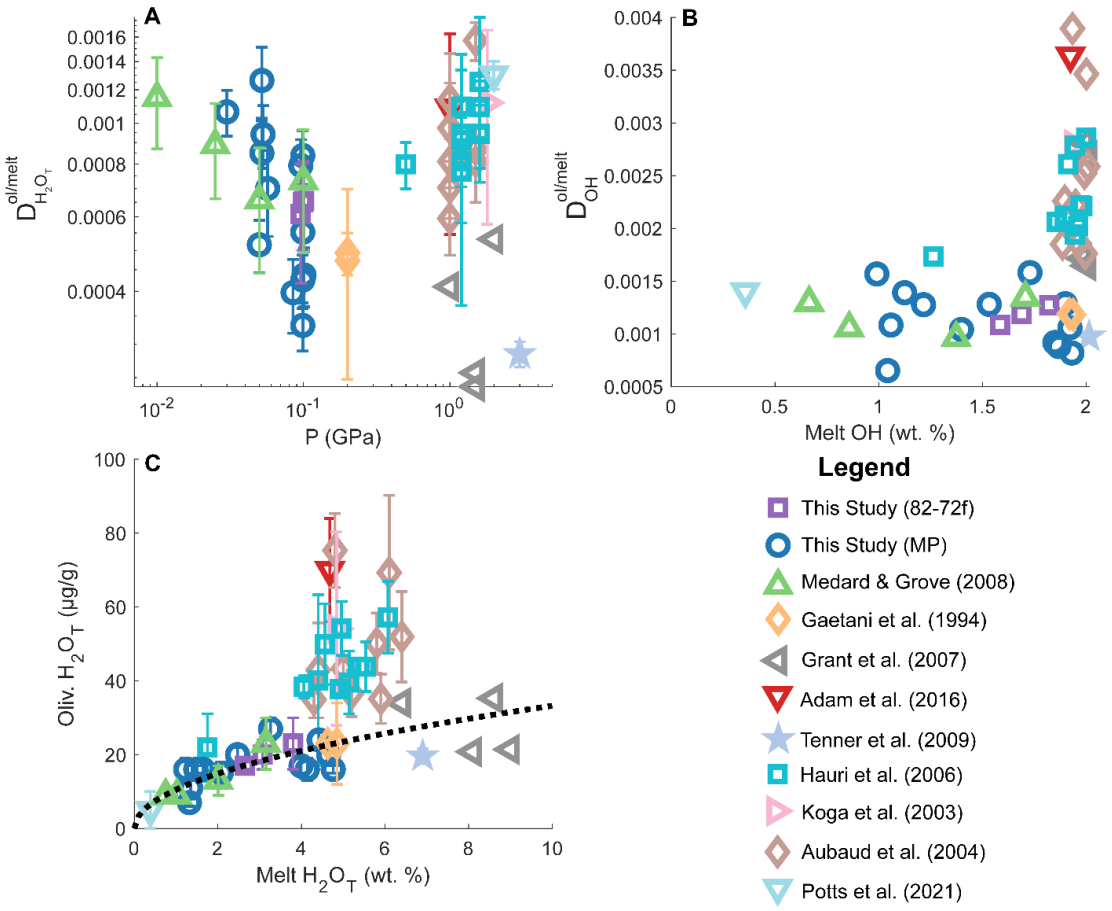

Fig. 5.11 a) $D_{H_2O_T}^{ol/melt}$ plotted against pressure, b) $D_{OH}^{ol/melt}$ plotted against melt OH, and c) $D_{H_2O_T}^{ol/melt}$ plotted against glass H_2O_T for data from this study and the literature for experiments conducted at pressures up to 3 GPa (see text for details). The black dotted line in c) is an empirical square root fit to the low-pressure experimental data form this study as in Fig. 5.6.

5.5.3.2 Changes in H incorporation mechanisms in olivine with pressure

For simplicity, we consider the four main H point defect substitutions in olivine as defined by Tollan et al. (2017; Table 1). A detailed discussion of structural and point defects in olivine can be found in Demouchy (2021). For our experiments (Fig. 5.6), the relationship between olivine H_2O_T and fH_2O is consistent with H substitution into the olivine structure as single protons coupled with 3^+ or 1^+ cations (Table 5.1). This observation is consistent with analytical and experimental studies which find olivine H_2O_T concentration can be coupled to the

concentrations of trivalent (e.g., Sc, Al; e.g., Berry et al., 2005, 2007; Hauri et al., 2006; Blanchard et al., 2017; Tollan et al., 2017) and monovalent cations (e.g., Na; Tollan et al., 2018), although we observed no correlation between olivine H_2O_T and individual minor and trace elements as measured by EPMA for isobaric experiments in this study.

Contrary to our experimental data, melt H_2O_T concentration, which is directly related to fH_2O, and olivine H_2O_T concentration for high pressure $D_{H_2O_T}^{ol/melt}$ experiments from the literature are not co-variant (Fig. 5.11c). In particular, the experiments of Hauri et al. (2006), Aubaud et al. (2004), Koga et al. (2003), and Adam et al. (2016) are offset to higher values than would be predicted from the fit to our data. This offset as well as the scatter in olivine H_2O_T concentrations with melt H_2O_T concentrations for high pressure experiments can likely be attributed to changes in defect stability in the olivine structure. The interplay between temperature, pressure, and their inter-related parameters, such as fH_2O of a pure fluid (Table 5.1), make it difficult to parameterize variations in the concentration of any given point defect. However, it is likely that the point defect concentrations in olivine vary at the elevated temperatures (≤ 1500 °C) and pressures (1 – 3 GPa) of the high pressure $D_{H_2O_T}^{ol/melt}$ experiments relative to our low-pressure experiments. For example, for forsterite and Fe-bearing olivine, it has been shown that H is primarily incorporated as 2 H^+ into Mg^{2+} defects at low pressures (≤ 300 MPa; e.g., Zhao et al., 2004) whereas incorporation as 4 H^+ in Si^{4+} defects dominates at high pressures (> 1 GPa; Fei and Katsura, 2020; references therein). For decreasing activity of H_2O (i.e., increasing H_2O-undersaturation), it is expected that the proportion of H dissolved as 4 H^+ in a Si^{4+} defect will decrease relative to other substitution mechanisms (Tollan et al., 2017). Similarly, if differences in vibrational entropy are of minor importance (Walker et al., 2007), then an increase of temperature should favor substitution mechanisms with higher configurational entropy (Tollan et

al., 2017). Therefore, at increasing temperatures H^+ preferentially substitutes coupled to trivalent cations relative to 2 H^+ substituting for Mg^{2+} or 4 H^+ substituting for Si^{4+} (Tollan et al., 2017). Furthermore, studies of defect site-specific diffusion of H in olivine suggest that H^+ can diffuse across defect sites, potentially clouding the utility of treating the pairs of H^+ and clusters of 4 H^+ as individual units (e.g., Ferriss et al., 2018; Yang et al., 2019; Jollands et al., 2019). Beyond simple point defect mechanisms, prior experimental and analytical work has identified "humite-related" defects in olivine for which a hydrous phase, such as talc humite-series minerals, is incorporated in the olivine structure as inclusions, planar defects, or potentially point-defect complexes (e.g., Kitamura et al., 1987; Khisina et al., 2001; Mosenfelder et al., 2006a). It has been proposed that "humite-related" defects are dominant at pressures < 2 GPa, with point defect mechanisms dominating at pressures > 2 GPa (J. Mosenfelder et al., 2006a,b). Unraveling the control of H incorporation in olivine for each defect would require careful infrared spectroscopy work for high pressure $D_{H_2O_T}^{ol/melt}$ experiments, however this is not possible for most studies due to small grain sizes in experimental run products. Overall, the offset and scatter in olivine H_2O_T concentration with melt H_2O_T concentration for high pressure experiments can reasonably be attributed to changes in olivine defect populations and equilibrium constants for H substitution in olivine defect sites.

5.6 Implications

5.6.1 Application to estimating the bulk H_2O_T of planetesimals

Several prior studies of the H_2O_T contents of meteoritic olivine, pyroxene, and feldspar have observed apparent disequilibrium for H_2O_T between the phases (Peterson et al., 2023b, accepted; Stephant et al., 2023). In these studies, the H_2O_T contents of olivine ≥ pyroxene ≥

feldspar, contrary to the experimentally determined relative partitioning of H_2O_T between the phases. We can re-evaluate apparent disequilibrium between olivine and clinopyroxene by directly comparing experimentally determined $D_{H_2O_T}^{ol/melt}$ and $D_{H_2O_T}^{cpx/melt}$ at 200 MPa as well $D_{OH}^{min/melt}$ for olivine and clinopyroxene. At 200 MPa, we have experimentally constrained $D_{H_2O_T}^{ol/melt}$ to 0.0005±0.0002, which is approximately an order of magnitude lower than $D_{H_2O_T}^{cpx/melt}$ (0.008±0.001; 1 std. dev.; Sarafian et al., 2019). Similarly, the constant $D_{OH}^{ol/melt}$ (0.0012±0.0002; 1 std. dev.) found in this study is approximately an order of magnitude lower than the $D_{OH}^{cpx/melt}$ value (0.05) from Adam et al. (2016). Together, these comparisons reinforce the observation of apparent disequilibrium with respect to H_2O_T, as assessed by experiments at terrestrial conditions. At face value, this suggests that equilibrium melting models cannot be used to calculate bulk parent body H_2O_T contents. However, it remains possible that the observed relative partitioning of H_2O_T in meteoritic olivine, pyroxene, and feldspar represents equilibrium due to a lack of constraints at sufficiently low fO_2 (Righter et al., 2020), highly H_2O-undersaturated conditions, and on appropriate bulk compositions.

5.6.2 Application to magma decompression rates

The relationships between olivine H_2O_T, melt H_2O_T, and pressure (i.e., $D_{H_2O_T}^{ol/melt}$ and pressure) are important parameters for constraining magma decompression rates (Peslier and Luhr, 2006; Demouchy et al., 2006; Ferriss et al., 2018; Newcombe et al., 2020). Prior studies have assumed a constant $D_{H_2O_T}^{ol/melt}$ value, which, to a first order, may be a reasonable assumption given that our experimental results are broadly consistent with the constant 0.5 – 3 GPa $D_{H_2O_T}^{ol/melt}$ value from Towbin et al. (2023). However, for pressures relevant to magma ascent from shallow

magma chambers, our experimental results suggest that $D_{H_2O_T}^{ol/melt}$ is variable and increases with decreasing pressure and melt H_2O_T. Allowing $D_{H_2O_T}^{ol/melt}$ to vary with melt H_2O_T or pressure may result in consistently lower estimates for magma decompression rates than constant $D_{H_2O_T}^{ol/melt}$ models. To assess the effect of a variable $D_{H_2O_T}^{ol/melt}$ on magma decompression rates, we apply our square root relation (hereafter the "square root relation") for H_2O_T between olivine and melt (Fig. 5.6) to sample Seguam-ol1 from Newcombe et al. (2020). Using the 1-D diffusion model of Newcombe et al. (2020), assuming no uncertainty in $D_{H_2O_T}^{ol/melt}$, an initial pressure of 320 MPa, and a final pressure of 1 bar, we calculate magma decompression rates for Seguam-ol1 using the square root relation and a constant $D_{H_2O_T}^{ol/melt}$ = 0.00052 (Fig. 5.12). We find that the median magma decompression rate calculated using the square root relation (0.031 MPa/s) is ~ 3× slower than the median magma decompression rate calculated using a constant $D_{H_2O_T}^{ol/melt}$ (0.086 MPa/s). We note that the median decompression rate for the model using the square root relation (0.031 MPa/s) is within uncertainty of the model results from Newcombe et al. (2020) for Seguam-ol1 (0.039±0.017 MPa/s), who assume a variable $D_{H_2O_T}^{ol/melt}$ of 0.0005 to 0.0009, but is offset to a slightly lower central value. For decompression to 1 bar as modelled here, we find that the model using the square root relation produces a better fit to the Seguam-ol1 data than the model with a constant $D_{H_2O_T}^{ol/melt}$ value. The good fit of the model using the square root relation allows for equilibrium degassing to 1-bar, contrary to the assumptions of Newcombe et al. (2020) who assumed a fragmentation and quench pressure of 20 MPa to fit their 1-D diffusion model to their data. We note that magma fragmentation is predominantly thought to occur at some depth and pressure within the conduit, up to a few 10s of MPa depending on magma

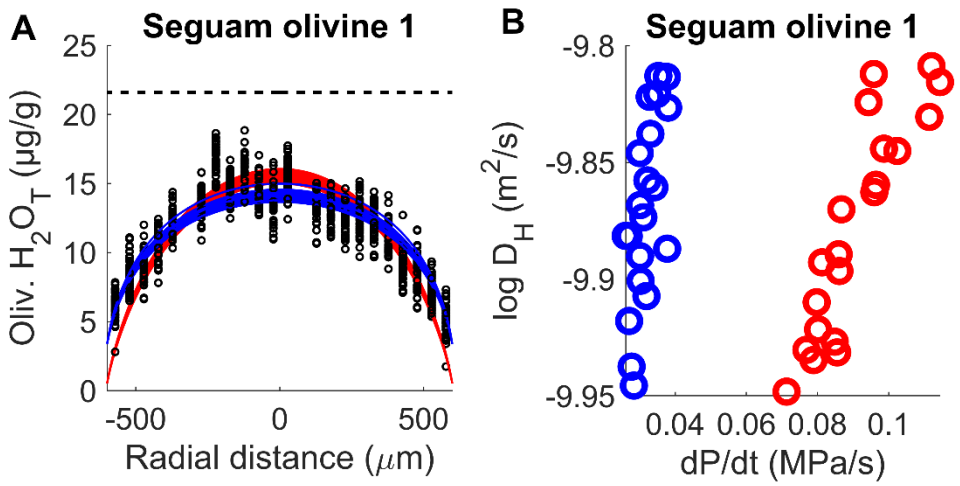

Fig. 5.12 a) Modeled fit to the measured H diffusion profile for Seguam-ol1 from Newcombe et al. (2020) using a constant $D_{H_2O_T}^{ol/melt}$ = 0.00052 (Red) and the square root relation (see text; blue). The horizontal dashed line is the modeled initial H_2O_T concentration at the center of the grain. b) Choice of diffusivity of H in olivine plotted against the calculated magma decompression rate (dP/dt) for the 1-D model of Newcombe et al. (2020) using a constant $D_{H_2O_T}^{ol/melt}$ = 0.00052 (Red) and the square root relation (see text; blue). Each model was run a total of 20 times.

viscosity and conduit geometry (e.g., Papale, 1999; Gonnermann and Manga, 2007; Gonnermann, 2015), potentially validating the assumption of Newcombe et al. (2020). Overall, our modelling results emphasize the need for careful choice of $D_{H_2O_T}^{ol/melt}$ when modelling magma decompression rates and that prior estimates for magma decompression rates based upon H diffusion in olivine may be slightly overestimated. Furthermore, our results permit equilibrium degassing of olivine to pressures of 1-bar, relaxing the need to invoke magma fragmentation at depth.

5.6.3 Summary and conclusions

We have measured the H_2O_T contents of experimentally derived olivine and glass at pressures ranging from 10 – 200 MPa. These data were used to provide the first constraints on $D_{H_2O_T}^{ol/melt}$ at H_2O-saturated conditions and pressures below 500 MPa. We find that $D_{H_2O_T}^{ol/melt}$

decreases with pressure for the conditions of our experiments, contrary to predictions of a constant (Towbin et al., 2023) or increasing (Novella et al., 2014; Adam et al., 2016) $D_{H_2O_T}^{ol/melt}$ value with pressure. The decrease of $D_{H_2O_T}^{ol/melt}$ with pressure over our experimental conditions is reasonably explained by a control of fH$_2$O or H speciation in the melt. In turn, this may imply that H speciation in the melt may exert a primary control on the partitioning of H_2O_T between melt and nominally anhydrous minerals (e.g., olivine, pyroxene, feldspar) by analogy to olivine and pyroxene (this study; Adam et al., 2016). We also find that differences in the extrinsic defect population (i.e., composition) of olivine grains exert some control on H_2O_T solubility in olivine. Overall, we suggest that fH$_2$O, the speciation of H in the melt, and the extrinsic defect population of olivine exert major controls on the partitioning of H_2O_T between olivine and melt.

Chapter 6: Conclusions

6.1 Summary and Key Findings

In this dissertation, I used *in situ* measurements of H in meteorites to characterize planetesimal bulk H contents, including the first constraints on incompletely melted planetesimals, and I conducted experiments to provide the first constraints on H partitioning between olivine and melt at low pressures (< 0.5 GPa). In Chapter 2, I measured the H contents of nominally anhydrous minerals (NAMs; e.g., olivine, pyroxene, feldspar) in aubrites, a group of meteorites derived from highly reduced, wholly melted planetesimals that are likely derived from enstatite chondrite-like materials. I used the measured H contents of aubrite NAMs in conjunction with published evaluations of their modal mineralogy to calculate bulk H contents and compared these values to prior bulk H analyses. In Chapters 3 and 4, I measured the H contents of meteoritic NAMs from the ureilite group and the acapulcoite-lodranite clan. I combined these measurements with simple petrogenetic models to provide the first estimates of the bulk H contents of incompletely melted planetesimals (i.e., primitive achondrite parent bodies). In Chapter 5, I used molybdenum-hafnium-carbide (MHC) cold-seal pressure vessels to conduct the first experiments that constrain the partitioning of H between olivine and melt at low pressures (< 0.5 GPa) and H_2O-saturated conditions. Key findings are summarized below:

1. **Measurements of bulk H on meteorites are prone to significant contamination due to inclusion of terrestrial contamination and terrestrial alteration phases.** The modal mineralogy and NAMs H contents of aubrites were combined with equilibrium partition coefficients to calculate the bulk H contents of individual meteorites. For the Norton County aubrite, my *in situ* measurements of H in enstatite and calculated bulk H contents are several orders of magnitude lower than bulk H measurements from Piani et al. (2020).

The discrepancy between *in situ* and bulk H measurements for Norton County are best accounted for by inclusion of terrestrial contamination (e.g., organics and adsorbed water) and common terrestrial alteration phases. This may in turn imply that the concurrent measurements of enstatite chondrites from Piani et al. (2020) reflect pervasive terrestrial contamination and alteration; however, further work is required to test this hypothesis.

2. **Incompletely melted planetesimals are nearly anhydrous.** Measurements of H concentrations in NAMs and quenched melts from ureilite group and acapulcoite-lodranite clan meteorites were combined with simple petrogenetic models to provide the first estimates of the H budget of incompletely melted planetesimals. I found that incompletely melted planetesimals have < a few 10's of μg/g H_2O_T (total H quantified as H_2O), requiring loss of > 99% of H_2O_T relative to primitive precursor materials (e.g., chondrites) prior to or at the onset of planetesimal melting. This further requires Earth's H budget to be accounted for by thermally primitive and/or ice-rich materials (e.g., chondrites, comets).
3. **The partitioning of H between olivine and melt is primarily dependent upon the speciation of H in the melt.** Using MHC cold-seal pressure vessels, I conducted the first study of olivine-melt H partitioning at low pressures (< 0.5 GPa) and H_2O-saturated conditions. I found, contrary to extrapolations from high pressure (≥ 0.5 GPa) experiments, that the olivine-melt total H partition coefficient decreases with increasing pressure for pressures ≤ 200 MPa. We find that the relationship between the olivine-melt total H partition coefficient and glass total H contents can be reproduced by a constant

olivine-melt OH partition coefficient, consistent with the speciation of H in the melt exerting a dominant control on the partitioning of H in olivine for our experiments.

6.2 Future Work

This dissertation has provided an initial evaluation of the bulk H contents of incompletely melted planetesimals; however, the existing data set does not sample all groups of primitive achondrites and is restricted to planetesimals derived from the inner solar system. A logical continuation of this work would be to measure the H contents of NAMs and phosphates in meteorites from the winonaite-SLm group, brachinites, and tissemouminites which represent uncharacterized incompletely melted planetesimals from the inner solar system. Similarly, measurements of H in NAMs from the tafassite grouplet should be conducted to characterize the H budgets of incompletely melted planetesimals that formed in the outer solar system (Ma et al., 2022; Jiang et al., 2023). A necessary step to robustly evaluate the sources of H in early-formed planetesimals is establishing H isotopic standards for olivine, pyroxene, and feldspar with low total H contents (less than a few 10's of μg/g H_2O_T). Currently, H isotopic analyses of meteoritic NAMs are calibrated against pyroxene standards with ~ 200 μg/g H_2O_T (e.g., Stephant et al., 2023) with no evaluation of matrix effects due to analyte composition or H_2O_T concentration, which have been shown to constitute matrix effects for H isotope analyses in silicate glasses (e.g., Hauri et al., 2006). Prior work has shown that closed-system partial melting of lherzolite results in small (~10 ‰) H isotopic fractionations for mantle melts (Bindeman et al., 2012). If H isotopes remain unfractionated between minerals and melts, then silicate melts in equilibrium with low H_2O_T NAMs may be used to constrain the H isotopic composition of NAMs (Hui et al., 2017). Therefore, the H isotopic composition of low H_2O_T NAM standards may be established

from natural or synthetic samples in equilibrium with a silicate glass of known H isotopic composition.

Beyond meteoritic studies, there are significant uncertainties surrounding the H concentration and isotopic compositions of Earth's transition zone, lower mantle, and core. Prior studies of the H isotopic composition of rocks related to deep-seated mantle plumes (e.g., komatiites, ocean island basalts, flood basalts) suggest material from the deep mantle can sample many H reservoirs in Earth's interior. For example, komatiites are thought to entrain subduction related H from the mantle transition zone (Sobolev et al., 2016, 2019; Asafov et al., 2018), similar to basalts from the Emeishan large igneous province (Chen et al., 2023), and ocean island basalts (OIBs) have been suggested to sample a primitive nebular H reservoir in the lower mantle (Hallis et al., 2015) or H from the ambient upper mantle (Craig and Lupton, 1976; Poreda et al., 1986; Loewen et al., 2019). Further work should be carried out on kimberlites, which are hydrous low-degree partial melts derived from the asthenospheric mantle and are frequently attributed to depths at or below the mantle transition zone. Therefore, kimberlites may preserve the H isotopic signature of the mantle transition zone. Ideally, this work would be paired with analyses of high-pressure phases derived from the transition zone and included in diamonds, although appropriate samples are exceedingly rare. Similarly, further work should be done studying the H-He-O-Cl-W composition of OIBs, with *in situ* analyses of H-O-Cl isotopes in melt inclusions to limit the effects of degassing and equilibration with secondary fluids. Under the assumption that the OIB source mantle has a distinct H isotopic composition from the core, a combined isotopic study of this nature may provide constraints on the H isotopic composition of the core if H isotopes are coupled to He and W, which may be partially derived from Earth's

core (e.g., Mundl-Petermeier et al., 2020). Similarly, combined analyses of H-O-Cl isotopes may be used to evaluate for assimilation or entrainment of seawater or slab-derived fluids.

In addition to studies evaluating the abundance and source(s) of H in early-formed planetesimals, additional work is required to constrain the partitioning of H between NAMs and melt at conditions relevant to planetesimals and Earth's crust and mantle. As a complement to the above work, mineral-melt H partitioning experiments should be carried out at low pressures (<100 MPa), an fO_2 near the iron-wüstite fugacity buffer, and on chondritic bulk compositions that are all relevant to planetesimals. For terrestrial systems, a self-consistent set of NAM-melt H partitioning experiments that isolate fH_2O and H_2O-saturation should be conducted at pressures from ~10 MPa to 2 GPa, which represents the pressure range in which experimental melts can be quenched to vitreous glasses. For experiments at pressures ≤ 0.5 GPa, two experimental series are required, H_2O-saturated and highly H_2O-undersaturated. For experiments at pressures > 0.5 GPa, quenching at H_2O-saturation is difficult, therefore experiments at variably H_2O-undersaturated conditions can be used as a rough evaluation for the control of fH_2O. I recommend continued use of sample 82-72f from Medicine Lake, Volcano, CA as an experimental starting material as low pressure olivine-melt H partitioning data are now available (Chapter 5) and it has been the subject of several prior experimental studies (Bartels et al., 1991; Médard and Grove, 2008; O'Leary et al., 2010; Mitchell et al., 2017). I also recommend conducting mineral-melt H partitioning studies in systems with a mixed fluid phase (e.g., C-H, H-S, H-Cl, C-H-S) to evaluate the effect of other volatile elements on H partitioning in NAMs. Prior studies on H partitioning between olivine and melt for mixed C-H fluids suggest that the olivine-melt H partition coefficient is lower relative to pure H fluids (e.g., Sokol et al., 2013).

Similarly, correlations between H, F, and Cl solubilities have been found in silicate melts (Dalou and Mysen, 2015; Botcharnikov et al., 2015).

Overall, constraining the sources and distribution of H in the bulk Earth based upon the work outlined above will be maximized by: 1) further modelling efforts to constrain the distribution of planetesimals thermal types (e.g., unmelted, incompletely melted, wholly melted) that formed the Earth; 2) observations of nebular disks in Sun-like systems to constrain snow-line migration and icy-pebble drift (e.g., Notsu et al., 2016; Zhang et al., 2020; Owen, 2020; Miley et al., 2021); and, 3) models of volatile cycling and loss between planetary mantles and atmospheres with paired observations of exoplanets (e.g., Gillmann et al., 2020; Kite and Barnett, 2020; Moore and Cowan, 2020). I would also like to emphasize the importance of sample return missions, such as Hayabusa, Hayabusa2, and Osiris-REx, which provide pristine materials that can be used to constrain the H budgets and isotopic compositions of planetesimals. The necessity of analyzing pristine materials is best highlighted by the study of Yokoyama et al. (2022) who found that the bulk H contents of Ivuna-type chondrites may be overestimated by more than a weight percent based upon paired analyses of return samples from Ryugu and the Ivuna meteorite.

Appendix A: The H content of aubrites: An evaluation of bulk versus *in situ* methods for quantifying water in meteorites

A1) Miller Range 13004 albitic glass

Within one of our aliquots of Miller Range (MIL) 13004, we analyzed albitic glass which was commonly associated with fractures and voids and is present as a minor to trace phase. Prior work has identified albitic glasses in aubrites, including MIL 13004 (Wilbur et al., 2022), which is commonly interpreted as a product of partial melting on the aubrite parent body. We find higher SiO_2 (74 wt.% vs. 67.8 wt.%) and Al_2O_3 (21 wt.% vs. 17.9 wt.%) contents and much lower Na_2O (3.9 wt.% vs. 10.97 wt.%) contents in albitic glass from our aliquot of MIL 13004 albitic glass (Table 2.4) than the values reported by Wilbur et al. (2022). We suggest this discrepancy in major element compositions likely reflects heterogeneity in glass compositions between sample aliquots as our measured values resemble the L871 glass of Fogel (2005), but a systematic study on several aliquots is needed to validate this hypothesis. Overall, albitic melts in aubrites have been suggested to be the product of high degrees of partial melting (≤ 50%) and late-stage melts (Fogel, 2005; Keil et al., 2011). The H_2O contents (~0.6 – 3.3 µg/g) of the MIL 13004 albitic glass are below the LOD (see Section 2.4.2) and have highly variable F (~95 – 190 µg/g) and Cl contents (560 – 640 µg/g) that are consistent across the 01/22 and 02/22 analytical sessions (Table A3, analyses 483 – 491; Table A5, analysis 1034). The F contents of the albitic glass are about 1 to 2 orders of magnitude higher than all other analyzed phases and the Cl contents are several orders of magnitude higher (Table 2.5). The origin of these high halogen contents is unclear, but it may be the result of interaction with a halogen rich-fluid on the aubrite parent body, partial dissolution of halogen-rich sulfides such as djerfisherite, or terrestrial weathering and alteration (e.g., Krähenbühl et al., 1998; Velbel, 2014). If we are to consider

equilibrium with respect to H_2O between the albitic glass (~0.6 – 3.3 µg/g H_2O) and enstatite (5±2 µg/g H_2O; 1 SD) in MIL 13004, then we have a minimum apparent mineral-melt H_2O partition coefficient $\left(D = \frac{[H_2O]_{mineral}}{[H_2O]_{melt}}\right)$ of ~0.9, which is orders of magnitude higher than experimentally determined mineral-melt partition coefficients for enstatite (Grant et al., 2006) and orthopyroxene (e.g., Aubaud et al., 2004; Grant et al., 2007; Hauri et al., 2006). This either reflects disequilibrium between the minerals and the melt for H_2O or previously uncharacterized partitioning behavior for H_2O at low total H_2O contents or pressure, as has been suggested for natural and experimental samples (Sarafian et al., 2019; Peterson et al., 2023b). More experimental work is required to evaluate these possibilities. Nevertheless, we elect to exclude these values for the albitic glass as they may represent disequilibrium, could have low H_2O contents as the result of production as a high-degree or late-stage partial melt, and the estimates for glass H_2O contents based upon experimentally derived partition coefficients give a higher estimate (~1500 µg/g H_2O vs. < ~3.3 µg/g H_2O). Notably, if we were to use the measured value of MIL 13004 albitic glass in our estimates for the bulk H_2O contents of aubrites, our bulk estimates would be lowered in glass-bearing cases (see Sections 2.5.1.3 and 2.5.2), thereby not affecting our conclusions.

A2) Potential, non-NAM, carriers of H in aubrites

We analyzed H_2O in enstatite, forsterite, diopside, and plagioclase in aubrites. NAMs constitute >~99 vol. % of aubrites on average; however, it is possible that other minor or trace phases (e.g., glass, sulfides, or metal) could concentrate water and represent major contributions to aubrite water budgets despite their low abundances. We consider this possibility in the following section.

A2.1 Other silicate minerals

On average, aubrites are ~75 – 98 vol. % enstatite (Keil, 2010) and lack primary hydrous phases. Rare instances of secondary fluor-amphibole (Bevan et al., 1977; Graham et al., 1977) and roedderite (Hsu, 1998; Fogel, 2002), which may reflect igneous crystallization or a low temperature event, have been identified in aubrites. Notably, fluor-amphibole has only been identified in vugs in Mayo Belwa, an impact melt breccia, and is nearly end-member fluororichterite (Bevan et al., 1977; Graham et al., 1977; Rubin, 2010). Considering that vugs in Mayo Belwa are modestly abundant (< 5 vol. %), not all vugs contain fluor-amphibole, vugs commonly contain several phases (Rubin, 2010), the fluor-amphibole is nearly end-member fluororichterite, indicating the W position in the structure is composed almost entirely of F instead of OH, and fluor-amphibole has only been identified as a secondary phase in Mayo Belwa, it likely constitutes a negligible contribution to the bulk H_2O content of average aubritic materials. Due to the rarity and potentially secondary origin of amphibole in Mayo Belwa, we suggest it is likely not reflective of the H_2O content of average aubritic material. Despite being an end-member in the H_2O-bearing Milarite-type mineral group (Seifert and Schreyer, 1969; Gagné and Hawthorne, 2016), we do not consider roedderite (end-member empirical formula: $Na_{1.5}K_{0.5}Mg_{3.75}Fe^{2+}_{1.25}Si_{12}O_{30}$) as a major carrier of H_2O as: 1) there is no clear indication of H_2O in the roedderite structure (Forbes et al., 1972); and 2) the H_2O contents of Milarite-type minerals are poorly constrained and many species are anhydrous (Gagné and Hawthorne, 2016). Therefore, any primary H_2O (or other H-bearing species) in aubrites is likely to be hosted in NAMs, silicate glass, sulfides, and FeNi metal. For phases not analyzed in this study, we provide a first order estimate of their H_2O contents based upon our measured H_2O concentrations and experimentally determined partition coefficients.

A2.2 Silicate glass

We can provide a first order estimate of the H_2O content of unmeasured phases by assuming all unmeasured phases are in equilibrium with enstatite and that partition coefficients determined under terrestrial conditions are applicable to aubrite parent bodies (see Section A3). We select enstatite as our reference mineral instead of forsterite or feldspar as our phase average for enstatite is based upon 86 analyses across all seven aubrites investigated compared to 4 analyses for feldspar, and 3 analyses for forsterite. Using our measured enstatite H_2O contents and published partition coefficients (Dobson et al., 1995), we estimate that silicate glass in equilibrium with enstatite would contain ~1500 μg/g H_2O. If we instead use Shallowater plagioclase (24 μg/g H_2O) as our reference phase, then we estimate that silicate glass would contain ~628 μg/g H_2O (Lin et al., 2019). We note, that with the exception of a feldspathic clast in LAR 04316, silicate glass is absent or a trace phase in aubrites (Keil, 2010), thereby limiting the contribution of silicate glass to the H_2O budget of aubrites.

A2.3 Metals and sulfides

Previous studies have experimentally constrained the partitioning of H between metal and silicate and suggest that H is incompatible in Fe metal at low pressures (Okuchi, 1997; Li et al., 2015; Clesi et al., 2018; Malavergne et al., 2019; Tagawa et al., 2021; Gaillard et al., 2022). We are unaware of any studies that experimentally constrain sulfide – silicate H partitioning. Therefore, we assume that metal and sulfides have similar H_2O partition coefficients. By combining our measured enstatite, forsterite, diopside, and feldspar H_2O contents, calculated glass H_2O contents (Table 2.6), and the modal mineralogy of our samples (Table 2.2), we estimate that the silicate portions of our analyzed main group aubrites all contain < ~5 μg/g H_2O (Supplementary File "Aubs_calcs.xlsx"). We take a metal – silicate H partition coefficient of 0.22 (Gaillard et al., 2022) and our calculated silicate H_2O contents (~5 μg/g H_2O), which yield

metal and sulfide H_2O (quantified from total H) concentrations of ~1 μg/g. Metal and sulfides in aubrites are minor to trace phases (Keil, 2010), and the low estimated H_2O content (~1 μg/g H_2O) suggests metal and sulfide in aubrites are unlikely to be an abundant source of H_2O in aubrites. Overall, we suggest trace silicate material (Section A2.1), silicate glass (Section A2.2), and metals and sulfides are either too low in abundance or too H_2O poor to serve as major reservoirs of H_2O in aubrites.

A3) Do our H_2O analyses reflect equilibrium or disequilibrium in aubrite NAMs?

Despite experimentally determined partition coefficients permitting equilibrium between the phases measured in this study (Section 2.5.1.3), it is possible that the measured H_2O concentrations in NAMs have been disturbed by disequilibrium processes such as H-loss due to thermal metamorphism or shock heating or H-enrichment due to hydrothermal alteration. To a first order, if disequilibrium processes affected our grains, we would expect to observe gradients in H_2O concentrations across grains, however, for samples where transects could be measured (i.e., MIL 13004, Norton County, Shallowater), no H_2O gradients are observed (Fig. A12 – A16). Aubrite enstatite H_2O contents exhibit a weak correlation with degree of shock (Fig. 2.2B), which may suggest that aubrite H_2O contents could have been modified by secondary processes. Notably, any thermal process (e.g., shock heating, thermal metamorphism) would be expected to reduce the H_2O content of aubrite silicates, resulting in normal zonation, which is not observed. Therefore, we suggest that H-loss processes such as thermal metamorphism or shock heating are unlikely to have caused major modifications to the measured H_2O contents of our NAMs. It is also possible that aubrite silicates may have undergone H-enrichment during hydrothermal events. However, hydrous phases are rare in aubrites and are of an unclear origin (see Section 2.5.3.1; Keil, 2010), arguing against any widespread hydrothermal events on aubrite parent

bodies. Overall, we suggest that the effect of secondary processes on the measured H_2O concentrations is likely minimal. Furthermore, regardless of whether or not our analyses reflect equilibrium, our analyses represent the most accurate determination of aubrite silicate H_2O contents, allowing for more precise evaluations of bulk Aubrite H_2O contents and the potential for H-delivery to the Earth by aubrite-like material.

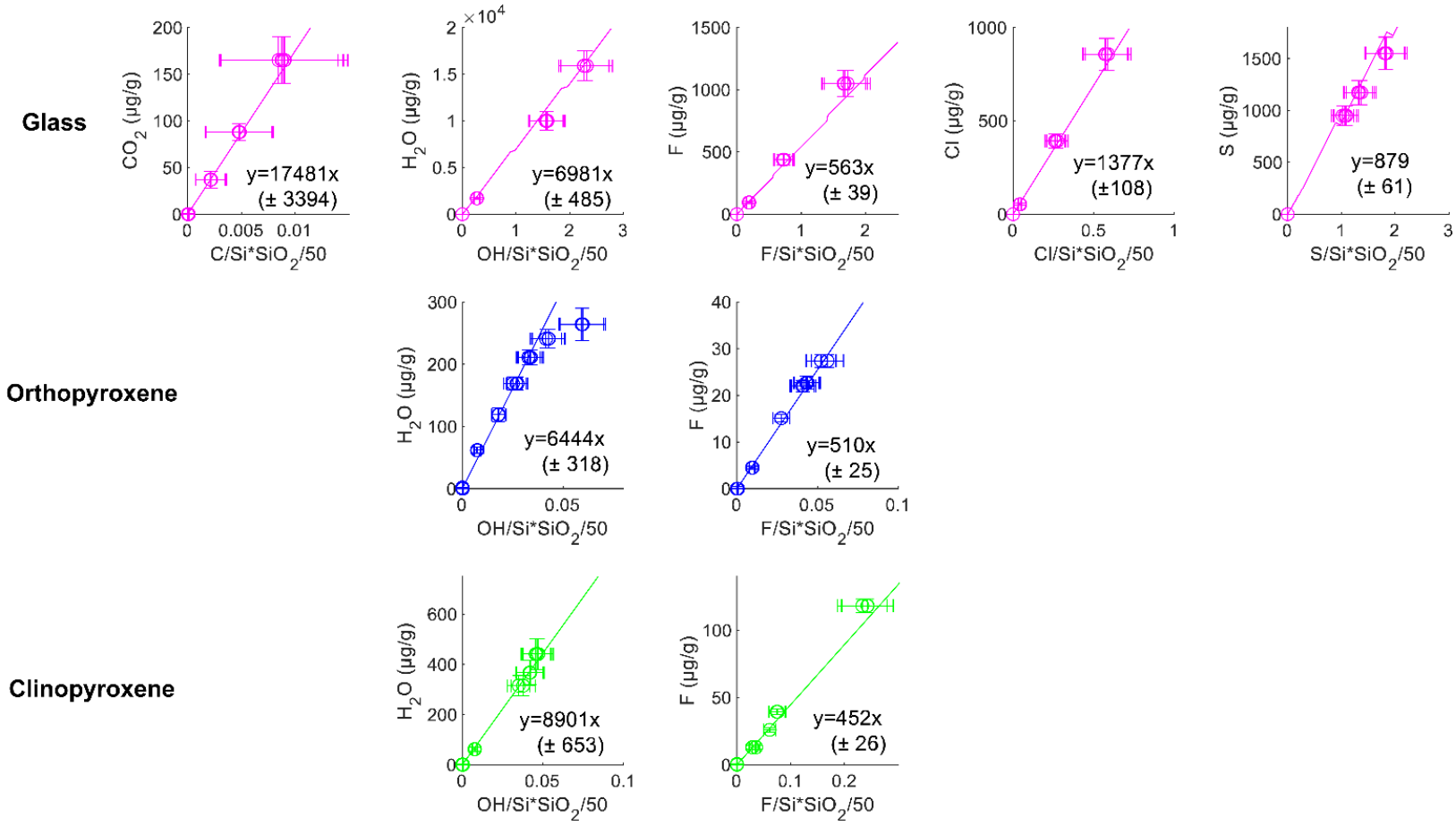

Fig. A1) Calibration curves for CO_2, H_2O, F, Cl, and S for glass, orthopyroxene, and clinopyroxene in the 01/22 analytical session. Uncertainties on slopes were determined using a York regression (York et al., 2004; Wiens, 2021).

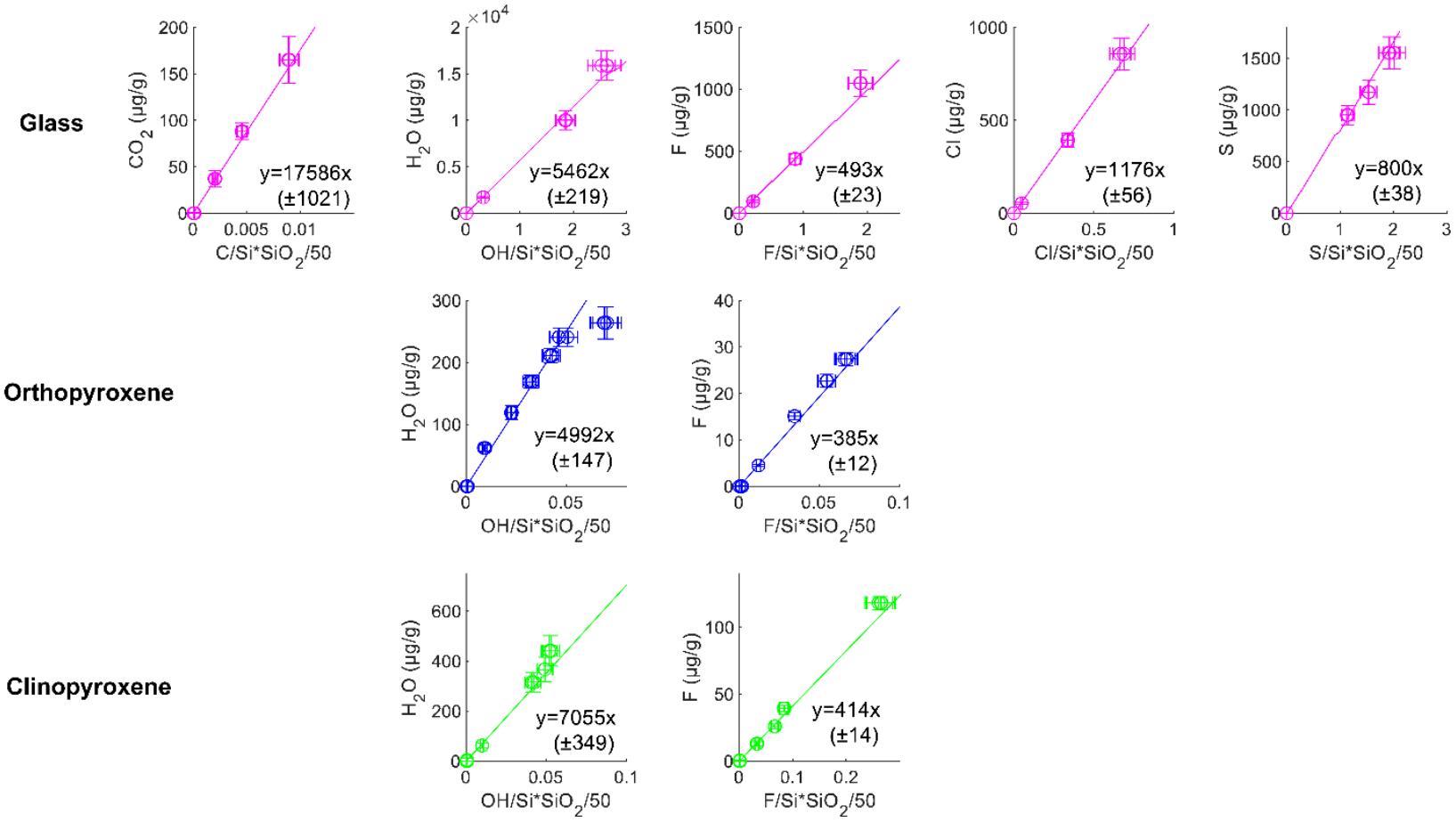

Fig. A2) Calibration curves for CO_2, H_2O, F, Cl, and S for glass, orthopyroxene, and clinopyroxene in the 02/22 analytical session. Uncertainties on slopes were determined using a York regression (York et al., 2004; Wiens, 2021).

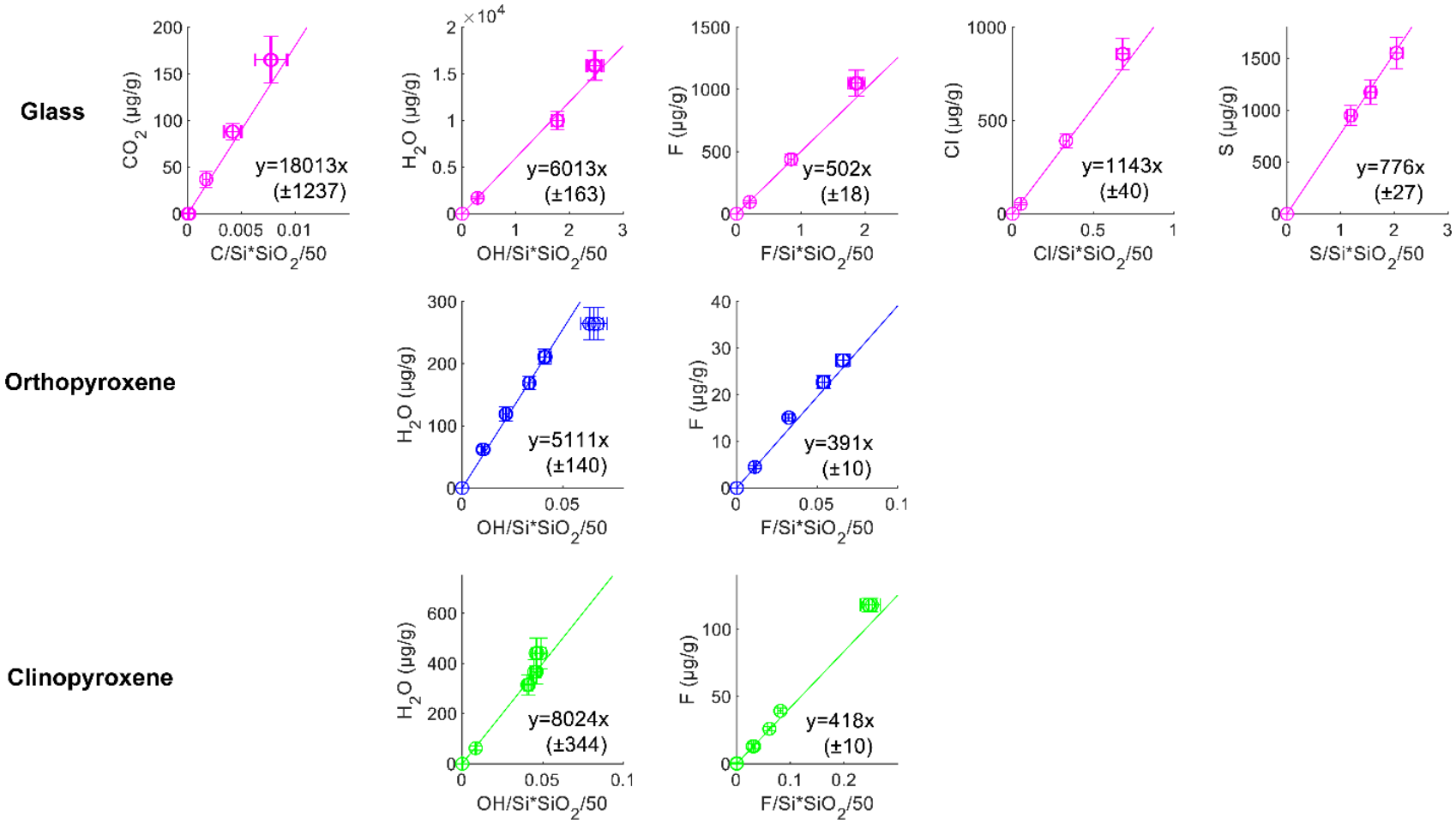

Fig. A3) Calibration curves for CO_2, H_2O, F, Cl, and S for glass, orthopyroxene, and clinopyroxene in the 08/22 analytical session. Uncertainties (indicated in parentheses) on slopes were determined using a York regression (York et al., 2004; Wiens, 2021).

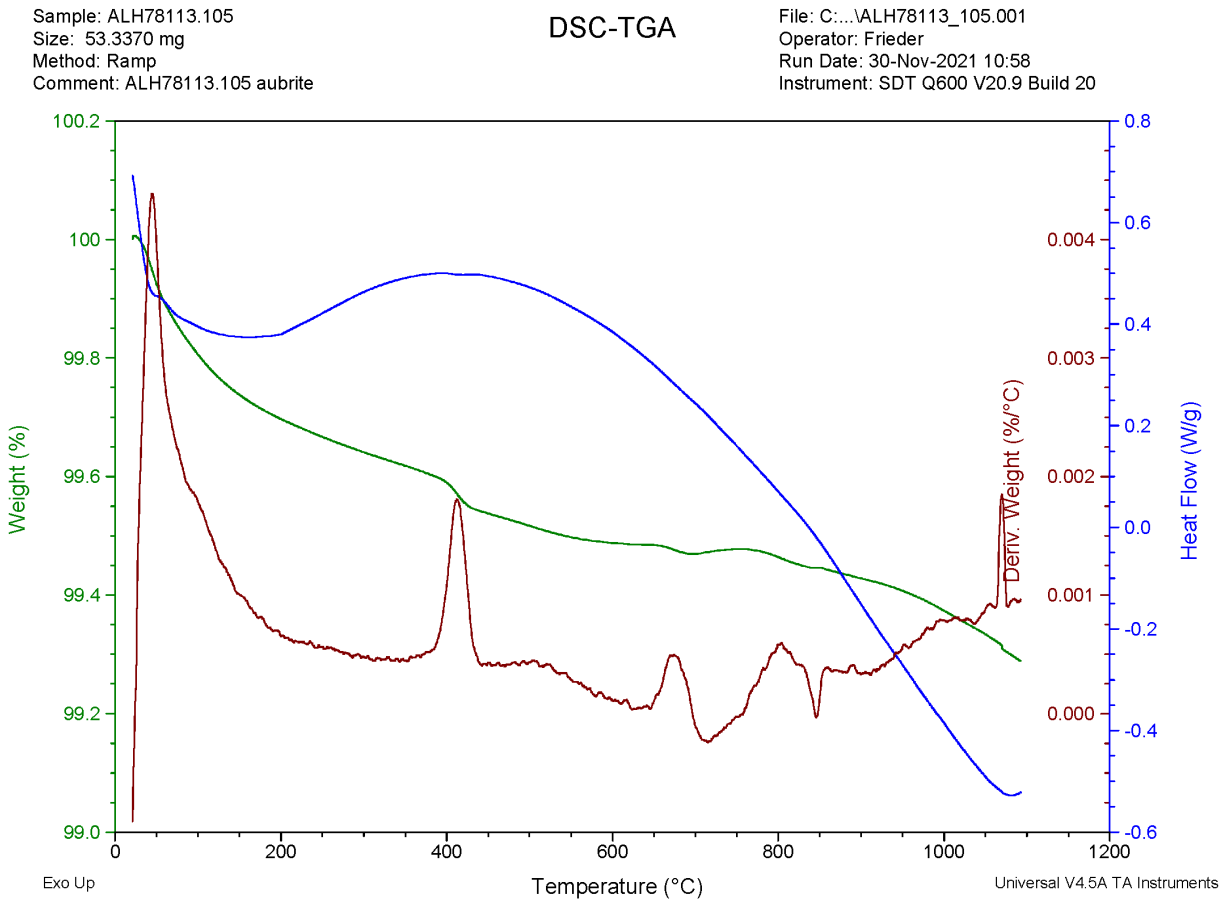

Fig. A4) Mass thermogram for sample ALH 78113. The green line represents mass loss in weight %. The red line represents the first derivative of the mass loss curve. The blue line represents the heat flow throughout the mass loss analysis.

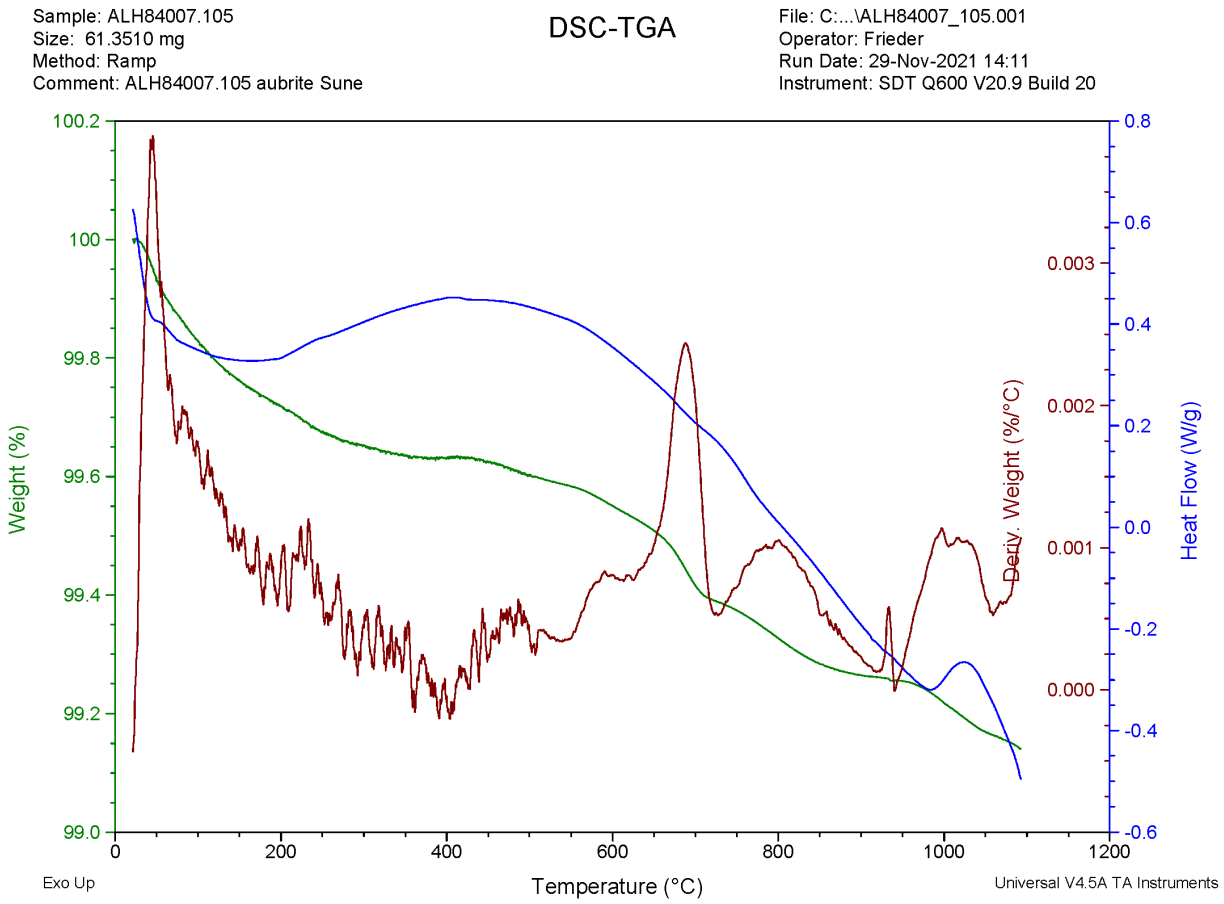

Fig. A5) Mass thermogram for sample ALH 84007. The green line represents mass loss in weight %. The red line represents the first derivative of the mass loss curve. The blue line represents the heat flow throughout the mass loss analysis.

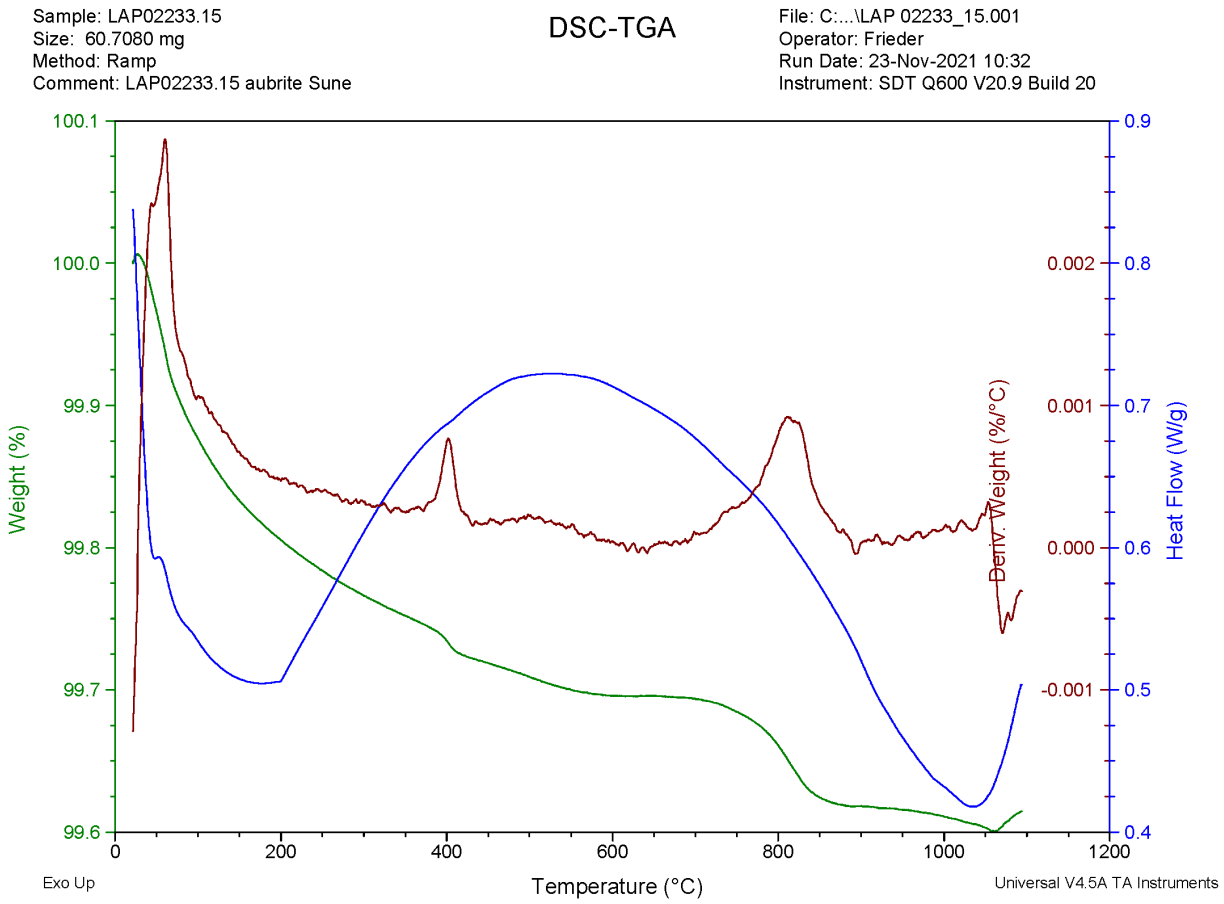

Fig. A6) Mass thermogram for sample LAP 02233. The green line represents mass loss in weight %. The red line represents the first derivative of the mass loss curve. The blue line represents the heat flow throughout the mass loss analysis.

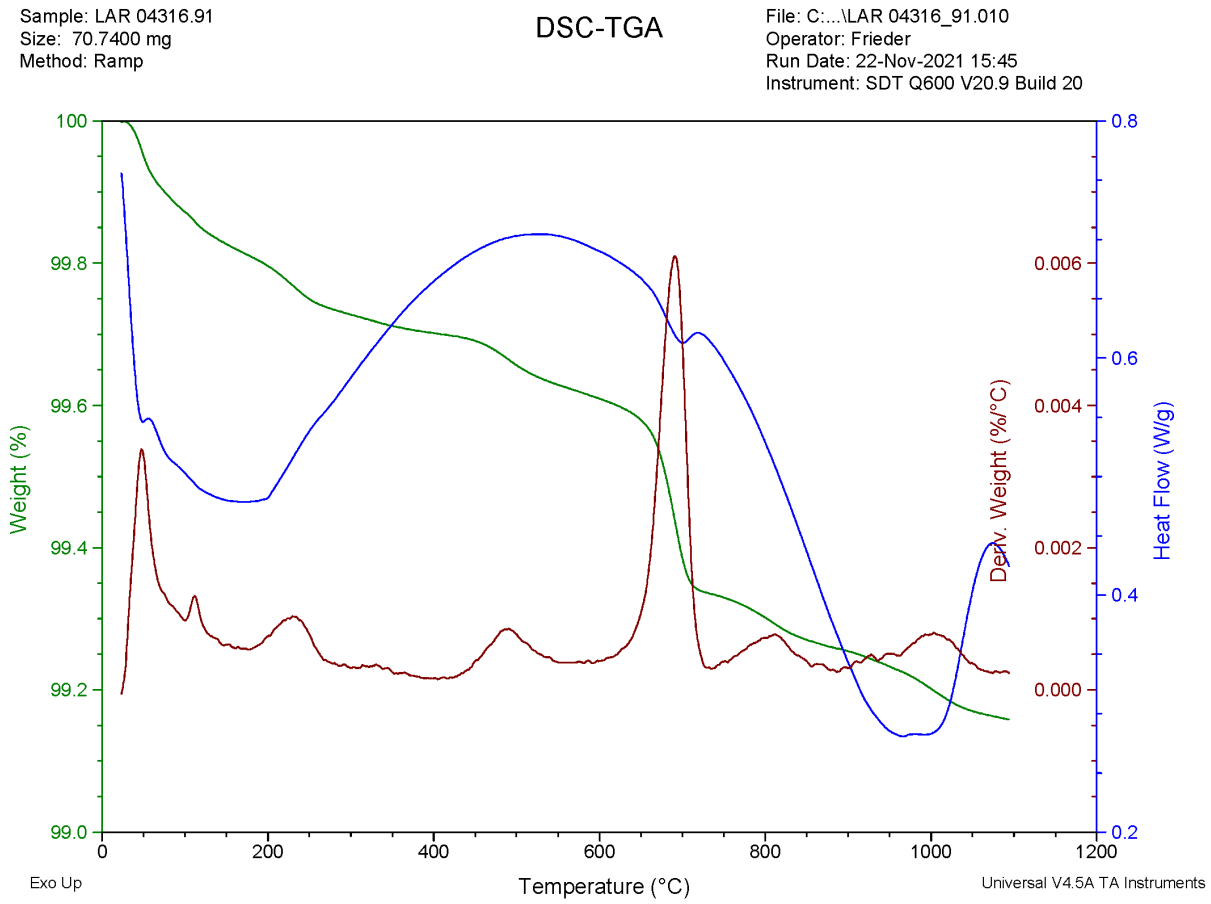

Fig. A7) Mass thermogram for sample LAR 04316. The green line represents mass loss in weight %. The red line represents the first derivative of the mass loss curve. The blue line represents the heat flow throughout the mass loss analysis.

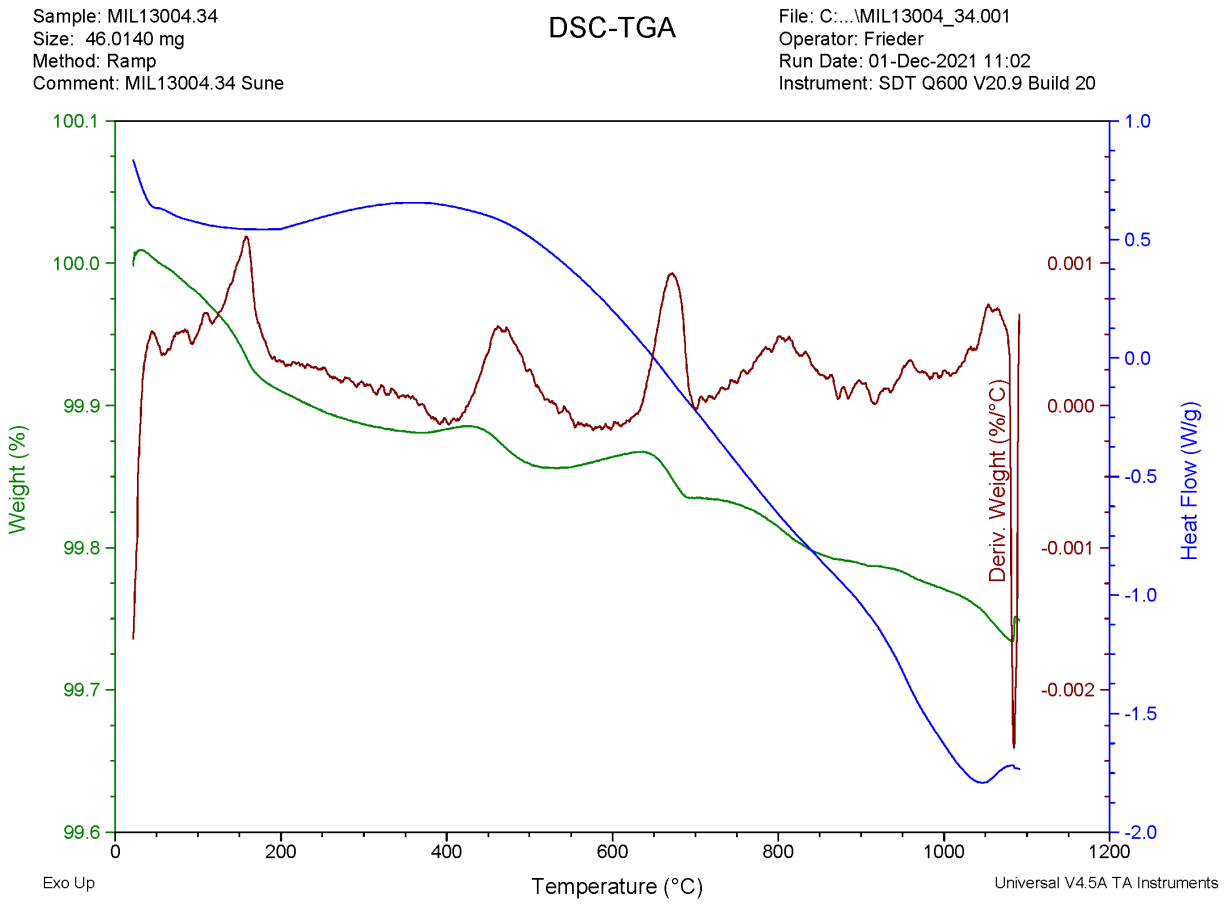

Fig. A8) Mass thermogram for sample MIL 13004. The green line represents mass loss in weight %. The red line represents the first derivative of the mass loss curve. The blue line represents the heat flow throughout the mass loss analysis.

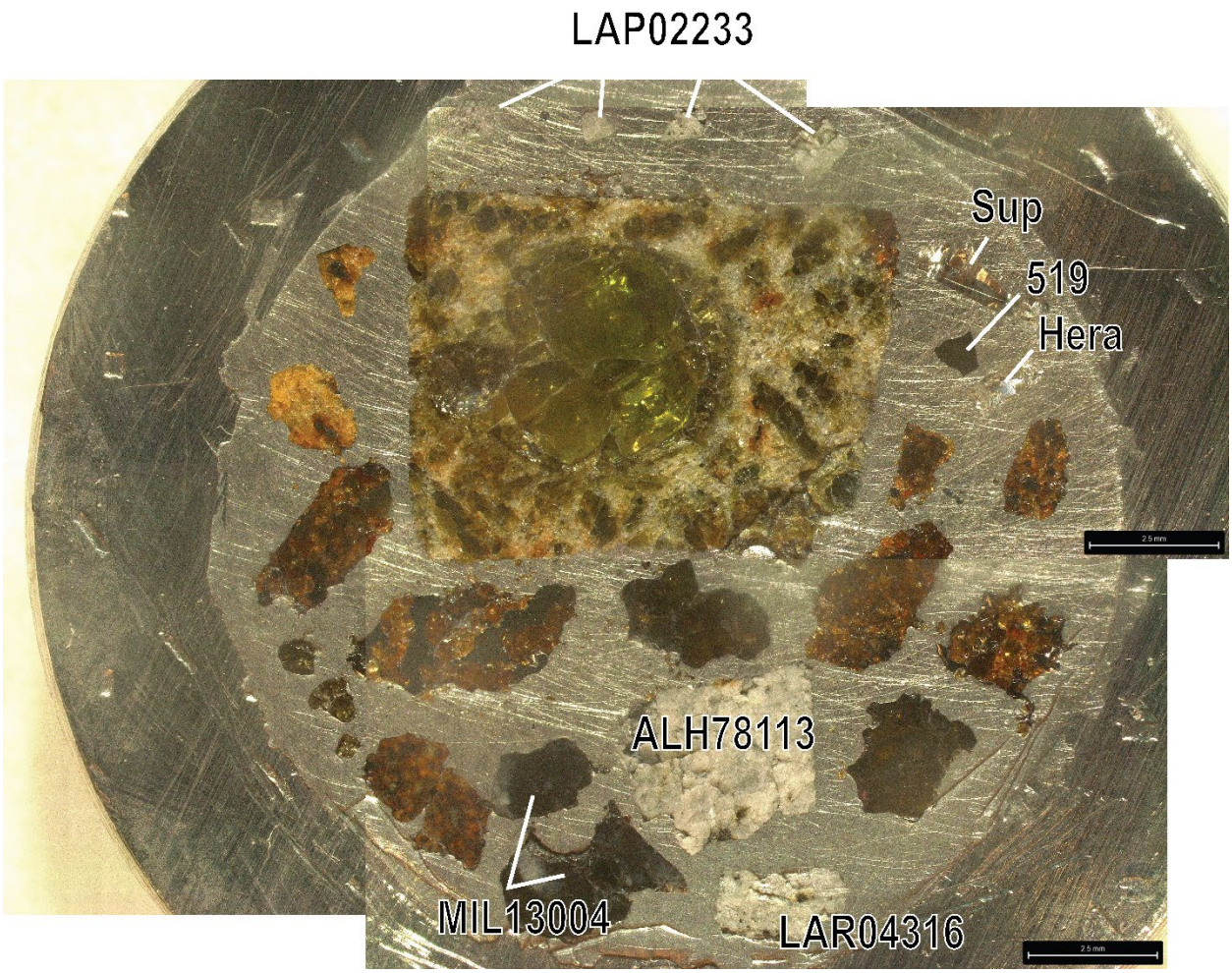

Fig. A9) Reflected light mosaic of 1 inch indium mount containing aubrite samples analyzed as part of this study. Unlabelled samples were not analyzed as part of this study. Scale bars are 2.5 mm.

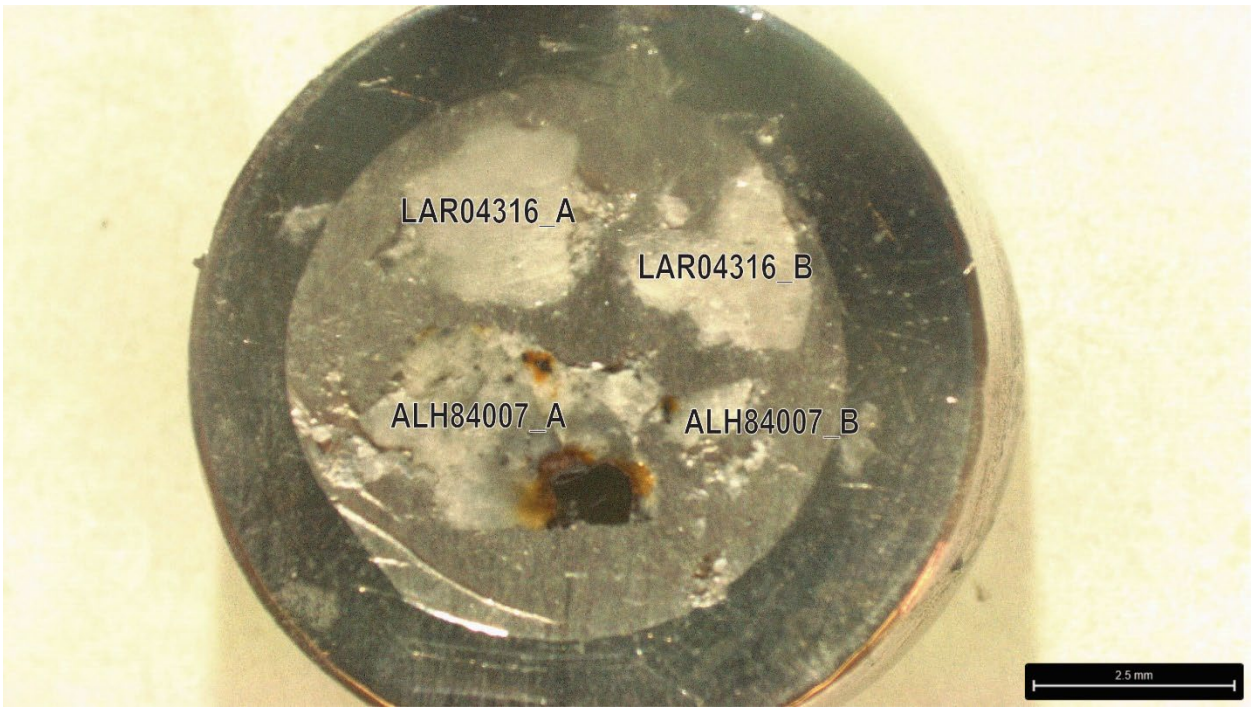

Fig. A10) Reflected light image of 10 mm indium mount holding additional chips of LAR 04316 and ALH 84007. Subsamples are denoted with "_A" and "_B". The scale bar is 2.5 mm.

Fig. A11) Reflected light image of 1 inch indium mount holding Norton County and Shallowater. The three small holes held the secondary standards Suprasil 3002, Herasil, and ALV-519-4-1 glass. The large hole held a sample that was not used in this study.

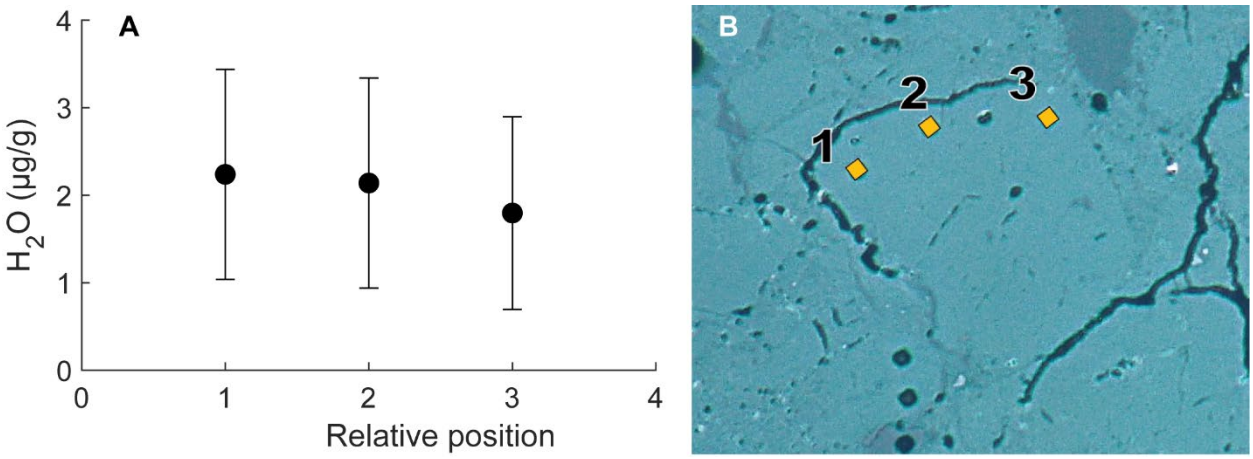

Fig. A12) NanoSIMS transects analyzed for H_2O from grain MIL 13004L-4. A) H_2O concentrations plotted against the relative position of SIMS pits as shown in B). Plotted uncertainties are the propagated uncertainty (Table S3). B) Reflected light image of MIL 13004L-4 showing SIMS pits from A) highlighted in orange and labelled. Note, SIMS pits are 15×15 µm. The image has a blue tint due to the light used on the microscope and polarizers. Unmarked SIMS pits are associated with other grains or were removed by the data filtering protocol (Section 3.3).

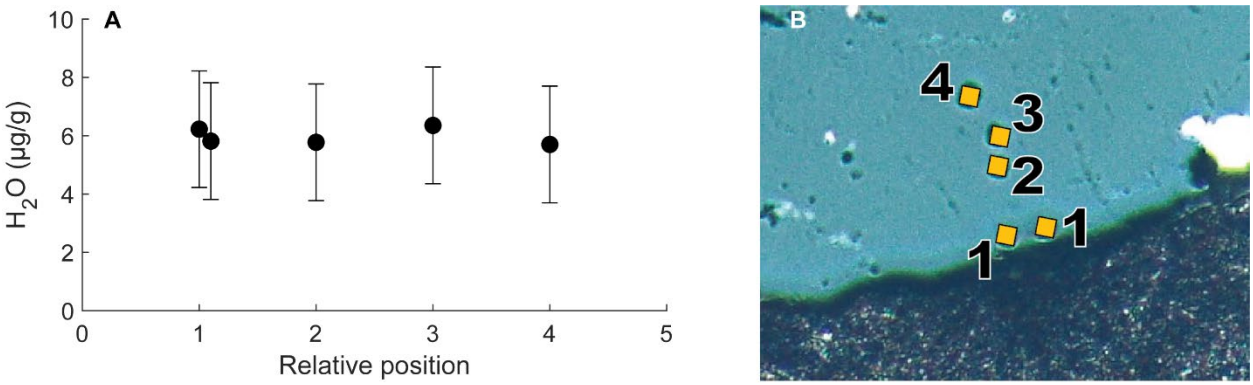

Fig. A13) NanoSIMS transects analyzed for H_2O from grain MIL 13004U-1. A) H_2O concentrations plotted against the relative position of SIMS pits as shown in B). Overlapping points were measured at the same approximate distance from the edge of the grain and represent "duplicate" analyses. Plotted uncertainties are the propagated uncertainty (Table S3). B) Reflected light image of MIL 13004U-1 showing SIMS pits from A) highlighted in orange and labelled. Note, SIMS pits are 15×15 µm. The image has a blue tint due to the light used on the microscope and polarizers.

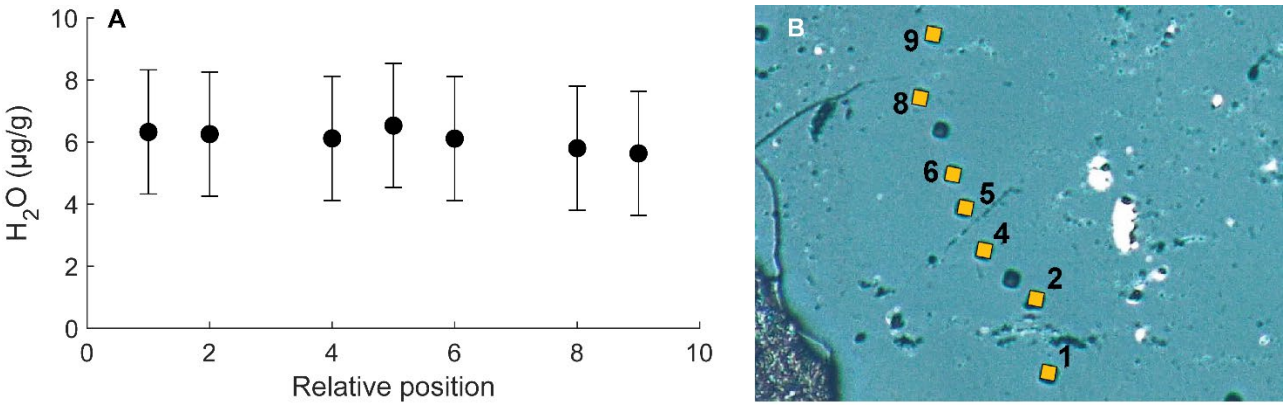

Fig. A14) NanoSIMS transects analyzed for H_2O from grain MIL 13004U-2. A) H_2O concentrations plotted against the relative position of SIMS pits as shown in B). Plotted uncertainties are the propagated uncertainty (Table S3). B) Reflected light image of MIL 13004U-2showing SIMS pits from A) highlighted in orange and labelled. Note, SIMS pits are 15×15 µm. The image has a blue tint due to the light used on the microscope and polarizers. Unmarked SIMS pits are associated with other grains or were removed by the data filtering protocol (Section 3.3).

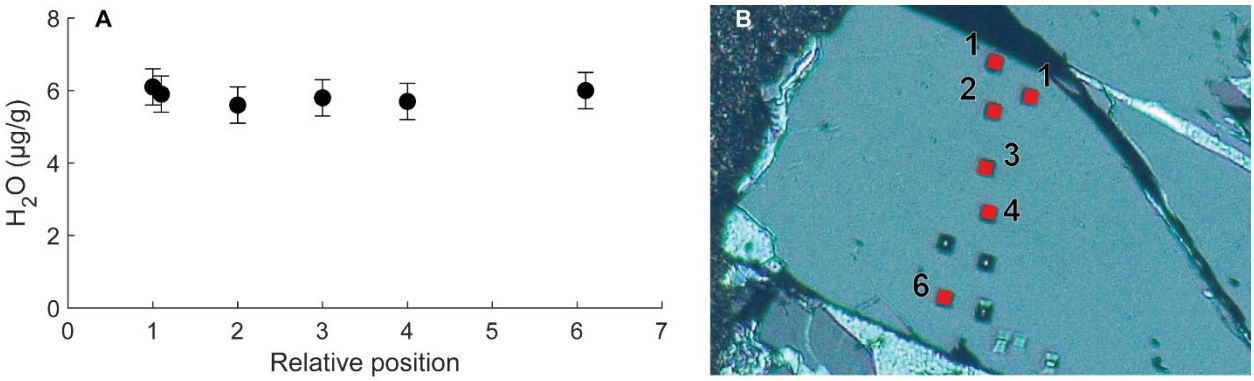

Fig. A15) NanoSIMS transects analyzed for H_2O from grain Shallowater-pyx1. A) H_2O concentrations plotted against the relative position of SIMS pits as shown in B). Overlapping points were measured at the same approximate distance from the edge of the grain and represent "duplicate" analyses. Plotted uncertainties are the propagated uncertainty (Table S7). B) Reflected light image of Shallowater-pyx1 showing SIMS pits from A) highlighted in red and labelled. Note, SIMS pits are 15×15 µm. The image has a blue tint due to the light used on the microscope and polarizers. Unmarked SIMS pits are associated with other grains or were removed by the data filtering protocol (Section 3.3).

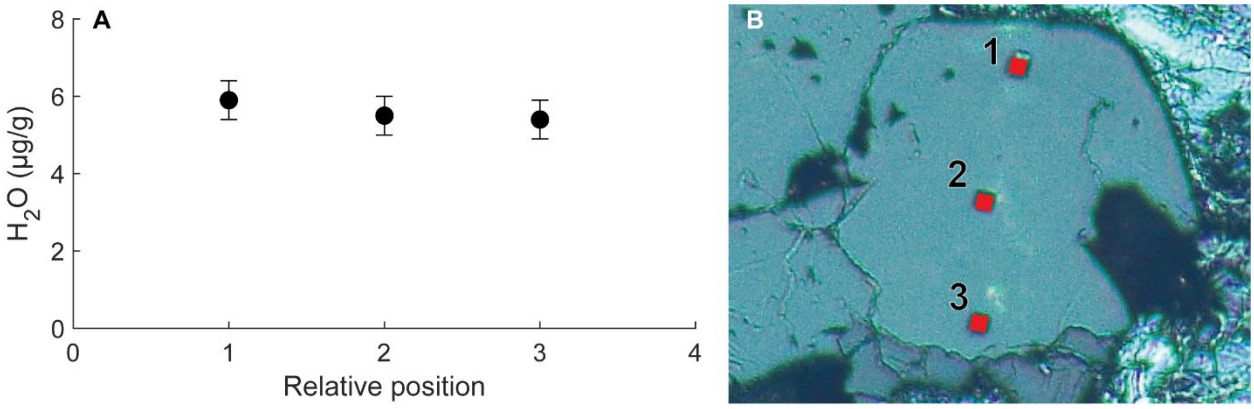

Fig. A16) NanoSIMS transects analyzed for H_2O from grain Shallowater-pyx4. A) H_2O concentrations plotted against the relative position of SIMS pits as shown in B). Overlapping points were measured at the same approximate distance from the edge of the grain and represent "duplicate" analyses. Plotted uncertainties are the propagated uncertainty (Table S7). B) Reflected light image of Shallowater-pyx4 showing SIMS pits from A) highlighted in red and labelled. Note, SIMS pits are 15×15 µm. The image has a blue tint due to the light used on the microscope and polarizers.

Appendix B: The H_2O content of the ureilite parent body

B1) Applicability of partition coefficients determined under terrestrial conditions

An assumption of the calculations performed in this manuscript is that mineral-melt H_2O partition coefficients determined under terrestrial conditions (e.g. P, T, fO_2) are applicable to the ureilite parent body (UPB). In particular, the UPB is considered to be strongly reduced based upon the high abundance of graphite in ureilites (French and Eugster, 1965; Deines et al., 1974; Holloway et al., 1992); this is supported by measurements of Cr valence states in olivine which yielded estimated an fO_2 of approximately 1 – 3 log units below the iron-wüstite (IW) buffer (Goodrich et al., 2013), which is several log units lower than the fO_2 of average terrestrial upper mantle (~ Quartz-Fayalite-Magnetite (QFM); Cottrell and Kelley, 2011; Berry et al., 2018; Berry and O'Neill, 2021). Additionally, the UPB is considered to be much smaller (> 345 km radially; Warren, 2012) than the Earth (~6370 km radially) so the main group ureilites likely equilibrated under lower pressures than samples of the terrestrial mantle.

In the following section, we describe the dependence of olivine and pyroxene H_2O partitioning on pressure, oxygen fugacity and mineral composition, based on the results of experiments conducted under terrestrial conditions. For all other phases considered (e.g. plagioclase, apatite, merrillite), partitioning data is limited and was selected to be consistent with prior investigations of meteoritic parent bodies when possible.

Effect of pressure on partition coefficients

O'Leary et al. (2010) showed that H_2O solubility in pyroxene is nearly invariant with pressure. Conversely, D_{Ol} has been found to be strongly dependent upon pressure (Hauri et al., 2006a; Adam et al., 2016). If we approximate the UPB as a uniform sphere with an average

density of 3300 kg m^{-3}, corresponding to the room-temperature average grain density of ureilites and consistent with previous calculations (Wilson et al., 2008; Macke et al., 2011; Warren, 2012), and a radius of 345 km (Warren, 2012), then the pressure at the center of the UPB is estimated to be ~180 MPa. To date, we are unaware of any published D_{Ol} values experimentally constrained at pressures below 0.5 GPa. However, Le Voyer et al. (2014) provided a D_{Ol} value of 0.0007±0.0003 based upon natural melt inclusion-olivine pairs thought to derive from pressures of ~100 to 400 MPa which provides the closest approximation to the likely pressures of the UPB.

Effect of fO_2 on partition coefficients

Oxygen fugacity may affect mineral-mineral and mineral-melt H_2O partitioning due to its control on the stability of H-bearing species in silicate melt; e.g., reducing conditions and high pressures (>0.7 GPa) may stabilize CH_4, H_2 and NH-bearing species at the expense of H_2O and OH (Armstrong et al. 2015; Hirschmann et al. 2012). As described above, the pressure at the center of the UPB was likely ~180 MPa. Under reducing conditions at this relatively low pressure, H_2O and OH are expected to be the dominant dissolved H-bearing species in silicate melt, and CH_4, H_2 and NH-bearing species are not thought to be stable (Hirschmann et al., 2012; Wetzel et al., 2013). Therefore, the majority of H dissolved in silicate melt on the UPB is expected to dissolve as H_2O or OH despite the low fO_2 of the UPB. This suggests that mineral-melt partition coefficients determined for oxidized conditions, where OH and H_2O are the predominant species in the melt, may also be applicable to the UPB.

Effect of mineral composition on partition coefficients

O'Leary et al. (2010) showed that H_2O partitioning in pyroxene is strongly correlated with Al content, therefore we use previously defined relationships or experiments with similar pyroxene compositions to estimate appropriate D_{Pyx} values. Furthermore, for olivine, mineral

composition has been shown to have a weak correlation over a wide range of compositions (Fo50 – 100; Withers et al., 2011) and instead is primarily a function of pressure (Hauri et al., 2006a; Adam et al., 2016).

B2) C, F, Cl, and S contents of the UPB

We have measured C, F, and Cl in olivine and pyroxene from main group ureilites, Hughes cluster ureilite EET 96314, and the Almahata Sitta ureilitic trachyandesite (ALM-A), and C, F, Cl, and S in glass (melt inclusions and interstitial glass) from ALM-A (Table 2). For C, F, Cl, and S, we do not provide batch or incremental melting estimates for the bulk UPB composition as the UPB contains non-silicate phases with abundant C (e.g. graphite; Grady et al., 1985), S (e.g. sulfides; Goodrich et al., 2013), and F and Cl (e.g. apatite; Bischoff et al., 2014, 2022). The presence of non-silicate phases bearing abundant C, F, Cl, and S invalidates the use of Henrian mineral-melt partition coefficients (e.g. partitioning between pyroxene and a basaltic melt) to estimate bulk UPB volatile budgets. Therefore, we do not perform batch or incremental melting estimates of the bulk UPB C, F, Cl, and S contents.

To provide a first order estimate of the bulk F and Cl content of the UPB, we can use a simple mass balance approach as in Section 3.5.3.1 which avoids the use of Henrian minral-melt partition coefficients provided that the solid (i.e. residue) and liquid (i.e. melt) compositions can be estimated. We use the mass balance equation:

$$C_0 = F \times C_l + (1 - F) \times C_s$$

where C_s is the concentration of a species in the solid (i.e., the mantle residue), C_l is the concentration of a species in the liquid, C_0 is the concentration of a species in the original system, and F is the melt fraction. We consider a melt fraction of 0.15 – 0.25 and liquid (C_l) concentrations of 190±50 µg/g F and 2400±800 µg/g Cl (Table 3) corresponding to our preferred

values for ALM-A glass. We make the simplifying assumption that the residue (C_s) contains negligible F or Cl (i.e. ~ 0 µg/g) as main group ureilite pigeonite F and Cl concentrations are << 1 µg/g (Table 3). Considering the range of considered melt fractions (F) and liquid concentrations (C_l) for F and Cl, we estimate the bulk UPB had ~21 – 60 µg/g F and 240 – 800 µg/g Cl. Our estimated bulk UPB F and Cl values overlap with those for chondrites (20 - 238 µg/g F; 76 - 700 µg/g Cl; Brearley and Jones, 2018) but are enriched relative to the angrite parent body (0.114 µg/g F; 3.5 µg/g Cl; Sarafian et al., 2017), eucrite parent body (3.0 – 7.2 µg/g F; 0.39 – 1.8 µg/g Cl; McCubbin et al., 2021), and the moon (0.54 – 4.5 µg/g F; 0.26 – 2.9 µg/g Cl; McCubbin et al., 2015).

B3) Apparent pyroxene – melt H_2O partition coefficient for ALM-A

Apparent partition coefficients are normally calculated using mineral-melt inclusion pairs (i.e. paired analyses of melt inclusions and the host mineral), however, no pyroxene – melt inclusion pairs were analyzed as part of this study. Our analyses of ALM-A pyroxene yielded a narrow range of ~13 – 19 µg/g H_2O despite highly variable pyroxene-hosted melt inclusion contents of ~44 – 216 µg/g H_2O. To provide a conservative estimate for the apparent pyroxene-melt H_2O partition coefficient for ALM-A, we consider the entire range of our measured pyroxene and melt inclusion H_2O contents. We estimate the apparent partition coefficient using the formula:

$$D_{H_2O}^{App} = \frac{C_{H_2O}^{Pyx}}{C_{H_2O}^{MI}}$$

where $D_{H_2O}^{App}$ is the apparent mineral – melt partition coefficient for H_2O, $C_{H_2O}^{Pyx}$ is the H_2O content measured in pyroxene, and $C_{H_2O}^{MI}$ is the H_2O content measured in melt inclusions. For the ranges of measured pyroxene and melt inclusion H_2O concentrations in ALM-A, we calculate $D_{H_2O}^{App}$ of

0.06 to 0.4. We note that this range of apparent partition coefficients overlaps with an experimental clinopyroxene – melt partition coefficient determined at a pressure of 1 atm (D = 0.1±0.05; Sarafian et al., 2019).

SUPPLEMENTARY FIGURES

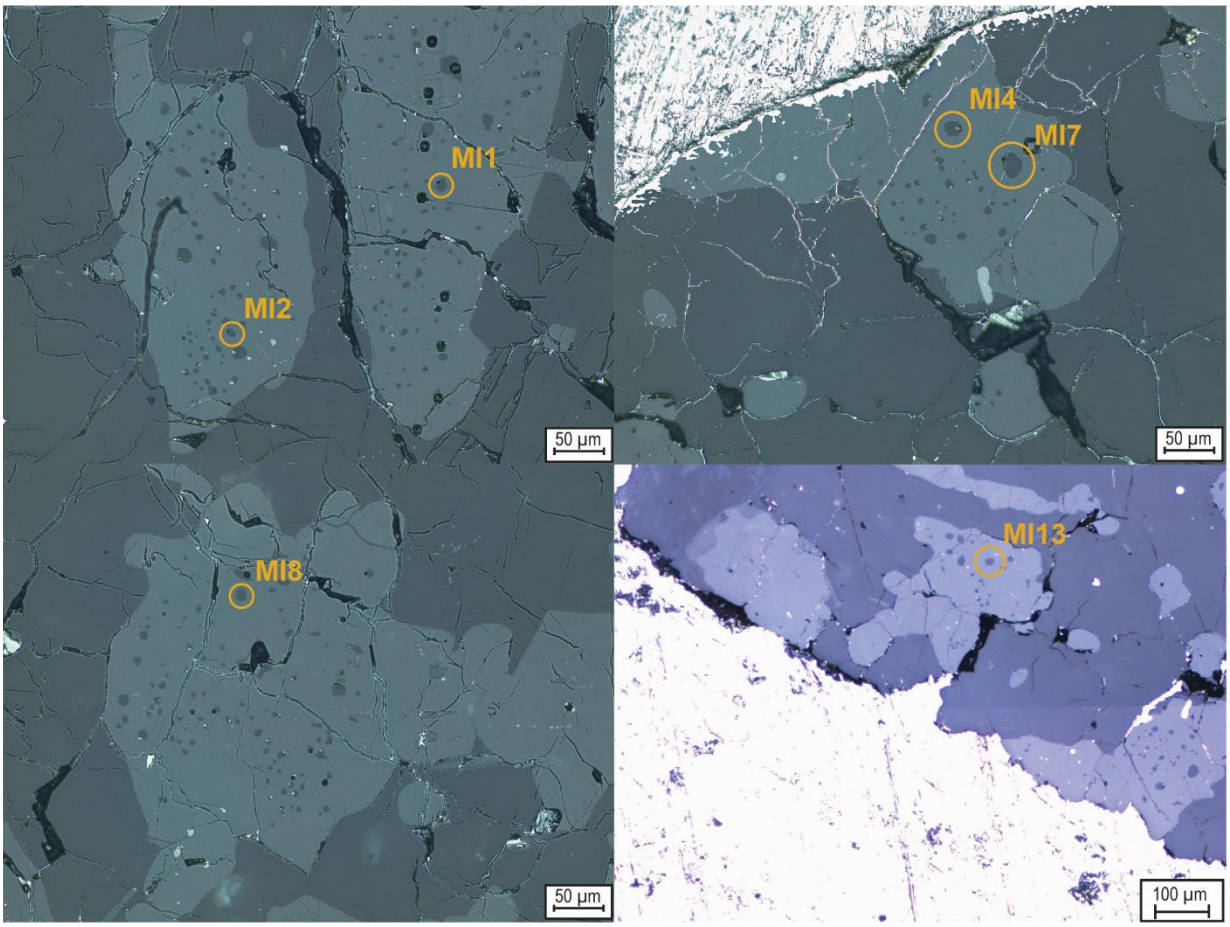

Fig. B1 Collage showing back reflected light images of pyroxene hosted melt inclusions in ALM-A analyzed using the nanoSIMS 50L.

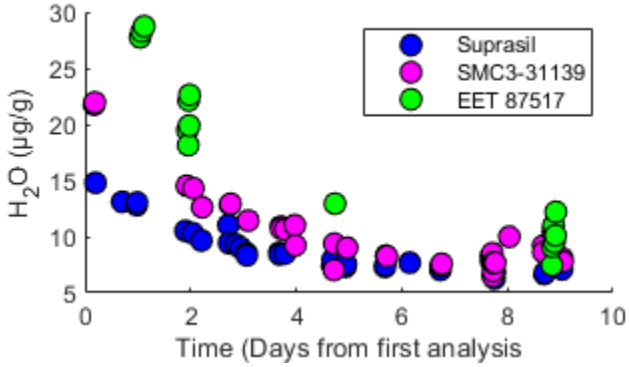

Fig. B2) Uncorrected Suprasil 3002 glass, clinopyroxene standard SMC3-31139, and main group ureilite EET 87517 olivine (green) from the 11/20 analytical session plotted with time. Low H_2O clinopyroxene standard SMC3-31139 (5 +8/-5 ppm H_2O) and EET 87517 olivine non-linearly drew-down relative to Suprasil with time, suggesting analyses at the beginning of the analytical session may not be quantitative.

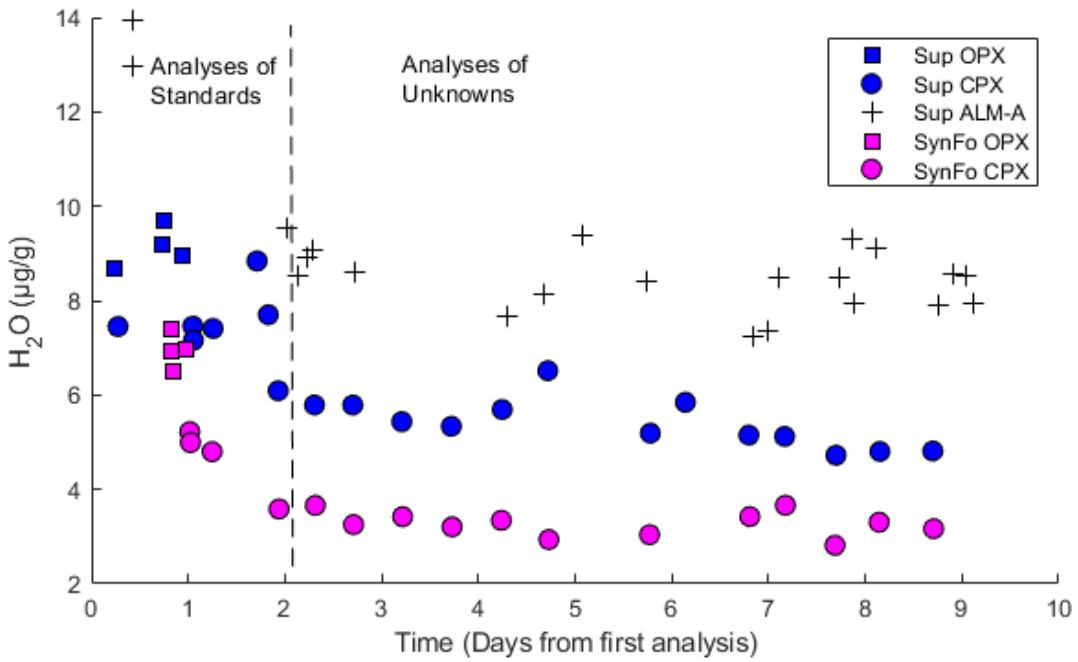

Fig. B3 Uncorrected Suprasil 3002 glass (Sup) and synthetic forsterite (SynFo) across the orthopyroxene (OPX) and clinopyroxene (CPX) standards mounts and ALM-A mount analyzed during the 10/21 analytical session. The dashed vertical line demarcates the time preceding the beginning of analyses of unknowns and after which analyses of Suprasil and synthetic forsterite are nearly invariant. Importantly, over the interval for analyses of unknowns, the average offset between Suprasil and synthetic forsterite mounted in the CPX standard mount is 1.7±0.3 µg/g H_2O which is inline with the value of 2±0.43 µg/g H_2O from Newcombe (2022).

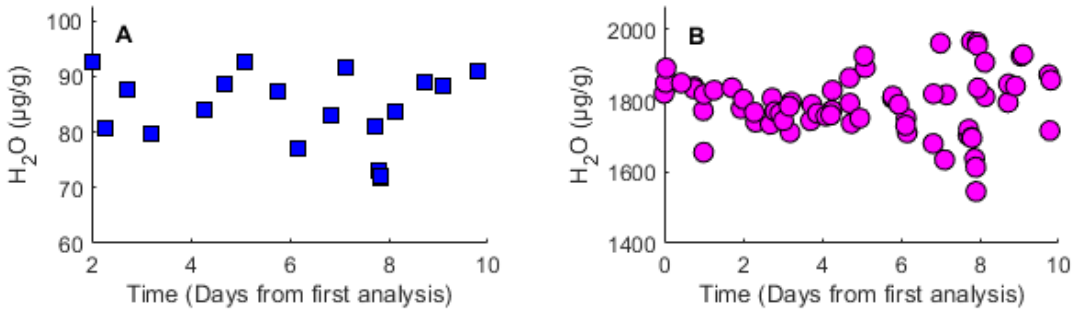

Fig. B4 Replicate analyses of A) Herasil glass and B) ALV-519-4-1 glass analyzed throughout the 10/21 analytical session. Measured H_2O concentrations are not time variant and therefore no drift correction is applied to data from the 10/21 session.

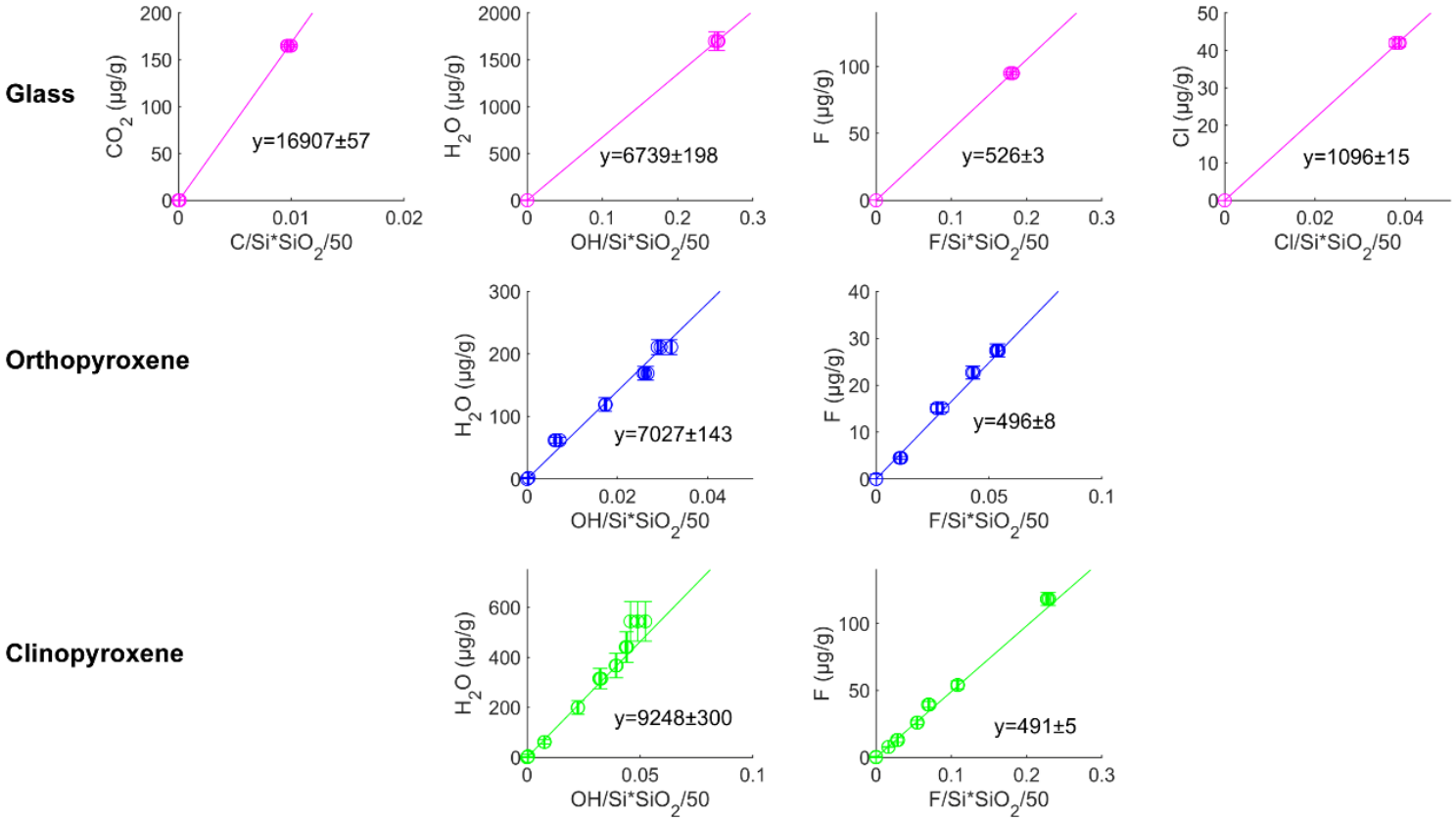

Fig. B5 Calibration curves for CO_2, H_2O, F, and Cl for glass, orthopyroxene, and clinopyroxene in the 11/20 analytical session. Uncertainties on slopes were determined using a York regression (York et al., 2004; Wiens, 2021).

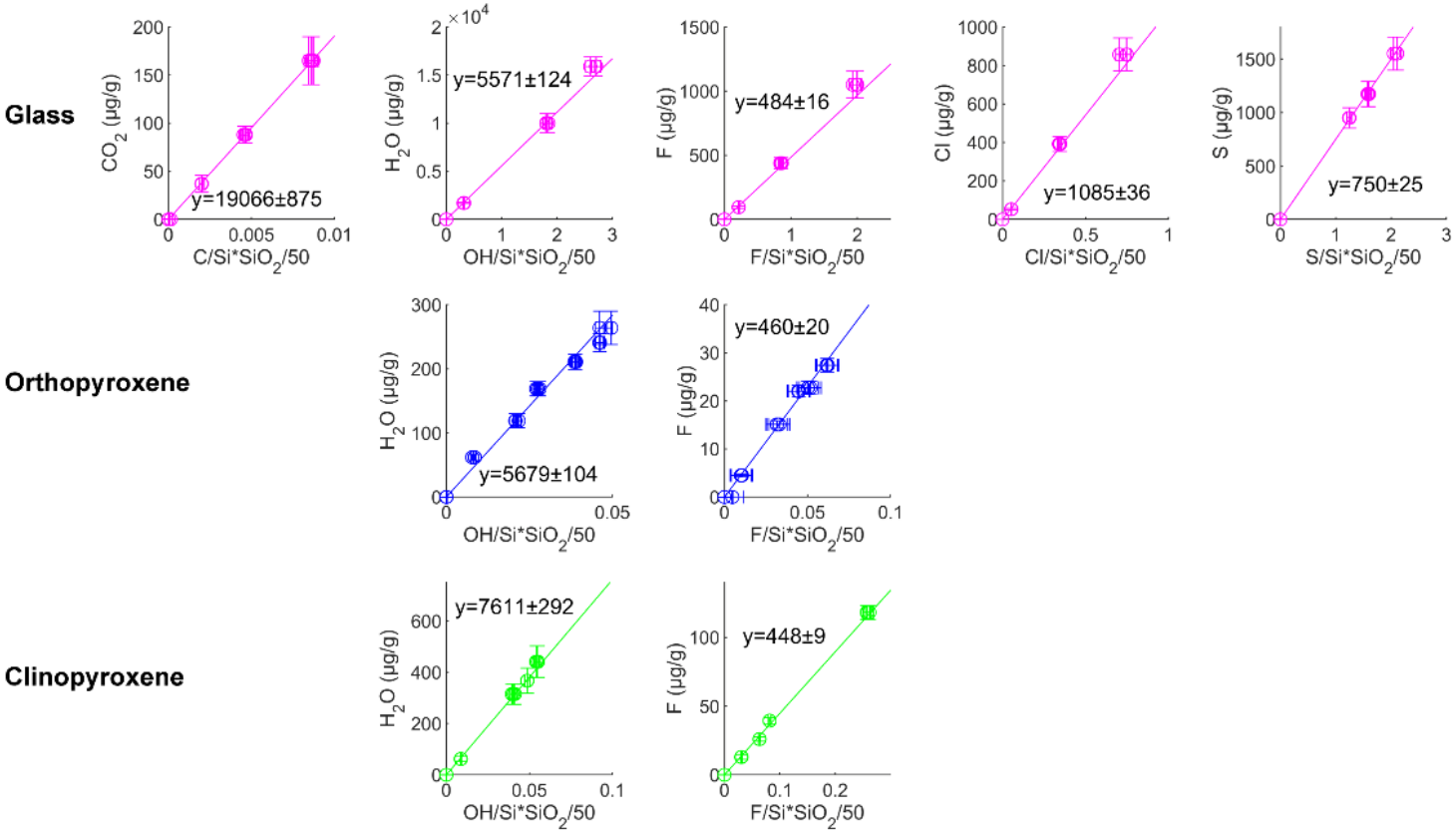

Fig. B6 Calibration curves for CO_2, H_2O, F, Cl, and S for glass, orthopyroxene, and clinopyroxene for the 10/21 analytical session. Uncertainties on slopes were determined using a York regression (York et al., 2004; Wiens, 2021).

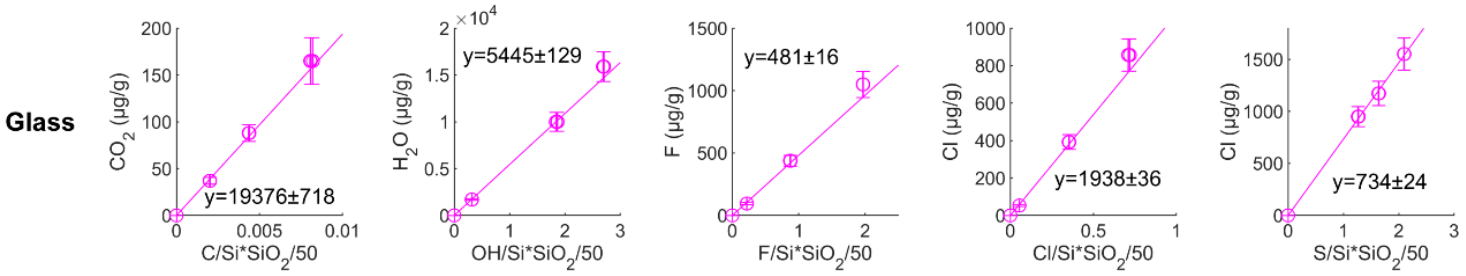

Fig. B7 Calibration curves for CO_2, H_2O, F, Cl, and S for glass for the 01/22 analytical session. Uncertainties on slopes were determined using a York regression (York et al., 2004; Wiens, 2021).

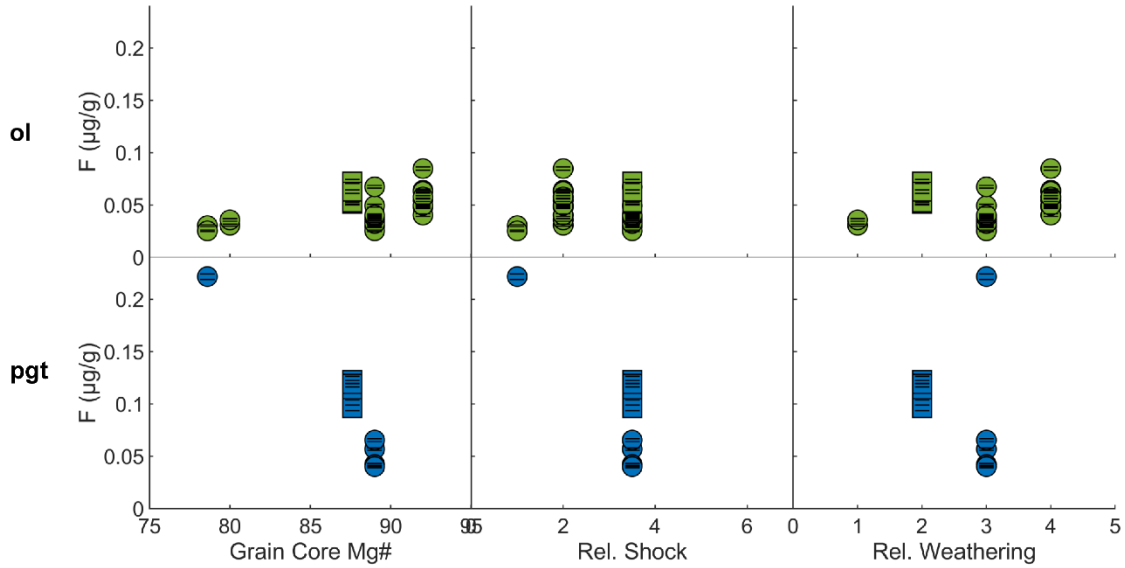

Fig. B8) Olivine (ol) and pigeonite (pgt) F concentrations from spot analyses plotted against grain core Mg# (A,B), bulk relative degree of shock (C,D), and bulk relative degree of weathering (E,F). Circles represent main group ureilites and squares represent the Hughes Cluster ureilite (EET 96314) analyzed as part of this study. Relative degrees of shock and weathering placed on arbitrary scales based upon qualitative descriptions and classifications of weathering and shock features. Error bars are one standard deviation from the mean. All data shown are blank- and drift- corrected and are discernable from the limit of detection (not shown as it is variable with time and therefore analysis number).

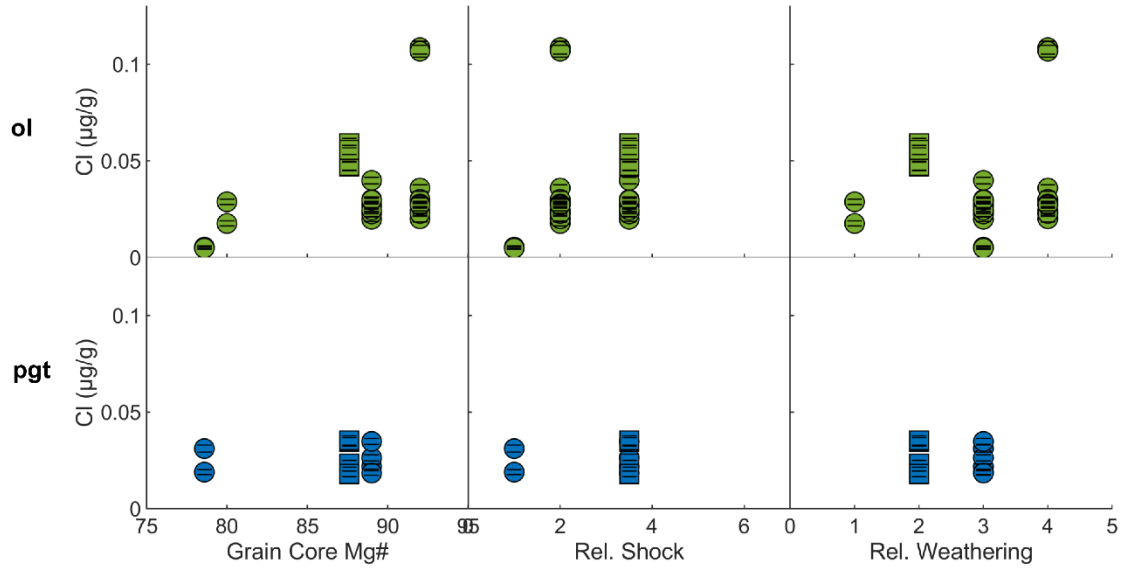

Fig. B9) Olivine (ol) and pigeonite (pgt) Cl concentrations from spot analyses plotted against grain core Mg# (A,B), bulk relative degree of shock (C,D), and bulk relative degree of weathering (E,F). Circles represent main group ureilites and squares represent the Hughes Cluster ureilite (EET 96314) analyzed as part of this study. Relative degrees of shock and weathering placed on arbitrary scales based upon qualitative descriptions and classifications of weathering and shock features. Error bars are one standard deviation from the mean. All data shown are blank- and drift- corrected and are discernable from the limit of detection (not shown as it is variable with time and therefore analysis number).

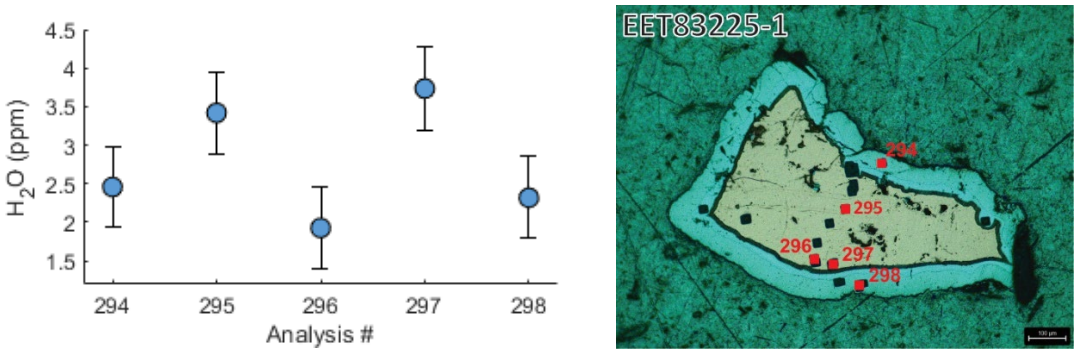

Fig. B10) A) Blank and drift-corrected H_2O concentrations plotted against analysis number. B) Reflected light image of an olivine from EET 83225 with SIMS pits corresponding to data in A indicated in red. Within the uncertainty of the data, no gradient with respect to H_2O concentration is discernable. The grain retains a gold color as the Au coat has not been removed from the grain. The apparent blue rims on the grain correspond to In which often migrates onto grain edges during sample preparation and analysis.

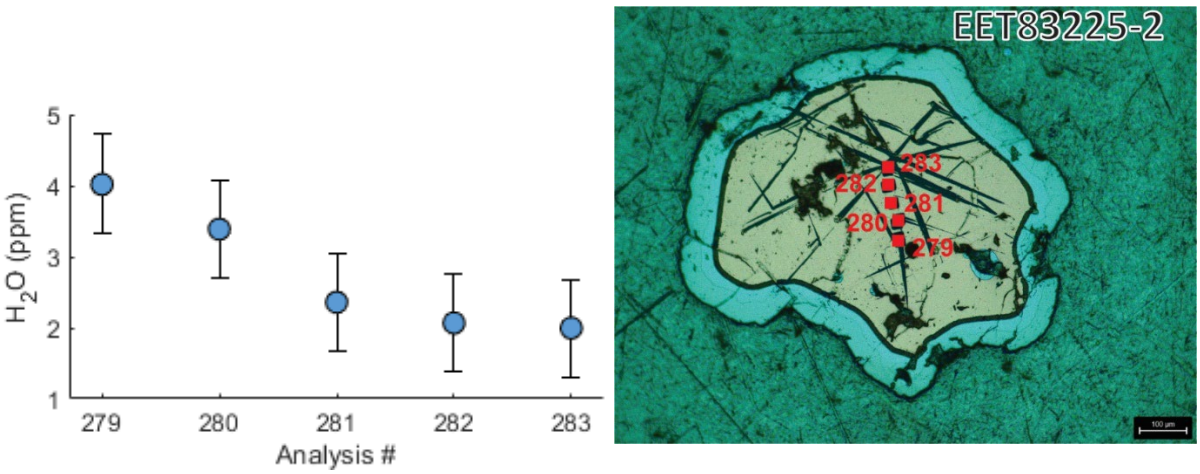

Fig. B11) A) Blank and drift-corrected H_2O concentrations plotted against analysis number. B) Reflected light image of a pigeonite grain with SIMS pits corresponding to data in A indicated in red. Within the uncertainty of the data, no clear gradient with respect to H_2O concentration is discernable, however reverse zonation may be present. Scratches in the grain surface occurred in transit to the analytical facility and were unable to be removed prior to analysis. The grain retains a gold color as the Au coat has not been removed from the grain. The apparent blue rims on the grain correspond to In which often migrates onto grain edges during sample preparation and analysis.

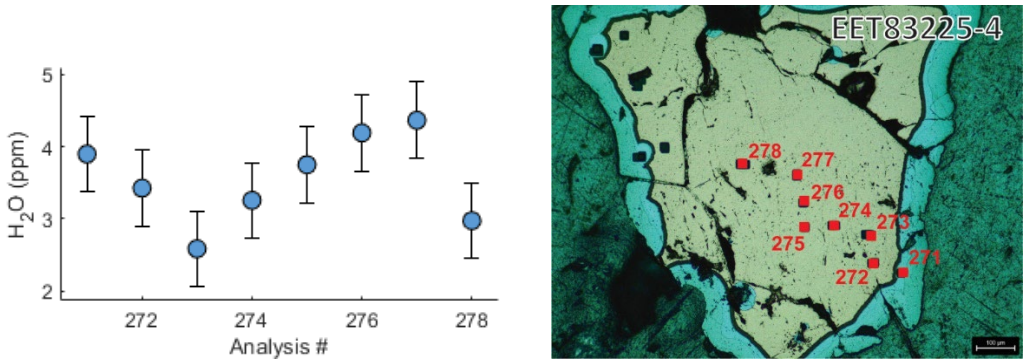

Fig. B12) A) Blank and drift-corrected H_2O concentrations plotted against analysis number. B) Reflected light image of an olivine grain with SIMS pits corresponding to data in A indicated in red. Within the uncertainty of the data, no clear gradient with respect to H_2O concentration is discernable. The grain retains a gold color as the Au coat has not been removed from the grain. The apparent blue rims on the grain correspond to In which often migrates onto grain edges during sample preparation and analysis.

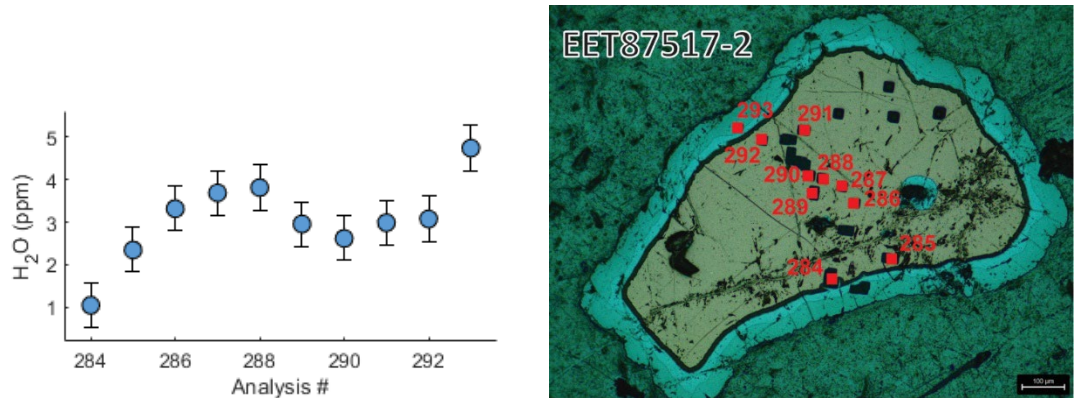

Fig. B13) A) Blank and drift-corrected H_2O concentrations plotted against analysis number. B) Reflected light image of an olivine grain with SIMS pits corresponding to data in A indicated in red. Within the uncertainty of the data, no clear gradient with respect to H_2O concentration is discernable. The grain retains a gold color as the Au coat has not been removed from the grain. The apparent blue rims on the grain correspond to In which often migrates onto grain edges during sample preparation and analysis.

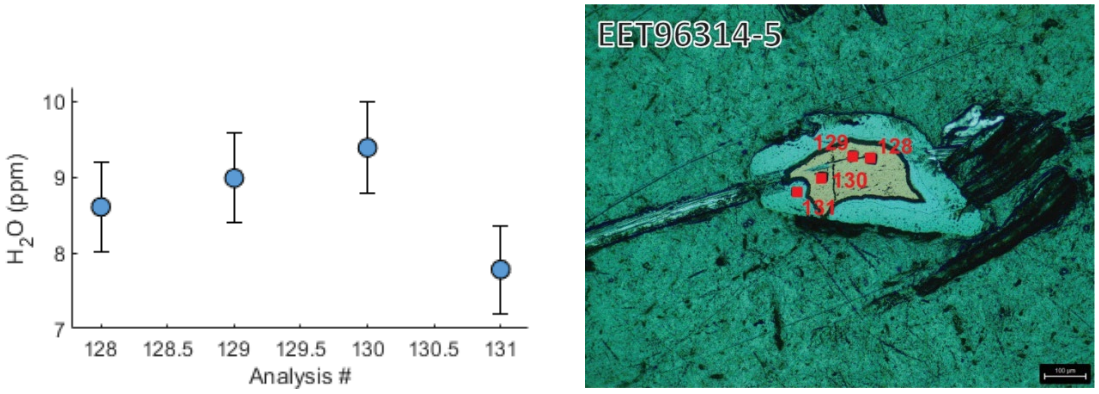

Fig. B14) A) Blank and drift-corrected H_2O concentrations plotted against analysis number. B) Reflected light image of an olivine grain with SIMS pits corresponding to data in A indicated in red. Within the uncertainty of the data, no clear gradient with respect to H_2O concentration is discernable. The grain retains a gold color as the Au coat has not been removed from the grain. The apparent blue rims on the grain correspond to In which often migrates onto grain edges during sample preparation and analysis.

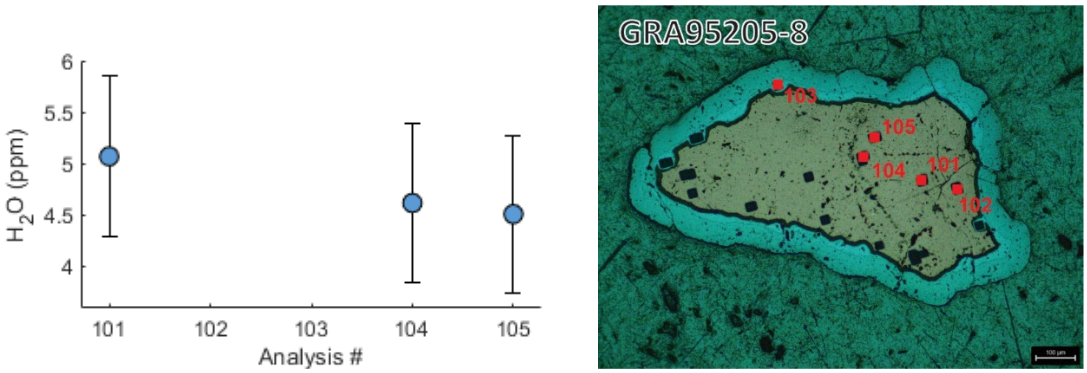

Fig. B15) A) Blank and drift-corrected H_2O concentrations plotted against analysis number. B) Reflected light image of a pigeonite grain with SIMS pits corresponding to data in A indicated in red. Within the uncertainty of the data, no clear gradient with respect to H_2O concentration is discernable. Analysis #102 is excluded due to contamination and analysis #103 is excluded as it is a significant outlier (see Sec. 4.1). The grain retains a gold color as the Au coat has not been removed from the grain. The apparent blue rims on the grain correspond to In which often migrates onto grain edges during sample preparation and analysis.

Appendix C: The H-poor nature of incompletely melted planetesimals: the view from acapulcoites and lodranites

C1) Use of Suprasil 3002 glass as a reference material for monitoring the analytical H background during SIMS analyses

C1.1) Quantification of H_2O concentration in Suprasil 3002 glass

Suprasil 3002 glass is an optically clear and highly pure fused silica glass produced by Heraeus with a manufacturer-reported H content of ≤ ~1 ppm OH (Heraus, 2019, 2020). Throughout the SIMS literature and across several labs (e.g., Carnegie, Caltech, CRPG, GIGCAS) Suprasil 3002 glass is reported or assumed to contain ~1 – 2 μg/g H_2O (Turner et al., 2015; Wetzel et al., 2015; Chin et al., 2016, 2020; Adam et al., 2016; Sarafian et al., 2017c; Wudarska et al., 2018; Simon et al., 2020; Füri et al., 2020; Piralla et al., 2021; Towbin et al., 2023; Yang et al., 2023). This very low H_2O content has made Suprasil 3002 glass a common analytical blank or reference material to estimate the analytical background for analyses of silicates.

We have constructed a compilation, dubbed "SIMSblank" of H_2O concentration data for Suprasil 3002 glass and nominally anhydrous synthetic forsterite (SynFo; <<1 μg/g H_2O) collected using the Cameca IMS 6f and NanoSIMS 50L at the Carnegie Earth and Planets Laboratory. The compiled dataset was collected across 3 sample mounts and 7 analytical sessions (Newcombe, 2022). Data are present within SIMSblank as $^{16}O^{1}H/^{30}Si$, $^{16}O^{1}H/^{30}Si \times SiO_2/50$, and H_2O concentrations determined using orthopyroxene standards for SynFo (Kumamoto et al., 2017) and the basaltic glass calibration for Suprasil 3002 glass. If we compare successive analyses of Suprasil 3002 glass and SynFo that have not been blank- or drift-corrected (Fig. C3), our SIMS analyses demonstrate that Suprasil 3002 glass is systematically

offset to higher values of $^{16}O^{1}H/^{30}Si$, $^{16}O^{1}H/^{30}Si \times SiO_2/50$, and H_2O. Importantly, if SynFo is taken as a "zero" standard (Koga et al., 2003), then the positive y-intercept for $^{16}O^{1}H/^{30}Si$, $^{16}O^{1}H/^{30}Si \times SiO_2/50$, and H_2O imply Suprasil 3002 glass has a non-zero H_2O (and total H) content (Fig. C3). Furthermore, the slope 1 in plots of $^{16}O^{1}H/^{30}Si \times SiO_2/50$ and H_2O demonstrate that the offset between Suprasil 3002 glass and SynFo is additive and not a function of the analytical blank (as approximated by SynFo), with an implied Suprasil 3002 glass H_2O content of 1.9±0.2 µg/g H_2O (Fig. C3c). Furthermore, if you consider data for Suprasil 3002 glass from SIMSblank that has been blank corrected using SynFo and drift-corrected (see file SIMSblank_v2.xlsx from SIMSblank; Newcombe, 2022; Peterson et al., 2023b, a; Newcombe et al., 2023), then the estimated H_2O content of Suprasil 3002 glass is 1.7±0.6 µg/g H_2O (1 St. Dev.). We prefer the estimate from the blank- and drift-corrected H_2O contents of Suprasil 3002 glass as it yields a more conservative of the long-term reproducibility of at or near-blank analyses for our analytical set-up.

C1.2) Why do we multiply $^{16}O^{1}H/^{30}Si$ by $SiO_2/50$?

We ratio volatile ion counts (^{12}C, $^{16}O^{1}H$, ^{19}F, ^{32}S, and ^{35}Cl) to ^{30}Si to mitigate the effects of instrumental drift (e.g., Kumamoto et al. 2017). We then multiply ^{30}Si ratioed volatile ion counts to the SiO_2 content of the material divided by 50 (e.g., $^{16}O^{1}H/^{30}Si \times SiO_2/50$), as determined by electron microprobe (hereafter SiO_2 correction; e.g., Hauri et al., 2002; Aubaud et al., 2007; Mosenfelder and Rossman, 2013). The factor of 1/50 is applied to the SiO_2 correction for ease of comparison as many silicates have ~50 wt.% SiO_2; however, we note that the 1/50 factor has no bearing on the final concentrations as the scalar is applied to all data, including calibration standards. We apply the SiO_2 correction for the following reasons: 1) the calibration curves for trace elements C, F, Cl, and S are improved by the SiO_2 correction (Shimizu and Hart,

1982; Hauri et al., 2002); 2) to account for differences in the SiO_2 content of target phases as variability in SiO_2 has been suggested as a dominant matrix effect for H analyses of silicates by SIMS (e.g., Ottolini et al., 1995); and 3) to be consistent with prior work which has shown that the SiO_2 correction results in close agreement of the H_2O calibration curves for basaltic to pure SiO_2 silicate glasses (Shimizu et al., 2022). For a pure SiO_2 material, like Suprasil 3002 glass, the SiO_2 correction results in a significant change, increasing the apparent H_2O concentration by a factor of two relative to non-SiO_2 corrected data. This factor of 2 difference highlights the importance of applying the SiO_2 correction or using matrix-matched standards to quantify the analytical background. Therefore, whenever possible, we recommend using anhydrous, matrix-matched standards to quantify the analytical background. However, in instances where anhydrous, matrix-matched standards are not available, we recommend applying the SiO_2 correction to account for variability in SiO_2 contents between phases.

C1.3) Why might there be a discrepancy in the H_2O content of Suprasil 3002 glass as determined by SIMS and IR?

As stated above, Suprasil 3002 glass is frequently reported or assumed to contain ≤ ~1 to 2 µg/g H_2O in the SIMS literature, with a value of ≤ ~1 µg/g OH reported by the manufacturer Heraeus (Heraus, 2019, 2020). One potential source of this variability within the literature is deviations in data normalization and processing, such as initially normalizing to O instead of Si or whether or not to apply the SiO_2 correction. As outlined in Section C1.1, the SiO_2 correction results in a factor of 2 difference in H_2O concentration when applied to Suprasil 3002 glass. All of the studies referred to before subsection C1.1 that report or assume ~1 – 2 µg/g H_2O in Suprasil 3002 glass ultimately refer back to the upper bound reported by Heraeus or to high precision SIMS data, collected across multiple sessions using the IMS 6f and NanoSIMS 50L,,

thought to have very low analytical backgrounds collected at Carnegie EPL, with and without the SiO_2 correction. To a first order, this suggests that Suprasil 3002 glass has some nominal dissolved H content, however further interlab comparison would be useful. One potential source of dissolved H is H_2 dissolved in Suprasil 3002 glass in trace quantities. Suprasil 3002 glass is manufactured by soot outside vapor deposition by flushing $SiCl_4 + H_2 + O_2$ vapors over a bait rod to form a porous silica body prior to an intermediate drying step and vitrification (Nurnberg et al., 2015). This process may have incompletely removed H_2, which is weakly IR active (Hirschmann et al., 2012). As SIMS measures total H contents, if weakly IR active species such as H_2 are present in nominal amounts they may result in higher measured H_2O (total H) contents by SIMS than by IR. If Suprasil 3002 glass is instead interpreted as a "zero" or "blank" material for H, then all our reported concentrations are increased by ~2 μg/g H_2O and our preferred estimate of the maximum ALPB H_2O content is increased to 48 μg/g. Similarly, if the SiO_2 normalization is demonstrated to be unnecessary, all reported concentrations for Suprasil 3002 glass will be decreased by a factor of ~2. We also acknowledge that industrial scale production of Suprasil 3002 glass may have resulted in heterogeneities on the scale of ~1 μg/g H_2O between batches and aliquots. Overall, it cannot be ruled out that Suprasil 3002 glass has no detectable H, however our interpretation that Suprasil 3002 glass has measurable H is consistent with reported and assumed values throughout the SIMS literature and is supported by a reproducible, non-zero offset between Suprasil 3002 glass and anhydrous SynFo for $^{16}O^{1}H/^{30}Si$, $^{16}O^{1}H/^{30}Si \times SiO_2/50$, and H_2O.

C2) Applicability of H_2O partition coefficients determined under terrestrial conditions

The applicability of equilibrium partition coefficients for H_2O determined under terrestrial conditions to meteoritic parent bodies is discussed in detail in Peterson et al. (2023a, b)

and is re-evaluated for the sample set presented here. Within our sample set, orthopyroxene, clinopyroxene, and olivine H_2O contents overlap and are greater than plagioclase. Considering the primary controls on partitioning for each phase (see below), the relative partitioning of H_2O in ALC NAMs does not agree with experimentally predicted partitioning relationships (Table 4.4; e.g., Aubaud et al., 2004, 2008; Hauri et al., 2006; Grant et al., 2007; O'Leary et al., 2010; Hamada et al., 2013; Adam et al., 2016; Lin et al., 2019). We first consider the effect of redox sensitive elements on the solubility, and therefore partitioning, of H_2O in NAMs. Then we discuss the primary controls on H_2O partitioning in pyroxene, olivine, and plagioclase. Finally, we discuss the mineral-melt H_2O partition coefficients used in this study.

C2.1 The influence of redox sensitive elements

The fO_2 of primitive achondritic parent bodies (~IW –1 to –2) tends to be lower than the fO_2 of the upper mantle (~IW –2 to 4; Righter et al., 2016). For olivine, pyroxene, and plagioclase, experimental results are consistent with H_2O being more compatible in Fe-bearing compositions under reducing conditions, which may suggest some redox sensitivity for all analyzed phases (e.g., Skogby and Rossman, 1989; Zhao et al., 2004; Bromiley et al., 2004; Mosenfelder et al., 2020). This redox effect has been suggested for plagioclase under lunar conditions (Lin et al., 2019), but is considered to be negligible for olivine and pyroxene, at least down to IW −2 (Potts et al., 2021). Nevertheless, if phases are rich in redox sensitive elements, such as Fe, relative to the mantle compositions targeted in experimental studies, then redox effects may increase the compatability of H_2O in NAMs. Furthermore, this increased compatibility may not be linear for all phases, thereby resulting in deviation from the predicted relative partitioning of H_2O in NAMs based upon the primary controls for each phase (see below). However, our phases are not rich in redox sensitive elements such as Fe, Ti, and Cr

relative to the experiments used to constrain the compatibility of H_2O at terrestrial conditions. This suggests that the primary controls on H_2O mineral-melt partitioning, as determined experimentally under terrestrial conditions, can reasonably be extended to ALCs.

C2.2 The compositional dependence of H_2O partitioning in pyroxene

It has been shown that mineral-melt H_2O partitioning for orthopyroxene and clinopyroxene is compositionally dependent, with a strong dependence on Al content (Hauri et al., 2006a; O'Leary et al., 2010). The Al content of ALC pyroxenes (Table C2) overlap with the lowest Al contents of pyroxene in MORBs. As experimental studies of H_2O partitioning in NAMs predominantly target mantle compositions and the composition of ALC NAMs overlap with mantle NAMs, we suggest that compositionally dependent formulations for pyroxene-melt H_2O partition coefficients (Section C2; O'Leary et al., 2010) can reasonably be extended to the ALCs.

C2.3 The pressure dependence of H_2O partitioning in olivine

Most experimentally determined partition coefficients are determined at pressures that are greater than those expected for the interiors of small, meteoritic parent bodies (<100 - 200 MPa; McCoy et al., 2006; Elkins-Tanton et al., 2011). This pressure difference may be important for olivine, in which the mineral-melt partition coefficient for H_2O has been shown to be strongly dependent on pressure (Adam et al., 2016) and has only been experimentally determined at pressures ≥500 MPa (Hauri et al., 2006a; Tenner et al., 2012; Adam et al., 2016; Potts et al., 2021). The observed pressure dependence is anchored by few high-pressure experiments (>5 GPa), and at lower pressures relevant to the upper mantle significant scatter is observed. Furthermore, recent work by Towbin et al. (2023) has found that the olivine-melt partition coefficient ($D_{H_2O}^{ol-melt}$) at upper mantle to crustal conditions (< 2 GPa) may be nearly uniform

with a value of $D_{H_2O}^{ol-melt}$ = 0.0009(3; 1 St. Dev.) after correcting for discrepancies in calibration methods between SIMS studies. The origin of this apparent discrepancy between the pressure dependence on $D_{H_2O}^{ol-melt}$ observed at >5 GPa and the lack of a pressure dependence observed at < 2 GPa is unclear, and resolution of this issue will require further experiments at both low and high pressures. Given the low pressures relevant to the ALPB (e.g., Lucas et al., 2022), we consider the $D_{H_2O}^{ol-melt}$ value proposed by Towbin et al. (2023) to be most applicable to the ALPB.

C2.4 The influence of fH_2O on H_2O partitioning in plagioclase

There is very limited work on the partitioning of H_2O between plagioclase and melt (Hamada et al., 2013; Lin et al., 2019). The limited experimental data suggests that fO_2 may exhibit a significant control on H_2O partitioning between plagioclase and melt (Lin et al., 2019). Additionally, all experimental data to date agrees that the partitioning of H_2O in plagioclase has a non-linear relationship with the total H_2O content of the system, and therefore fH_2O (Hamada et al., 2013; Lin et al., 2019). Experiments suggest that the plagioclase-melt H_2O partition coefficient increases at low fH_2O. This is consistent with the higher than expected clinopyroxene-melt partition coefficient at 1-atm and low total H_2O contents (Sarafian et al., 2019) and the high orthopyroxene-melt partition coefficient in the H_2O-poor experiment of Potts et al. (2021) relative to all other charges. Overall, this suggests that fH_2O exerts a primary control on H_2O partitioning in plagioclase and may influence partitioning in other phases, however further experimental work is required to constrain this effect.

C2.5 Summary of mineral-melt partition coefficients used in this study

Considering the range of conditions and uncertainties associated with the experimentally determined primary controls on H_2O partitioning in NAMs, we suggest it is reasonable to apply

experimentally determined partition coefficients to ALC NAMs (Section C1.1). Using the formulation of O'Leary et al. (2010) for clinopyroxene and two compositionally dependent formulations for orthopyroxene (Section C2), we calculate mineral-melt partition coefficients ($D_{H_2O}^{X-melt}$; where X is a mineral) $D_{H_2O}^{cpx-melt}$ = 0.015(2) and $D_{H_2O}^{opx-melt}$ = 0.003(1) and 0.0061(9) (uncertainty in parentheses is 2 SD from the mean) for all acapulcoites and lodranites in our sample set. For olivine, we elect to retain the value of $D_{H_2O}^{ol-melt}$ = 0.0009(3) from Towbin et al. (2023) as it overlaps with olivine-melt partition coefficients determined from olivine – melt inclusion pairs with entrapment pressures of < ~600 MPa (Newcombe et al., 2020). For plagioclase, we consider the values of Lin et al. (2019), which are determined under lunar conditions, which suggests $D_{H_2O}^{pl-melt}$ = 0.002 to 0.046. Overall, the best-fitting partition coefficients for ALCs follow the expected relative partitioning behavior of plagioclase = clinopyroxene > orthopyroxene > olivine. However, within our sample set, the H_2O contents of ALC olivine, pyroxene, and plagioclase do not adhere to the expected relative partitioning behavior. As detailed in Section 4.5.2.1, we suggest this is likely explained by poorly characterized partitioning behavior at low total H contents or defect-controlled uptake or loss of H that resulted in a metastable steady-state with respect to H. Considering that the H_2O contents of ALC NAMs do not adhere to their expected relative partitioning, we suggest that plagioclase and clinopyroxene, which are expected to be the most H_2O-rich phases, are the best hygrometers (Peterson et al., 2023b; Newcombe et al., 2023). Furthermore, for clinopyroxene, we consider the $D_{H_2O}^{cpx-melt}$ value of Sarafian et al. (2019), which was determined at 1-atm pressure and low total H_2O contents, is most applicable to the low pressure (Lucas et al., 2022) and H_2O poor conditions of the ALPB (this study; Stephant et al., 2023). The partition coefficients used in our calculations and corresponding references are given in Table 4.5.

C3) Compositional dependency of orthopyroxene-melt H_2O partition coefficient

Water primarily substitutes into the orthopyroxene structure by two main mechanisms, coupled OH^- defects in metal vacancies (Mierdel and Keppler, 2004; Rauch and Keppler, 2002; Stalder and Skogby, 2002), and paired H and Al defects in Si vacancies (Hauri et al., 2006a; O'Leary et al., 2010). In particular, several studies have demonstrated that H_2O solubility (and partitioning) in orthopyroxene is strongly correlated with the Al content of orthopyroxene (Rauch and Keppler, 2002; Stalder and Skogby, 2002; Stalder, 2004; Mierdel and Keppler, 2004; Hauri et al., 2006a; K. J. Grant et al., 2007; Tenner et al., 2009a; Sakurai et al., 2014). Prior studies have either provided regressions combining orthopyroxene and clinopyroxene (Hauri et al., 2006a) or provided no equation for the fit to their data (K. J. Grant et al., 2007; Adam et al., 2016). We have compiled experimental orthopyroxene-melt H_2O partition coefficients ($D_{H_2O}^{opx-melt}$; Table C9), and where applicable, have selected orthopyroxene H_2O concentrations determined using the Bell et al. (1995) absorption coefficient for Fourier transform infrared analyses. Similar to prior studies (Hauri et al., 2006a; K. J. Grant et al., 2007; Tenner et al., 2009a), we have elected to fit a linear relationship to $D_{H_2O}^{opx-melt}$ and the Al content of orthopyroxene. We use *fitlm* in MATLAB r2022a to construct a linear model for $D_{H_2O}^{opx-melt}$ based upon the Al content in apfu (Fig. C4). Our model has an R^2 value of 0.81 and a RMSE of 0.0036. All model coefficients are given in Table C10.

C4) Equilibrium degassing of a silicate melt

We model the equilibrium H isotopic evolution of the ALPB during silicate melting using a modified version of the model of Giachetti et al. (2020). Notably, the model of Giachetti et al. (2020) only considers degassing of OH and H_2O in the melt (hereafter OH^m and H_2O^m) to H_2O in

the vapor (hereafter H_2O^v), however, under reducing conditions like those experienced by ALCs, the predominant H-species in the vapor is H_2 (hereafter H_2^v). Under reducing conditions and high total H contents, it is possible that H dissolves as H_2 in silicate melt (Hirschmann et al., 2012); however, experimental work on lunar melts has demonstrated that at low pressures (1 atm), < 4 µg/g H_2 dissolves in silicate melt in equilibrium with H_2-rich vapor (Newcombe et al., 2017). This is consistent with extrapolation from high pressure (0.7 to 3 GPa) experiments, which suggest < 0.4 µg/g H_2 is soluble in silicate melts at 1 atm (Hirschmann et al., 2012; Newcombe et al., 2017). Therefore, it is likely that H_2 played a subordinate role in the H isotopic evolution of ALC melts, especially considering the acapulcoite-lodranite parent body is considered to be extremely H-poor (this study; Stephant et al., 2023). We simplify our system by excluding any contribution from H_2 in the melt, thereby leaving us with a system of OH^m, H_2O^m, H_2O^v, and H_2^v (Fig. C5). Within this system, we have the reactions:

$$2OH^m \rightleftharpoons H_2^v + O_2 \quad (S1)$$

$$2OH^m \rightleftharpoons H_2O^v + 0.5O_2 \quad (S2)$$

$$H_2O^m \rightleftharpoons H_2^v + 0.5O_2 \quad (S3)$$

$$H_2O^m \rightleftharpoons H_2O^v \quad (S4)$$

$$H_2O^m \rightleftharpoons H_2^v + 0.5O_2 \quad (S5)$$

Note that the reduction of OH and H_2O to H_2 results in the production of O_2 during the majority of these reactions. This O_2 may enter the vapor phase and/or remain in the melt, where it may also participate in redox reactions (e.g., the oxidation of Fe to FeO).

Within reactions C1 – C5, D can substitute for H, and the isotopic fractionation factor α_{a-b}^{X-Y} can be determined by dividing the D/H ratio of species *X* in phase *a* and species *Y* in phase

b. For example, in equation (1), $\alpha_{H_2-OH}^{v-m}$ is calculated by dividing the concentration of H_2, HD, and D_2 in the vapor by the D/H of OH and OD species in the melt. Additionally, the assumption of equilibrium requires that where multiple species, such as OH^m, H_2O^m, and H_2O^v, can exchange with each other, the fractionation factors must be multiplicative (Fig. C5). We have elected to keep the values of $\alpha_{H_2O-OH}^{v-m}$ (1.041) and $\alpha_{H_2O-H_2O}^{v-m}$(0.982) from Giachetti et al. (2020). By using the calculated equilibrium fractionation factor for $\alpha_{H_2O-H_2}^{v-v}$ from Richet et al. (1977), we can calculate $\alpha_{OH-H_2}^{m-v}$ and $\alpha_{H_2O-H_2}^{m-v}$ (Fig. C5), thereby completing our system. The model of Giachetti et al. (2020) only accounted for outgassing of OH^m and H_2O^m to H_2O^v, and therefore only had to weight the bulk fractionation factor against the mole fractions of OH and H_2O in the melt; however, in our system OH^m and H_2O^m can outgas to H_2O^v and H_2^v. To account for the reactions described in equations S1 and S3, we calculate combined fractionation factors for OH and H_2O weighted against the mole fractions of H_2 and H_2O in the vapor, which describes the proportion of OH^m and H_2O^m that will degas as H_2O^v and H_2^v:

$$\alpha_{OH} = X_{H_2}^v \times \alpha_{H_2-OH}^{v-m} + X_{H_2O}^v \times \alpha_{H_2O-OH}^{v-m} \quad (S6)$$

$$\alpha_{H_2O} = X_{H_2}^v \times \alpha_{H_2-H_2O}^{v-m} + X_{H_2O}^v \times \alpha_{H_2O-H_2O}^{v-m} \quad (S7)$$

These combined fractionation factors are then weighted against the mole fractions of OH and H_2O in the melt, yielding a bulk fractionation factor of:

$$\alpha_{bulk} = X_{H_2O}^m \times \alpha_{H_2O} + X_{OH}^m \times \alpha_{OH} \quad (S8)$$

For simplicity, we have assumed that the vapor pressure is constant. We have followed the same method as Giachetti et al. (2020) to calculate the mole fractions of H_2O and OH in the melt. To calculate the mole fractions of H_2 and H_2O in the vapor, we use the formulations of Deines et al. (1974) to calculate the partial pressures of H_2 and H_2O in the O-H system, giving us pH_2 and

pH$_2$O. At the low total pressure and high temperatures relevant to the ALPB, we can make the assumption that the vapor behaves as an ideal gas Deines et al. (1974):

$$\frac{p_x}{p_t} = \frac{n_x}{n_t} \quad (S9)$$

where p_x is the partial pressure of a species x, p_t is the total pressure, n_x is the moles of species x, and n_t is the total moles. Therefore, in our system:

$$p_t = p_{H_2} + p_{H_2O} + p_{O_2} \quad (S10)$$

$$X^v_{H_2} = \frac{p_{H_2}}{p_t} \quad (S11)$$

For our calculations, we assume a pressure of 1 bar, a temperature of 980 °C, which corresponds to the lowest melting temperature for ALCs (McCoy et al., 1996), and an oxygen fugacity corresponding to IW −1 (Righter et al., 2016).

SUPPLEMENTARY FIGURES

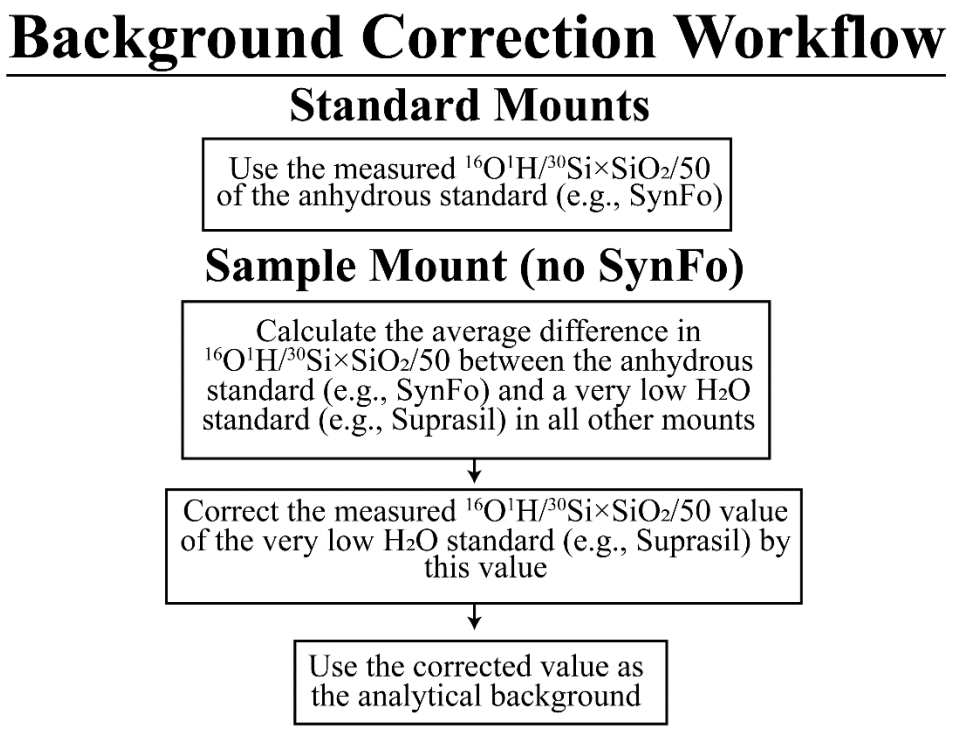

Fig. C1 Flow-chart illustrating the steps used to background-correct data for the 01/22 and 02/22 analytical sessions. Note, the sample mount did not contain SynFo (<<1 µg/g H_2O) unlike the orthopyroxene and clinopyroxene standard mounts. All mounts contained Suprasil 3002 glass (1.7±0.6 µg/g H_2O; 1 SD; Newcombe, 2022).

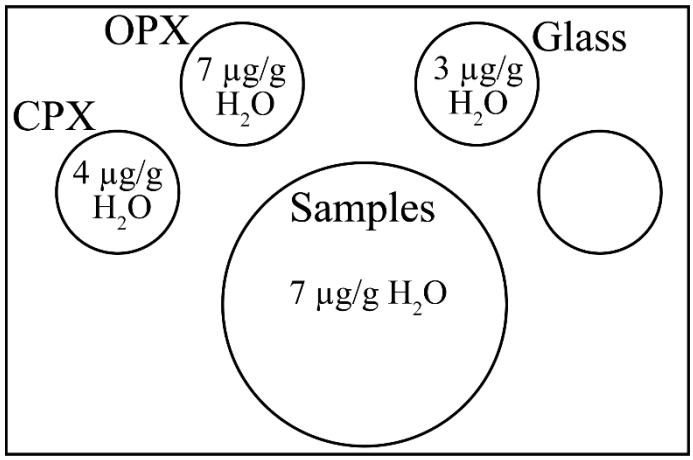

Fig. C2 Schematic illustrating the measured analytical blank across mounts held in the same sample holder from the 01/22 analytical session. Note that the blank varies from mount to mount in a single sample holder, emphasizing the importance of including Suprasil 3002 (or an equivalently homogeneous low-H_2O material) on every mount.

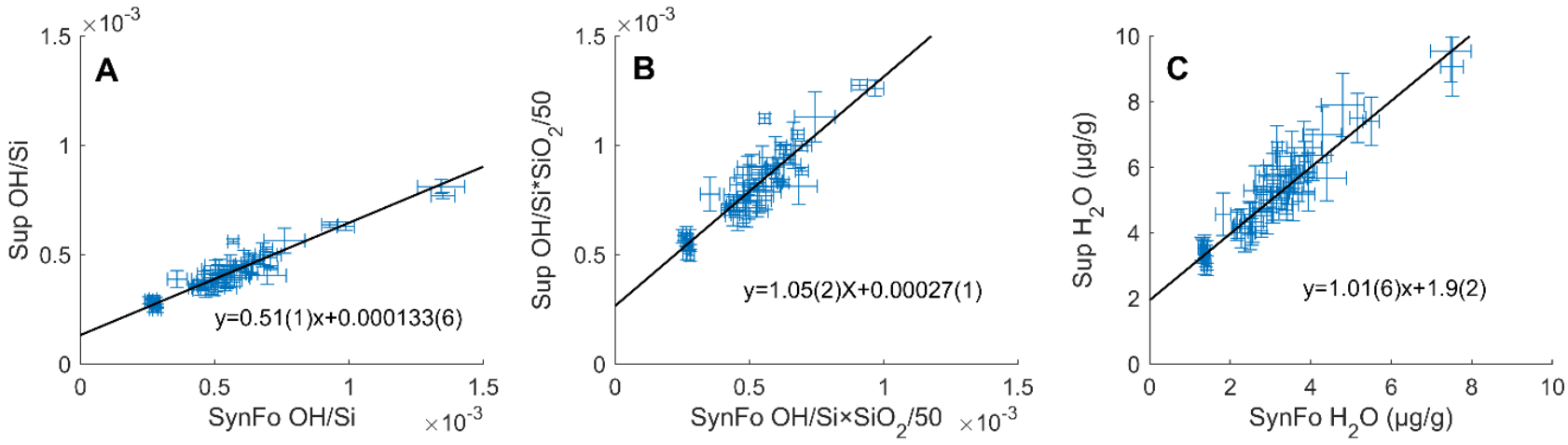

Fig. C3 Non-blank corrected and paired analyses of Suprasil 3002 glass (Sup) and synthetic forsterite (SynFo) from the SIMSblank database (Newcombe, 2022). A) OH/Si, B) OH/Si×SiO_2/50, and C) H_2O. H_2O concentrations are determined from OH/Si×SiO_2/50 values with a basaltic glass calibration curve used for Suprasil 3002 glass and an orthopyroxene calibration curve used for olivine (Kumamoto et al., 2017). Plotted regressions are York regressions considering the uncertainty in *x* and *y*. Panel A corresponds to the correction for variations in ion intensities, panel B corresponds to matrix corrected data, and panel C corresponds to concentrations (see Section 4.5.1.1).

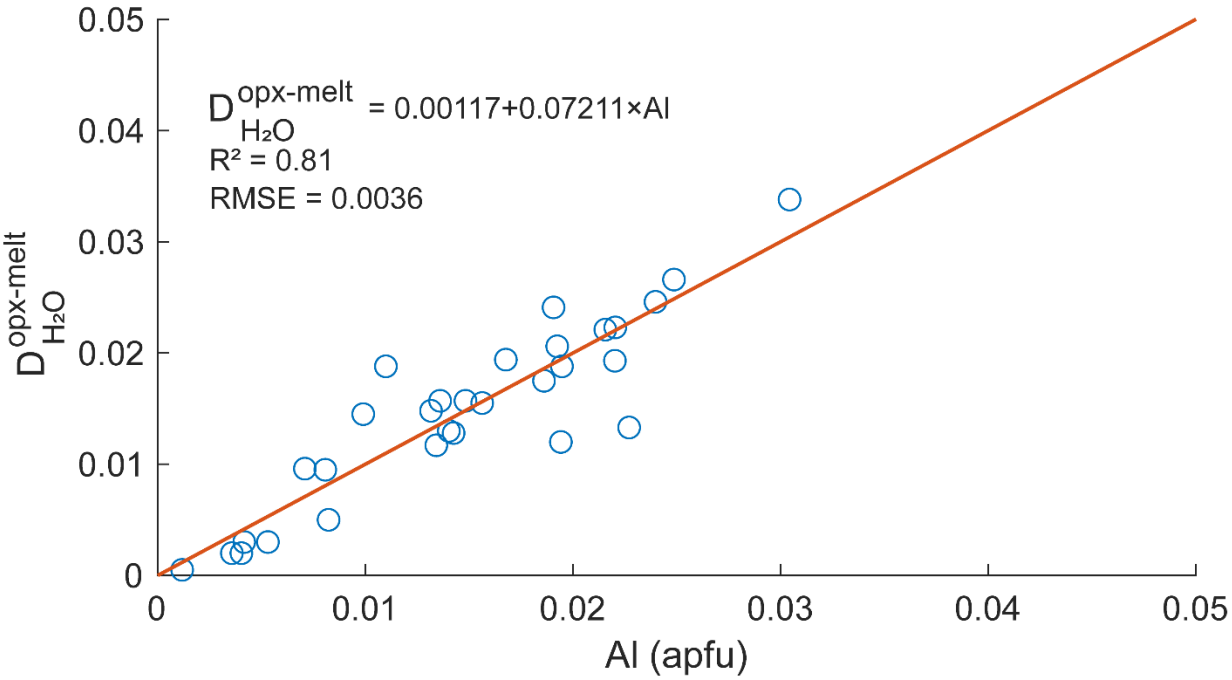

Fig. C4 Regression of orthopyroxene-melt H_2O partition coefficients against Al (apfu). Data are from a literature compilation (Table C9). Regression coefficients and associated uncertainties are also given in Table C10.

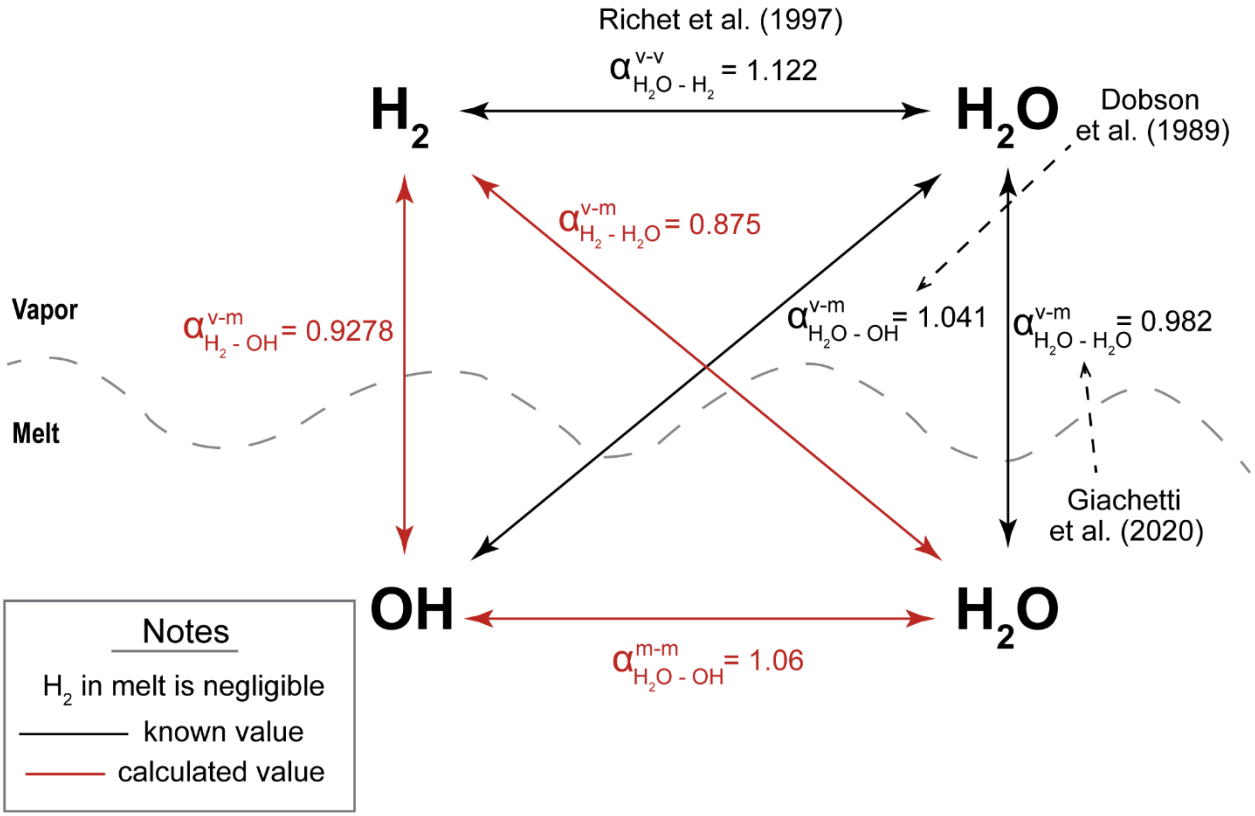

Fig. C5 Schematic illustrating the model equilibrium degassing system described in Sections 4.5.3.1 and C3. "Melt" refers to a silicate melt and "vapor" refers to a vapor composed of H and O bearing species. "α" is the isotopic fractionation factor (see Section S3 for details). Detailed descriptions for the values of $\alpha^{v-m}_{H_2O-OH}$ and $\alpha^{v-m}_{H_2O-H_2O}$ can be found in Giachetti et al. (2020).

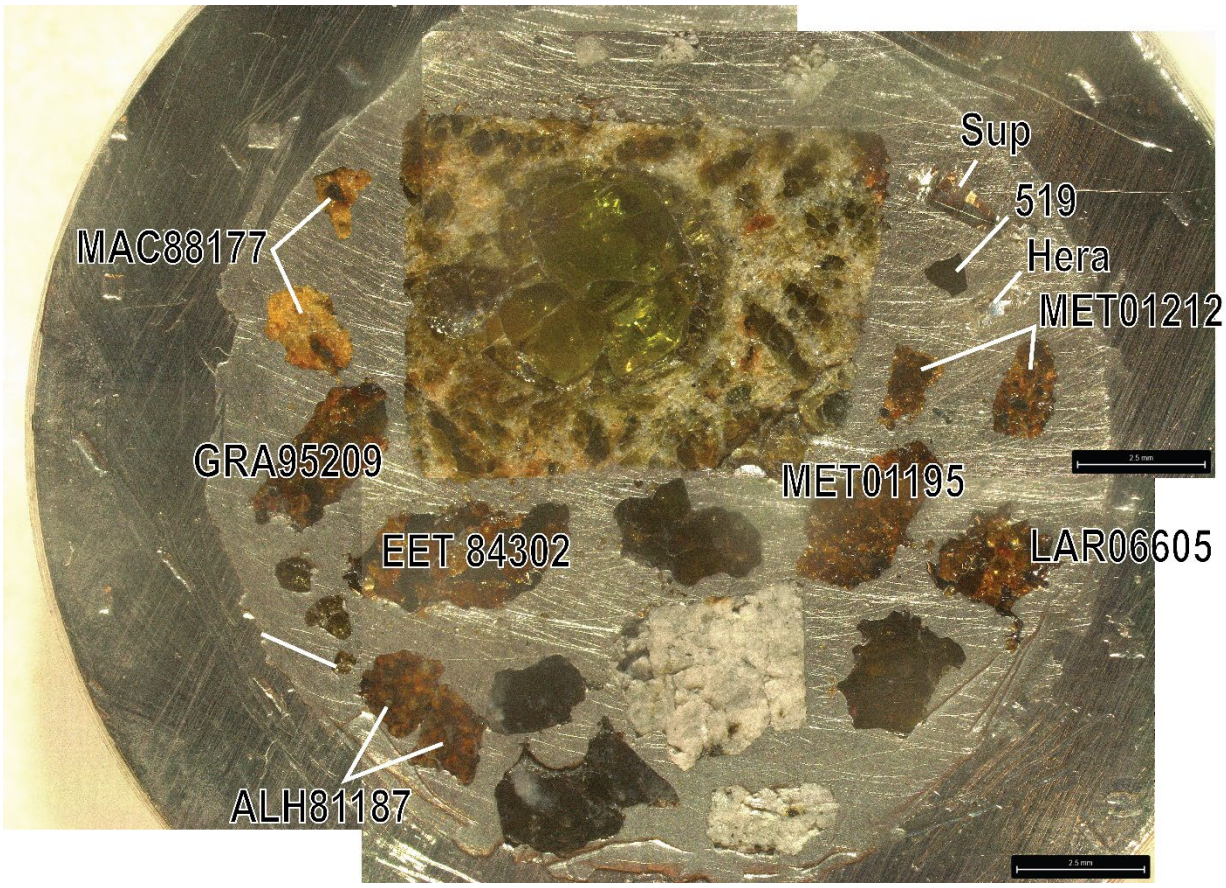

Fig. C6) Reflected light image showing 1" indium mount that held acapulcoites and lodranites studied. Unlabelled samples were not analyzed as part of this study.

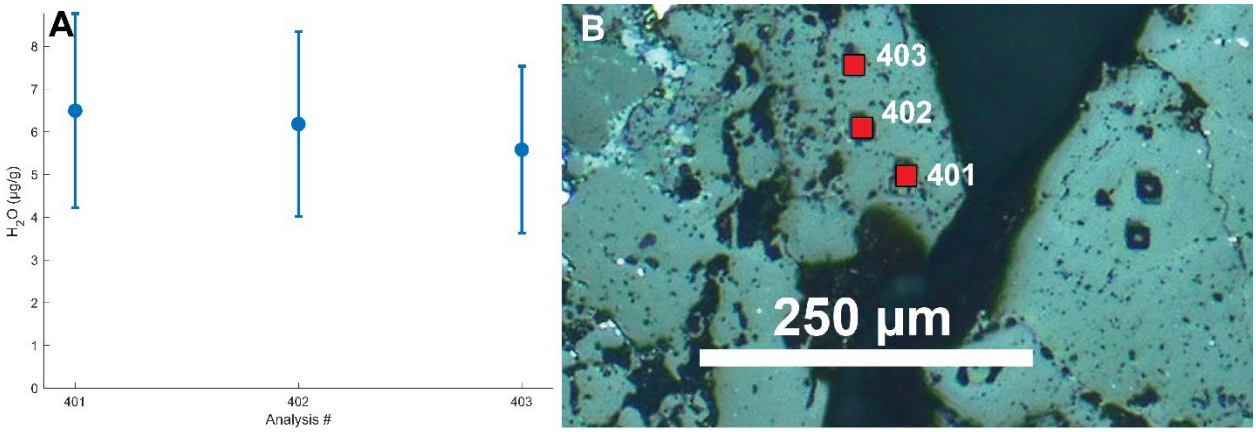

Fig. C7) A) H_2O concentrations measured along a transect of olivine ALH 81187-2. Uncertainties plotted are the larger value between the propagated uncertainty and the reproducibility based on the long-term reproducibility of Suprasil 3002 glass (35%; Section 4.5.1). B) Reflected light image of the measured grain. SIMS pits are highlighted by red-squares and numerical labels correspond to the analysis number. The blue tinting of the sample is an artifact of the light used and the polarizer set-up on the imaging scope. The very fine dark grey/black material on grain surfaces is remnant 0.25 µm alumina polish that was not removed by isopropanol spray following removal of the Au coat after SIMS analyses.

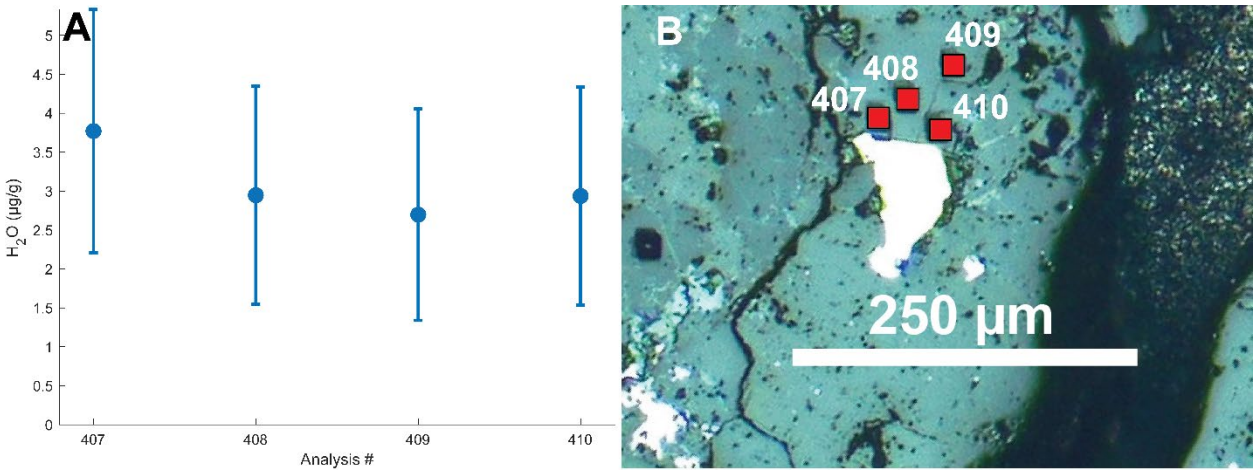

Fig. C8) A) H_2O concentrations measured along a transect of orthopyroxene ALH 81187-5. Uncertainties plotted are the larger value between the propagated uncertainty and the reproducibility based on the long-term reproducibility of Suprasil 3002 glass (35%; Section 4.5.1). B) Reflected light image of the measured grain. SIMS pits are highlighted by red-squares and numerical labels correspond to the analysis number. The blue tinting of the sample is an artifact of the light used and the polarizer set-up on the imaging scope. The very fine dark grey/black material on grain surfaces is remnant 0.25 µm alumina polish that was not removed by isopropanol spray following removal of the Au coat after SIMS analyses.

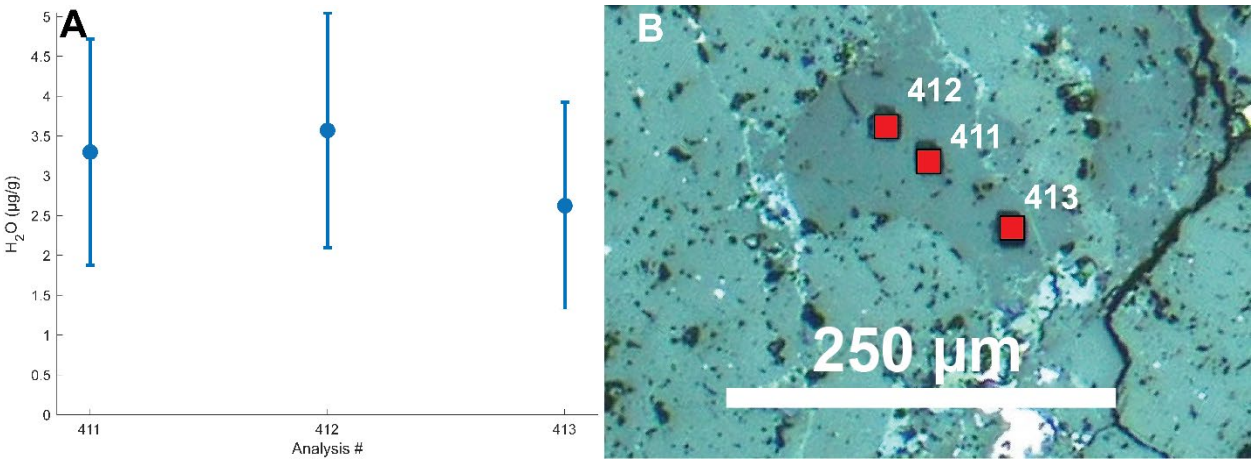

Fig. C9) A) H_2O concentrations measured along a transect of plagioclase ALH 81187-6. Uncertainties plotted are the larger value between the propagated uncertainty and the reproducibility based on the long-term reproducibility of Suprasil 3002 glass (35%; Section 4.5.1). B) Reflected light image of the measured grain. SIMS pits are highlighted by red-squares and numerical labels correspond to the analysis number. The blue tinting of the sample is an artifact of the light used and the polarizer set-up on the imaging scope. The very fine dark grey/black material on grain surfaces is remnant 0.25 µm alumina polish that was not removed by isopropanol spray following removal of the Au coat after SIMS analyses.

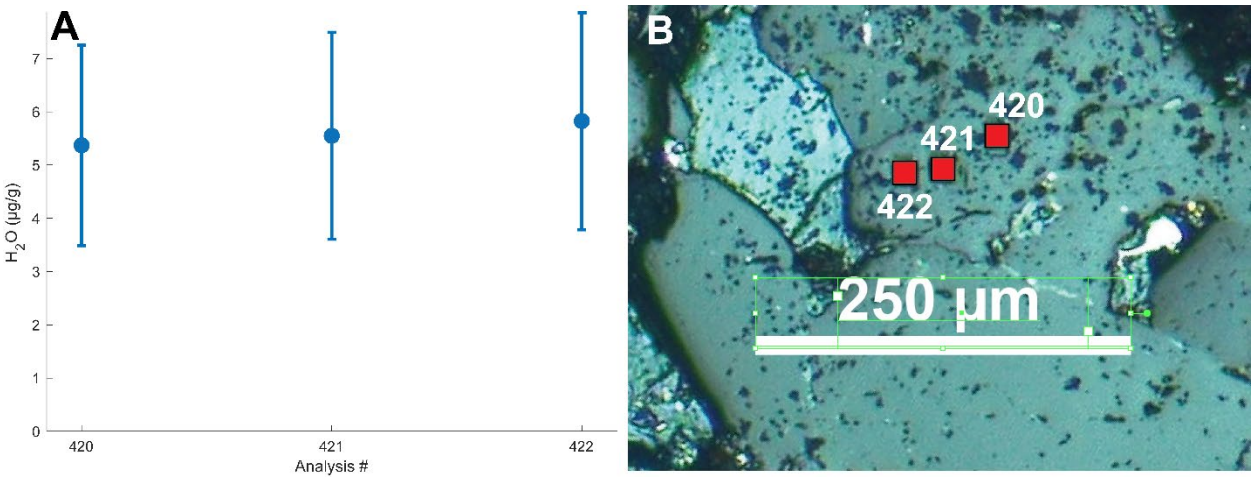

Fig. C10) A) H_2O concentrations measured along a transect of olivine ALH 81187-10. Uncertainties plotted are the larger value between the propagated uncertainty and the reproducibility based on the long-term reproducibility of Suprasil 3002 glass (35%; Section 4.5.1). B) Reflected light image of the measured grain. SIMS pits are highlighted by red-squares and numerical labels correspond to the analysis number. The blue tinting of the sample is an artifact of the light used and the polarizer set-up on the imaging scope. The very fine dark grey/black material on grain surfaces is remnant 0.25 µm alumina polish that was not removed by isopropanol spray following removal of the Au coat after SIMS analyses.

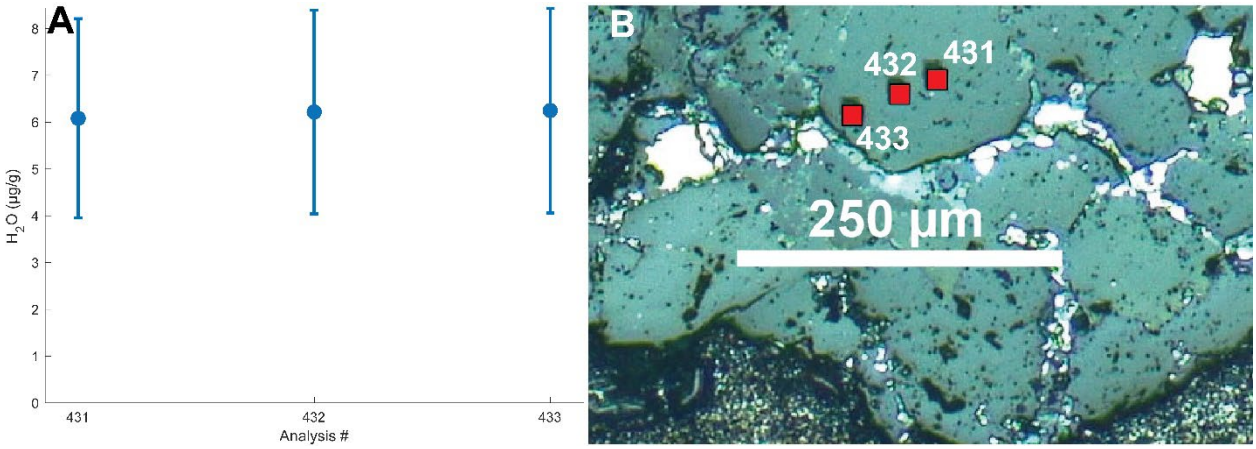

Fig. C11) A) H_2O concentrations measured along a transect of orthopyroxene ALH 81187-15. Uncertainties plotted are the larger value between the propagated uncertainty and the reproducibility based on the long-term reproducibility of Suprasil 3002 glass (35%; Section 4.5.1). B) Reflected light image of the measured grain. SIMS pits are highlighted by red-squares and numerical labels correspond to the analysis number. The blue tinting of the sample is an artifact of the light used and the polarizer set-up on the imaging scope. The very fine dark grey/black material on grain surfaces is remnant 0.25 µm alumina polish that was not removed by isopropanol spray following removal of the Au coat after SIMS analyses.

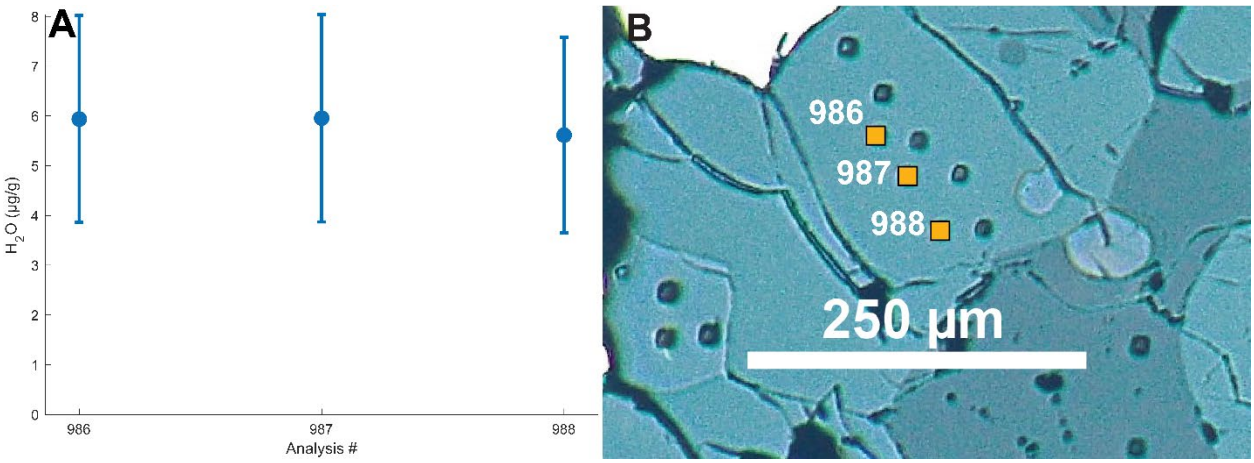

Fig. C12) A) H_2O concentrations measured along a transect of orthopyroxene EET 84302-1. Uncertainties plotted are the larger value between the propagated uncertainty and the reproducibility based on the long-term reproducibility of Suprasil 3002 glass (35%; Section 4.5.1). B) Reflected light image of the measured grain. SIMS pits are highlighted by orange-squares and numerical labels correspond to the analysis number. The blue tinting of the sample is an artifact of the light used and the polarizer set-up on the imaging scope.

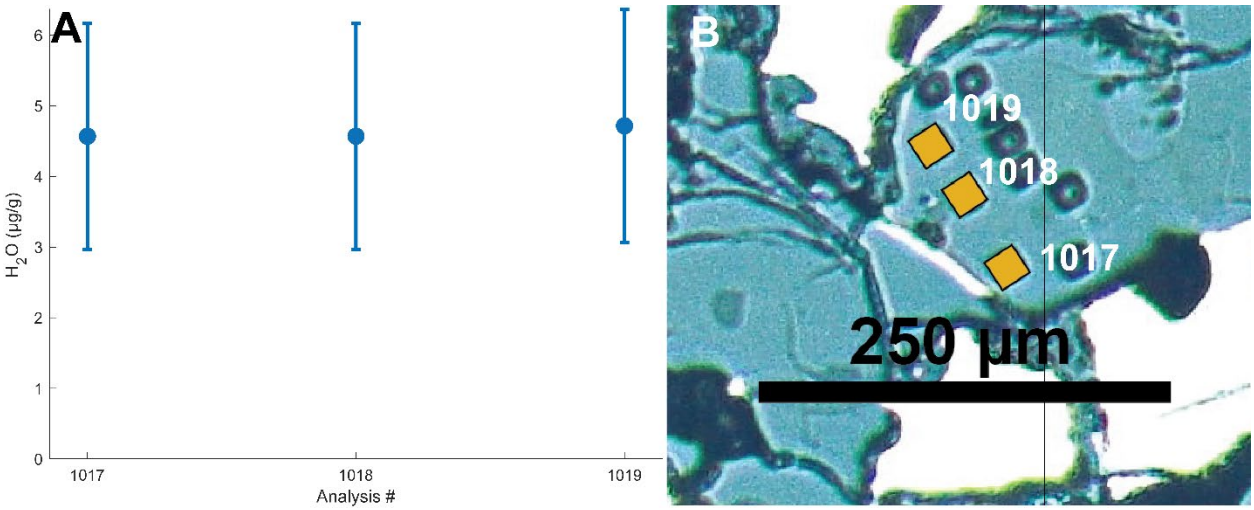

Fig. C13) A) H_2O concentrations measured along a transect of orthoopyroxene GRA 95209-2. Uncertainties plotted are the larger value between the propagated uncertainty and the reproducibility based on the long-term reproducibility of Suprasil 3002 glass (35%; Section 4.5.1). B) Reflected light image of the measured grain. SIMS pits are highlighted by orange-squares and numerical labels correspond to the analysis number. The blue tinting of the sample is an artifact of the light used and the polarizer set-up on the imaging scope.

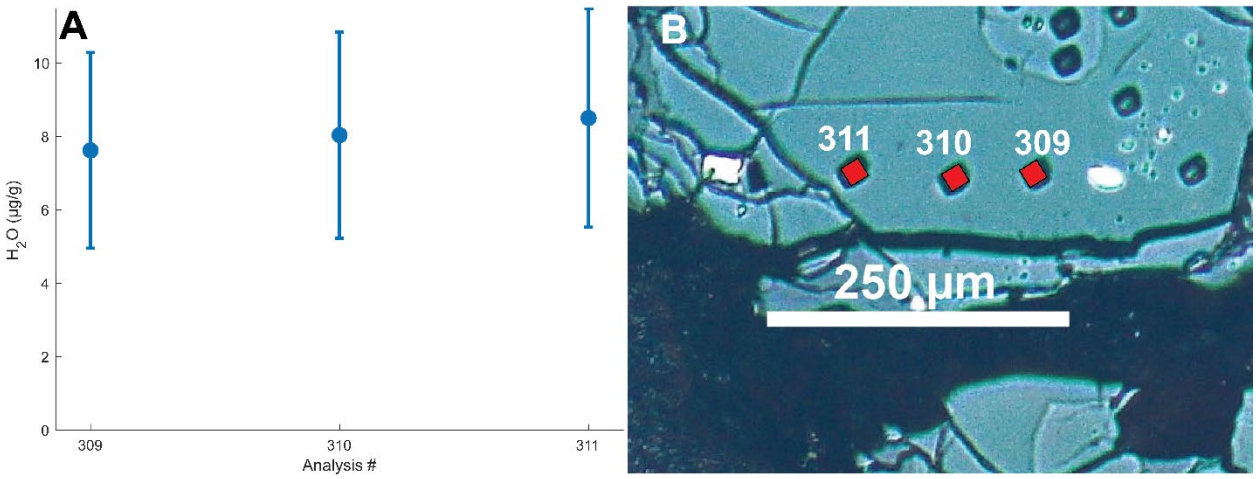

Fig. C14) A) H_2O concentrations measured along a transect of orthopyroxene GRA 95209-3. Uncertainties plotted are the larger value between the propagated uncertainty and the reproducibility based on the long-term reproducibility of Suprasil 3002 glass (35%; Section 4.5.1). B) Reflected light image of the measured grain. SIMS pits are highlighted by red-squares and numerical labels correspond to the analysis number. The blue tinting of the sample is an artifact of the light used and the polarizer set-up on the imaging scope.

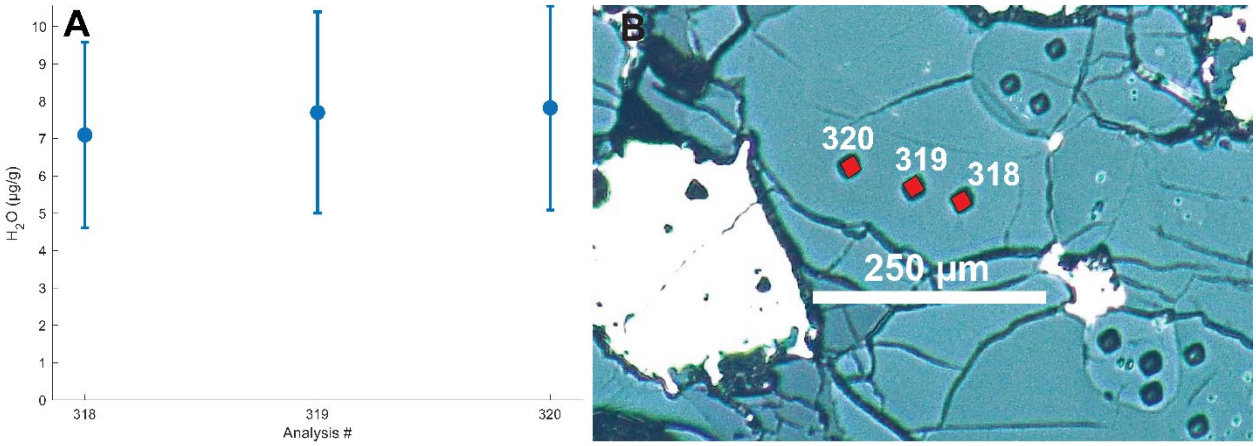

Fig. C15) A) H_2O concentrations measured along a transect of olivine GRA 95209-6. Uncertainties plotted are the larger value between the propagated uncertainty and the reproducibility based on the long-term reproducibility of Suprasil 3002 glass (35%; Section 4.5.1). B) Reflected light image of the measured grain. SIMS pits are highlighted by red-squares and numerical labels correspond to the analysis number. The blue tinting of the sample is an artifact of the light used and the polarizer set-up on the imaging scope.

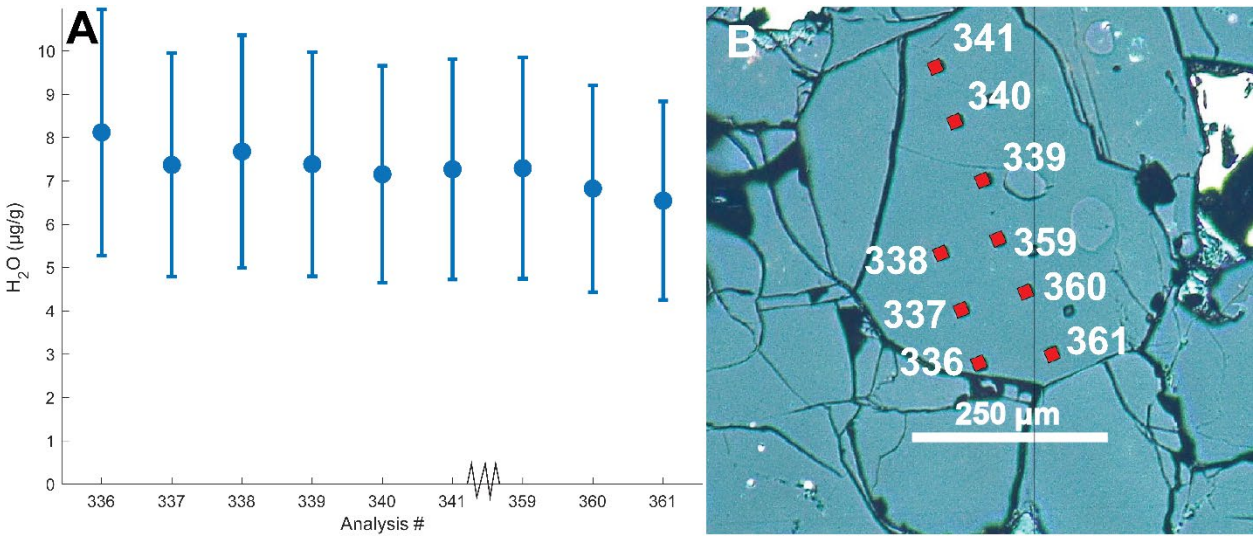

Fig. C16) A) H_2O concentrations measured along a transect of orthopyroxene LAR 06605-1. Uncertainties plotted are the larger value between the propagated uncertainty and the reproducibility based on the long-term reproducibility of Suprasil 3002 glass (35%; Section 4.5.1). B) Reflected light image of the measured grain. SIMS pits are highlighted by red-squares and numerical labels correspond to the analysis number. The blue tinting of the sample is an artifact of the light used and the polarizer set-up on the imaging scope.

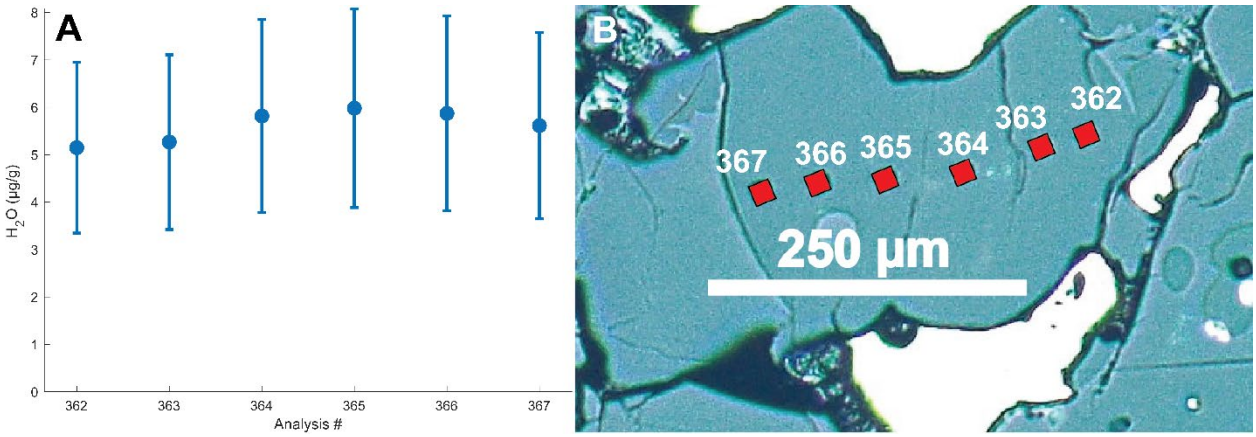

Fig. C17) A) H_2O concentrations measured along a transect of orthopyroxene LAR 06605-2. Uncertainties plotted are the larger value between the propagated uncertainty and the reproducibility based on the long-term reproducibility of Suprasil 3002 glass (35%; Section 4.5.1). B) Reflected light image of the measured grain. SIMS pits are highlighted by red-squares and numerical labels correspond to the analysis number. The blue tinting of the sample is an artifact of the light used and the polarizer set-up on the imaging scope.

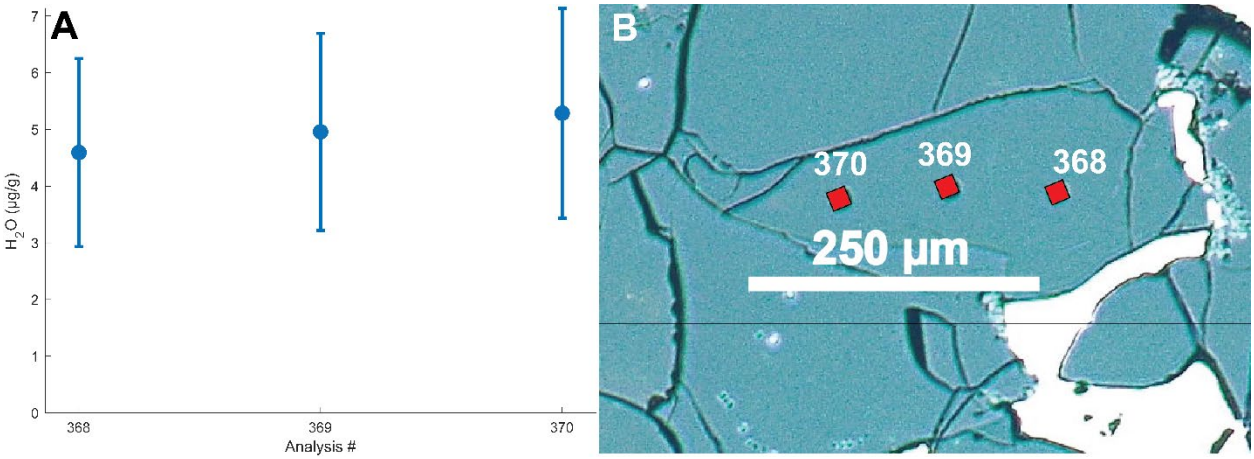

Fig. C18) A) H_2O concentrations measured along a transect of orthopyroxene LAR 06605-3. Uncertainties plotted are the larger value between the propagated uncertainty and the reproducibility based on the long-term reproducibility of Suprasil 3002 glass (35%; Section 4.5.1). B) Reflected light image of the measured grain. SIMS pits are highlighted by red-squares and numerical labels correspond to the analysis number. The blue tinting of the sample is an artifact of the light used and the polarizer set-up on the imaging scope.

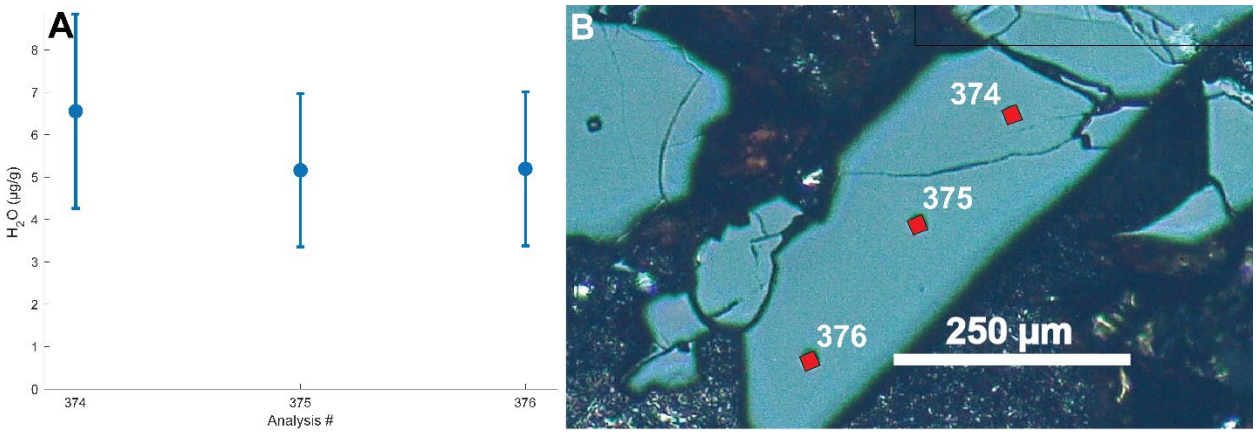

Fig. C19) A) H_2O concentrations measured along a transect of orthopyroxene LAR 06605-5. Uncertainties plotted are the larger value between the propagated uncertainty and the reproducibility based on the long-term reproducibility of Suprasil 3002 glass (35%; Section 4.5.1). B) Reflected light image of the measured grain. SIMS pits are highlighted by red-squares and numerical labels correspond to the analysis number. The blue tinting of the sample is an artifact of the light used and the polarizer set-up on the imaging scope.

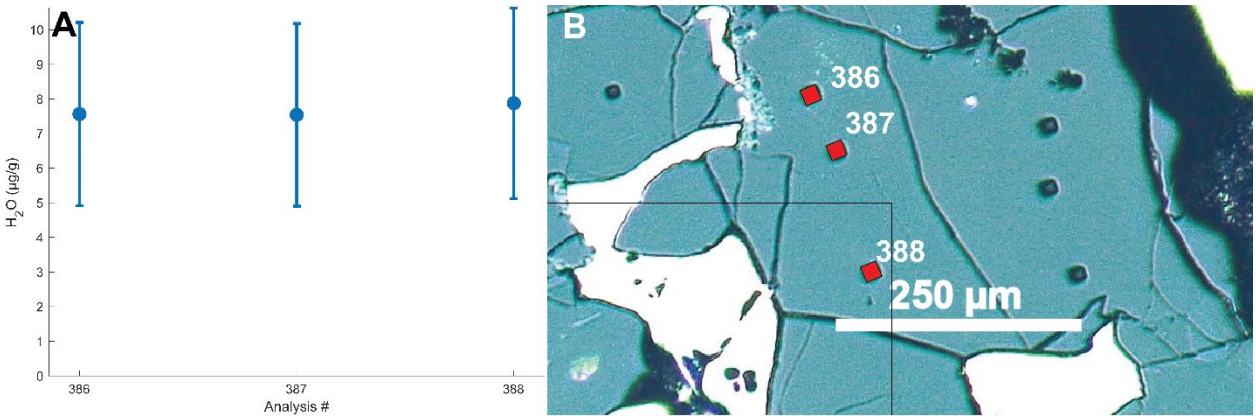

Fig. C20) A) H_2O concentrations measured along a transect of olivine LAR 06605-9. Uncertainties plotted are the larger value between the propagated uncertainty and the reproducibility based on the long-term reproducibility of Suprasil 3002 glass (35%; Section 4.5.1). B) Reflected light image of the measured grain. SIMS pits are highlighted by red-squares and numerical labels correspond to the analysis number. The blue tinting of the sample is an artifact of the light used and the polarizer set-up on the imaging scope.

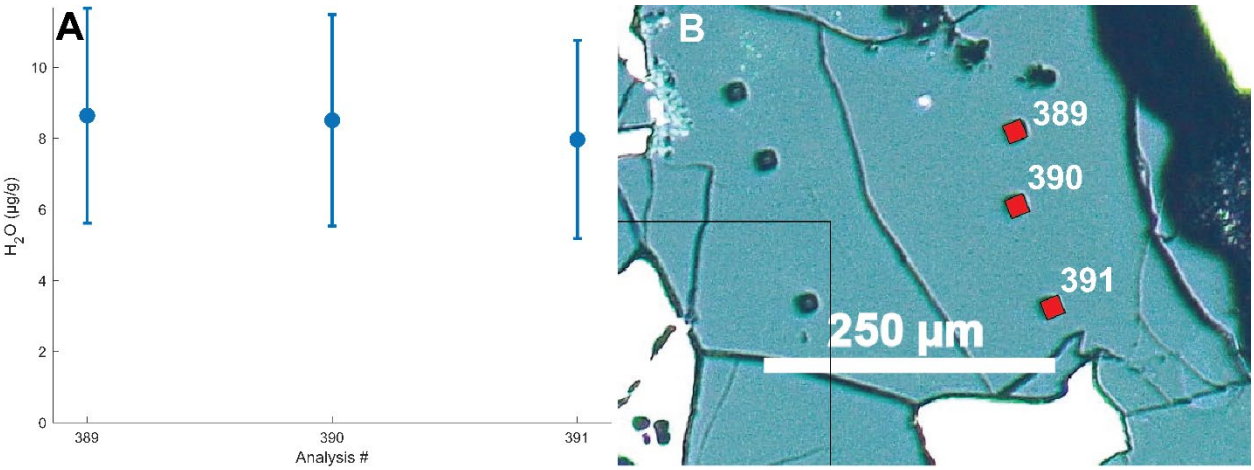

Fig. C21) A) H_2O concentrations measured along a transect of olivine LAR 06605-10. Uncertainties plotted are the larger value between the propagated uncertainty and the reproducibility based on the long-term reproducibility of Suprasil 3002 glass (35%; Section 4.5.1). B) Reflected light image of the measured grain. SIMS pits are highlighted by red-squares and numerical labels correspond to the analysis number. The blue tinting of the sample is an artifact of the light used and the polarizer set-up on the imaging scope.

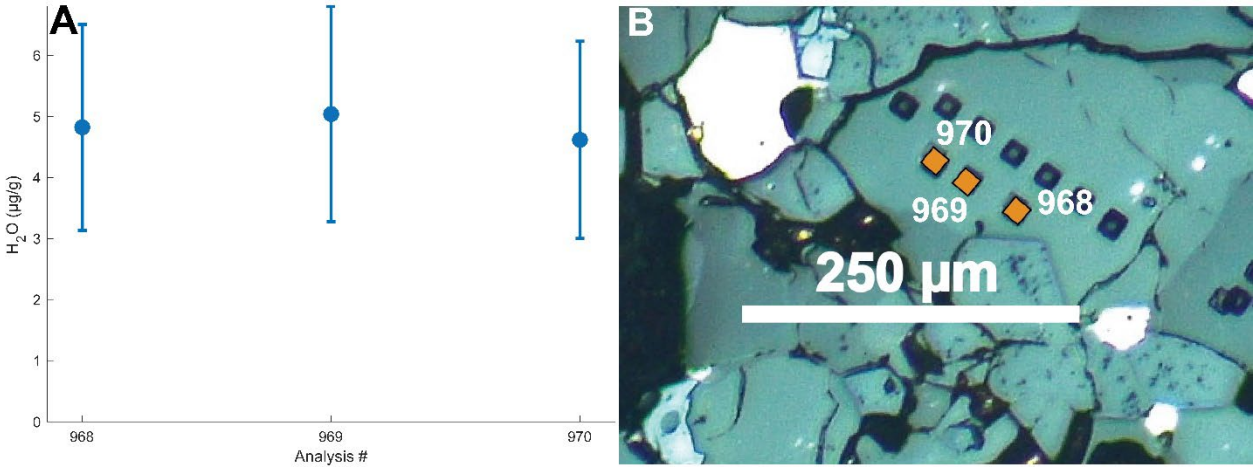

Fig. C22) A) H_2O concentrations measured along a transect of orthopyroxene MET 01195-2. Uncertainties plotted are the larger value between the propagated uncertainty and the reproducibility based on the long-term reproducibility of Suprasil 3002 glass (35%; Section 4.5.1). B) Reflected light image of the measured grain. SIMS pits are highlighted by red-squares and numerical labels correspond to the analysis number. The blue tinting of the sample is an artifact of the light used and the polarizer set-up on the imaging scope. The very fine dark grey/black material on some grain surfaces is remnant 0.25 µm alumina polish that was not removed by isopropanol spray following removal of the Au coat after SIMS analyses.

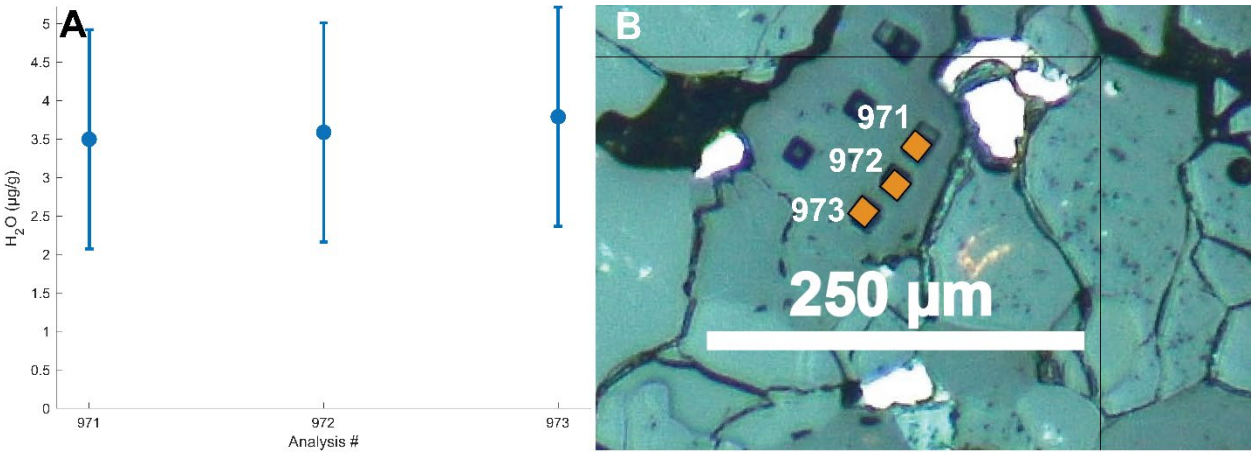

Fig. C23) A) H_2O concentrations measured along a transect of plagioclase MET 01195-8. Uncertainties plotted are the larger value between the propagated uncertainty and the reproducibility based on the long-term reproducibility of Suprasil 3002 glass (35%; Section 4.5.1). B) Reflected light image of the measured grain. SIMS pits are highlighted by red-squares and numerical labels correspond to the analysis number. The blue tinting of the sample is an artifact of the light used and the polarizer set-up on the imaging scope. The very fine dark grey/black material on some grain surfaces is remnant 0.25 µm alumina polish that was not removed by isopropanol spray following removal of the Au coat after SIMS analyses.

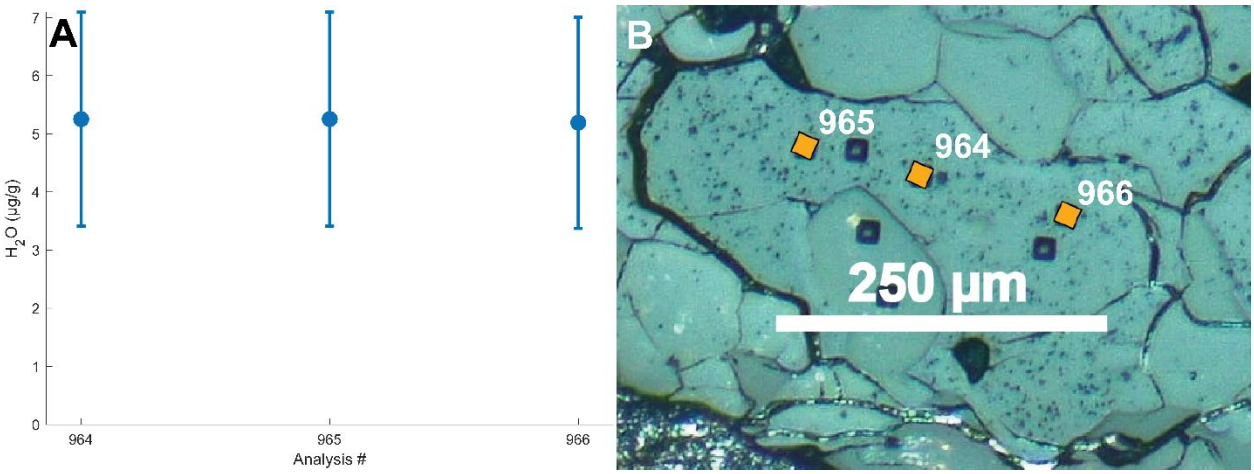

Fig. C24) A) H_2O concentrations measured along a transect of olivine MET 01212L-2. Uncertainties plotted are the larger value between the propagated uncertainty and the reproducibility based on the long-term reproducibility of Suprasil 3002 glass (35%; Section 4.5.1). B) Reflected light image of the measured grain. SIMS pits are highlighted by red-squares and numerical labels correspond to the analysis number. The blue tinting of the sample is an artifact of the light used and the polarizer set-up on the imaging scope. The very fine dark grey/black material on some grain surfaces is remnant 0.25 µm alumina polish that was not removed by isopropanol spray following removal of the Au coat after SIMS analyses.

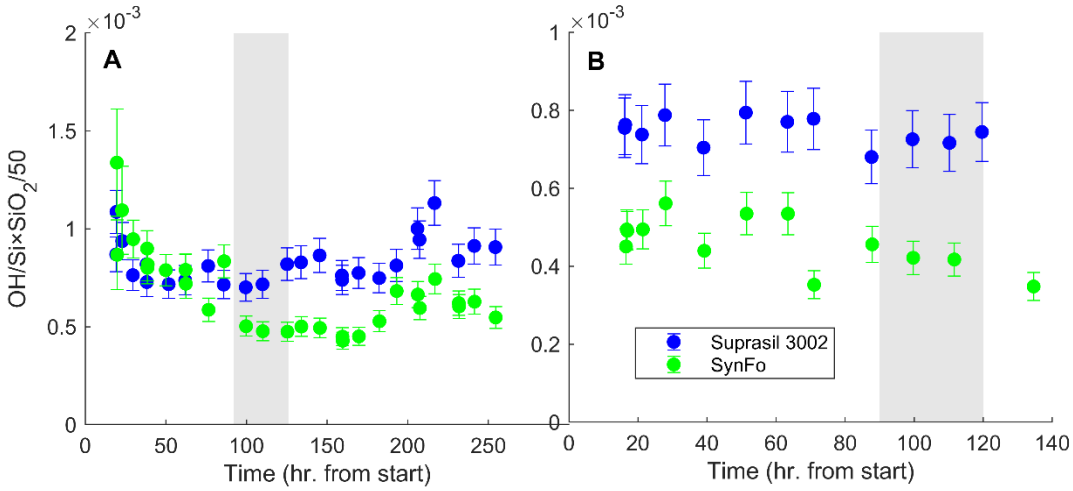

Fig. C25) Comparison of non- blank and drift-corrected OH/Si×SiO_2/50 data for Suprasil 3002 glass and synthetic forsterite (SynFo) held in the clinopyroxene standard mount and frequently re-analyzed throughout the a) 01/22 session and b) the 02/22 session. Grey vertical bars denote the subsection of analyses for which data was gathered for this study.

Appendix D: The partitioning of H between olivine and melt at low pressures (10 - 200 MPa)

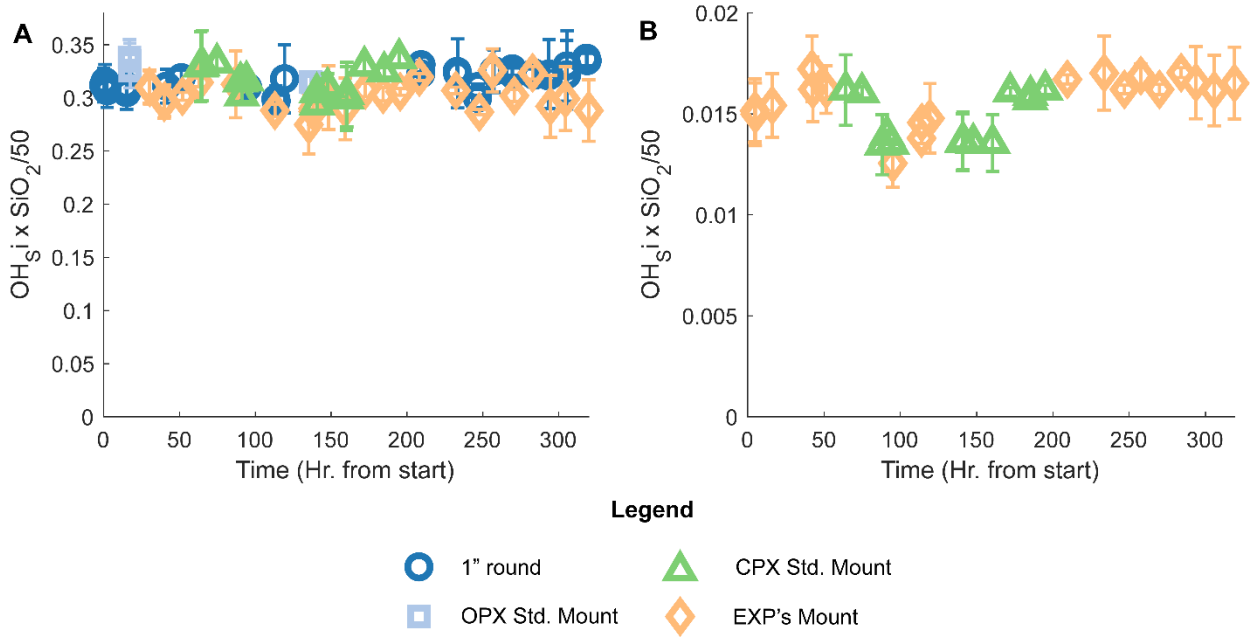

Fig. D1) Plots of OH/Si × SiO_2/50 for reference materials A) ALV-519-4-1 and B) Herasil glass for the 03/23 NAMs analytical session. No unknowns used in this study were held in the 1" round in panel A. Uncertainties are the propagated uncertainty due to counting statistics and an assumed 5% uncertainty for the SiO_2 correction.

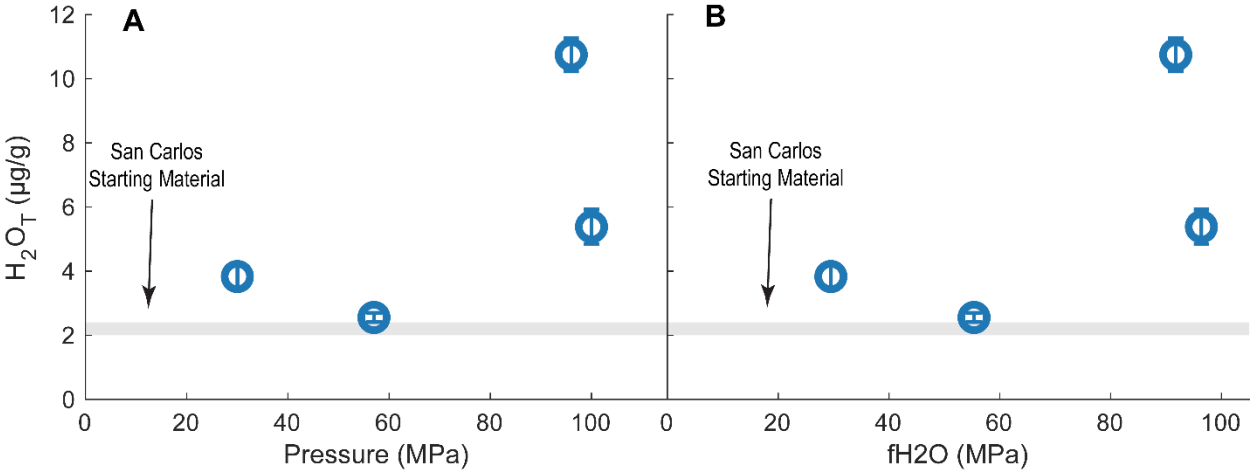

Fig. D2) Plots of San Carlos olivine seed grain H_2O_T concentrations from 82-72f run products plotted against A) pressure and B) fH_2O. The grey bar represents the H_2O_T concentration of the San Carlos olivine used as the starting material for seed grains. Uncertainties are 1 standard deviation from the mean.

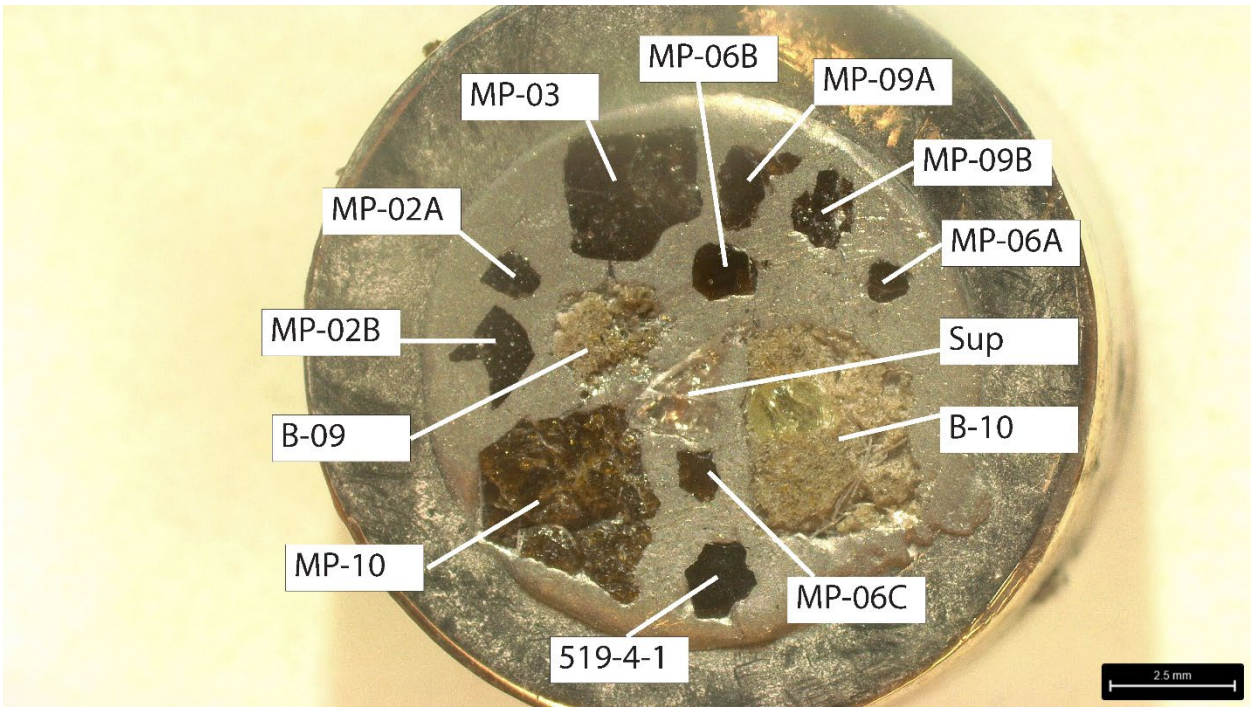

Fig. D3) Overview map of mount 1 holding run products of newly conducted experiments. Sup – Suprasil 3002 glass.

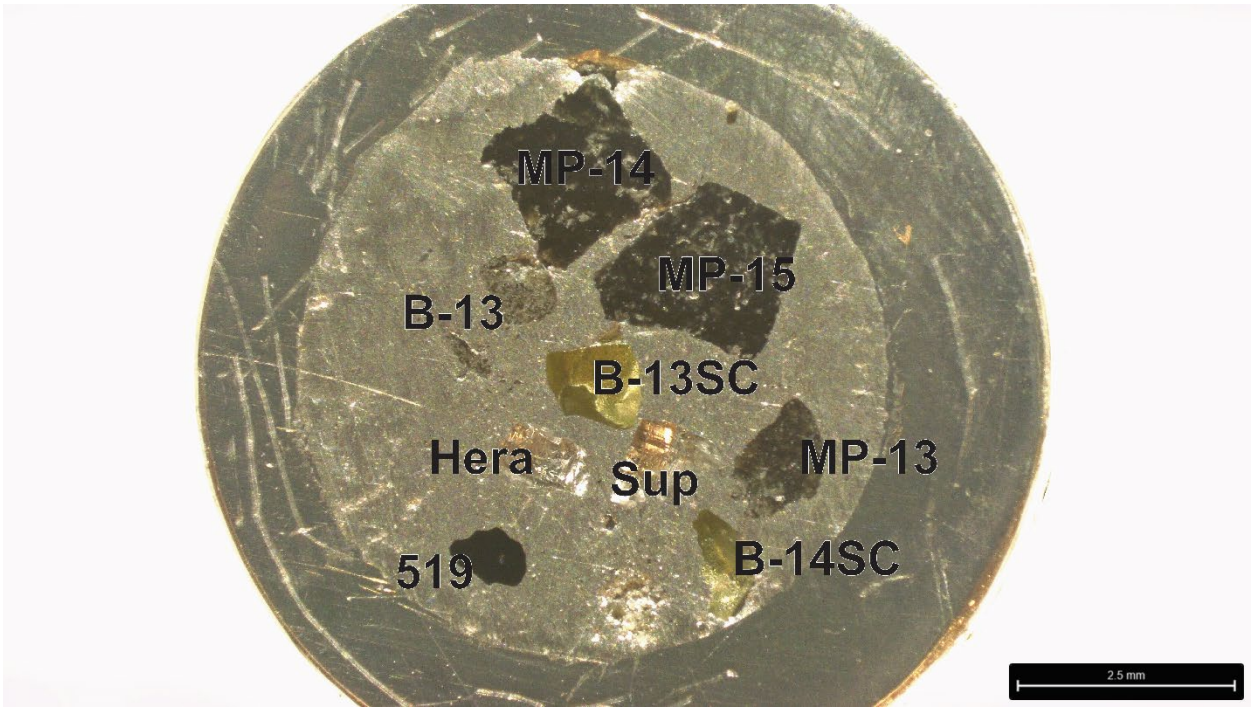

Fig. D4) Overview map of mount 2 holding run products of newly conducted experiments. Sup – Suprasil 3002 glass; Hera – Herasil glass; 519 – ALV-519-4-1.

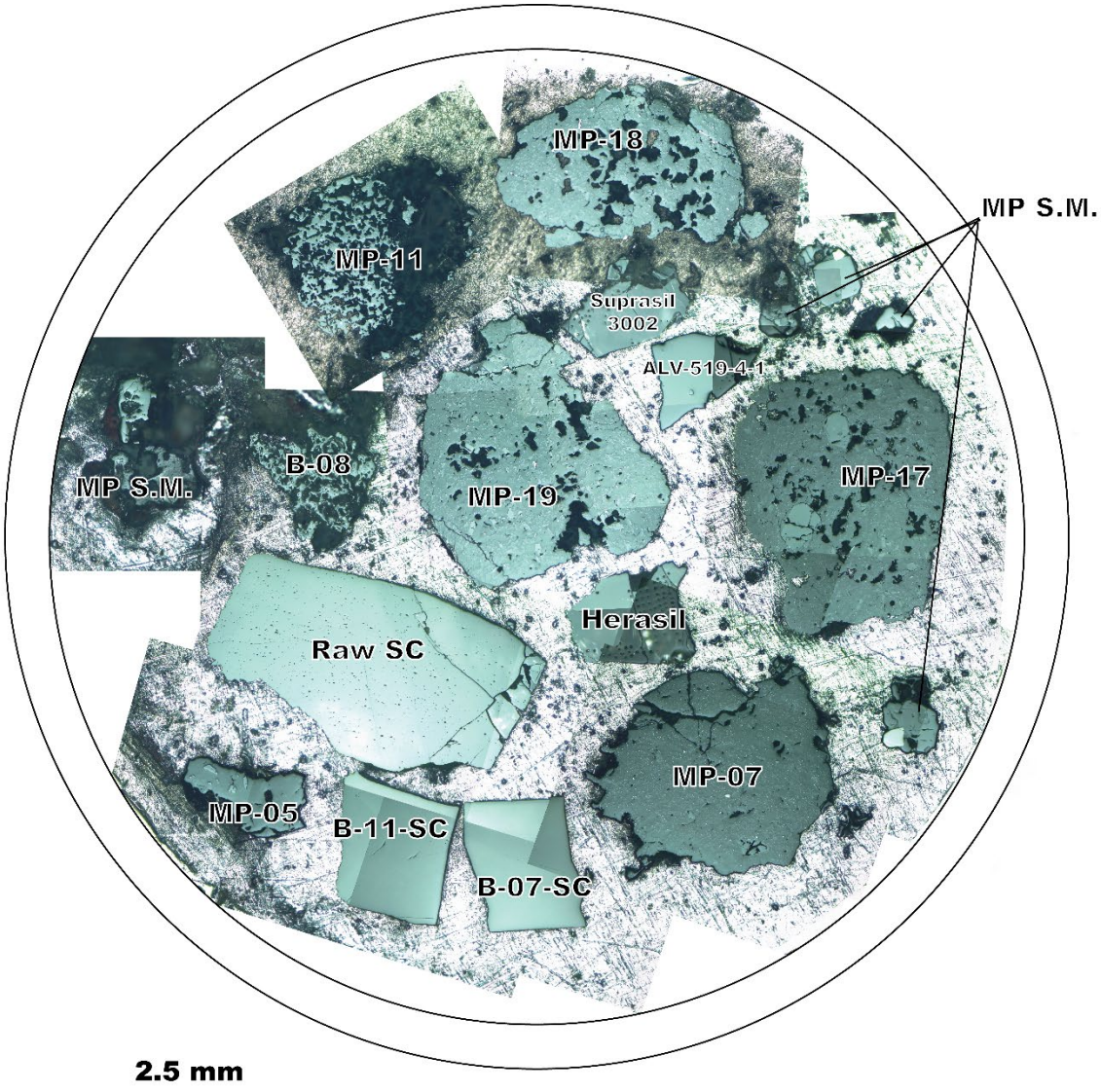

Fig. D5) Overview map of mount 3 holding run products of newly conducted experiments.

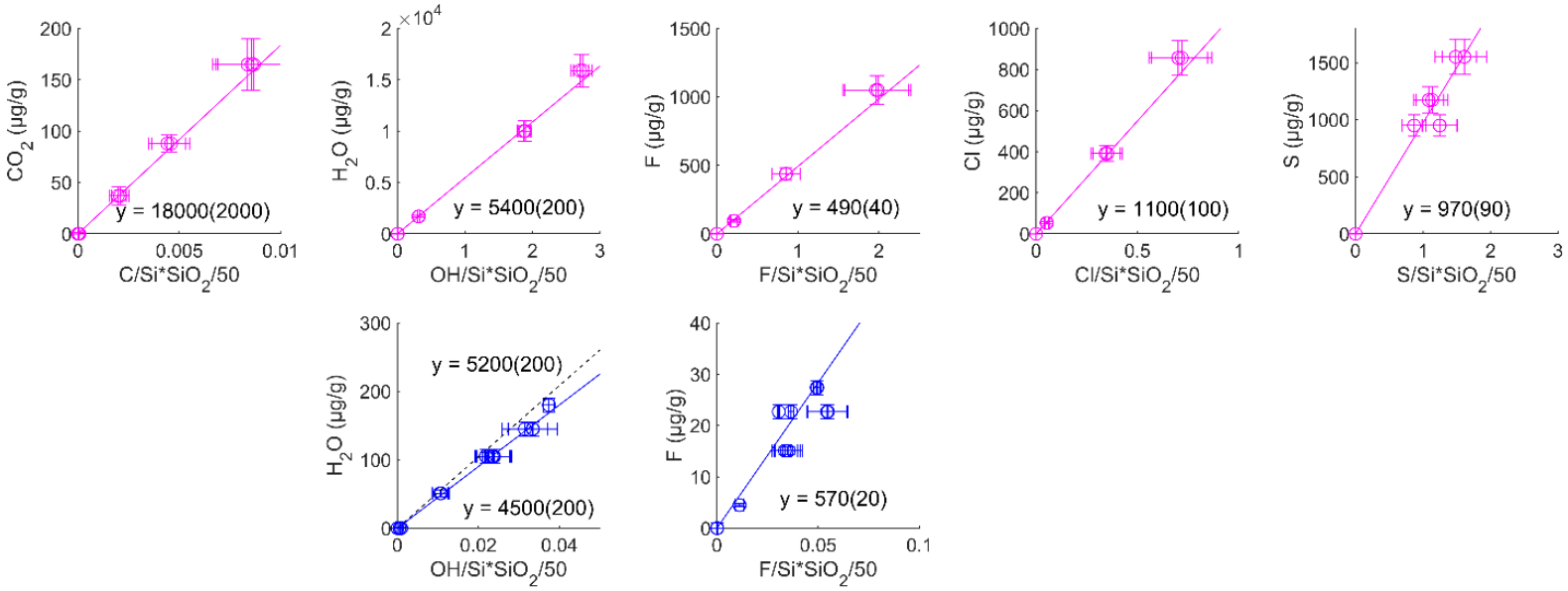

Fig. D6) SIMS calibration curves for C, H, F, Cl, and S in glass (pink) and orthopyroxene (blue) for the 03/23 NAMs analytical session. Uncertainties reported in parentheses are 1 standard error as determined using a York regression. For the H_2O calibration curve for orthopyroxene, the dotted line is the calibration curve generated using the standard values from Kumamoto et al. (2017) and the solid line is generated using the revised values from Towbin et al. (2023).

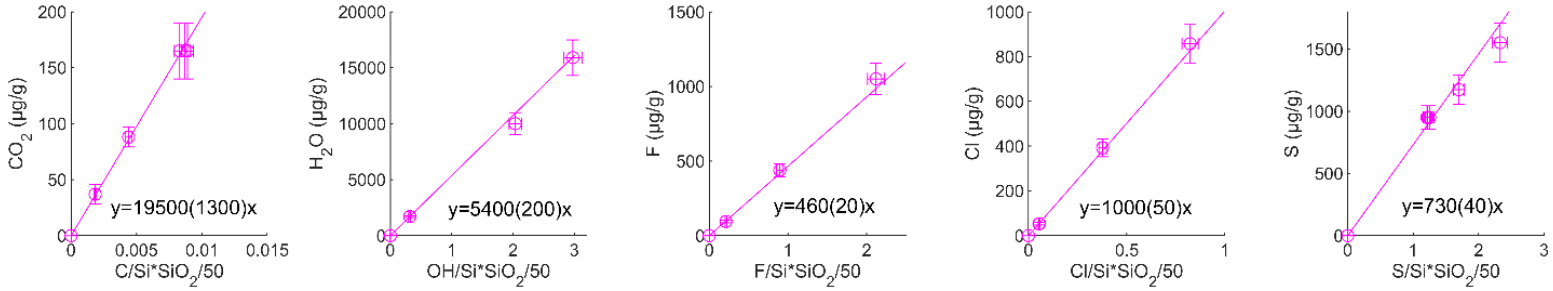

Fig. D7) SIMS calibration curves for C, H, F, Cl, and S in glass for the 08/22 glass analytical session. Uncertainties reported in parentheses are 1 standard error as determined using a York regression.

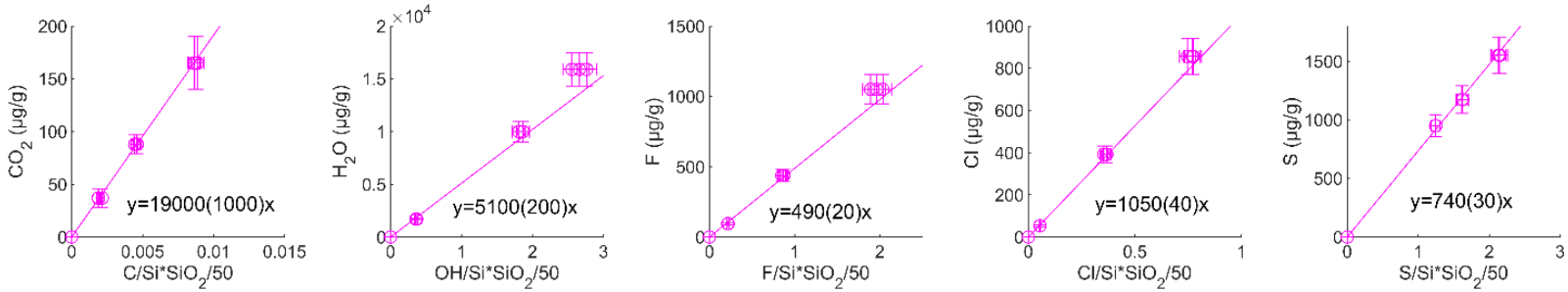

Fig. D8) SIMS calibration curves for C, H, F, Cl, and S in glass for the 03/23 glass analytical session. Uncertainties reported in parentheses are 1 standard error as determined using a York regression.

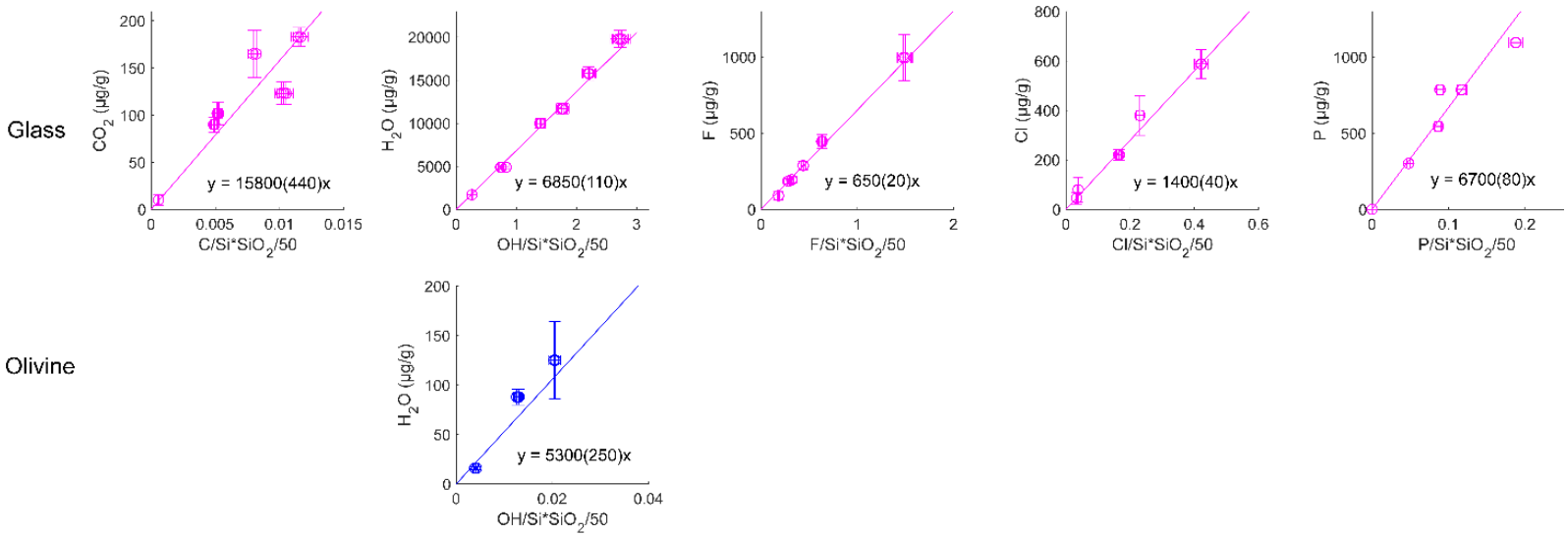

Fig. D9) SIMS calibration curves for C, H, F, Cl, and P in glass and H in olivine for analyses of "prior experiments" (see Main text). Uncertainties reported in parentheses are 1 standard error as determined using a York regression.

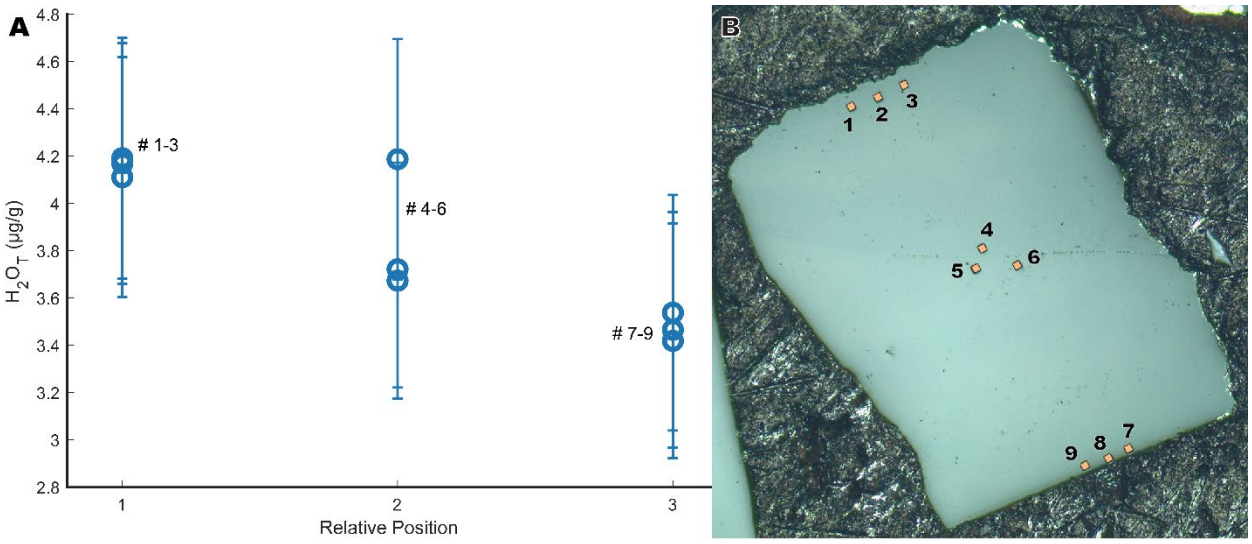

Fig. D10) Approximate transect for NanoSIMS analyses of the San Carlos olivine seed grain from charge B-07 (i.e., B-07-SC). A) H_2O_T concentration vs. relative position, and B) map of analyses showing points from A. Yellow squares are about 15 × 15µm. A rescalable map with a scale bar can be found in supplementary file "Spot_Maps.zip".

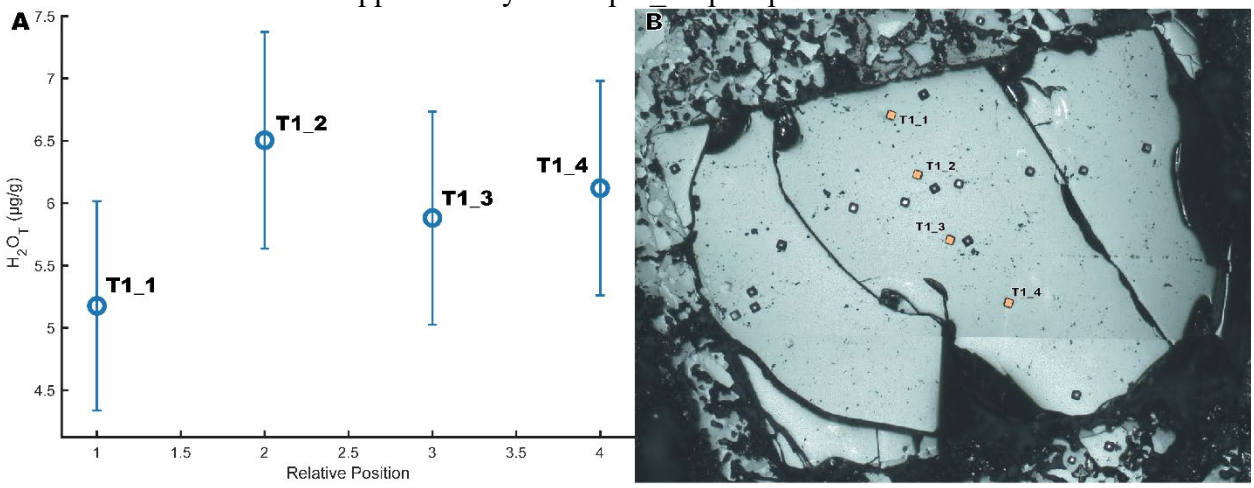

Fig. D11) Approximate transect for NanoSIMS analyses of the San Carlos olivine seed grain from charge B-10 (i.e., B-10-SC). A) H_2O_T concentration vs. relative position, and B) map of analyses showing points from A. Yellow squares are about 15 × 15µm. A rescalable map with a scale bar can be found in supplementary file "Spot_Maps.zip".

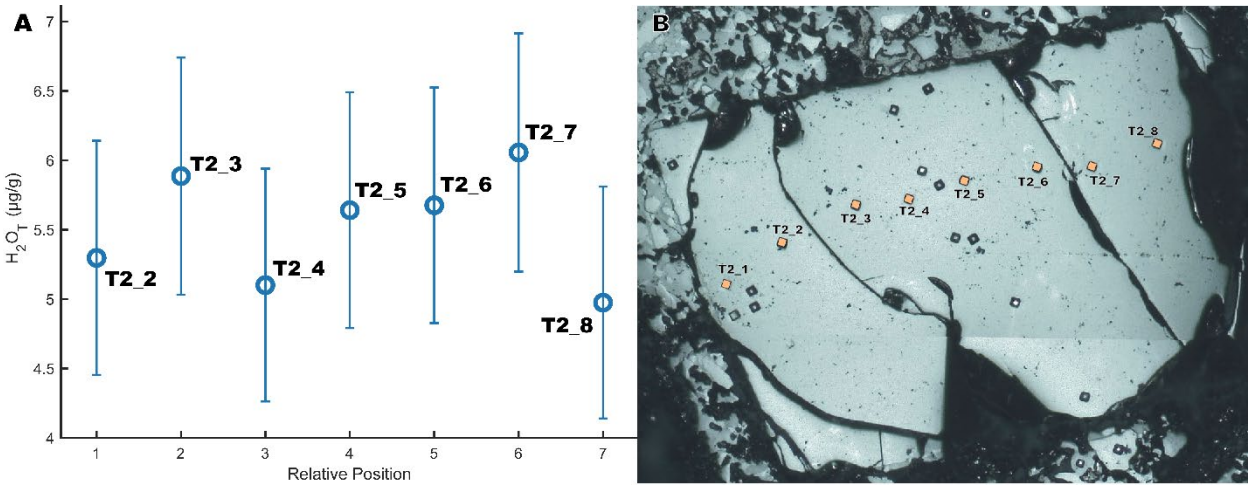

Fig. D12) Approximate transect for NanoSIMS analyses of the San Carlos olivine seed grain from charge B-10 (i.e., B-10-SC). A) H_2O_T concentration vs. relative position, and B) map of analyses showing points from A. Yellow squares are about 15 × 15µm. A rescalable map with a scale bar can be found in supplementary file "Spot_Maps.zip".

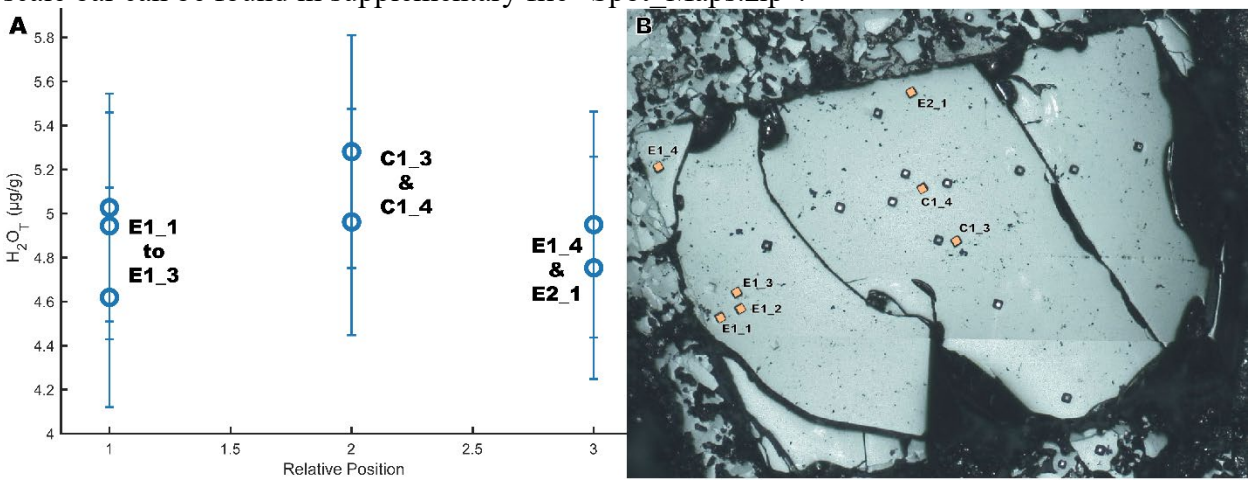

Fig. D13) Approximate transect for NanoSIMS analyses of the San Carlos olivine seed grain from charge B-10 (i.e., B-10-SC). A) H_2O_T concentration vs. relative position, and B) map of analyses showing points from A. Yellow squares are about 15 × 15µm. A rescalable map with a scale bar can be found in supplementary file "Spot_Maps.zip".

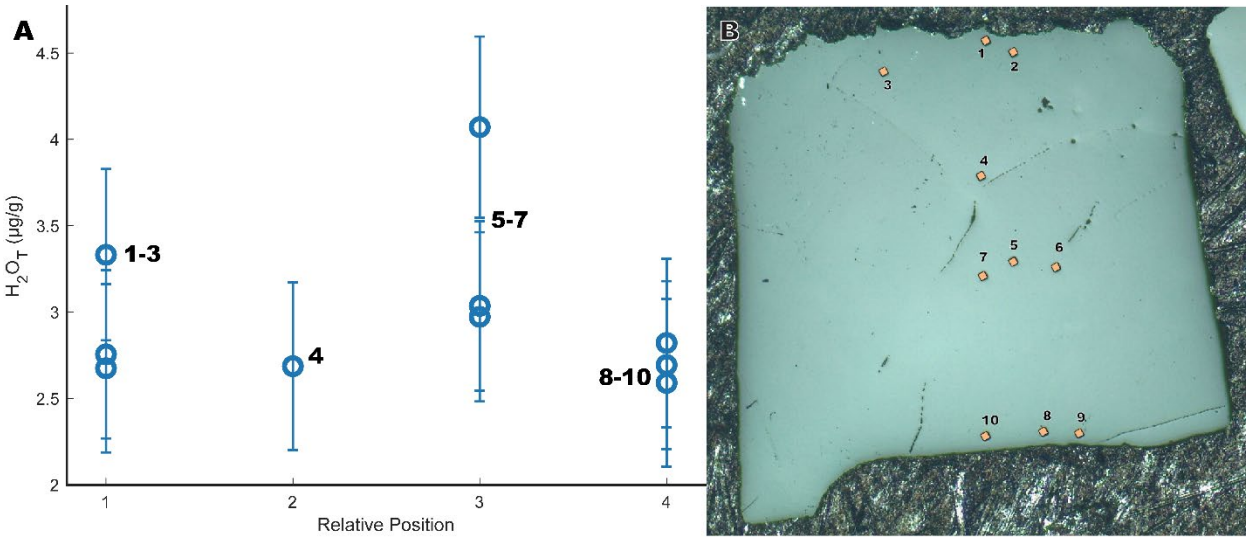

Fig. D14) Approximate transect for NanoSIMS analyses of the San Carlos olivine seed grain from charge B-11 (i.e., B-11-SC). A) H_2O_T concentration vs. relative position, and B) map of analyses showing points from A. Yellow squares are about 15 × 15µm. A rescalable map with a scale bar can be found in supplementary file "Spot_Maps.zip".

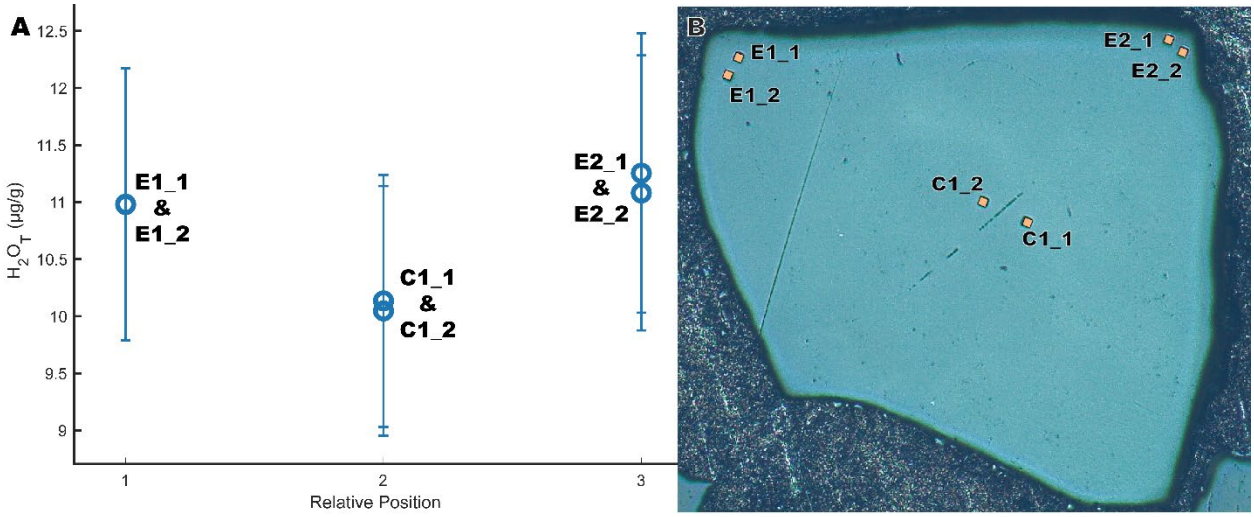

Fig. D15) Approximate transect for NanoSIMS analyses of the San Carlos olivine seed grain from charge B-13 (i.e., B-13-SC). A) H_2O_T concentration vs. relative position, and B) map of analyses showing points from A. Yellow squares are about 15 × 15µm. A rescalable map with a scale bar can be found in supplementary file "Spot_Maps.zip".

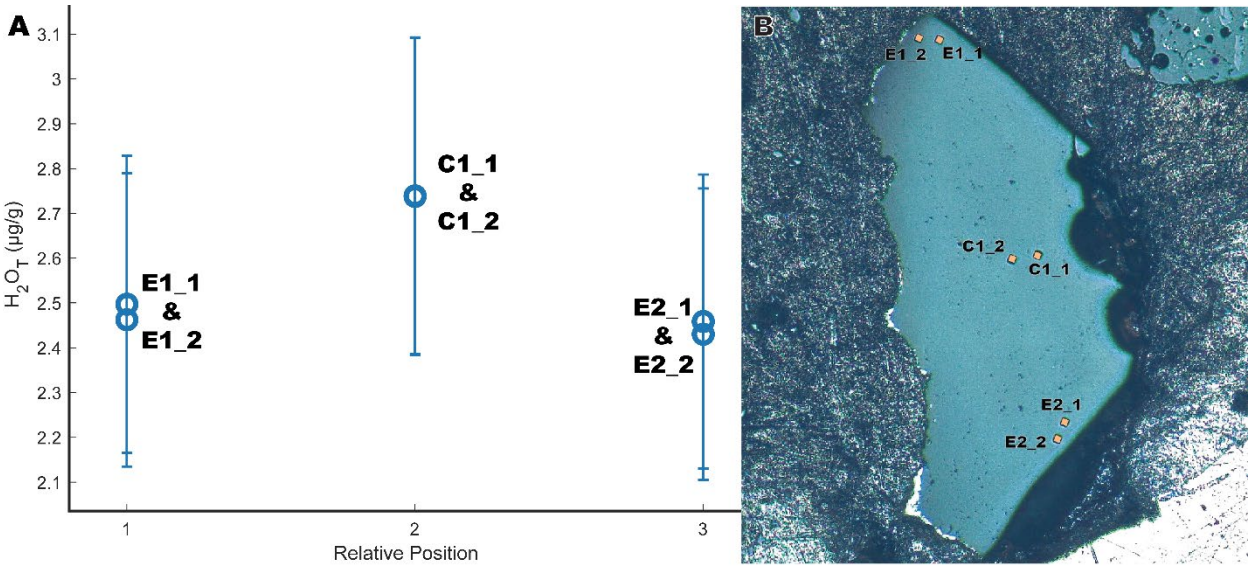

Fig. D16) Approximate transect for NanoSIMS analyses of the San Carlos olivine seed grain from charge B-14 (i.e., B-14-SC). A) H_2O_T concentration vs. relative position, and B) map of analyses showing points from A. Yellow squares are about 15 × 15µm. A rescalable map with a scale bar can be found in supplementary file "Spot_Maps.zip".

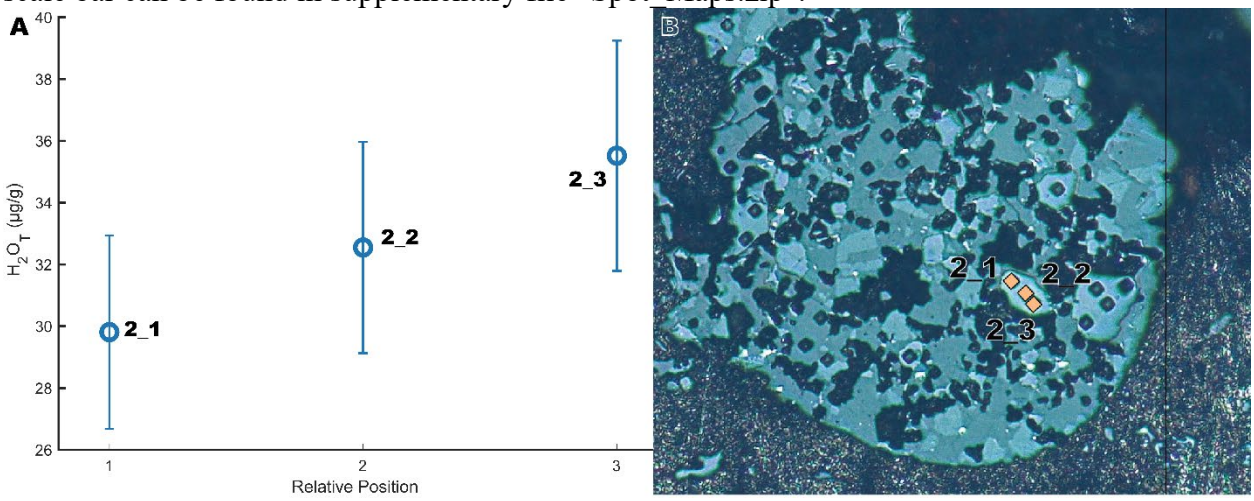

Fig. D17) Approximate transect for NanoSIMS analyses of a grown olivine from charge B-13 (i.e., B-13-Ol2). A) H_2O_T concentration vs. relative position, and B) map of analyses showing points from A. Yellow squares are about 15 × 15µm. A rescalable map with a scale bar can be found in supplementary file "Spot_Maps.zip".

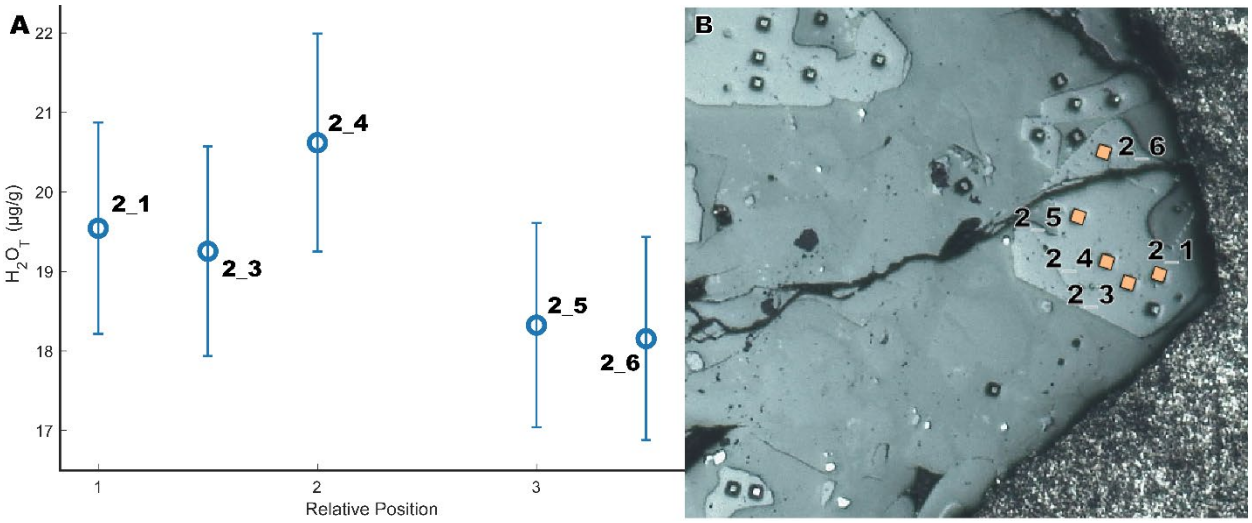

Fig. D18) Approximate transect for NanoSIMS analyses of a likely seed grain from charge MP-10 (i.e., MP-10-G2). A) H_2O_T concentration vs. relative position, and B) map of analyses showing points from A. Yellow squares are about 15 × 15µm. A rescalable map with a scale bar can be found in supplementary file "Spot_Maps.zip".

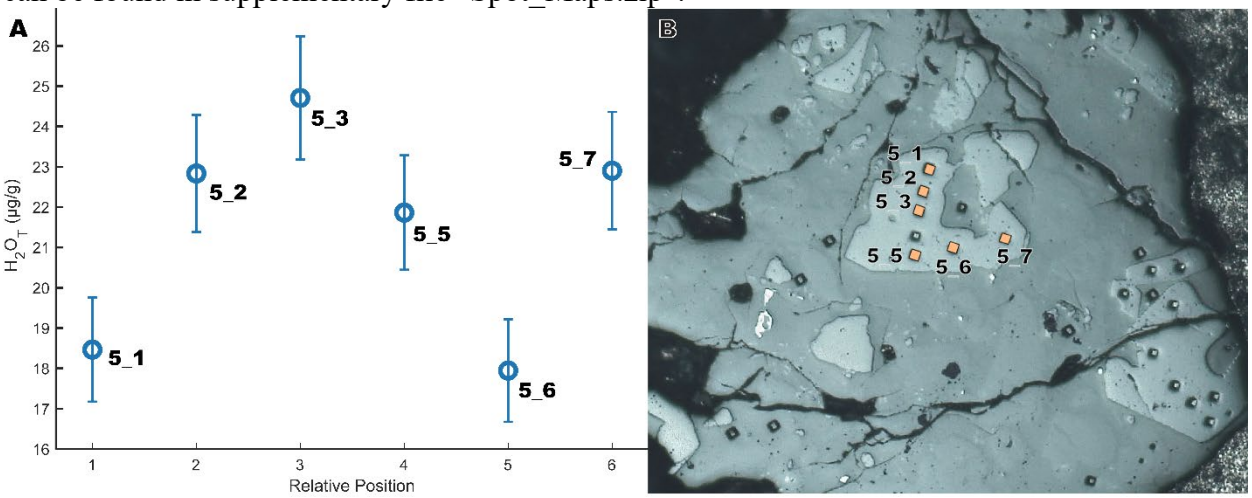

Fig. D19) Approximate transect for NanoSIMS analyses of a likely seed grain from charge MP-10 (i.e., MP-10-G5). A) H_2O_T concentration vs. relative position, and B) map of analyses showing points from A. Yellow squares are about 15 × 15µm. A rescalable map with a scale bar can be found in supplementary file "Spot_Maps.zip".

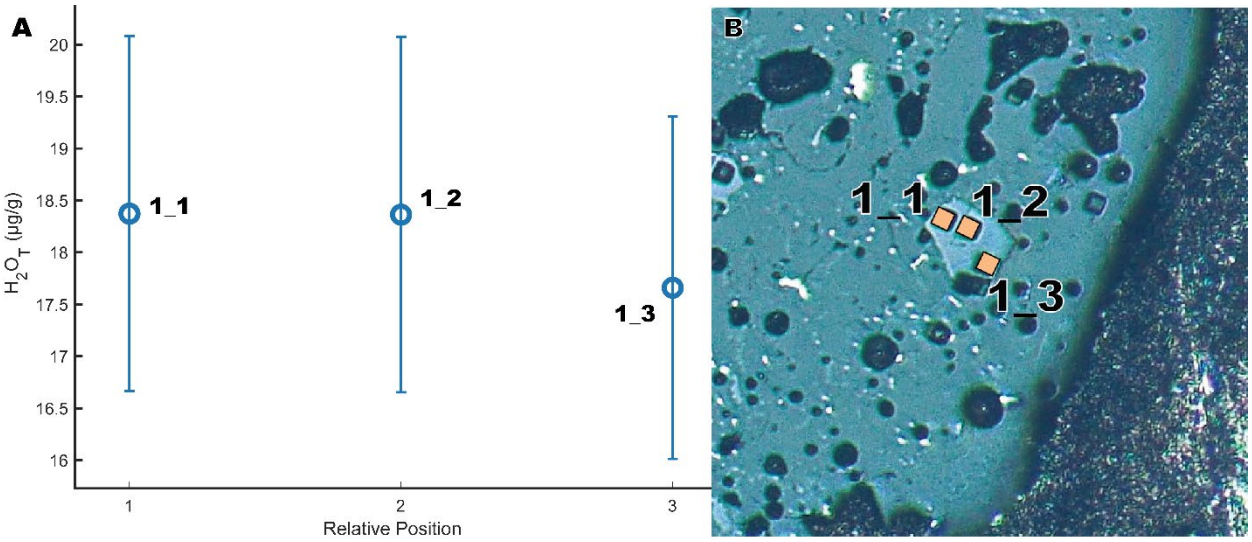

Fig. D20) Approximate transect for NanoSIMS analyses of a potentially grown grain from charge MP-13 (i.e., MP-13-Ol1). A) H_2O_T concentration vs. relative position, and B) map of analyses showing points from A. Yellow squares are about 15 × 15µm. A rescalable map with a scale bar can be found in supplementary file "Spot_Maps.zip".

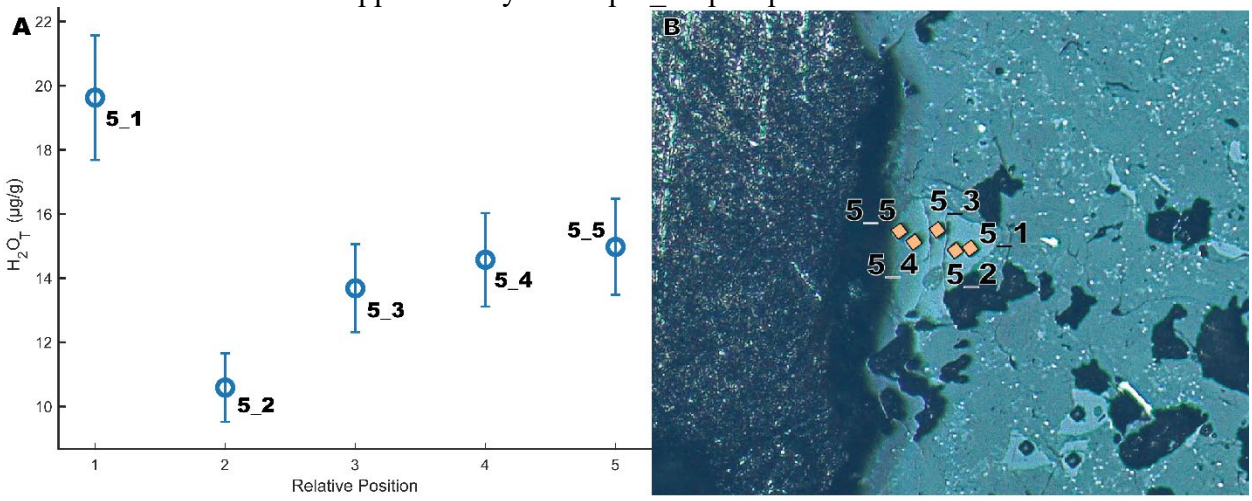

Fig. D21) Approximate transect for NanoSIMS analyses of a likely seed grain from charge MP-14 (i.e., MP-14-Ol5). A) H_2O_T concentration vs. relative position, and B) map of analyses showing points from A. Yellow squares are about 15 × 15µm. A rescalable map with a scale bar can be found in supplementary file "Spot_Maps.zip".

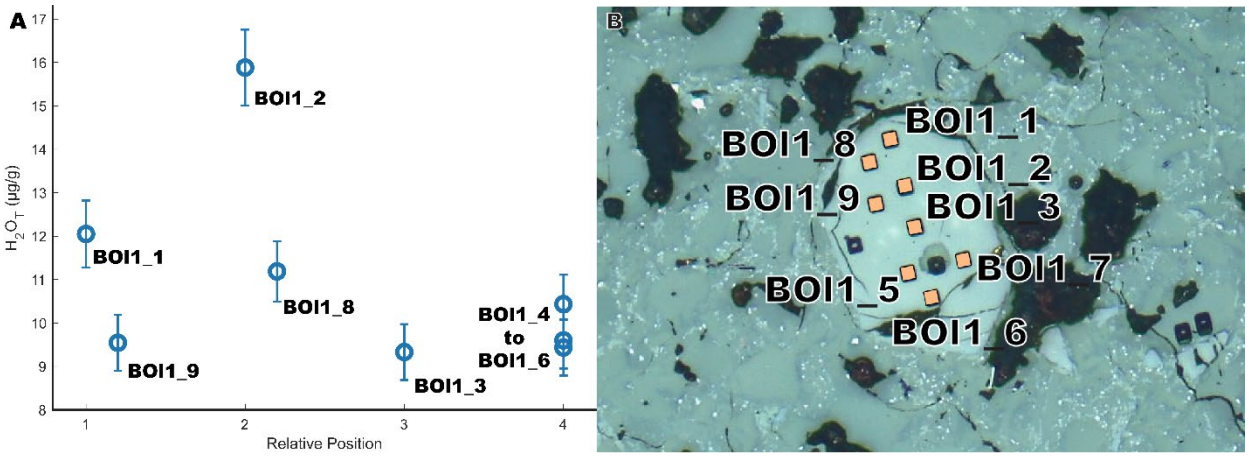

Fig. D22) Approximate transect for NanoSIMS analyses of a likely seed grain from charge MP-17 (i.e., MP-17-BOl1). A) H_2O_T concentration vs. relative position, and B) map of analyses showing points from A. Yellow squares are about 15 × 15µm. A rescalable map with a scale bar can be found in supplementary file "Spot_Maps.zip".

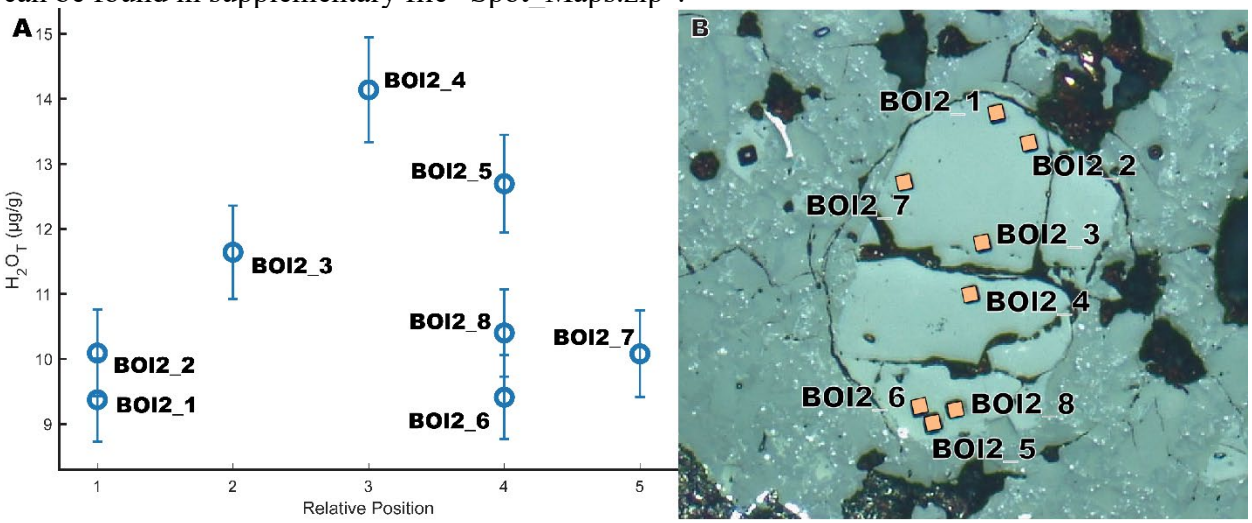

Fig. D23) Approximate transect for NanoSIMS analyses of a likely seed grain from charge MP-17 (i.e., MP-17-BOl2). A) H_2O_T concentration vs. relative position, and B) map of analyses showing points from A. Yellow squares are about 15 × 15µm. A rescalable map with a scale bar can be found in supplementary file "Spot_Maps.zip".

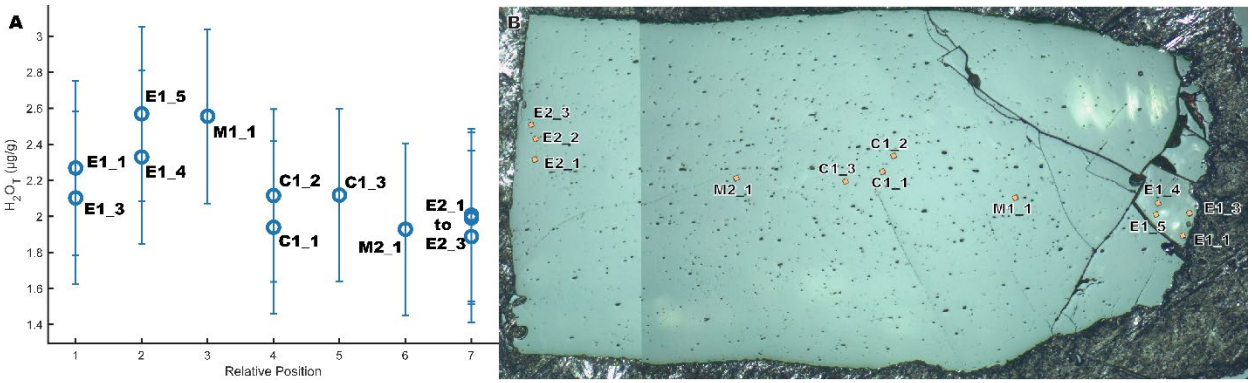

Fig. D24) Approximate transect for NanoSIMS analyses of an unprocessed piece of San Carlos olivine starting material. A) H_2O_T concentration vs. relative position, and B) map of analyses showing points from A. Yellow squares are about 15 × 15µm. A rescalable map with a scale bar can be found in supplementary file "Spot_Maps.zip".

Bibliography

Adam J., Turner M., Hauri E. H. and Turner S. (2016) Crystal/melt partitioning of water and other volatiles during the near-solidus melting of mantle peridotite: Comparisons with non-volatile incompatible elements and implications for the generation of intraplate magmatism. *American Mineralogist* **101**, 876–888.

Alex A. and Zajacz Z. (2020) A new method to quantitatively control oxygen fugacity in externally heated pressure vessel experiments. *European Journal of Mineralogy* **32**, 219–234.

Alexander C. M. O'D. (2022) An exploration of whether Earth can be built from chondritic components, not bulk chondrites. *Geochimica et Cosmochimica Acta* **318**, 428–451.

Alexander C. M. O'D. (2017) The origin of inner Solar System water. *Phil. Trans. R. Soc. A* **375**, 20150384.

Alexander C. M. O'D., Barber D. J. and Hutchison R. (1989a) The microstructure of Semarkona and Bishunpur. *Geochimica et Cosmochimica Acta* **53**, 3045–3057.

Alexander C. M. O'D., Bowden R., Fogel M. L., Howard K. T., Herd C. D. K. and Nittler L. R. (2012) The Provenances of Asteroids, and Their Contributions to the Volatile Inventories of the Terrestrial Planets. *Science* **337**, 721–723.

Alexander C. M. O'D., Cody G. D., De Gregorio B. T., Nittler L. R. and Stroud R. M. (2017) The nature, origin and modification of insoluble organic matter in chondrites, the major source of Earth's C and N. *Geochemistry* **77**, 227–256.

Alexander C. M. O'D., Fogel M., Yabuta H. and Cody G. D. (2007) The origin and evolution of chondrites recorded in the elemental and isotopic compositions of their macromolecular organic matter. *Geochimica et Cosmochimica Acta* **71**, 4380–4403.

Alexander C. M. O'D., Hutchison R. and Barber D. J. (1989b) Origin of chondrule rims and interchondrule matrices in unequilibrated ordinary chondrites. *Earth and Planetary Science Letters* **95**, 187–207.

Alexander C. M. O'D., McKeegan K. D. and Altwegg K. (2018) Water Reservoirs in Small Planetary Bodies: Meteorites, Asteroids, and Comets. *Space Sci Rev* **214**, 36.

Alexander C. M. O'D., Newsome S. D., Fogel M. L., Nittler L. R., Busemann H. and Cody G. D. (2010) Deuterium enrichments in chondritic macromolecular material—Implications for the origin and evolution of organics, water and asteroids. *Geochimica et Cosmochimica Acta* **74**, 4417–4437.

Asaduzzaman A. and Ganguly J. (2021) Hydrogen Isotope Fractionation in the Talc–Serpentine–Brucite–Water System: Theoretical Studies and Implications. *ACS Earth Space Chem.* **5**, 880–889.

Asafov E. V., Sobolev A. V., Gurenko A. A., Arndt N. T., Batanova V. G., Portnyagin M. V., Garbe-Schönberg D. and Krasheninnikov S. P. (2018) Belingwe komatiites (2.7 Ga) originate from a plume with moderate water content, as inferred from inclusions in olivine. *Chemical Geology* **478**, 39–59.

Asimow P. D. and Langmuir C. H. (2003) The importance of water to oceanic mantle melting regimes. *Nature* **421**, 815–820.

Aubaud C., Hauri E. H. and Hirschmann M. M. (2004) Hydrogen partition coefficients between nominally anhydrous minerals and basaltic melts. *Geophysical Research Letters* **31**, 1–4.

Aubaud C., Hirschmann M. M., Withers A. C. and Hervig R. L. (2008) Hydrogen partitioning between melt, clinopyroxene, and garnet at 3 GPa in a hydrous MORB with 6 wt.% H_2O. *Contrib Mineral Petrol* **156**, 607–625.

Aubaud C., Withers A. C., Hirschmann M. M., Guan Y., Leshin L. A., Mackwell S. J. and Bell D. R. (2007) Intercalibration of FTIR and SIMS for hydrogen measurements in glasses and nominally anhydrous minerals. *American Mineralogist* **92**, 811–828.

Barrat J.-A., Jambon A., Yamaguchi A., Bischoff A., Rouget M.-L. and Liorzou C. (2016) Partial melting of a C-rich asteroid: Lithophile trace elements in ureilites. *Geochimica et Cosmochimica Acta* **194**, 163–178.

Barrat J.-A., Sansjofre P., Yamaguchi A., Greenwood R. C. and Gillet P. (2017) Carbon isotopic variation in ureilites: Evidence for an early, volatile-rich Inner Solar System. *Earth and Planetary Science Letters* **478**, 143–149.

Barrett T. J., Barnes J. J., Tartèse R., Anand M., Franchi I. A., Greenwood R. C., Charlier B. L. A. and Grady M. M. (2016) The abundance and isotopic composition of water in eucrites. *Meteoritics & Planetary Science* **51**, 1110–1124.

Bartels K. S., Kinzler R. J. and Grove T. L. (1991) High pressure phase relations of primitive high-alumina basalts from Medicine Lake volcano, northern California. *Contr. Mineral. and Petrol.* **108**, 253–270.

Barth A., Newcombe M., Plank T., Gonnermann H., Hajimirza S., Soto G. J., Saballos A. and Hauri E. (2019) Magma decompression rate correlates with explosivity at basaltic volcanoes — Constraints from water diffusion in olivine. *Journal of Volcanology and Geothermal Research* **387**, 106664.

Barth A., Plank T. and Towbin H. (2023) Rates of dehydration in hydrous, high-Fo, magmatic olivines. *Geochimica et Cosmochimica Acta* **342**, 62–73.

Behrens H. (2010) Ar, CO_2 and H_2O diffusion in silica glasses at 2 kbar pressure. *Chemical Geology* **272**, 40–48.

Behrens H. (2021) Hydrogen defects in feldspars: defect properties and implications for water solubility in feldspar. *Phys Chem Minerals* **48**, 8.

Behrens H. (2020) Water speciation in oxide glasses and melts. *Chemical Geology* **558**, 119850.

Bekaert D. V., Broadley M. W. and Marty B. (2020) The origin and fate of volatile elements on Earth revisited in light of noble gas data obtained from comet 67P/Churyumov-Gerasimenko. *Sci Rep* **10**, 5796.

Bell D. R., Ihinger P. D. and Rossman G. R. (1995) Quantitative analysis of trace OH in garnet and pyroxenes. *American Mineralogist* **80**, 465–474.

Berkley J. L. and Jones J. H. (1982) Primary igneous carbon in ureilites: Petrological implications. *Journal of Geophysical Research: Solid Earth* **87**, A353–A364.

Berkley J. L., Taylor G. J., Keil K., Harlow G. E. and Prinz M. (1980) The nature and origin of ureilites. *Geochimica et Cosmochimica Acta* **44**, 1579–1597.

Bermingham K. R., Füri E., Lodders K. and Marty B. (2020) The NC-CC Isotope Dichotomy: Implications for the Chemical and Isotopic Evolution of the Early Solar System. *Space Sci Rev* **216**, 133.

Berry A. J., Hermann J., O'Neill H. S. C. and Foran G. J. (2005) Fingerprinting the water site in mantle olivine. *Geology* **33**, 869–872.

Berry A. J. and O'Neill H. St. C. (2021) Oxygen Content, Oxygen Fugacity, the Oxidation State of Iron, and Mid-Ocean Ridge Basalts. In *Magma Redox Geochemistry* American Geophysical Union (AGU). pp. 155–163.

Berry A. J., O'Neill H. St. C., Hermann J. and Scott D. R. (2007) The infrared signature of water associated with trivalent cations in olivine. *Earth and Planetary Science Letters* **261**, 134–142.

Berry A. J., Stewart G. A., O'Neill H. St. C., Mallmann G. and Mosselmans J. F. W. (2018) A re-assessment of the oxidation state of iron in MORB glasses. *Earth and Planetary Science Letters* **483**, 114–123.

Bevan A. W. R., Bevan J. C. and Francis J. G. (1977) Amphibole in the Mayo Belwa meteorite: first occurrence in an enstatite achondrite. *Mineralogical Magazine* **41**, 531–534.

Bindeman I. N., Kamenetsky V. S., Palandri J. and Vennemann T. (2012) Hydrogen and oxygen isotope behaviors during variable degrees of upper mantle melting: Example from the basaltic glasses from Macquarie Island. *Chemical Geology* **310–311**, 126–136.

Bischoff A., Bannemann L., Decker S., Ebert S., Haberer S., Heitmann U., Horstmann M., Klemm K. I., Kraemer A.-K., Lentfort S., Patzek M., Storz J. and Weyrauch M. (2022) Asteroid 2008 TC3, not a polymict ureilitic but a polymict C1 chondrite parent body? Survey of 249 Almahata Sitta fragments. *Meteoritics & Planetary Science* **57**, 1339–1364.

Bischoff A., Horstmann M., Barrat J.-A., Chaussidon M., Pack A., Herwartz D., Ward D., Vollmer C. and Decker S. (2014) Trachyandesitic volcanism in the early Solar System. *PNAS* **111**, 12689–12692.

Bizzarro M., Baker J. A., Haack H. and Lundgaard K. L. (2005) Rapid Timescales for Accretion and Melting of Differentiated Planetesimals Inferred from ^{26}Al- ^{26}Mg Chronometry. *ApJ* **632**, L41–L44.

Blanchard M., Ingrin J., Balan E., Kovács I. and Withers A. C. (2017) Effect of iron and trivalent cations on OH defects in olivine. *American Mineralogist* **102**, 302–311.

Borg L. E. and Carlson R. W. (2023) The Evolving Chronology of Moon Formation. *Annual Review of Earth and Planetary Sciences* **51**, 25–52.

Botcharnikov R. E., Holtz F. and Behrens H. (2015) Solubility and fluid–melt partitioning of H_2O and Cl in andesitic magmas as a function of pressure between 50 and 500 MPa. *Chemical Geology* **418**, 117–131.

Bouvier A., Blichert-Toft J., Moynier F., Vervoort J. D. and Albarède F. (2007) Pb–Pb dating constraints on the accretion and cooling history of chondrites. *Geochimica et Cosmochimica Acta* **71**, 1583–1604.

Boynton W. V., Starzyk P. M. and Schmitt R. A. (1976) Chemical evidence for the genesis of the ureilites, the achondrite Chassigny and the nakhlites. *Geochimica et Cosmochimica Acta* **40**, 1439–1447.

Brearley A. J. and Jones R. H. (2018) Halogens in Chondritic Meteorites. In *The Role of Halogens in Terrestrial and Extraterrestrial Geochemical Processes: Surface, Crust, and Mantle* (eds. D. E. Harlov and L. Aranovich). Springer Geochemistry. Springer International Publishing, Cham. pp. 871–958.

Broadley M. W., Bekaert D. V., Marty B., Yamaguchi A. and Barrat J.-A. (2020) Noble gas variations in ureilites and their implications for ureilite parent body formation. *Geochimica et Cosmochimica Acta* **270**, 325–337.

Bromiley G. D., Keppler H., McCammon C., Bromiley F. A. and Jacobsen S. D. (2004) Hydrogen solubility and speciation in natural, gem-quality chromian diopside. *American Mineralogist* **89**, 941–949.

Budde G., Kruijer T. S., Fischer-Gödde M., Irving A. J. and Kleine T. (2015) Planetesimal differentiation revealed by the Hf–W systematics of ureilites. *Earth and Planetary Science Letters* **430**, 316–325.

Burkhardt C., Spitzer F., Morbidelli A., Budde G., Render J. H., Kruijer T. S. and Kleine T. (2021) Terrestrial planet formation from lost inner solar system material. *Science Advances* **7**, eabj7601.

Chaussidon M. and Gounelle M. (2007) Short-lived radioactive nuclides in meteorites and early solar system processes. *Comptes Rendus Geoscience* **339**, 872–884.

Chen H. and Jacobson S. A. (2022) Impact induced atmosphere-mantle exchange sets the volatile elemental ratios on primitive Earths. *Earth and Planetary Science Letters* **594**, 117741.

Chen Q., Ren Z.-Y., Xia X.-P., Zhang L., Yang Q. and Yuan C. (2023) Water Content and Hydrogen Isotopes of Olivine-Hosted Melt Inclusions in the Dali Picrites, SW China: Reassessing the Role of Water in the Formation of the Emeishan Large Igneous Province. *Journal of Geophysical Research: Solid Earth* **128**, e2023JB027547.

Chin E. J., Curran S. T. and Farmer G. L. (2020) Squeezing Water From a Stone: H_2O In Nominally Anhydrous Minerals From Granulite Xenoliths and Deep, Hydrous Fractional Crystallization. *Journal of Geophysical Research: Solid Earth* **125**, e2020JB020416.

Chin E. J., Soustelle V., Hirth G., Saal A. E., Kruckenberg S. C. and Eiler J. M. (2016) Microstructural and geochemical constraints on the evolution of deep arc lithosphere. *Geochemistry, Geophysics, Geosystems* **17**, 2497–2521.

Chopra P. N. and Paterson M. S. (1984) The role of water in the deformation of dunite. *Journal of Geophysical Research: Solid Earth* **89**, 7861–7876.

Chyba C. F. (1987) The cometary contribution to the oceans of primitive Earth. *Nature* **330**, 632–635.

Clesi V., Bouhifd M. A., Bolfan-Casanova N., Manthilake G., Schiavi F., Raepsaet C., Bureau H., Khodja H. and Andrault D. (2018) Low hydrogen contents in the cores of terrestrial planets. *Science Advances* **4**, e1701876.

Cohen B. A., Goodrich C. A. and Keil K. (2004) Feldspathic clast populations in polymict ureilites: Stalking the missing basalts from the ureilite parent body. *Geochimica et Cosmochimica Acta* **68**, 4249–4266.

Collinet M. and Grove T. L. (2020a) Formation of primitive achondrites by partial melting of alkali-undepleted planetesimals in the inner solar system. *Geochimica et Cosmochimica Acta* **277**, 358–376.

Collinet M. and Grove T. L. (2020b) Incremental melting in the ureilite parent body: Initial composition, melting temperatures, and melt compositions. *Meteoritics & Planetary Science* **55**, 832–856.

Collinet M. and Grove T. L. (2020c) Widespread production of silica- and alkali-rich melts at the onset of planetesimal melting. *Geochimica et Cosmochimica Acta* **277**, 334–357.

Connelly J. N., Bizzarro M., Krot A. N., Nordlund Å., Wielandt D. and Ivanova M. A. (2012) The Absolute Chronology and Thermal Processing of Solids in the Solar Protoplanetary Disk. *Science* **338**, 651–655.

Connelly J. N., Schiller M. and Bizzarro M. (2019) Pb isotope evidence for rapid accretion and differentiation of planetary embryos. *Earth and Planetary Science Letters* **525**, 115722.

Cottrell E. and Kelley K. A. (2011) The oxidation state of Fe in MORB glasses and the oxygen fugacity of the upper mantle. *Earth and Planetary Science Letters* **305**, 270–282.

Craig H. and Lupton J. E. (1976) Primordial neon, helium, and hydrogen in oceanic basalts. *Earth and Planetary Science Letters* **31**, 369–385.

Dalou C. and Mysen B. O. (2015) The effect of H_2O on F and Cl solubility and solution mechanisms of in aluminosilicate melts at high pressure and high temperature. *American Mineralogist* **100**, 633–643.

Dauphas N. (2017) The isotopic nature of the Earth's accreting material through time. *Nature* **541**, 521–524.

Day J. M. D., Walker R. J., Ash R. D., Liu Y., Rumble D., Irving A. J., Goodrich C. A., Tait K., McDonough W. F. and Taylor L. A. (2012) Origin of felsic achondrites Graves Nunataks 06128 and 06129, and ultramafic brachinites and brachinite-like achondrites by partial melting of volatile-rich primitive parent bodies. *Geochimica et Cosmochimica Acta* **81**, 94–128.

Deines P., Nafziger R. H., Ulmer G. C. and Woermann E. (1974) Temperature-oxygen fugacity tables for selected gas mixtures in the system C-H-O at one atmosphere total pressure. *Earth and Mineral Sciences Experiment Station*.

Deligny C., Füri E. and Deloule E. (2021) Origin and timing of volatile delivery (N, H) to the angrite parent body: Constraints from in situ analyses of melt inclusions. *Geochimica et Cosmochimica Acta* **313**, 243–256.

Delsemme A. H. (1998) The deuterium enrichment observed in recent comets is consistent with the cometary origin of seawater. *Planetary and Space Science* **47**, 125–131.

Delsemme A. H., Runcorn S. K., Turner G. and Woolfson M. M. (1988) The chemistry of comets. *Philosophical Transactions of the Royal Society of London. Series A, Mathematical and Physical Sciences* **325**, 509–523.

Demouchy S. (2021) Defects in olivine. *European Journal of Mineralogy* **33**, 249–282.

Demouchy S., Jacobsen S. D., Gaillard F. and Stern C. R. (2006) Rapid magma ascent recorded by water diffusion profiles in mantle olivine. *Geology* **34**, 429–432.

Demouchy S. and Mackwell S. (2006) Mechanisms of hydrogen incorporation and diffusion in iron-bearing olivine. *Phys Chem Minerals* **33**, 347–355.

Dixon J. E., Dixon T. H., Bell D. R. and Malservisi R. (2004) Lateral variation in upper mantle viscosity: role of water. *Earth and Planetary Science Letters* **222**, 451–467.

Dobson P. F., Skogby H. and Rossman G. R. (1995) Water in boninite glass and coexisting orthopyroxene: concentration and partitioning. *Contr. Mineral. and Petrol.* **118**, 414–419.

Donnelly-Nolan J. M., Champion D. E., Grove T. L., Baker M. B., Taggart J. E. and Bruggman P. E. (1991) The Giant Crater Lava Field: Geology and geochemistry of a compositionally zoned, high-alumina basalt to basaltic andesite eruption at Medicine Lake Volcano, California. *Journal of Geophysical Research: Solid Earth* **96**, 21843–21863.

Dottin J. W., Labidi J., Farquhar J., Piccoli P., Liu M.-C. and McKeegan K. D. (2018) Evidence for oxidation at the base of the nakhlite pile by reduction of sulfate salts at the time of lava emplacement. *Geochimica et Cosmochimica Acta* **239**, 186–197.

Downes H., Mittlefehldt D. W., Kita N. T. and Valley J. W. (2008) Evidence from polymict ureilite meteorites for a disrupted and re-accreted single ureilite parent asteroid gardened by several distinct impactors. *Geochimica et Cosmochimica Acta* **72**, 4825–4844.

Dyl K. A., Bischoff A., Ziegler K., Young E. D., Wimmer K. and Bland P. A. (2012) Early Solar System hydrothermal activity in chondritic asteroids on 1–10-year timescales. *Proceedings of the National Academy of Sciences* **109**, 18306–18311.

Eggler D. H. (1972) Water-saturated and undersaturated melting relations in a Paricutin andesite and an estimate of water content in the natural magma. *Contr. Mineral. and Petrol.* **34**, 261–271.

Eiler J. M. and Kitchen N. (2004) Hydrogen isotope evidence for the origin and evolution of the carbonaceous chondrites. *Geochimica et Cosmochimica Acta* **68**, 1395–1411.

Elkins-Tanton L. T., Weiss B. P. and Zuber M. T. (2011) Chondrites as samples of differentiated planetesimals. *Earth and Planetary Science Letters* **305**, 1–10.

Fei H. and Katsura T. (2020) Pressure Dependence of Proton Incorporation and Water Solubility in Olivine. *Journal of Geophysical Research: Solid Earth* **125**, e2019JB018813.

Ferriss E., Plank T., Newcombe M., Walker D. and Hauri E. (2018) Rates of dehydration of olivines from San Carlos and Kilauea Iki. *Geochimica et Cosmochimica Acta* **242**, 165–190.

Flock M., Turner N. J., Mulders G. D., Hasegawa Y., Nelson R. P. and Bitsch B. (2019) Planet formation and migration near the silicate sublimation front in protoplanetary disks. *A&A* **630**, A147.

Floss C. (2000) Complexities on the acapulcoite-lodranite parent body: Evidence from trace element distributions in silicate minerals. *Meteoritics & Planetary Science* **35**, 1073–1085.

Fogel R. A. (2005) Aubrite basalt vitrophyres: The missing basaltic component and high-sulfur silicate melts. *Geochimica et Cosmochimica Acta* **69**, 1633–1648.

Fogel R. A. (2002) The Composition of Roedderite in Aubrites. *Meteoritics and Planetary Science Supplement* **37**, A48.

Forbes W. C., Baur W. H. and Khan A. A. (1972) Crystal chemistry of milarite-type minerals. *American Mineralogist* **57**, 463–472.

French B. M. and Eugster H. P. (1965) Experimental control of oxygen fugacities by graphite-gas equilibriums. *Journal of Geophysical Research (1896-1977)* **70**, 1529–1539.

Füri E., Zimmermann L., Deloule E. and Trappitsch R. (2020) Cosmic ray effects on the isotope composition of hydrogen and noble gases in lunar samples: Insights from Apollo 12018. *Earth and Planetary Science Letters* **550**, 116550.

Gaetani G. A., Grove T. L. and Bryan W. B. (1994) Experimental phase relations of basaltic andesite from hole 839B under hydrous and anhydrous conditions. *Proceedings of the Ocean Drilling Program, scientific results* **135**.

Gagné O. C. and Hawthorne F. C. (2016) Chemographic Exploration of the Milarite-type Structure. *The Canadian Mineralogist* **54**, 1229–1247.

Gaillard F., Malavergne V., Bouhifd M. A. and Rogerie G. (2022) A speciation model linking the fate of carbon and hydrogen during core – magma ocean equilibration. *Earth and Planetary Science Letters* **577**, 117266.

Giachetti T., Hudak M. R., Shea T., Bindeman I. N. and Hoxsie E. C. (2020) D/H ratios and H_2O contents record degassing and rehydration history of rhyolitic magma and pyroclasts. *Earth and Planetary Science Letters* **530**, 115909.

Gillmann C., Golabek G. J., Raymond S. N., Schönbächler M., Tackley P. J., Dehant V. and Debaille V. (2020) Dry late accretion inferred from Venus's coupled atmosphere and internal evolution. *Nat. Geosci.* **13**, 265–269.

Gion A. M., Piccoli P. M. and Candela P. A. (2018) Partitioning of indium between ferromagnesian minerals and a silicate melt. *Chemical Geology* **500**, 30–45.

Golabek G. J., Bourdon B. and Gerya T. V. (2014) Numerical models of the thermomechanical evolution of planetesimals: Application to the acapulcoite-lodranite parent body. *Meteoritics & Planetary Science* **49**, 1083–1099.

Gonnermann H. M. (2015) Magma Fragmentation. *Annual Review of Earth and Planetary Sciences* **43**, 431–458.

Gonnermann H. M. and Manga M. (2007) The Fluid Mechanics Inside a Volcano. *Annual Review of Fluid Mechanics* **39**, 321–356.

Goodrich C. A. (1999) Are ureilites residues from partial melting of chondritic material? The answer from MAGPOX. *Meteoritics & Planetary Science* **34**, 109–119.

Goodrich C. A. (1992) Ureilites: A critical review. *Meteoritics* **27**, 327–352.

Goodrich C. A., Ash R. D., Van Orman J. A., Domanik K. and McDonough W. F. (2013a) Metallic phases and siderophile elements in main group ureilites: Implications for ureilite petrogenesis. *Geochimica et Cosmochimica Acta* **112**, 340–373.

Goodrich C. A. and Berkley J. L. (1986) Primary magmatic carbon in ureilites: Evidence from cohenite-bearing metallic spherules. *Geochimica et Cosmochimica Acta* **50**, 681–691.

Goodrich C. A., Fioretti A. M., Tribaudino M. and Molin G. (2001) Primary trapped melt inclusions in olivine in the olivine-augite-orthopyroxene ureilite Hughes 009. *Geochimica et Cosmochimica Acta* **65**, 621–652.

Goodrich C. A., Hartmann W. K., O'Brien D. P., Weidenschilling S. J., Wilson L., Michel P. and Jutzi M. (2015) Origin and history of ureilitic material in the solar system: The view from asteroid 2008 TC3 and the Almahata Sitta meteorite. *Meteoritics & Planetary Science* **50**, 782–809.

Goodrich C. A., Sutton S. R., Wirick S. and Jercinovic M. J. (2013b) Chromium valences in ureilite olivine and implications for ureilite petrogenesis. *Geochimica et Cosmochimica Acta* **122**, 280–305.

Goodrich C. A., Van Orman J. A. and Wilson L. (2007) Fractional melting and smelting on the ureilite parent body. *Geochimica et Cosmochimica Acta* **71**, 2876–2895.

Goodrich Cyrena A., Wilson L., Van Orman J. A. and Michel P. (2013) Comment on "Parent body depth-pressure-temperature relationships and the style of the ureilite anatexis" by P. H. Warren (MAPS 47:209-227). *Meteorit Planet Sci* **48**, 1096–1106.

Grady M. M., Wright I. P., Swart P. K. and Pillinger C. T. (1985) The carbon and nitrogen isotopic composition of ureilites: Implications for their genesis. *Geochimica et Cosmochimica Acta* **49**, 903–915.

Graham A. L., Easton A. J. and Hutchison R. (1977) The Mayo Belwa meteorite: a new enstatite achondrite fall. *Mineralogical Magazine* **41**, 487–492.

Grant H., Tartèse R., Jones R., Piani L., Marrocchi Y., King A. and Rigaudier T. (2023) Bulk mineralogy, water abundance, and hydrogen isotope composition of unequilibrated ordinary chondrites. *Meteoritics & Planetary Science* **58**, 1365–1381.

Grant K., Ingrin J., Lorand J. P. and Dumas P. (2007) Water partitioning between mantle minerals from peridotite xenoliths. *Contrib Mineral Petrol* **154**, 15–34.

Grant K. J., Kohn S. C. and Brooker R. A. (2006) Solubility and partitioning of water in synthetic forsterite and enstatite in the system $MgO–SiO_2–H_2O±Al_2O_3$. *Contrib Mineral Petrol* **151**, 651–664.

Grant K. J., Kohn S. C. and Brooker R. A. (2007) The partitioning of water between olivine, orthopyroxene and melt synthesised in the system albite–forsterite–H_2O. *Earth and Planetary Science Letters* **260**, 227–241.

Green D. H. (1973) Experimental melting studies on a model upper mantle composition at high pressure under water-saturated and water-undersaturated conditions. *Earth and Planetary Science Letters* **19**, 37–53.

Greenwood R. C., Burbine T. H. and Franchi I. A. (2020) Linking asteroids and meteorites to the primordial planetesimal population. *Geochimica et Cosmochimica Acta* **277**, 377–406.

Greenwood R. C., Franchi I. A., Findlay R., Malley J. A., Ito M., Yamaguchi A., Kimura M., Tomioka N., Uesugi M., Imae N., Shirai N., Ohigashi T., Liu M.-C., McCain K. A., Matsuda N., McKeegan K. D., Uesugi K., Nakato A., Yogata K., Yuzawa H., Kodama Y., Tsuchiyama A., Yasutake M., Hirahara K., Tekeuchi A., Sekimoto S., Sakurai I., Okada I., Karouji Y., Nakazawa S., Okada T., Saiki T., Tanaka S., Terui F., Yoshikawa M., Miyazaki A., Nishimura M., Yada T., Abe M., Usui T., Watanabe S. and Tsuda Y. (2023) Oxygen isotope evidence from Ryugu samples for early water delivery to Earth by CI chondrites. *Nat Astron* **7**, 29–38.

Greenwood R. C., Franchi I. A., Gibson J. M. and Benedix G. K. (2012) Oxygen isotope variation in primitive achondrites: The influence of primordial, asteroidal and terrestrial processes. *Geochimica et Cosmochimica Acta* **94**, 146–163.

Grewal D. S., Dasgupta R., Sun C., Tsuno K. and Costin G. (2019) Delivery of carbon, nitrogen, and sulfur to the silicate Earth by a giant impact. *Science Advances* **5**, eaau3669.

Grossman J. N., Alexanders C. M. O'D., Wang J. and Brearley A. J. (2002) Zoned chondrules in Semarkona: Evidence for high- and low-temperature processing. *Meteoritics & Planetary Science* **37**, 49–73.

Halliday A. N. (2013) The origins of volatiles in the terrestrial planets. *Geochimica et Cosmochimica Acta* **105**, 146–171.

Halliday A. N. and Canup R. M. (2023) The accretion of planet Earth. *Nat Rev Earth Environ* **4**, 19–35.

Hallis L. J., Huss G. R., Nagashima K., Taylor G. J., Halldórsson S. A., Hilton D. R., Mottl M. J. and Meech K. J. (2015) Evidence for primordial water in Earth's deep mantle. *Science* **350**, 795–797.

Hamada M., Ushioda M., Fujii T. and Takahashi E. (2013) Hydrogen concentration in plagioclase as a hygrometer of arc basaltic melts: Approaches from melt inclusion analyses and hydrous melting experiments. *Earth and Planetary Science Letters* **365**, 253–262.

Hamilton D. L., Burnham C. W. and Osborn E. F. (1964) The Solubility of Water and Effects of Oxygen Fugacity and Water Content on Crystallization in Mafic Magmas. *Journal of Petrology* **5**, 21–39.

Harries D., Zhao X. and Franchi I. (2023) Upper limits of water contents in olivine and orthopyroxene of equilibrated chondrites and several achondrites. *Meteoritics & Planetary Science* **58**, 705–721.

Hartmann L., Ciesla F., Gressel O. and Alexander R. (2019) *Disk Evolution and the Fate of Water*.,

Hauri E. (2002) SIMS analysis of volatiles in silicate glasses, 2: isotopes and abundances in Hawaiian melt inclusions. *Chemical Geology* **183**, 115–141.

Hauri E. H., Gaetani G. A. and Green T. H. (2006a) Partitioning of water during melting of the Earth's upper mantle at H_2O-undersaturated conditions. *Earth and Planetary Science Letters* **248**, 715–734.

Hauri E. H., Shaw A. M., Wang J., Dixon J. E., King P. L. and Mandeville C. (2006b) Matrix effects in hydrogen isotope analysis of silicate glasses by SIMS. *Chemical Geology* **235**, 352–365.

Hauri E., Wang J., Dixon J. E., King P. L., Mandeville C. and Newman S. (2002) SIMS analysis of volatiles in silicate glasses 1. Calibration, matrix effects and comparisons with FTIR. *Chemical Geology*, 16.

Heraus (2020) Fused Silica for Applications in the Near Infrared (NIR).

Heraus (2019) Quartz Glass for Optics Data and Properties. Heraeus Brochure.

Heraus Quarzglass (2011) Quartz Glass for optics Data and Properties.

Heraus Quarzglass (2006) SUPRASIL® 3001 and 3002 Data Sheet.

Herrin J. S., Zolensky M. E., Ito M., Le L., Mittlefehldt D. W., Jenniskens P., Ross A. J. and Shaddad M. H. (2010) Thermal and fragmentation history of ureilitic asteroids: Insights from the Almahata Sitta fall. *Meteoritics & Planetary Science* **45**, 1789–1803.

Hirschmann M. M. (2016) Constraints on the early delivery and fractionation of Earth's major volatiles from C/H, C/N, and C/S ratios. *American Mineralogist* **101**, 540–553.

Hirschmann M. M. and Dasgupta R. (2009) The H/C ratios of Earth's near-surface and deep reservoirs, and consequences for deep Earth volatile cycles. *Chemical Geology* **262**, 4–16.

Hirschmann M. M., Withers A. C., Ardia P. and Foley N. T. (2012) Solubility of molecular hydrogen in silicate melts and consequences for volatile evolution of terrestrial planets. *Earth and Planetary Science Letters* **345–348**, 38–48.

Hirth G. and Kohlstedt D. L. (1996) Water in the oceanic upper mantle: implications for rheology, melt extraction and the evolution of the lithosphere. *Earth and Planetary Science Letters* **144**, 93–108.

Holloway J. R. (1973) The system pargasite-H_2O-CO_2: a model for melting of a hydrous mineral with a mixed-volatile fluid—I. Experimental results to 8 kbar. *Geochimica et Cosmochimica Acta* **37**, 651–666.

Holloway J. R., Pan V. and Gudmundsson G. (1992) High-pressure fluid-absent melting experiments in the presence of graphite; oxygen fugacity, ferric/ferrous ratio and dissolved CO_2. *European Journal of Mineralogy* **4**, 105–114.

Horstmann M. and Bischoff A. (2014) The Almahata Sitta polymict breccia and the late accretion of asteroid 2008 TC3. *Geochemistry* **74**, 149–183.

Hsu W. (1998) Geochemical and petrographic studies of oldhamite, diopside, and roedderite in enstatite meteorites. *Meteoritics & Planetary Science* **33**, 291–301.

Hui H., Guan Y., Chen Y., Peslier A. H., Zhang Y., Liu Y., Flemming R. L., Rossman G. R., Eiler J. M., Neal C. R. and Osinski G. R. (2017) A heterogeneous lunar interior for hydrogen isotopes as revealed by the lunar highlands samples. *Earth and Planetary Science Letters* **473**, 14–23.

Hui H., Peslier A. H., Zhang Y. and Neal C. R. (2013) Water in lunar anorthosites and evidence for a wet early Moon. *Nature Geosci* **6**, 177–180.

Hui H., Zhang Y., Xu Z. and Behrens H. (2008) Pressure dependence of the speciation of dissolved water in rhyolitic melts. *Geochimica et Cosmochimica Acta* **72**, 3229–3240.

Iacovino K., Matthews S., Wieser P. E., Moore G. M. and Bégué F. (2021) VESIcal Part I: An Open-Source Thermodynamic Model Engine for Mixed Volatile (H_2O-CO_2) Solubility in Silicate Melts. *Earth and Space Science* **8**, e2020EA001584.

Inoue T., Weidner D. J., Northrup P. A. and Parise J. B. (1998) Elastic properties of hydrous ringwoodite (γ-phase) in Mg_2SiO_4. *Earth and Planetary Science Letters* **160**, 107–113.

Izidoro A., Dasgupta R., Raymond S. N., Deienno R., Bitsch B. and Isella A. (2022) Planetesimal rings as the cause of the Solar System's planetary architecture. *Nat Astron* **6**, 357–366.

Jacobsen S. D., Smyth J. R., Spetzler H., Holl C. M. and Frost D. J. (2004) Sound velocities and elastic constants of iron-bearing hydrous ringwoodite. *Physics of the Earth and Planetary Interiors* **143–144**, 47–56.

Javoy M., Kaminski E., Guyot F., Andrault D., Sanloup C., Moreira M., Labrosse S., Jambon A., Agrinier P., Davaille A. and Jaupart C. (2010) The chemical composition of the Earth: Enstatite chondrite models. *Earth and Planetary Science Letters* **293**, 259–268.

Jiang Y., Li Y., Liu J., Wang Q., Qin L.-P., Zhu K., Liao S., Yin Z., Peng Y., Koefoed P. and Hsu W. (2023) Tracking and dating incipient melting of a new grouplet of primitive achondrites. *Geochimica et Cosmochimica Acta* **345**, 1–15.

Jin Z. and Bose M. (2019) New clues to ancient water on Itokawa. *Science Advances* **5**, eaav8106.

Jin Z., Bose M., Lichtenberg T. and Mulders G. D. (2021) New Evidence for Wet Accretion of Inner Solar System Planetesimals from Meteorites Chelyabinsk and Benenitra. *Planet. Sci. J.* **2**, 244.

Johansen A., Ronnet T., Bizzarro M., Schiller M., Lambrechts M., Nordlund Å. and Lammer H. (2021) A pebble accretion model for the formation of the terrestrial planets in the Solar System. *Science Advances* **7**, eabc0444.

Johansen A., Ronnet T., Schiller M., Deng Z. and Bizzarro M. (2023) Anatomy of rocky planets formed by rapid pebble accretion - III. Partitioning of volatiles between planetary core, mantle, and atmosphere. *A&A* **671**, A76.

Jollands M. C., Dohmen R. and Padrón-Navarta J. A. (2023) Hide and Seek—Trace Element Incorporation and Diffusion in Olivine. *Elements* **19**, 144–150.

Jollands M. C., Kempf E., Hermann J. and Müntener O. (2019) Coupled inter-site reaction and diffusion: Rapid dehydrogenation of silicon vacancies in natural olivine. *Geochimica et Cosmochimica Acta* **262**, 220–242.

Jung H. and Karato S. (2001) Water-Induced Fabric Transitions in Olivine. *Science* **293**, 1460–1463.

Kaminski É. (2002) The influence of water on the development of lattice preferred orientation in olivine aggregates. *Geophysical Research Letters* **29**, 17-1-17–4.

Karato S. (2006) Remote Sensing of Hydrogen in Earth's Mantle. *Reviews in Mineralogy and Geochemistry* **62**, 343–375.

Karato S. (1990) The role of hydrogen in the electrical conductivity of the upper mantle. *Nature* **347**, 272–273.

Karato S. (2011) Water distribution across the mantle transition zone and its implications for global material circulation. *Earth and Planetary Science Letters* **301**, 413–423.

Karato S.-I., Paterson M. S. and FitzGerald J. D. (1986) Rheology of synthetic olivine aggregates: Influence of grain size and water. *Journal of Geophysical Research: Solid Earth* **91**, 8151–8176.

Keil K. (2010) Enstatite achondrite meteorites (aubrites) and the histories of their asteroidal parent bodies. *Geochemistry* **70**, 295–317.

Keil K. and McCoy T. J. (2018) Acapulcoite-lodranite meteorites: Ultramafic asteroidal partial melt residues. *Geochemistry* **78**, 153–203.

Keil K., McCoy T. J., Wilson L., Barrat J.-A., Rumble D., Meier M. M. M., Wieler R. and Huss G. R. (2011) A composite FeNi-FeS and enstatite-forsterite-diopside-glass vitrophyre clast in the Larkman Nunatak 04316 aubrite: Origin by pyroclastic volcanism. *Meteoritics & Planetary Science* **46**, 1719–1741.

Keppler H. and Bolfan-Casanova N. (2006) Thermodynamics of Water Solubility and Partitioning. *Reviews in Mineralogy and Geochemistry* **62**, 193–230.

Kerridge J. F. (1985) Carbon, hydrogen and nitrogen in carbonaceous chondrites: Abundances and isotopic compositions in bulk samples. *Geochimica et Cosmochimica Acta* **49**, 1707–1714.

Khisina N. R., Wirth R., Andrut M. and Ukhanov A. V. (2001) Extrinsic and intrinsic mode of hydrogen occurrence in natural olivines: FTIR and TEM investigation. *Phys Chem Min* **28**, 291–301.

Kitamura M., Kondoh S., Morimoto N., Miller G. H., Rossman G. R. and Putnis A. (1987) Planar OH-bearing defects in mantle olivine. *Nature* **328**, 143–145.

Kite E. S. and Barnett M. N. (2020) Exoplanet secondary atmosphere loss and revival. *Proceedings of the National Academy of Sciences* **117**, 18264–18271.

Kleine T., Budde G., Burkhardt C., Kruijer T. S., Worsham E. A., Morbidelli A. and Nimmo F. (2020) The Non-carbonaceous–Carbonaceous Meteorite Dichotomy. *Space Sci Rev* **216**, 55.

Kleine T., Hans U., Irving A. J. and Bourdon B. (2012) Chronology of the angrite parent body and implications for core formation in protoplanets. *Geochimica et Cosmochimica Acta* **84**, 186–203.

Kleine T., Steller T., Burkhardt C. and Nimmo F. (2023) An inner solar system origin of volatile elements in Mars. *Icarus* **397**, 115519.

Kleine T. and Walker R. J. (2017) Tungsten Isotopes in Planets. *Annual Review of Earth and Planetary Sciences* **45**, 389–417.

Koga K., Hauri E., Hirschmann M. and Bell D. (2003) Hydrogen concentration analyses using SIMS and FTIR: Comparison and calibration for nominally anhydrous minerals: hydrogen concentration analyses. *Geochem. Geophys. Geosyst.* **4**, 1–20.

Kohlstedt D. L. and Mackwell S. J. (1998) Diffusion of Hydrogen and Intrinsic Point Defects in Olivine. *Zeitschrift für Physikalische Chemie* **207**, 147–162.

Kolodny Y., Kerridge J. F. and Kaplan I. R. (1980) Deuterium in carbonaceous chondrites. *Earth and Planetary Science Letters* **46**, 149–158.

Kovacs I., O'Neill H. St. C., Hermann J. and Hauri E. H. (2010) Site-specific infrared O-H absorption coefficients for water substitution into olivine. *American Mineralogist* **95**, 292–299.

Kovalenko V. I., Naumov V. B., Girnis A. V., Dorofeeva V. A. and Yarmolyuk V. V. (2010) Average composition of basic magmas and mantle sources of island arcs and active continental margins estimated from the data on melt inclusions and quenched glasses of rocks. *Petrology* **18**, 1–26.

Krähenbühl U., Noll K., Döbeli M., Grambole D., Herrmann F. and Tobler L. (1998) Exposure of Allan Hills 84001 and other achondrites on the Antarctic ice. *Meteoritics & Planetary Science* **33**, 665–670.

Kruijer T. S., Burkhardt C., Budde G. and Kleine T. (2017) Age of Jupiter inferred from the distinct genetics and formation times of meteorites. *PNAS* **114**, 6712–6716.

Kruijer T. S., Kleine T. and Borg L. E. (2020) The great isotopic dichotomy of the early Solar System. *Nature Astronomy* **4**, 32–40.

Kumamoto K. M., Warren J. M. and Hauri E. H. (2017) New SIMS reference materials for measuring water in upper mantle minerals. *American Mineralogist* **102**, 537–547.

Kuramoto K. (1997) Accretion, core formation, H and C evolution of the Earth and Mars. *Physics of the Earth and Planetary Interiors* **100**, 3–20.

Kushiro I. (1972) Effect of Water on the Composition of Magmas Formed at High Pressures. *J Petrology* **13**, 311–334.

La Spina G., Arzilli F., Burton M. R., Polacci M. and Clarke A. B. (2022) Role of volatiles in highly explosive basaltic eruptions. *Commun Earth Environ* **3**, 1–13.

Lammer H., Zerkle A. L., Gebauer S., Tosi N., Noack L., Scherf M., Pilat-Lohinger E., Güdel M., Grenfell J. L., Godolt M. and Nikolaou A. (2018) Origin and evolution of the atmospheres of early Venus, Earth and Mars. *Astron Astrophys Rev* **26**, 2.

Le Voyer M., Asimow P. D., Mosenfelder J. L., Guan Y., Wallace P. J., Schiano P., Stolper E. M. and Eiler J. M. (2014) Zonation of H_2O and F Concentrations around Melt Inclusions in Olivines. *J Petrology* **55**, 685–707.

Le Voyer M., Cottrell E., Kelley K. A., Brounce M. and Hauri E. H. (2015) The effect of primary versus secondary processes on the volatile content of MORB glasses: An example from the equatorial Mid-Atlantic Ridge (5°N–3°S). *Journal of Geophysical Research: Solid Earth* **120**, 125–144.

Lecar M., Podolak M., Sasselov D. and Chiang E. (2006) On the Location of the Snow Line in a Protoplanetary Disk. *ApJ* **640**, 1115–1118.

Lee M. R. and Bland P. A. (2004) Mechanisms of weathering of meteorites recovered from hot and cold deserts and the formation of phyllosilicates. *Geochimica et Cosmochimica Acta* **68**, 893–916.

Lee M. R., Cohen B. E., Boyce A. J., Hallis L. J. and Daly L. (2021) The pre-atmospheric hydrogen inventory of CM carbonaceous chondrites. *Geochimica et Cosmochimica Acta* **309**, 31–44.

Lewis J. A., Jones R. H. and Brearley A. J. (2022) Plagioclase alteration and equilibration in ordinary chondrites: Metasomatism during thermal metamorphism. *Geochimica et Cosmochimica Acta* **316**, 201–229.

Li S., Yin Q.-Z., Bao H., Sanborn M. E., Irving A., Ziegler K., Agee C., Marti K., Miao B., Li X., Li Y. and Wang S. (2018) Evidence for a multilayered internal structure of the chondritic acapulcoite-lodranite parent asteroid. *Geochimica et Cosmochimica Acta* **242**, 82–101.

Li Y., Dasgupta R. and Tsuno K. (2015) The effects of sulfur, silicon, water, and oxygen fugacity on carbon solubility and partitioning in Fe-rich alloy and silicate melt systems at 3 GPa and 1600 °C: Implications for core–mantle differentiation and degassing of magma oceans and reduced planetary mantles. *Earth and Planetary Science Letters* **415**, 54–66.

Li Y., Dasgupta R., Tsuno K., Monteleone B. and Shimizu N. (2016) Carbon and sulfur budget of the silicate Earth explained by accretion of differentiated planetary embryos. *Nature Geosci* **9**, 781–785.

Lichtenberg T., Drążkowska J., Schönbächler M., Golabek G. J. and Hands T. O. (2021) Bifurcation of planetary building blocks during Solar System formation. *Science* **371**, 365–370.

Lichtenberg T., Golabek G. J., Burn R., Meyer M. R., Alibert Y., Gerya T. V. and Mordasini C. (2019) A water budget dichotomy of rocky protoplanets from ^{26}Al-heating. *Nat Astron* **3**, 307–313.

Lin Y. H., Hui H., Li Y., Xu Y. and van Westrenen W. (2019) A lunar hygrometer based on plagioclase-melt partitioning of water. *Geochem. Persp. Let.* **10**, 14–19.

Liu W., Zhang Y., Tissot François. L. H., Avice G., Ye Z. and Yin Q.-Z. (2023) I/Pu reveals Earth mainly accreted from volatile-poor differentiated planetesimals. *Science Advances* **9**, eadg9213.

Lodders K. (2021) Relative Atomic Solar System Abundances, Mass Fractions, and Atomic Masses of the Elements and Their Isotopes, Composition of the Solar Photosphere, and Compositions of the Major Chondritic Meteorite Groups. *Space Sci Rev* **217**, 44.

Lodders K., Palme H. and Gail H.-P. (2009) Abundances of the elements in the solar system. In *The Solar System* Springer-Verlag, Berlin, Heidelberg, New York. pp. 712–770.

Loewen M. W., Graham D. W., Bindeman I. N., Lupton J. E. and Garcia M. O'D. (2019) Hydrogen isotopes in high $^{3}He/^{4}He$ submarine basalts: Primordial vs. recycled water and the veil of mantle enrichment. *Earth and Planetary Science Letters* **508**, 62–73.

Long G. L. and Winefordner J. D. (1983) Limit of Detection A Closer Look at the IUPAC Definition. *Anal. Chem.* **55**, 712A-724A.

Lucas M. P., Dygert N., Ren J., Hesse M. A., Miller N. R. and McSween H. Y. (2022) Thermochemical evolution of the acapulcoite–lodranite parent body: Evidence for fragmentation-disrupted partial differentiation. *Meteoritics & Planetary Science* **57**, 2248–2275.

Ma N., Neumann W., Néri A., Schwarz W. H., Ludwig T., Trieloff M., Klahr H. and Bouvier A. (2022) Early formation of primitive achondrites in an outer region of the protoplanetary disc. *Geochem. Persp. Let.* **23**, 33–37.

Macke R. J., Consolmagno G. J. and Britt D. T. (2011) Density, porosity, and magnetic susceptibility of carbonaceous chondrites. *Meteoritics & Planetary Science* **46**, 1842–1862.

Mackwell S. J., Kohlstedt D. L. and Paterson M. S. (1985) The role of water in the deformation of olivine single crystals. *Journal of Geophysical Research: Solid Earth* **90**, 11319–11333.

Malavergne V., Bureau H., Raepsaet C., Gaillard F., Poncet M., Surblé S., Sifré D., Shcheka S., Fourdrin C., Deldicque D. and Khodja H. (2019) Experimental constraints on the fate of H and C during planetary core-mantle differentiation. Implications for the Earth. *Icarus* **321**, 473–485.

Marty B. (2022) Meteoritic noble gas constraints on the origin of terrestrial volatiles. *Icarus* **381**, 115020.

Marty B. (2012) The origins and concentrations of water, carbon, nitrogen and noble gases on Earth. *Earth and Planetary Science Letters* **313–314**, 56–66.

Mason B., Clarke Jr. R. S., Martinez R., Satterwhite C., Schwarz C. and Score R. (1988) Antarctic Meteorite Newsletter. **11**.

Mason B., MacPherson G., Schwarz C., Score R., Martinez R. and Delaney J. (1985) Antarctic Meteorite Newsletter. **8**.

Mason B., Reid A. and Clarke Jr. R. S. (1980) Antarctic Meteorite Newsletter. **3**.

McCanta M. C., Treiman A. H., Dyar M. D., Alexander C. M. O'D., Rumble D. and Essene E. J. (2008) The LaPaz Icefield 04840 meteorite: Mineralogy, metamorphism, and origin of an amphibole- and biotite-bearing R chondrite. *Geochimica et Cosmochimica Acta* **72**, 5757–5780.

McCoy T. J., Corrigan C. M., Dickinson T. L., Benedix G. K., Schrader D. L. and Davidson J. (2019) Grove Mountains (GRV) 020043: Insights into acapulcoite-lodranite genesis from the most primitive member. *Geochemistry* **79**, 125536.

McCoy T. J., Keil K., Ash R. D., Morse A. D., Pillinger C. T., Wieler R., Mayeda T. K., Clayton R. N., Benoit P. H., Sears D. W. G., Casanova I., Muenow D. W., Moore C. B., Lewis C. F. and Wilson I. E. (1993) Roosevelt County 075: A petrologic, chemical and isotopic study of the most unequilibrated known H chondrite. *Meteoritics* **28**, 681–691.

McCoy T. J., Keil K., Clayton R. N., Mayeda T. K., Bogard D. D., Garrison D. H., Huss G. R., Hutcheon I. D. and Wieler R. (1996) A petrologic, chemical, and isotopic study of Monument Draw and comparison with other acapulcoites: Evidence for formation by incipient partial melting. *Geochimica et Cosmochimica Acta* **60**, 2681–2708.

McCoy T. J., Keil K., Clayton R. N., Mayeda T. K., Bogard D. D., Garrison D. H. and Wieler R. (1997) A petrologic and isotopic study of lodranites: Evidence for early formation as partial melt residues from heterogeneous precursors. *Geochimica et Cosmochimica Acta* **61**, 623–637.

McCoy T. J., Mittlefehldt D. W. and Wilson L. (2006) *Asteroid Differentiation*.,

McCubbin F. M. and Barnes J. J. (2019) Origin and abundances of H_2O in the terrestrial planets, Moon, and asteroids. *Earth and Planetary Science Letters* **526**, 115771.

McCubbin F. M., Lewis J. A., Barnes J. J., Elardo S. M. and Boyce J. W. (2021) The abundances of F, Cl, and H_2O in eucrites: Implications for the origin of volatile depletion in the asteroid 4 Vesta. *Geochimica et Cosmochimica Acta* **314**, 270–293.

McCubbin F. M., Vander Kaaden K. E., Tartèse R., Klima R. L., Liu Y., Mortimer J., Barnes J. J., Shearer C. K., Treiman A. H., Lawrence D. J., Elardo S. M., Hurley D. M., Boyce J. W. and Anand M. (2015) Magmatic volatiles (H, C, N, F, S, Cl) in the lunar mantle, crust, and regolith: Abundances, distributions, processes, and reservoirs†. *American Mineralogist* **100**, 1668–1707.

McNaughton N. J., Fallick A. E. and Pillinger C. T. (1982) Deuterium enrichments in type 3 ordinary chondrites. *Journal of Geophysical Research: Solid Earth* **87**, A297–A302.

Médard E. and Grove T. L. (2008) The effect of H_2O on the olivine liquidus of basaltic melts: experiments and thermodynamic models. *Contrib Mineral Petrol* **155**, 417–432.

Mezger K., Schönbächler M. and Bouvier A. (2020) Accretion of the Earth—Missing Components? *Space Sci Rev* **216**, 27.

Mierdel K. and Keppler H. (2004) The temperature dependence of water solubility in enstatite. *Contrib Mineral Petrol* **148**, 305–311.

Miley J. M., Panić O., Booth R. A., Ilee J. D., Ida S. and Kunitomo M. (2021) The impact of pre-main sequence stellar evolution on mid-plane snowline locations and C/O in planet forming discs. *Monthly Notices of the Royal Astronomical Society* **500**, 4658–4670.

Mills R. D., Simon J. I., Alexander C. M. O'D., Wang J. and Hauri E. H. (2017) Water in alkali feldspar: The effect of rhyolite generation on the lunar hydrogen budget. *Geochem. Persp. Let.* **3**, 115–123.

Min M., Dullemond C. P., Kama M. and Dominik C. (2011) The thermal structure and the location of the snow line in the protosolar nebula: Axisymmetric models with full 3-D radiative transfer. *Icarus* **212**, 416–426.

Mitchell A. L., Gaetani G. A., O'Leary J. A. and Hauri E. H. (2017) H_2O solubility in basalt at upper mantle conditions. *Contrib Mineral Petrol* **172**, 85.

Moore G., Vennemann T. and Carmichael I. S. E. (1998) An empirical model for the solubility of H_2O in magmas to 3 kilobars. *American Mineralogist* **83**, 36–42.

Moore K. and Cowan N. B. (2020) Keeping M-Earths habitable in the face of atmospheric loss by sequestering water in the mantle. *Monthly Notices of the Royal Astronomical Society* **496**, 3786–3795.

Morbidelli A., Baillié K., Batygin K., Charnoz S., Guillot T., Rubie D. C. and Kleine T. (2022) Contemporary formation of early Solar System planetesimals at two distinct radial locations. *Nat Astron* **6**, 72–79.

Morbidelli A., Bitsch B., Crida A., Gounelle M., Guillot T., Jacobson S., Johansen A., Lambrechts M. and Lega E. (2016) Fossilized condensation lines in the Solar System protoplanetary disk. *Icarus* **267**, 368–376.

Morbidelli A., Lunine J. I., O'Brien D. P., Raymond S. N. and Walsh K. J. (2012) Building Terrestrial Planets. *Annual Review of Earth and Planetary Sciences* **40**, 251–275.

Mosenfelder J. L., Andrys J. L., von der Handt A., Kohlstedt D. L. and Hirschmann M. M. (2020) Hydrogen incorporation in plagioclase. *Geochimica et Cosmochimica Acta* **277**, 87–110.

Mosenfelder J. L., Deligne N. I., Asimow P. D. and Rossman G. R. (2006) Hydrogen incorporation in olivine from 2–12 GPa. *American Mineralogist* **91**, 285–294.

Mosenfelder J. L. and Rossman G. R. (2013) Analysis of hydrogen and fluorine in pyroxenes: I. Orthopyroxene. *American Mineralogist* **98**, 1026–1041.

Mosenfelder Jed L. and Rossman G. R. (2013) Analysis of hydrogen and fluorine in pyroxenes: II. Clinopyroxene. *American Mineralogist* **98**, 1042–1054.

Mosenfelder J. L., Rossman G. R. and Johnson E. A. (2015) Hydrous species in feldspars: A reassessment based on FTIR and SIMS. *American Mineralogist* **100**, 1209–1221.

Mosenfelder J., Sharp T., Asimow P. and Rossman G. R. (2006) Hydrogen Incorporation in Natural Mantle Olivines. *Earth's Deep Water Cycle* **168**, 45–56.

Mulders G. D., Ciesla F. J., Min M. and Pascucci I. (2015) The Snow Line in Viscous Disks Around Low-Mass Stars: Implications for Water Delivery to Terrestrial Planets in the Habitable Zone. *ApJ* **807**, 9.

Mundl-Petermeier A., Walker R. J., Fischer R. A., Lekic V., Jackson M. G. and Kurz M. D. (2020) Anomalous ^{182}W in high $^{3}He/^{4}He$ ocean island basalts: Fingerprints of Earth's core? *Geochimica et Cosmochimica Acta* **271**, 194–211.

Murty S. V. S., Mahajan R. R., Jenniskens P., Shaddad M. H. and Eldien B. (2010) Noble gases and nitrogen in the Almahata Sitta ureilite. *Meteoritics & Planetary Science* **45**, 1751–1764.

Newcombe M. E. (2022) SIMSblank. v2.0 (Version 2.0). Zenodo. doi.org/10.5281/zenodo.7220990.

Newcombe M. E., Brett A., Beckett J. R., Baker M. B., Newman S., Guan Y., Eiler J. M. and Stolper E. M. (2017) Solubility of water in lunar basalt at low pH_2O. *Geochimica et Cosmochimica Acta* **200**, 330–352.

Newcombe M. E., Nielsen S. G., Peterson L. D., Wang J., Alexander C. M. O'D., Sarafian A. R., Shimizu K., Nittler L. R. and Irving A. J. (2023) Degassing of early-formed planetesimals restricted water delivery to Earth. *Nature* **615**, 854–857.

Newcombe M. E., Plank T., Barth A., Asimow P. D. and Hauri E. (2020) Water-in-olivine magma ascent chronometry: Every crystal is a clock. *Journal of Volcanology and Geothermal Research* **398**, 106872.

Newman S., Epstein S. and Stolper E. (1988) Water, carbon dioxide, and hydrogen isotopes in glasses from the ca. 1340 A.D. eruption of the Mono Craters, California: Constraints on degassing phenomena and initial volatile content. *Journal of Volcanology and Geothermal Research* **35**, 75–96.

Newman S. and Lowenstern J. B. (2002) VolatileCalc: a silicate melt–H_2O–CO_2 solution model written in Visual Basic for excel. *Computers & Geosciences* **28**, 597–604.

Nittler L. R. and Weider S. Z. (2019) The surface composition of Mercury. *Elements* **15**, 33–38.

Notsu S., Nomura H., Ishimoto D., Walsh C., Honda M., Hirota T. and Millar T. J. (2016) Candidate water vapor lines to locate the H_2O snowline through high-dispersion spectroscopic observations. I. The case of a T Tauri star. *ApJ* **827**, 113.

Novella D., Frost D. J., Hauri E. H., Bureau H., Raepsaet C. and Roberge M. (2014) The distribution of H_2O between silicate melt and nominally anhydrous peridotite and the onset of hydrous melting in the deep upper mantle. *Earth and Planetary Science Letters* **400**, 1–13.

Nurnberg F., Schotz G. and Vydra J. (2015) Fused Silica Challenges.

O'Brien D. P., Izidoro A., Jacobson S. A., Raymond S. N. and Rubie D. C. (2018) The Delivery of Water During Terrestrial Planet Formation. *Space Sci Rev* **214**, 47.

O'Brien D. P., Walsh K. J., Morbidelli A., Raymond S. N. and Mandell A. M. (2014) Water delivery and giant impacts in the 'Grand Tack' scenario. *Icarus* **239**, 74–84.

Okuchi T. (1997) Hydrogen Partitioning into Molten Iron at High Pressure: Implications for Earth's Core. *Science* **278**, 1781–1784.

O'Leary J. A., Gaetani G. A. and Hauri E. H. (2010) The effect of tetrahedral Al^{3+} on the partitioning of water between clinopyroxene and silicate melt. *Earth and Planetary Science Letters* **297**, 111–120.

Olson P. L. and Sharp Z. D. (2019) Nebular atmosphere to magma ocean: A model for volatile capture during Earth accretion. *Physics of the Earth and Planetary Interiors* **294**, 106294.

Ottolini L., Bottazzi P., Zanetti A. and Vannucci R. (1995) Determination of hydrogen in silicates by secondary ion mass spectrometry. *Analyst* **120**, 1309–1313.

Owen J. E. (2020) Snow lines can be thermally unstable. *Monthly Notices of the Royal Astronomical Society* **495**, 3160–3174.

Papale P. (1999) Strain-induced magma fragmentation in explosive eruptions. *Nature* **397**, 425–428.

Patzer A., Hill D. H. and Boynton W. V. (2004) Evolution and classification of acapulcoites and lodranites from a chemical point of view. *Meteoritics & Planetary Science* **39**, 61–85.

Peplowski P. N., Klima R. L., Lawrence D. J., Ernst C. M., Denevi B. W., Frank E. A., Goldsten J. O., Murchie S. L., Nittler L. R. and Solomon S. C. (2016) Remote sensing evidence for an ancient carbon-bearing crust on Mercury. *Nature Geosci* **9**, 273–276.

Peslier A. H. and Luhr J. F. (2006) Hydrogen loss from olivines in mantle xenoliths from Simcoe (USA) and Mexico: Mafic alkalic magma ascent rates and water budget of the sub-continental lithosphere. *Earth and Planetary Science Letters* **242**, 302–319.

Peslier A. H., Schönbächler M., Busemann H. and Karato S.-I. (2017) Water in the Earth's Interior: Distribution and Origin. *Space Sci Rev* **212**, 743–810.

Peterson L. D., Newcombe M., Alexander C. M. O'D., Wang J. and Nielsen S. G. (accepted) The H-poor nature of incompletely melted planetesimals: the view from acapulcoites and lodranites. *Geochimica et Cosmochimica Acta*.

Peterson L. D., Newcombe M. E., Alexander C. M. O'D., Wang J., Klein F., Bekaert D. V. and Nielsen S. G. (2023a) The H content of aubrites: An evaluation of bulk versus in situ

methods for quantifying water in meteorites. *Earth and Planetary Science Letters* **620**, 118341.

Peterson L. D., Newcombe M. E., Alexander C. M. O'D., Wang J., Sarafian A. R., Bischoff A. and Nielsen S. G. (2023b) The H_2O content of the ureilite parent body. *Geochimica et Cosmochimica Acta* **340**, 141–157.

Piani L., Marrocchi Y., Rigaudier T., Vacher L. G., Thomassin D. and Marty B. (2020) Earth's water may have been inherited from material similar to enstatite chondrite meteorites. *Science* **369**, 1110–1113.

Piani L., Marrocchi Y., Vacher L. G., Yurimoto H. and Bizzarro M. (2021) Origin of hydrogen isotopic variations in chondritic water and organics. *Earth and Planetary Science Letters* **567**, 117008.

Pineau F., Shilobreeva S., Kadik A. and Javoy M. (1998) Water solubility and D/H fractionation in the system basaltic andesite–H_2O at 1250°C and between 0.5 and 3 kbars. *Chemical Geology* **147**, 173–184.

Piralla M., Tartèse R., Marrocchi Y. and Joy K. H. (2021) Apatite halogen and hydrogen isotope constraints on the conditions of hydrothermal alteration in carbonaceous chondrites. *Meteoritics & Planetary Science* **56**, 809–828.

Pitzer K. S. and Sterner S. M. (1994) Equations of state valid continuously from zero to extreme pressures for H_2O and CO_2. *The Journal of Chemical Physics* **101**, 3111–3116.

Popa R.-G., Bachmann O. and Huber C. (2021) Explosive or effusive style of volcanic eruption determined by magma storage conditions. *Nat. Geosci.* **14**, 781–786.

Poreda R., Schilling J.-G. and Craig H. (1986) Helium and hydrogen isotopes in ocean-ridge basalts north and south of Iceland. *Earth and Planetary Science Letters* **78**, 1–17.

Potts N. J., Bromiley G. D. and Brooker R. A. (2021) An experimental investigation of F, Cl and H_2O mineral-melt partitioning in a reduced, model lunar system. *Geochimica et Cosmochimica Acta* **294**, 232–254.

Rai N., Downes H. and Smith C. (2020) Ureilite meteorites provide a new model of early planetesimal formation and destruction. *Geochemical Perspectives Letters* **14**, 20–25.

Rankenburg K., Humayun M., Brandon A. D. and Herrin J. S. (2008) Highly siderophile elements in ureilites. *Geochimica et Cosmochimica Acta* **72**, 4642–4659.

Rasmussen D. and Plank T. (2021) Bulk rock data for the central-eastern Aleutian volcanoes.

Rauch M. and Keppler H. (2002) Water solubility in orthopyroxene. *Contrib Mineral Petrol* **143**, 525–536.

Remusat L., Bonnet J.-Y., Bernard S., Buch A. and Quirico E. (2019) Molecular and isotopic behavior of insoluble organic matter of the Orgueil meteorite upon heating. *Geochimica et Cosmochimica Acta* **263**, 235–247.

Remusat L., Piani L. and Bernard S. (2016) Thermal recalcitrance of the organic D-rich component of ordinary chondrites. *Earth and Planetary Science Letters* **435**, 36–44.

Richet P., Bottinga Y. and Javoy M. (1977) A Review of Hydrogen, Carbon, Nitrogen, Oxygen, Sulphur, and Chlorine Stable Isotope Fractionation Among Gaseous Molecules. *Annual Review of Earth and Planetary Sciences* **5**, 65–110.

Righter K. and Drake M. J. (1997) A magma ocean on Vesta: Core formation and petrogenesis of eucrites and diogenites. *Meteoritics & Planetary Science* **32**, 929–944.

Righter K., Herd C. D. K. and Boujibar A. (2020) Redox Processes in Early Earth Accretion and in Terrestrial Bodies. *Elements* **16**, 161–166.

Righter K., Sutton S. R., Danielson L., Pando K. and Newville M. (2016) Redox variations in the inner solar system with new constraints from vanadium XANES in spinels. *American Mineralogist* **101**, 1928–1942.

Robert F., Javoy M., Halbout J., Dimon B. and Merlivat L. (1987) Hydrogen isotope abundances in the solar system. Part II: Meteorites with terrestrial-like D/H ratio. *Geochimica et Cosmochimica Acta* **51**, 1807–1822.

Rosenberg N. D., Browning L. and Bourcier W. L. (2001) Modeling aqueous alteration of CM carbonaceous chondrites. *Meteoritics & Planetary Science* **36**, 239–244.

Rosenthal A., Hauri E. H. and Hirschmann M. M. (2015) Experimental determination of C, F, and H partitioning between mantle minerals and carbonated basalt, CO_2/Ba and CO_2/Nb systematics of partial melting, and the CO_2 contents of basaltic source regions. *Earth and Planetary Science Letters* **412**, 77–87.

Roskosz M., Deloule E., Ingrin J., Depecker C., Laporte D., Merkel S., Remusat L. and Leroux H. (2018) Kinetic D/H fractionation during hydration and dehydration of silicate glasses, melts and nominally anhydrous minerals. *Geochimica et Cosmochimica Acta* **233**, 14–32.

Rubie D. C., Jacobson S. A., Morbidelli A., O'Brien D. P., Young E. D., de Vries J., Nimmo F., Palme H. and Frost D. J. (2015) Accretion and differentiation of the terrestrial planets with implications for the compositions of early-formed Solar System bodies and accretion of water. *Icarus* **248**, 89–108.

Rubin A. E. (2010) Impact melting in the Cumberland Falls and Mayo Belwa aubrites. *Meteoritics & Planetary Science* **45**, 265–275.

Rubin A. E. (2006) Shock, post-shock annealing, and post-annealing shock in ureilites. *Meteoritics & Planetary Science* **41**, 125–133.

Saal A. E., Hauri E. H., Orman J. A. V. and Rutherford M. J. (2013) Hydrogen Isotopes in Lunar Volcanic Glasses and Melt Inclusions Reveal a Carbonaceous Chondrite Heritage. *Science* **340**, 1317–1320.

Saccocia P. J., Seewald J. S. and Shanks W. C. (2009) Oxygen and hydrogen isotope fractionation in serpentine–water and talc–water systems from 250 to 450°C, 50MPa. *Geochimica et Cosmochimica Acta* **73**, 6789–6804.

Sakurai M., Tsujino N., Sakuma H., Kawamura K. and Takahashi E. (2014) Effects of Al content on water partitioning between orthopyroxene and olivine: Implications for lithosphere–asthenosphere boundary. *Earth and Planetary Science Letters* **400**, 284–291.

Sanders I. S., Scott E. R. D. and Delaney J. S. (2017) Origin of mass-independent oxygen isotope variation among ureilites: Clues from chondrites and primitive achondrites. *Meteoritics & Planetary Science* **52**, 690–708.

Sarafian A. R., Hauri E. H., McCubbin F. M., Lapen T. J., Berger E. L., Nielsen S. G., Marschall H. R., Gaetani G. A., Righter K. and Sarafian E. (2017a) Early accretion of water and volatile elements to the inner Solar System: evidence from angrites. *Phil. Trans. R. Soc. A* **375**, 20160209.

Sarafian A. R., John T., Roszjar J. and Whitehouse M. J. (2017b) Chlorine and hydrogen degassing in Vesta's magma ocean. *Earth and Planetary Science Letters* **459**, 311–319.

Sarafian A. R., Nielsen S. G., Marschall H. R., Gaetani G. A., Hauri E. H., Righter K. and Sarafian E. (2017c) Angrite meteorites record the onset and flux of water to the inner solar system. *Geochimica et Cosmochimica Acta* **212**, 156–166.

Sarafian A. R., Nielsen S. G., Marschall H. R., Gaetani G. A., Righter K. and Berger E. L. (2019) The water and fluorine content of 4 Vesta. *Geochimica et Cosmochimica Acta* **266**, 568–581.

Sarafian A. R., Nielsen S. G., Marschall H. R., McCubbin F. M. and Monteleone B. D. (2014) Early accretion of water in the inner solar system from a carbonaceous chondrite-like source. *Science* **346**, 623–626.

Satterwhite C. and Lindstrom M. (1998) Antarctic Meteorite Newsletter. **21**.

Satterwhite C. and Lindstrom M. (1997) Antarctic Meteorite Newsletter. **20**, 14.

Schiller M., Bizzarro M. and Fernandes V. A. (2018) Isotopic evolution of the protoplanetary disk and the building blocks of Earth and the Moon. *Nature* **555**, 507–510.

Schiller M., Bizzarro M. and Siebert J. (2020) Iron isotope evidence for very rapid accretion and differentiation of the proto-Earth. *Science Advances* **6**, eaay7604.

Schimmelmann A., Sessions A. L. and Mastalerz M. (2006) Hydrogen Isotopic (D/H) Composition of Organic Matter During Diagenesis and Thermal Maturation. *Annual Review of Earth and Planetary Sciences* **34**, 501–533.

Schmidt M. W. and Jagoutz O. (2017) The global systematics of primitive arc melts. *Geochemistry, Geophysics, Geosystems* **18**, 2817–2854.

Scott E. R. D. (2020) Iron Meteorites: Composition, Age, and Origin. In *Oxford Research Encyclopedia of Planetary Science*

Seifert F. and Schreyer W. (1969) Stability relations of $K_2Mg_5Si_{12}O_{30}$, and end member of the merrihueite-roedderite group of meteoritic minerals. *Contr. Mineral. and Petrol.* **22**, 190–207.

Sessions A. L. (2016) Factors controlling the deuterium contents of sedimentary hydrocarbons. *Organic Geochemistry* **96**, 43–64.

Sharp Z. D. (2017) Nebular ingassing as a source of volatiles to the Terrestrial planets. *Chemical Geology* **448**, 137–150.

Sharp Z. D. and Olson P. L. (2022) Multi-element constraints on the sources of volatiles to Earth. *Geochimica et Cosmochimica Acta*.

Shaw D. M. (2000) Continuous (dynamic) melting theory revisited. *The Canadian Mineralogist* **38**, 1041–1063.

Shimizu K., Alexander C. M. O'D., Hauri E. H., Sarafian A. R., Nittler L. R., Wang J., Jacobsen S. D. and Mendybaev R. A. (2021) Highly volatile element (H, C, F, Cl, S) abundances and H isotopic compositions in chondrules from carbonaceous and ordinary chondrites. *Geochimica et Cosmochimica Acta* **301**, 230–258.

Shimizu K., Ushikubo T., Kuritani T., Hirano N. and Yamashita S. (2022) Modification for the matrix effect in SIMS-derived water contents of silicate glasses. *Geochemical Journal* **56**, 223–230.

Shimizu N. and Hart S. R. (1982) Applications of the Ion Microprobe to Geochemistry and Cosmochemistry. *Annual Review of Earth and Planetary Sciences* **10**, 483–526.

Shinohara H. (2009) A missing link between volcanic degassing and experimental studies on chloride partitioning. *Chemical Geology* **263**, 51–59.

Shuai K., Hui H., Zhou L. and Li W. (2022) Accretion regions of meteorite parent bodies inferred from a two-endmember isotopic mixing model. *Monthly Notices of the Royal Astronomical Society* **513**, 363–373.

Silver L. A., Ihinger P. D. and Stolper E. (1990) The influence of bulk composition on the speciation of water in silicate glasses. *Contr. Mineral. and Petrol.* **104**, 142–162.

Silver L. and Stolper E. (1985) A Thermodynamic Model for Hydrous Silicate Melts. *The Journal of Geology* **93**, 161–177.

Silver L. and Stolper E. (1989) Water in Albitic Glasses. *Journal of Petrology* **30**, 667–709.

Simon J. I., Christoffersen R., Wang J., Mouser M. D., Mills R. D., Ross D. K., Rahman Z. and Alexander C. M. O'D. (2020) Volatiles in lunar felsite clasts: Impact-related delivery of hydrous material to an ancient dry lunar crust. *Geochimica et Cosmochimica Acta* **276**, 299–326.

Singletary S. J. and Grove T. L. (2003) Early petrologic processes on the ureilite parent body. *Meteoritics & Planetary Science* **38**, 95–108.

Sisson T. W. and Grove T. L. (1993) Temperatures and H_2O contents of low-MgO high-alumina basalts. *Contr. Mineral. and Petrol.* **113**, 167–184.

Skogby H. and Rossman G. R. (1989) OH- in pyroxene; an experimental study of incorporation mechanisms and stability. *American Mineralogist* **74**, 1059–1069.

Sobolev A. V., Asafov E. V., Gurenko A. A., Arndt N. T., Batanova V. G., Portnyagin M. V., Garbe-Schönberg D. and Krasheninnikov S. P. (2016) Komatiites reveal a hydrous Archaean deep-mantle reservoir. *Nature* **531**, 628–632.

Sobolev A. V., Asafov E. V., Gurenko A. A., Arndt N. T., Batanova V. G., Portnyagin M. V., Garbe-Schönberg D., Wilson A. H. and Byerly G. R. (2019) Deep hydrous mantle reservoir provides evidence for crustal recycling before 3.3 billion years ago. *Nature* **571**, 555–559.

Sokol A. G., Kupriyanov I. N. and Palyanov Y. N. (2013) Partitioning of H_2O between olivine and carbonate–silicate melts at 6.3 GPa and 1400 °C: Implications for kimberlite formation. *Earth and Planetary Science Letters* **383**, 58–67.

Stalder R. (2004) Influence of Fe, Cr and Al on hydrogen incorporation in orthopyroxene. *European Journal of Mineralogy* **16**, 703–711.

Stalder R. and Skogby H. (2002) Hydrogen incorporation in enstatite. *European Journal of Mineralogy* **14**, 1139–1144.

Steller T., Burkhardt C., Yang C. and Kleine T. (2022) Nucleosynthetic zinc isotope anomalies reveal a dual origin of terrestrial volatiles. *Icarus* **386**, 115171.

Stephant A., Remusat L. and Robert F. (2017) Water in type I chondrules of Paris CM chondrite. *Geochimica et Cosmochimica Acta* **199**, 75–90.

Stephant A., Wadhwa M., Hervig R., Bose M., Zhao X., Barrett T. J., Anand M. and Franchi I. A. (2021) A deuterium-poor water reservoir in the asteroid 4 Vesta and the inner solar system. *Geochimica et Cosmochimica Acta* **297**, 203–219.

Stephant A., Zhao X., Anand M., Davidson J., Carli C., Cuppone T., Pratesi G. and Franchi I. A. (2023) Hydrogen in acapulcoites and lodranites: A unique source of water for planetesimals in the inner Solar System. *Earth and Planetary Science Letters* **615**, 118202.

Stock M. J., Humphreys M. C. S., Smith V. C., Isaia R. and Pyle D. M. (2016) Late-stage volatile saturation as a potential trigger for explosive volcanic eruptions. *Nature Geosci* **9**, 249–254.

Stöffler D., Keil K. and Edward R.D S. (1991) Shock metamorphism of ordinary chondrites. *Geochimica et Cosmochimica Acta* **55**, 3845–3867.

Stolper E. (1982a) The speciation of water in silicate melts. *Geochimica et Cosmochimica Acta* **46**, 2609–2620.

Stolper E. (1982b) Water in silicate glasses: An infrared spectroscopic study. *Contr. Mineral. and Petrol.* **81**, 1–17.

Sugiura N. and Fujiya W. (2014) Correlated accretion ages and ε^{54}Cr of meteorite parent bodies and the evolution of the solar nebula. *Meteoritics & Planetary Science* **49**, 772–787.

Sutton S., Alexander C. M. O'D., Bryant A., Lanzirotti A., Newville M. and Cloutis E. A. (2017) The bulk valence state of Fe and the origin of water in chondrites. *Geochimica et Cosmochimica Acta* **211**, 115–132.

Tagawa S., Sakamoto N., Hirose K., Yokoo S., Hernlund J., Ohishi Y. and Yurimoto H. (2021) Experimental evidence for hydrogen incorporation into Earth's core. *Nat Commun* **12**, 2588.

Taliaferro M. (2022) generalized_esd(x,alpha,k). (https://www.mathworks.com/matlabcentral/fileexchange/63701-generalized_esd-x-alpha-k), MATLAB Central File Exchange. Retrieved March 18, 2022.

Tartèse R., Anand M. and Franchi I. A. (2019) H and Cl isotope characteristics of indigenous and late hydrothermal fluids on the differentiated asteroidal parent body of Grave Nunataks 06128. *Geochimica et Cosmochimica Acta* **266**, 529–543.

Tenner T. J., Hirschmann M. M., Withers A. C. and Ardia P. (2012) H_2O storage capacity of olivine and low-Ca pyroxene from 10 to 13 GPa: consequences for dehydration melting above the transition zone. *Contrib Mineral Petrol* **163**, 297–316.

Tenner T. J., Hirschmann M. M., Withers A. C. and Hervig R. L. (2009a) Hydrogen partitioning between nominally anhydrous upper mantle minerals and melt between 3 and 5 GPa and applications to hydrous peridotite partial melting. *Chemical Geology* **262**, 42–56.

Tenner T. J., Hirschmann M. M., Withers A. C. and Hervig R. L. (2009b) Hydrogen partitioning between nominally anhydrous upper mantle minerals and melt between 3 and 5 GPa and applications to hydrous peridotite partial melting. *Chemical Geology* **262**, 42–56.

Thomassin D., Piani L., Villeneuve J., Caumon M.-C., Bouden N. and Marrocchi Y. (2023) The high-temperature origin of hydrogen in enstatite chondrite chondrules and implications for the origin of terrestrial water. *Earth and Planetary Science Letters* **616**, 118225.

Tollan P. M. E., O'Neill H. St. C. and Hermann J. (2018) The role of trace elements in controlling H incorporation in San Carlos olivine. *Contrib Mineral Petrol* **173**, 89.

Tollan P. M. E., Smith R., O'Neill H. St. C. and Hermann J. (2017) The responses of the four main substitution mechanisms of H in olivine to H_2O activity at 1050 °C and 3 GPa. *Prog. in Earth and Planet. Sci.* **4**, 14.

Touboul M., Kleine T., Bourdon B., Van Orman J. A., Maden C. and Zipfel J. (2009) Hf–W thermochronometry: II. Accretion and thermal history of the acapulcoite–lodranite parent body. *Earth and Planetary Science Letters* **284**, 168–178.

Towbin H., Plank T., Klein E. and Hauri E. H. (2023) Measuring H_2O Concentrations in Olivine by Secondary Ion Mass Spectrometry: Challenges and Paths Forward. *msam* **108**, 982–940.

Treiman A. H. and Berkley J. L. (1994) Igneous petrology of the new ureilites Nova 001 and Nullarbor 010. *Meteoritics* **29**, 843–848.

Turner M., Ireland T., Hermann J., Holden P., Alberto Padrón-Navarta J., H. Hauri E. and Turner S. (2015) Sensitive high resolution ion microprobe – stable isotope (SHRIMP-SI) analysis of water in silicate glasses and nominally anhydrous reference minerals. *Journal of Analytical Atomic Spectrometry* **30**, 1706–1722.

Urann B. M., Le Roux V., Jagoutz O., Müntener O., Behn M. D. and Chin E. J. (2022) High water content of arc magmas recorded in cumulates from subduction zone lower crust. *Nat. Geosci.* **15**, 501–508.

Vacher L. G., Piani L., Rigaudier T., Thomassin D., Florin G., Piralla M. and Marrocchi Y. (2020) Hydrogen in chondrites: Influence of parent body alteration and atmospheric contamination on primordial components. *Geochimica et Cosmochimica Acta* **281**, 53–66.

Velbel M. A. (2014) Terrestrial weathering of ordinary chondrites in nature and continuing during laboratory storage and processing: Review and implications for Hayabusa sample integrity. *Meteoritics & Planetary Science* **49**, 154–171.

Velbel M. A. (1988) The Distribution and Significance of Evaporitic Weathering Products on Antarctic Meteorites. *Meteoritics* **23**, 151–159.

Velbel M. A., Long D. T. and Gooding J. L. (1991) Terrestrial weathering of Antarctic stone meteorites: Formation of Mg-carbonates on ordinary chondrites. *Geochimica et Cosmochimica Acta* **55**, 67–76.

Walker A. M., Hermann J., Berry A. J. and O'Neill H. St. C. (2007) Three water sites in upper mantle olivine and the role of titanium in the water weakening mechanism. *Journal of Geophysical Research: Solid Earth* **112**.

Walker R. J. (2009) Highly siderophile elements in the Earth, Moon and Mars: Update and implications for planetary accretion and differentiation. *Geochemistry* **69**, 101–125.

Wang C., Eley Y., Oakes A. and Hren M. (2017) Hydrogen isotope and molecular alteration of n-alkanes during heating in open and closed systems. *Organic Geochemistry* **112**, 47–58.

Wang C.-Y., Flesch L. M., Silver P. G., Chang L.-J. and Chan W. W. (2008) Evidence for mechanically coupled lithosphere in central Asia and resulting implications. *Geology* **36**, 363–366.

Wang S.-J., Wang W., Zhu J.-M., Wu Z., Liu J., Han G., Teng F.-Z., Huang S., Wu H., Wang Y., Wu G. and Li W. (2021) Nickel isotopic evidence for late-stage accretion of Mercury-like differentiated planetary embryos. *Nat Commun* **12**, 294.

Warren P. H. (2012) Parent body depth–pressure–temperature relationships and the style of the ureilite anatexis. *Meteoritics & Planetary Science* **47**, 209–227.

Warren P. H. (2011a) Stable isotopes and the noncarbonaceous derivation of ureilites, in common with nearly all differentiated planetary materials. *Geochimica et Cosmochimica Acta* **75**, 6912–6926.

Warren P. H. (2011b) Stable-isotopic anomalies and the accretionary assemblage of the Earth and Mars: A subordinate role for carbonaceous chondrites. *Earth and Planetary Science Letters* **311**, 93–100.

Warren P. H. and Kallemeyn G. W. (1989) Geochemistry of polymict ureilite EET83309, and a partially-disruptive impact model for ureilite origin. *Meteoritics* **24**, 233–246.

Warren P. H., Ulff-Møller F., Huber H. and Kallemeyn G. W. (2006) Siderophile geochemistry of ureilites: A record of early stages of planetesimal core formation. *Geochimica et Cosmochimica Acta* **70**, 2104–2126.

Weis F. A., Skogby H., Troll V. R., Deegan F. M. and Dahren B. (2015) Magmatic water contents determined through clinopyroxene: Examples from the Western Canary Islands, Spain. *Geochemistry, Geophysics, Geosystems* **16**, 2127–2146.

Weisberg M. K., McCoy T. J. and Krot A. N. (2006) Systematics and Evaluation of Meteorite Classification. In *Meteorites and the Early Solar System II* University of Arizona Press, Tucson, Arizona. pp. 19–52.

Wetzel D. T., Hauri E. H., Saal A. E. and Rutherford M. J. (2015) Carbon content and degassing history of the lunar volcanic glasses. *Nature Geosci* **8**, 755–758.

Wetzel D. T., Rutherford M. J., Jacobsen S. D., Hauri E. H. and Saal A. E. (2013) Degassing of reduced carbon from planetary basalts. *Proceedings of the National Academy of Sciences* **110**, 8010–8013.

Wiens T. (2021) Linear Regression with Errors in X and Y. (https://www.mathworks.com/matlabcentral/fileexchange/26586-linear-regression-with-errors-in-x-and-y), MATLAB Central File Exchange. Retrieved November 12, 2021.

Wilbur Z. E., Udry A., McCubbin F. M., vander Kaaden K. E., DeFelice C., Ziegler K., Ross D. K., McCoy T. J., Gross J., Barnes J. J., Dygert N., Zeigler R. A., Turrin B. D. and McCoy C. (2022) The effects of highly reduced magmatism revealed through aubrites. *Meteoritics & Planetary Science* **57**, 1387–1420.

Wilson L., Goodrich C. A. and Van Orman J. A. (2008) Thermal evolution and physics of melt extraction on the ureilite parent body. *Geochimica et Cosmochimica Acta* **72**, 6154–6176.

Wilson L. and Keil K. (2012) Volcanic activity on differentiated asteroids: A review and analysis. *Geochemistry* **72**, 289–321.

Wilson L., Keil K., Browning L. B., Krot A. N. and Bourcier W. (1999) Early aqueous alteration, explosive disruption, and reprocessing of asteroids. *Meteoritics & Planetary Science* **34**, 541–557.

Wilson L., Keil K. and McCoy T. J. (2010) Pyroclast loss or retention during explosive volcanism on asteroids: Influence of asteroid size and gas content of melt. *Meteoritics & Planetary Science* **45**, 1284–1301.

Withers A. C., Hirschmann M. M. and Tenner T. J. (2011) The effect of Fe on olivine H_2O storage capacity: Consequences for H_2O in the martian mantle. *American Mineralogist* **96**, 1039–1053.

Wlotzka F. (1972) Haverö Ureilite: Evidence for Recrystallization and Partial Reduction. *Meteoritics* **7**, 591–600.

Wood B. J., Smythe D. J. and Harrison T. (2019) The condensation temperatures of the elements: A reappraisal. *American Mineralogist* **104**, 844–856.

Wu J., Desch S. J., Schaefer L., Elkins-Tanton L. T., Pahlevan K. and Buseck P. R. (2018) Origin of Earth's Water: Chondritic Inheritance Plus Nebular Ingassing and Storage of Hydrogen in the Core. *Journal of Geophysical Research: Planets* **123**, 2691–2712.

Wudarska A., Wiedenbeck M., Słaby E., Lepland A., Birski Ł. and Simon K. (2018) Halogen chemistry and hydrogen isotopes of apatite from the >3.7 Ga Isua supracrustal belt, SW Greenland. *Precambrian Research* **310**, 153–164.

Yang Y., Liu W., Qi Z., Wang Z., Smyth J. R. and Xia Q. (2019) Re-configuration and interaction of hydrogen sites in olivine at high temperature and high pressure. *American Mineralogist* **104**, 878–889.

Yang Y.-N., Du Z., Lu W., Qi Y., Zhang Y.-Q., Zhang W.-F. and Zhang P.-F. (2023) NanoSIMS analysis of water content in bridgmanite at the micron scale: An experimental approach to probe water in Earth's deep mantle. *Frontiers in Chemistry* **11**, 1166593.

Yokoyama T., Nagai Y., Fukai R. and Hirata T. (2019) Origin and Evolution of Distinct Molybdenum Isotopic Variabilities within Carbonaceous and Noncarbonaceous Reservoirs. *ApJ* **883**, 62.

Yokoyama T., Nagashima K., Nakai I., Young E. D., Abe Y., Aléon J., Alexander C. M. O'D., Amari S., Amelin Y., Bajo K., Bizzarro M., Bouvier A., Carlson R. W., Chaussidon M., Choi B.-G., Dauphas N., Davis A. M., Di Rocco T., Fujiya W., Fukai R., Gautam I., Haba M. K., Hibiya Y., Hidaka H., Homma H., Hoppe P., Huss G. R., Ichida K., Iizuka T., Ireland T. R., Ishikawa A., Ito M., Itoh S., Kawasaki N., Kita N. T., Kitajima K., Kleine T., Komatani S., Krot A. N., Liu M.-C., Masuda Y., McKeegan K. D., Morita M., Motomura K., Moynier F., Nguyen A., Nittler L., Onose M., Pack A., Park C., Piani L., Qin L., Russell S. S., Sakamoto N., Schönbächler M., Tafla L., Tang H., Terada K., Terada Y., Usui T., Wada S., Wadhwa M., Walker R. J., Yamashita K., Yin Q.-Z., Yoneda S., Yui H., Zhang A.-C., Connolly H. C., Lauretta D. S., Nakamura T., Naraoka H., Noguchi T., Okazaki R., Sakamoto K., Yabuta H., Abe M., Arakawa M., Fujii A., Hayakawa M., Hirata Naoyuki, Hirata Naru, Honda R., Honda C., Hosoda S., Iijima Y., Ikeda H., Ishiguro M., Ishihara Y., Iwata T., Kawahara K., Kikuchi S., Kitazato K., Matsumoto K., Matsuoka M., Michikami T., Mimasu Y., Miura A., Morota T., Nakazawa S., Namiki N., Noda H., Noguchi R., Ogawa N., Ogawa K., Okada T., Okamoto C., Ono G., Ozaki M., Saiki T., Sakatani N., Sawada H., Senshu H., Shimaki Y., Shirai K., Sugita S., Takei Y., Takeuchi H., Tanaka S., Tatsumi E., Terui F., Tsuda Y., Tsukizaki R., Wada K., Watanabe S., Yamada M., Yamada T., Yamamoto Y., Yano H., Yokota Y., Yoshihara K., Yoshikawa M., Yoshikawa K., Furuya S., Hatakeda K., Hayashi T., Hitomi Y., Kumagai K., Miyazaki A., Nakato A., Nishimura M., Soejima H., Suzuki A., Yada T., Yamamoto D., Yogata K., Yoshitake M., Tachibana S. and Yurimoto H. (2022) Samples returned from the asteroid Ryugu are similar to Ivuna-type carbonaceous meteorites. *Science* **0**, eabn7850.

York D., Evensen N. M., Martínez M. L. and De Basabe Delgado J. (2004) Unified equations for the slope, intercept, and standard errors of the best straight line. *American Journal of Physics* **72**, 367–375.

Yoshizaki T. and McDonough W. F. (2020) The composition of Mars. *Geochimica et Cosmochimica Acta* **273**, 137–162.

Yugami K., Miyamoto M. and Takeda H. (1995) The Similar Reduction Processes of Primitive Achondrites from Different Parent Bodies. *Meteoritics* **30**, 605.

Zhang K., Bosman A. D. and Bergin E. A. (2020) Excess C/H in Protoplanetary Disk Gas from Icy Pebble Drift Across the CO Snowline. *ApJL* **891**, L16.

Zhao Y.-H., Ginsberg S. B. and Kohlstedt D. L. (2004) Solubility of hydrogen in olivine: dependence on temperature and iron content. *Contrib Mineral Petrol* **147**, 155–161.

Zhu K., Moynier F., Schiller M., Wielandt D., Larsen K. K., Kooten E. M. M. E. van, Barrat J.-A. and Bizzarro M. (2020) Chromium Isotopic Constraints on the Origin of the Ureilite Parent Body. *ApJ* **888**, 126.